Assessment of Ground-Based Microwave Radiometer Calibration to Enable Investigation of Gas Absorption Models

Inaugural-Dissertation
zur
Erlangung des Doktorgrades
der Mathematisch-Naturwissenschaftlichen Fakultät
der Universität zu Köln

vorgelegt von
Gerrit Maschwitz

aus Hannover

2013

Berichterstatter (Gutachter):	Prof. Dr. Susanne Crewell
	PD Dr. Ulrich Löhnert
Tag der mündlichen Prüfung:	22.01.2013

Abstract

Ground-based microwave radiometers are becoming more and more common for remotely sensing the atmospheric temperature and humidity profile, as well as path integrated cloud liquid water content. Several studies have been published, which compare radiosonde profiles with temperature profiles derived from microwave radiometer measurements and find biases of up to 1 K. The retrieved temperature profile is based on radiometric measurements and radiative transfer calculations. Once the accuracy of radiometer measurements is known, these can be used to validate existing gas absorption models. As the absolute accuracy of microwave radiometer measurements is determined by the quality of the calibration, this work investigates the uncertainty of two calibration techniques, which are commonly used with microwave radiometers. Namely, these are the liquid nitrogen calibration and the tipping curve calibration (*Han and Westwater*, 2000). Both methods are known to have open issues concerning systematic offsets and calibration repeatability. In this regard, this work focuses on the error assessment for the absolute calibration of the network suitable microwave radiometer HATPRO-G2 (Humidity And Temperature PROfiler – Generation 2), which makes up a significant part of the worldwide available systems (*Rose et al.*, 2005). In order to capture dry high altitude conditions on the one side and mid-latitude, close to sea level conditions on the other side, the analysis is based on two deployments. Between August and October 2009, HATPRO-G2 was part of the Radiative Heating of Underexplored Bands Campaign – Part 2 (RHUBC-II) in Northern Chile (5320 m above mean sea level) conducted within the Atmospheric Radiation Measurement (ARM) program. Since 2010, it is part of the JOYCE (Jülich ObservatorY for Cloud Evolution) site located in Germany 92 m above mean sea level. For each of the deployments, a detailed error propagation for both techniques is performed.

The uncertainty range of brightness temperature (T_b) measurements based on a single liquid nitrogen calibration is mainly caused by a reflective component from the liquid nitrogen surface of the cold calibration target. The overall calibration uncertainty is assessed for typical T_b values measured at each deployment. For RHUBC-II, the maximum uncertainty of T_b has been determined to ± 1.6 K in the K-band and to ± 1.0 K in the V-band. For JOYCE, the maximum uncertainty is assessed to be ± 1.5 K in the K-band and ± 0.6 K in the V-band. When a standing wave phenomena at the cold calibration point is eliminated by averaging several calibrations, the

uncertainty in the K-band can be reduced to ±0.8 K for both deployments. In the V-band, the uncertainties are reduced to values less or equal ±0.7 K for both deployments. Furthermore, the analyses of the liquid nitrogen calibration has revealed, that the pressure dependent boiling point correction for liquid nitrogen, originally used by HATPRO-G2, is only exact for standard pressure conditions. Therefore, the boiling point correction has been modified and is now valid for all altitudes. At the low pressure conditions of RHUBC-II (530 hPa), the improved boiling point correction shifts the cold target temperature compared to the previously used formulation by more than 1 K.

HATPRO-G2 has seven channels in the K-band and seven channels in the V-band. At standard pressure conditions, only the K-band channels are transparent enough to be calibrated by the tipping curve calibration. However, at 530 hPa, the technique can be applied to two low opacity channels in the V-band as well. This offers the unique opportunity of an independent validation of the liquid nitrogen calibration in the V-band. The analysis shows, that the uncertainty in the tipping curve calibration is mainly due to atmospheric inhomogeneities. For RHUBC-II, the total uncertainty is assessed to be ±0.1 K to ±0.2 K in the K-band and ±0.6 K and ±0.7 K for the two V-band channels at 51 GHz and 52 GHz. For the low altitude deployment at JOYCE, the total uncertainties for K-band channels are ±0.2 K to ±0.6 K.

Finally, the well-characterized radiometer measurements are used to investigate current absorption models. The profiles of temperature, humidity, and pressure from 62 clear sky radiosondes are used for T_b simulations at zenith and compared to HATPRO-G2 measurements. Biases, outside the uncertainty range of the calibration can be ascribed to errors within the gas absorption coefficients. It is found that the results of the Atmospheric Model (AM) (*Paine*, 2012), which uses the most recent oxygen absorption parameters (*Tretyakov et al.*, 2005, *Makarov et al.*, 2011), are closest to RHUBC-II measurements.

Zusammenfassung

Bodengebundene Mikrowellenradiometer werden zunehmend für die Fernerkundung von Temperatur- und Feuchteprofilen, sowie die integrierten Flüssigwassergehalte genutzt. In mehreren publizierten Vergleichsstudien zwischen Radiosondenaufstiegen und aus Mikrowellenradiometermessungen abgeleiteten Temperaturprofilen sind Abweichungen von bis zu 1 K festgestellt worden. Die Ableitung der Temperaturprofile basiert auf Mikrowellenradiometermessungen und Strahlungstransportrechnungen. Daher können Mikrowellenradiometermessungen mit bekannter Genauigkeit zur Validierung von Gasabsorptionsmodellen verwendet werden. Da die absolute Messgenauigkeit von der Güte der Kalibration abhängt, untersucht diese Arbeit die Unsicherheiten, die mit zwei für Mikrowellenradiometer üblichen Kalibrationsverfahren vebunden sind. Namentlich sind dies die Flüssigstickstoffkalibration und die sogenannte „tipping curve“ Kalibration (*Han und Westwater*, 2000). Beide Verfahren zeichnen sich durch noch ungelöste Fragen bezüglich systematischer Fehler und der Wiederholbarkeit aus. Von diesen Fragestellungen ausgehend, liegt der Fokus dieser Arbeit auf der Untersuchung der Kalibrationsverfahren anhand des Mikrowellenradiometers HATPRO-G2 (Humidity and Temperature PROfiler – Generation 2), welches einen Großteil der weltweit operierenden Radiometer dieser Art ausmacht (*Rose et al.*, 2005). Die Analyse basiert auf Daten von zwei verschiedene Messstandorten, um auf der einen Seite trockene Bedingungen in großen Höhen und auf der anderen Seite typische Bedingungen der mittleren Breiten auf Meeresniveau, abzudecken. Zwischen August und Oktober 2009 war HATPRO-G2 im Rahmen des „Atmospheric Radiation Measurement“ (ARM) Programms teil der zweiten Phase der Messkampagne „Radiative Heating of Underexplored Bands Campaign“ (RHUBC-II) im Norden von Chile (5320 m über NN). Seit 2011 ist das Radiometer fester Bestanteil des Jülich ObservatorY for Cloud Evolution, kurz JOYCE (92 m über NN). Für beide Messstandorte wird eine detaillierte Fehlerbetrachtung von zwei Kalibrationsverfahren durchgeführt.

Der Unsicherheitsbereich von Messungen der Helligkeitstemperatur (T_b), die auf einer einzelnen Flüssigstickstoffkalibration beruhen, rührt größtenteils von einer reflektiven Komponente her, die von der Oberfläche des Flüssigstickstoffs empfangen wird. Die Gesamtunsicherheit für beide Messstandorte wird für typische Werte der gemessenen Helligkeitstemperatur T_b ausgewertet. Für RHUBC-II werden die maximalen T_b Unsicherheiten im K-Band zu ± 1.6 K und im V-Band zu ± 1.0 K bestimmt.

Für JOYCE sind die entsprechenden Werte ±1.5 K im K-Band und ±0.6 K im V-Band. Wenn ein beobachtetes Stehwellenphänomen am kalten Kalibrationspunkt durch Mittelung mehrerer Kalibrationen eliminiert wird, werden die Unsicherheiten im K-Band für beide Messstandorte auf ±0.8 K reduziert. Im V-Band, sind die reduzierten Unsicherheiten kleiner oder gleich ±0.7 K. Weiterhin hat die Analyse der Flüssigstickstoffkalibration ergeben, daßdie ursprünglich verwendete druckabhängige Siedepunktkorrektur für flüssigen Stickstoff, nur unter Standarddruck ausreichend exakte Ergebnisse liefert. Daher wurde die Siedepunktkorrektur modifiziert und ist nun auf allen Höhen anwendbar. Auf dem während RHUBC-II herschenden Druckniveau von 530 hPa, verschiebt die verbesserte Siedepunktkorrektur die angenommene Temperatur der kalten Last um mehr als 1 K.

HATPRO-G2 besitzt sieben Kanäle im K-Band und sieben Kanäle im V-Band. Unter Standarddruckbedingungen sind nur die Kanäle im K-Band ausreichend transparent, um mit der „tipping curve“ Methode kalibriert zu werden. Allerdings können bei einem Druck von 530 hPa auch zwei V-Band Kanäle mit niedriger Opazität per „tipping curve“ kalibriert werden. Dies bietet die Möglichkeit einer unabhängigen Validierung der Flüssigstickstoffkalibration im V-Band. Die Analyse zeigt, dass die Unsicherheit der „tipping curve“ Kalibration hauptsächlich durch atmosphärische Inhomogenitäten verursacht wird. Für RHUBC-II, wird die Gesamtunsicherheit im K-Band zu ±0.1 K bis ±0.2 K und für die beiden Kanäle im V-Band bei 51 GHz und 52 GHz zu ±0.6 K und ±0.7 K bestimmt. Für den Messstandort nahe dem Meeresniveau (JOYCE) bewegen sich die Unsicherheiten im K-Band zwischen ±0.2 K und ±0.6 K.

Nach Abschätzung der absoluten Genauigkeit der Radiometermessungen, werden diese letztendlich zur Untersuchung existierender Gasabsorptionsmodelle verwendet. Die Temperatur-, Feuchte- und Druckprofile von 62 wolkenfreien Radiosondenaufstiegen werden zur T_b Simulation im Zenit verwendet. Diese T_b Simulationen werden dann mit HATPRO-G2 Messungen verglichen. Abweichungen zwischen Modell und Messung außerhalb der bestimmten Unsicherheitsbereiche, können Fehlern innerhalb der Gasabsorptionsmodelle zugeschrieben werden. Es wird festgestellt, dass die Resultate des "Atmospheric Model“ (AM) (*Paine*, 2012), welches die aktuellsten Sauerstoffabsorptionsparameter verwendet (*Tretyakov et al.*, 2005, *Makarov et al.*, 2011), die geringsten Abweichungen zu den RHUBC-II Messungen zeigen.

TABLE OF CONTENTS

1. Introduction

Microwave radiometers (MWRs) are passive remote sensing instruments. The advantage of using microwave frequencies is, that the atmosphere is mostly transparent for these wavelengths, even in cloudy conditions. Therefore, MWRs have become a main pillar within the global space-borne Earth monitoring system. Radiometers, flown on orbiting satellites, operationally provide global information on atmospheric water and temperature. The sensors are either imagers, like the Special Sensor Microwave Imager (SSM/I) (*Hollinger et al.*, 1990), which measure column information, or sounders, like for example the Advanced Microwave Sounding Unit (AMSU) (*Kidder et al.*, 1998), which can deliver profile information by measuring along atmospheric absorption lines. Furthermore, microwave radiances observed from space are operationally assimilated in Numerical Weather Prediction (NWP) models (*Bauer et al.*, 2010, *Geer and Bauer*, 2011).

However, research of the recent years suggests, that satellite observations should be complemented by ground-based MWR networks, which add valuable information from the lower troposphere. Compared to space-borne instruments, ground-based observations have the advantage that they do not suffer from background emission of the Earth's surface, when observing the lower troposphere. Therefore, they are very valuable for observing the planetary boundary layer. In comparison to radiosonde profiles, ground-based instruments provide a high temporal resolution. Again, this is useful for observing the temporal development of the lower troposphere.

The aim is to build up ground-based networks continuously providing temperature and humidity profiles, which can be assimilated into NWP models (*Cimini et al.*, 2012). The ongoing work towards an operational MWR network mainly divides into the improvement of retrieval algorithms, on the one hand, and development of accurate and reproducible radiometer calibration techniques, on the other hand. This work focuses on the error assessment for the absolute calibration of a network suitable MWR, which makes up a significant part of the world-wide available systems (*Rose et al.*, 2005).

Ground-based temperature profiling using frequencies in the V-band ($50 - 75\,\mathrm{GHz}$) has first been suggested by *Westwater* (1965) and is now performed operationally at several sites worldwide (e.g., *Güldner and Spänkuch* (2000)). However, compared to radiosondes profiles, temperature profiles derived from MWR brightness temperature

(T_b) measurements can show biases up to 1 K (*Liljegren*, 2002, *Gaffard and Hewison*, 2003, *Löhnert and Maier*, 2012). The retrieved temperature profile is based on radiometric measurements and radiative transfer calculations. Therefore, deviations from radiosonde profiles can be caused by uncertainties: 1) of radiosonde measurements, 2) within the used oxygen absorption model, and 3) of radiometer measurements.

Firstly, in contrast to humidity profiles taken by radiosondes (*Miloshevich et al.*, 2009), there is no known systematic bias of the temperature profile. This means, that the total accuracy of the temperature profile, which is typically ≈ 0.5 K in the troposphere (*Nash et al.*, 2010), should not lead to a persistent bias, when analyzing large sets of radio soundings.

Secondly, the bias can be caused by uncertainties in the oxygen absorption parameters. Particularly close to 60 GHz, the simulation of total absorption is complex, because several single absorption lines overlap due to pressure broadening. Moreover, T_b calculations are very sensitive on how line broadening and mixing are parameterized in the absorption model (*Boukabara et al.*, 2005). *Cadeddu et al.* (2007) evaluate oxygen absorption characteristics around 60 GHz by radiometer measurements and test different sets of absorption coefficients. They show, that different sets of oxygen absorption line parameters lead to retrieved temperature profiles that may differ by more than 2 K. Similar issues are present in the K-band ($18 - 27$ GHz) for the remote sensing of water vapor (*Hewison*, 2007). Existing oxygen absorption models are validated with field measurements, because the oxygen line parameters mostly originate from different versions of the HIgh-resolution TRANsmission (HITRAN) database, which is based on laboratory measurements (*Rothman et al.*, 2009). Several studies compare T_b simulations, which use radiosonde profiles as input, directly to simultaneous MWR zenith measurements. In the V-band, *Cimini et al.* (2004), *Liljegren* (2002), *Hewison et al.* (2006) find biases between -2 K and $+3$ K for close to sea level deployments. Furthermore, the deviation between radiative transfer calculations that use different existing oxygen absorption models, are of the same order (*Cimini et al.*, 2004, *Hewison et al.*, 2006).

Thirdly, the retrieved profiles directly depend on the accuracy of radiometer measurements. While state-of-the-art radiometers are capable of detecting T_b changes in the order of 0.1 K, there is still potential to improve the absolute measurement accuracy. The absolute accuracy is determined by the uncertainty of the calibration. MWR channels in the V-band are commonly calibrated by a Liquid Nitrogen (LN_2) calibration, where a black body target, cooled by LN_2, is used as reference. The uncertainty within the LN_2 target measurement dominates the total calibration uncertainty for non-saturated radiometer channels and reduces the absolute measurement accuracy (*Hewison and Gaffard*, 2003). They show that the LN_2 calibration of a MWR induces T_b uncertainties in the V-band below 1 K for typical mid-latitude, close to sea level conditions. However, the uncertainty depends on the calibration setup of the individual radiometer. Furthermore, the calibration uncertainty of each channel

depends on the difference between measured T_b and the cold reference temperature and therefore as well on the atmospheric conditions.

As an alternative to the LN_2 calibration, *Han and Westwater* (2000) suggest to use the tipping curve calibration to reduce the calibration accuracy to 0.5 K. This technique is commonly used to calibrate MWR channels in the K-band (*Mattioli et al.*, 2005, *Cimini et al.*, 2004, *Hewison et al.*, 2006). However, the tipping curve calibration can only be performed under horizontally homogeneous, i.e. clear sky, conditions. Even more, it can only be applied to radiometer channels that measure at low-opacity frequencies. For these channels, the uncertainty hardly depends on measured T_b, because clear sky measurements are used instead of a fixed LN_2 target. Unfortunately, this is not applicable for V-band channels, as their opacity is too large under standard pressure conditions. Nevertheless, the comparison of the tipping curve calibration with the LN_2 calibration may help to identify systematic calibrations errors. The lessons learned might also be valuable for measurements at channels that solely rely on the LN_2 calibration method.

It can be summarized, that the total MWR calibration uncertainty may be in the same order as the uncertainty within the gas absorption line parameters. Therefore, a detailed assessment of error sources within MWR calibration procedures is necessary. If the uncertainty is sufficiently small, oxygen absorption parameters can be adapted to MWR measurements. Otherwise, the used calibration technique is still to be improved.

Finally, to come back to the idea of a MWR network, a well characterized measurement is essential for the comparability of the different instruments. The calibration uncertainty and repeatability and the total measurement uncertainty depends on the atmospheric conditions and the individual instrument design. Therefore, measurement uncertainties have to be assessed for each deployment. In this regard, the main goal of this work is to the investigate the LN_2 calibration and the tipping curve calibration in order to

- investigate multiple error sources that contribute to the calibration uncertainty,
- quantify the impact of the total calibration uncertainty on the absolute measurement accuracy,
- improve the overall calibration accuracy by a comparative assessment of both techniques.

In this respect, MWR measurements from a extremely dry, high altitude deployment within the Radiative Heating of Underexplored Bands Campaign – Part II (RHUBC-II) are exploited. As part of the Atmospheric Radiation Measurement (ARM) program, this campaign was conducted at an altitude of 5322 m in the Atacama desert in Northern Chile between August and October 2009. Amongst several

other instruments, which measure the atmospheric radiation thoughout the electromagnetic spectrum, microwave frequency observations in the K- and V-band are provided by the 14-channel MWR HATPRO-G2 Humidity And Temperature PROfiler – Generation 2 (*Rose et al.*, 2005). HATPRO-G2 measurements are used within this work.

Observing at a high altitude deployment has different advantages. One aspect is related to the radiometer calibration. At the RHUBC-II pressure level of 530 hPa, not only K-band channels, but also two low opacity channels in the V-band can be calibrated by the tipping curve calibration. This offers the unique opportunity of an independent validation of the LN_2 calibration of V-band channels.

The Humidity And Temperature PROfiler – Generation 2 (HATPRO-G2) uses the LN_2 calibration for the initial calibration of all 14 channels. Besides the LN_2 target an internal ambient temperature target is used. Additionally, HATPRO-G2 perform tipping curve calibrations. The tipping curve calibration method exploits the fact that under horizontally homogeneous conditions, atmospheric opacity linearly scales with the air mass along the observed path (*Han and Westwater*, 2000). Practically, it uses elevation scans to determine the zenith opacity τ from a number of opacity-air mass pairs (*Han and Westwater*, 2000). The impact of atmospheric inhomogeneities is minimized by setting quality thresholds for the linearity of obtained opacity-air mass pairs. In order to gain the most accurate tipping curve calibration, the exact air mass at each observed elevation angle is determined. The air mass is derived from a ray tracing algorithm and includes the effect of Earth's curvature and atmospheric refraction. Furthermore, measured T_b is corrected for the finite beam width. Eventually, the total uncertainty is determined by the residual impact of atmospheric inhomogeneities and the derivation of the mean radiative temperature of the atmosphere.

Finally, the well-characterized radiometer measurements are used to investigate current absorption models in the K- and V-band. Biases outside the uncertainty range of the calibration can be assigned to errors within the gas absorption parameters. At this point, another advantage of a high altitude deployment comes into play. Radiometric observations at low opacities give insight into absorption processes in the middle-to-upper-troposphere, while the atmospheric states at these altitudes are usually not adequately represented within gas absorption models that are based on laboratory measurements.

During RHUBC-II, radiometric measurements were accompanied by regular radiosonde launches under clear skies. The given profiles of temperature and humidity and pressure are used to simulate T_b for HATPRO-G2 channels in order to investigate different existing absorption models. Furthermore, differences between the oxygen absorption models in the assumed line broadening and mixing parameters are expected to have different impact at high altitudes, because at low pressures the absorption complex 60 GHz starts to split up into single absorption lines. For comparison, simi-

lar investigations as for RHUBC-II are made for a typical low altitude, mid-latitude HATPRO-G2 deployment at JOYCE[1] (Jülich ObservatorY for Cloud Evolution).

The work is structured as follows:

- The second chapter gives a short introduction into radiative transfer theory. It provides the basis for microwave absorption of atmospheric gases. Furthermore, existing gas absorption models are introduced.
- The third chapter provides basic information about microwave radiometry. The measurement principle and the hardware of microwave radiometers are discussed.
- The fourth chapter gives a short overview on the used observations from two deployments, which are characterized by different atmospheric regimes. On the one hand, high altitude, low water vapor conditions and, on the other hand, low altitude, mid-latitude conditions. Particularly, the radiometer HATPRO-G2, which provides the data for this work, is introduced with a focus on the implemented calibration procedures.
- In the fifth chapter, an adequate simulation of HATPRO-G2 measurements is investigated. The effects of the Earth's curvature and refraction, the antenna beam width, and the effect of band-pass filters are analyzed.
- The core of this work is the sixth chapter, which assesses the two absolute calibration techniques used with HATPRO-G2. Namely, these are the LN_2 calibration and the tipping curve calibration. Both techniques are discussed with regard to their total uncertainty and repeatability.
- Finally, the seventh chapter uses the results from chapter six to validate gas absorption models. Brightness temperatures derived from radiative transfer simulations, which use clear radiosonde profile of temperature, humidity, and pressure as input, are compared to HATPRO-G2 measurements.

[1] http://www.geomet.uni-koeln.de/allgemein/forschung/joyce/

2. Microwave Radiative Transfer

The atmosphere's energy budget is driven by the short-wave solar radiation and the long-wave thermal emission from the Earth's surface. Throughout the electromagnetic spectrum both components interact with the atmospheric gases and hydrometeors by reflection, scattering, and absorption. Radiative transfer forward models simulate these processes for radiation passing though the atmosphere.

More than 99% of the total radiation energy is contained in wavelengths between 0.1 µm and 100 µm (*Petty*, 2006, p. 68). The microwave spectrum includes wavelengths between 10 cm to 1 mm, corresponding to frequencies between 3 GHz to 300 GHz (*Janssen*, 1993, p. 1). In contrast to the other spectral regions, these frequencies do not contribute significantly to the atmospheric energy budget. Still, microwave frequencies are very valuable for atmospheric sciences, because the transmittance of radiation within the atmosphere is very high (Fig. 2.1). This fact allows to observe atmospheric columns with remote-sensing instruments.

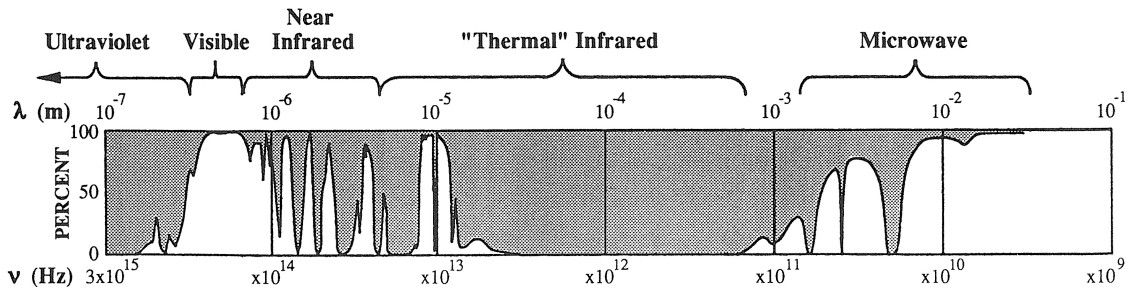

Figure 2.1: Electro-magnetic spectrum of atmospheric transmittance from microwave to visible frequencies in percent, extracted from *Grody* (1993, p. 260).

2.1 Atmospheric Radiation

At each point of the atmosphere, characterized by the temperature T and the pressure p, the atmosphere's dielectric properties are given by the complex dielectric constant ϵ . For non-magnetic substances, ϵ_ν – given at a frequency ν – is related to the monochromatic complex refractive index n_ν:

$$n_\nu = \sqrt{\epsilon_\nu(T, p, c)}, \tag{2.1}$$

where c is the substance concentration. n_ν combines the effect of absorption and refraction:

$$n_\nu = n'_\nu + i\, n''_\nu. \tag{2.2}$$

While the real part of Equation 2.2 is important for atmospheric refraction (cf. Sec. 5.2), the imaginary part n''_ν is connected to the linear absorption coefficient β_a by:

$$\beta_a = \frac{4\,\pi\, n''_\nu}{\lambda} \tag{2.3}$$

in $Np\,m^{-1}$ (Eq. 2.20), with the wavelength λ (*Petty*, 2006, p. 77). The sum of β_a and the scattering coefficient β_s gives the extinction coefficient:

$$\beta_e = \beta_a + \beta_s \tag{2.4}$$

However, β_s becomes negligibly small, if the wavelength is much larger than the size of scattering particles. Therefore, the contribution of scattering at atmospheric constituents to the total extinction can be estimated by the size parameter

$$x = \frac{2\,\pi\, r}{\lambda}, \tag{2.5}$$

with the particle radius r (*Petty*, 2006, p. 345). In the microwave spectral range, x is in the order of 10^{-6} for air molecules ($r \approx 10^{-4}\,\mu m$). For $x < 0.002$ scattering is negligible (*Petty*, 2006, p. 346). As this work focuses on the radiative properties of the atmospheric gases, scattering can be neglected in the following. Atmospheric extinction is solely determined by gas absorption:

$$\beta_e \approx \beta_a, \tag{2.6}$$

2.1.1 Emission/Absorption

The normal component of the energy dE that is emitted by a surface dA within a frequency range $d\nu$ and a time range dt into the solid angle $d\Omega$ is given by:

$$dE = I_\nu \cdot cos(\theta)\, dA\, d\nu\, dt\, d\Omega, \tag{2.7}$$

with the spectral radiance I_ν is the spectral radiance in $W\,m^{-2}\,Hz^{-1}\,sr^{-1}$ (*Kraus*, 1986, Sec. 3-16). For a black body at a physical temperature T, I_ν is the spectral radiance B_ν given by Planck's law:

$$B_\nu(T) = \frac{2h\nu^3}{c^2} \cdot \frac{1}{exp\left(\frac{h\nu}{kT}\right) - 1} \tag{2.8}$$

in $W\,m^{-2}\,Hz^{-1}\,sr^{-1}$, with the speed of light in vacuum c, the frequency ν, the Boltzmann constant k, and Planck's constant h. $B_\nu(T)$ gives the radiation that is emitted by a black body at a physical temperature T. However, the gaseous atmosphere is not a black body. It is composed of different gas species with different emission/absorption characteristics that strongly depend on the frequency ν . Nevertheless, within an atmospheric volume V local thermal equilibrium (LTE) can be assumed. This means, emission and absorption processes are in equilibrium. The gas molecules' energy states follow a Maxwell-Boltzmann distribution and the volume V is characterized by a local temperature T. In particular, the atmospheric emission is isotropic, because the gases are diffuse emitters. Consequently, the emission at frequency ν does only depend on the temperature T and the pressure p. Under these conditions Kirchhoff's law relates the mass absorption coefficient (κ_ν) to the emission coefficient (j_ν) (*Chandrasekhar*, 1960, p. 8)

$$j_\nu = \kappa_\nu\, B_\nu(T), \tag{2.9}$$

in $W\,Hz^{-1}\,sr^{-1}\,kg^{-1}$, with the mass density ρ. κ_ν is related to the volume linear absorption coefficient by:

$$\beta_a = \kappa_\nu\, \rho. \tag{2.10}$$

The frequency spectrum of β_a can be described by a composition of resonant line absorption and the non-resonant continuum absorption. In the microwave frequency range, line absorption is dominating. Absorption lines are characterized by the center frequency ν_0, the line width $\Delta\nu$, the line intensity $\mathcal{S}$, and the line shape F. $\mathcal{S}$ and $\Delta\nu$ are determined by laboratory measurements like the HITRAN database (*Rothman et al.*, 2009). The total resonant absorption coefficient $\beta_a^{line}(\nu)$ is the superposition of n_{line} considered absorption lines by various gaseous components (*Rosenkranz*, 1993, p. 45):

$$\beta_a^{line}(\nu) = \rho_n \sum_{i=0}^{n_{line}} \mathcal{S}_i\, F_i, \tag{2.11}$$

in $Np\,m^{-1}$ (Eq. 2.20), where ρ_n is the number density of gas molecules in $[m^{-3}]$. In the microwave spectral range, these resonances result from rotational transitions of the gas molecules. The transitions do not comply to a singular resonant frequency, but are described by a finite absorption line. Its natural width is determined by Heisenberg's uncertainty principle. However, at a temperature T, the velocities of atmospheric molecules follow a Maxwell-Boltzmann distribution. The corresponding

frequency shifts lead to a Doppler broadened Gaussian-shaped absorption line (*Petty*, 2006, p. 263):

$$F(\nu - \nu_0) = \frac{1}{\Delta\nu\sqrt{\pi}}\, e^{\left(\frac{\nu-\nu_0}{\Delta\nu}\right)^2}, \tag{2.12}$$

where ν_0 is the center frequency in GHz. Equation 2.12 is only valid as long as the single gas molecules do not interact. In the atmosphere, collisions of the absorbing molecules with other molecules lead to further broadening of the absorption line. The broadening is proportional to the air pressure and is therefore called pressure broadening. In the troposphere, pressure broadening dominates over the Doppler broadening effect. In case that $\Delta\nu << \nu_0$ this effect is considered by a Lorentz shape (*Petty*, 2006, p. 264). In the microwave region, where this condition is usually not fulfilled, the Vleck-Weisskopf shape is more appropriate (*van Vleck and Weisskopf*, 1945):

$$F(\nu - \nu_0) = \frac{1}{\pi}\left(\frac{\nu}{\nu_0}\right)^2 \left(\frac{\Delta\nu}{(\nu-\nu_0)^2 + \Delta\nu^2} + \frac{\Delta\nu}{(\nu+\nu_0)^2 + \Delta\nu^2}\right). \tag{2.13}$$

Besides the resonant absorption features there are also non-resonant contributions. Absorption models usually consider these contributions by the so-called water vapour and dry air continua. For microwave frequencies, absorption is mainly due to oxygen, nitrogen and atmospheric water vapor. These species are discussed in the following.

Oxygen

Oxygen molecules have a permanent magnetic dipole moment, which allows rotational excitations. Its spectrum in the microwave frequency range consists of the spin-rotational transitions between 50 GHz and 70 GHz and at 118 GHz (*Rosenkranz*, 1993, pp. 52). These transitions are related to discrete energy states, which are characterized by the quantum number of the total angular momentum $J = |\vec{N} + \vec{S}|$. J couples the rotational state of the oxygen molecule (N) with its spin angular momentum $S = 1$. As Hund's case (*Townes and Schawlow*, 1955, p. 178) allows only transitions with $\Delta J = 1$, only transitions between $N \rightarrow N - 1$ and $N \rightarrow N + 1$ are observed. *Tretyakov et al.* (2005) provide the most recent measurements of the pressure broadening and central frequencies of the oxygen absorption lines.

Around 60 GHz, the spectral distance between single lines is less than 1 GHz. Due to pressure broadening, the single absorption lines overlap. This effect, firstly introduced by *Rosenkranz* (1975), is considered by line mixing coefficients Y, which couple the absorption lines. Y is specific to the individual absorption line. The line mixing coefficients lead to a modified Van Vleck-Weisskopf line shape (*Rosenkranz*, 1988):

$$F(\nu) = \frac{1}{\pi}\left(\frac{\nu}{\nu_0}\right)^2 \left(\frac{\Delta\nu + (\nu - \nu_0)\,Y}{(\nu - \nu_0)^2 + \Delta\nu^2} + \frac{\Delta\nu - (\nu + \nu_0)\,Y}{(\nu + \nu_0)^2 + \Delta\nu^2)}\right). \tag{2.14}$$

The half-width $\Delta\nu$ and the line mixing coefficients Y are pressure and temperature dependent. Apart from line absorption, there is a non-resonant contribution relaxation spectrum ($\nu_0 = 0$) of oxygen molecules, which is included in the dry air continuum (*Liebe et al.*, 1992). It is described by the complex shape function

$$F_0(\nu) = \frac{\nu}{\nu + i\,\gamma_0}, \tag{2.15}$$

with the Debye broadening coefficients γ_0.

Nitrogen

Although nitrogen is the most abundant atmospheric gas, it has only a small role in microwave absorption, because it neither has a permanent electric nor an magnetic dipole moment. Consequently, there is no line absorption due to nitrogen. However, collisions between nitrogen molecules and other air molecules can induce a dipole moment that allows rotational transitions. As the collision time is very short, the resulting resonance is so broad that it only contributes to continuum absorption. This small contribution can be described as an additional contribution of the dry air continuum (Eq. 2.15).

Water Vapor

In contrast to oxygen, water molecules are not linear, but asymmetric rotors. This means, rotational transitions may result from a superposition of three rotational modes. The two most important absorption lines in the microwave are centered at 22.235 GHz and 183.310 GHz (cf. *Payne et al.* (2008)). The first one corresponds to a symmetric spin function, the second one to an asymmetric spin function of the water molecule.

For water vapor, there are non-resonant contributions, too. They are considered by the water vapor continuum absorption. Although the physical origin is still under discussion, the most likely explanation for the continuum is that it results from the superposition of far-wing contributions from absorption lines in the infrared (*Mlawer et al.*, 1999). These lines are broadened by collisions during the absorption process (*Rosenkranz*, 1993, p. 61). The broadening depends on the partial pressures of each collision partner. Therefore, it splits up into a self-broadened (C_s, $H_2O - H_2O$-collisions) and a foreign-broadened (C_f) term. In the microwave spectral range, water vapor continuum absorption can be described semi-empirically (*Rosenkranz*, 1993, p. 70):

$$\beta_a^{cont}(\nu) = \Big(C_s\, e^2\, \theta^{k_s} + C_f\, e\, p_d\, \theta^{k_f} \Big) \nu^2, \tag{2.16}$$

where e is the partial pressure of water vapor, p_d the dry air pressure in hPa, and $\theta = T_0/T$ the normalized inverse temperature ($T_0 = 300\,\mathrm{K}$). C_s and C_f $[(mol\, cm^{-2}\, cm^{-1})^{-1}]$ weakly depend on the frequency and C_s is temperature dependent (*Turner et al.*, 2009). C_s, C_f, and the coefficients k_s and k_f are typically derived from laboratory measurements. The most recent values for C_s and C_f are derived from ground-based observations 150 GHz (*Turner et al.*, 2009).

2.1.2 Extinction

The extinction coefficient β_e gives the attenuation of a signal with intensity I along an infinitesimal signal path ds:

$$I(s + ds) = I(s)\, e^{-\beta_e ds}. \tag{2.17}$$

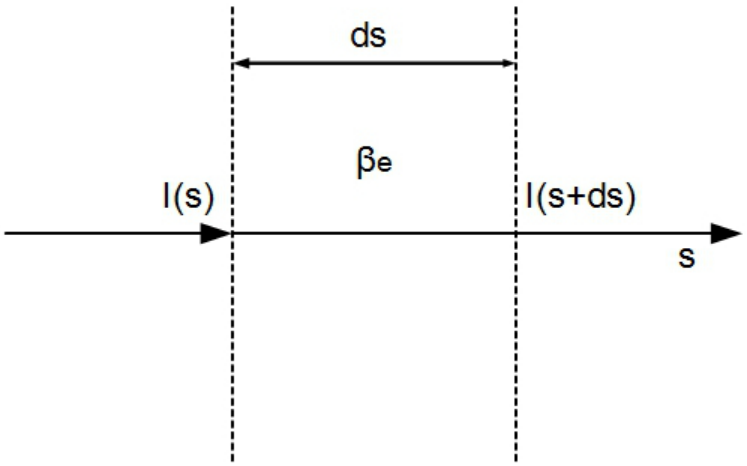

Figure 2.2: Illustration of radiative transfer: The intensity of radiance I is attenuated along its propagation path $\mathcal{P} = \int ds$.

Along a finite propagation path $\mathcal{P} = \int_{s_0}^{s_1} ds$, attenuation can be described by Lambert-Beer's law:

$$I(s_1) = I(s_0) \cdot e^{-\tau}, \tag{2.18}$$

with the opacity τ defined as:

$$\tau = \int_{\mathcal{P}} \beta_e(s)\, ds. \tag{2.19}$$

τ is equal to the signal attenuation

$$L = ln\left(\frac{I(s_0)}{I(s_1)}\right) = \tau \tag{2.20}$$

and is given in Nepers (Np). $1\,Np$ is dimensionless and corresponds to a signal attenuation by $1/e$ after the free path $\lambda_e = 1/\beta_e$. Consequently, β_e is given in Np/m. L, β_e, and τ can also be expressed in terms of dB by (*Ulaby et al.*, 1981, p. 270):

$$1\,Np = 4.343\,dB. \tag{2.21}$$

2.2 Radiative Transfer

Radiative transfer means to calculate the modification of an intensity I_ν along its propagation path. In the non-scattering case it is assumed that any change in the intensity is caused by absorption and emission (*Chandrasekhar*, 1960, pp. 9):

$$\frac{dI_\nu}{ds} = -\beta_a(s)\,I_\nu + \rho\,j_\nu(s), \tag{2.22}$$

with the linear absorption coefficient β_a (Eq. 2.3), the emission coefficient j_ν, and the mass density ρ. $\rho\,j_\nu$ is the source for thermal radiation emitted by an atmospheric volume at temperature $T = T(s)$. Using Kirchhoff's law (Eq. 2.9) gives:

$$\frac{dI_\nu}{ds} = \beta_a\,(B_\nu(T) - I_\nu) \tag{2.23}$$

For a ground-based radiometer, with a the propagation path $\mathcal{P} = \int_\infty^0 ds$, Equation 2.23 is solved by (cf. *Chandrasekhar* (1960, pp. 9) and App. A):

$$I_\nu(s) = I_\nu(\infty)\,e^{-\tau(\infty,0)} + \int_0^s B_\nu(T)\,e^{-\tau(\infty,0)}\,\beta_a(s)\,ds, \tag{2.24}$$

using Equation 2.19. $I_\nu(0)$ is replaced by the cosmic background radiance. A detailed derivation of Equation 2.24 is given in Appendix A. Within the limits of the Rayleigh-Jeans approximation (cf. Sec. 3.1.1), Equation 2.24 can be expressed in terms of the brightness temperature T_b:

$$T_b(\nu) = T_{back}\,e^{-\tau(\infty,0)} + \int_0^\infty T(s)\,e^{-\tau(\infty,s)}\,\beta_a\,ds, \tag{2.25}$$

with the cosmic background temperature $T_{back} \approx 2.736\,\mathrm{K}$ (*Noterdaeme et al.*, 2011). Furthermore, the mean radiative temperature T_{mr} of the atmosphere is defined as:

$$T_{mr}(\nu) = \frac{\int_0^\infty T\beta_a e^{-\tau(0,s)}\,ds}{1 - e^{-\tau(0,\infty)}}. \tag{2.26}$$

Then Equation 2.25 simplifies to:

$$T_b(\nu) = T_{back} \cdot e^{-\tau_\nu} + T_{mr}(\nu) \cdot (1 - e^{-\tau_\nu}). \tag{2.27}$$

In Section 3.3.2 it is shown, that the surface temperature is normally a good proxy to estimate $T_{mr}(\nu)$.

2.3 Gas Absorption Models

Radiative transfer models describe the propagation of radiation through the atmosphere by solving Equation 2.24 along the propagation path. For one-dimensional radiative transfer simulations the propagation path $\mathcal{P}$ is discretized by n plane-parallel propagation layers:

$$\mathcal{P} = \sum_{i=0}^{n} \Delta s_i, \tag{2.28}$$

with a variable layer thickness Δs_i. The transfer models employ different gas absorption models, which provide the atmospheric absorption coefficient $\beta_a(s)$ (Eq. 2.3) at each level n (cf. *Rosenkranz* (1993)). For this work, only clear sky cases are considered. This means, it is assumed that no hydrometeors are present in the atmosphere. In the observed frequency range, scattering is therefore negligible. In this case, the opacity $\tau_\nu(s)$ is solely given by the summation of $\beta_a(s)$ along the propagation path $\mathcal{P}$. Finally, $T_b(s)$ can be calculated from Equation 2.27.

For line-by-line gas absorption models, the monochromatic absorption coefficient β_a is determined by a superposition of absorption lines (Eq. 2.11) and continuum absorption. The absorption lines are parameterized by a set of absorption coefficients that describe the line's intensity $\mathcal{S}(T)$ and its shape $F(\nu, \nu_0, \Delta\nu, Y)$. The temperature and pressure dependencies of F can be modeled as:

$$\Delta\nu = \gamma_d(T)\, p_d\, \theta^{x_d} + \gamma_e\, e\, \theta^{x_e}, \tag{2.29a}$$

$$Y = y(T)\, p_d\, \theta^{x_y}, \tag{2.29b}$$

with the broadening coefficients γ_d, γ_e, x_d, x_e, and the mixing coefficients y and x_y. $\Delta\nu$ is given in GHz and the line mixing parameter Y is dimensionless. Detailed information about atmospheric lines in the microwave region is given by *Rosenkranz* (1993, pp. 80).

In this work, different existing absorption models are compared to radiometer measurements between 22 GHz and 58 GHz (cf. Chap. 7). First of all, there are different versions of the Millimeter-wave Propagation Model (MPM), which is widely used in the radiative transfer community: "Liebe'87" (*Liebe and Layton*, 1987), an updated version "Liebe'93" (*Liebe et al.*, 1993), and the "Rosenkranz'98" (*Rosenkranz*, 1998,

1999), which combines the water vapor absorption modules of the previous ones. The ARM program uses the Monochromatic Radiative Transfer Model (MonoRTM) (*Clough et al.*, 2005). For this analysis, the most recent version 4.2 is used. Finally, there is the Atmospheric Model (AM) developed by *Paine* (2012) in the current version 7.2, which is widely used in the astronomer's sub-millimeter community.

The applicable frequency range of the used models is given in Table 2.1. All five models are able to calculate the Planck equivalent brightness temperature (inverse of Eq. 2.8) for water vapor, oxygen and continuum absorption. The absorption parameters are mainly derived from laboratory measurements. The MPM-based models are used with a corrected water vapor continuum following *Turner et al.* (2009) and a modified line width of the 22.235 GHz line suggested by *Liljegren et al.* (2005).

Table 2.1: Frequency range of gas absorption models

Model	Range
Liebe'87	$1 - 1000$ GHz
Liebe'93	$1 - 1000$ GHz
Rosenkranz'98	$1 - 800$ GHz
MonoRTM	$0 - 1648$ GHz
AM	4825 MHz-5775 GHz

2.3.1 MPM87 (Liebe'87)

The Liebe'87 model (*Liebe and Layton*, 1987), is an early version of the MPM model by *Liebe* (1985). It contains 48 oxygen lines and 30 water vapor lines between 22 GHz and 988 GHz. The line intensities $\mathcal{S}$ and line widths $\Delta\nu$ are mostly taken from *Liebe* (1985). At 60 GHz, the modified Van-Fleck-Weisskopf line shape (Eq. 2.14) is used to include line overlapping. In the version used here, the line mixing parameters Y are not taken from *Rosenkranz* (1988), but are updated referring to *Liebe* (1989). The water vapor continuum is derived from measurements at 138 GHz (*Liebe*, 1987).

2.3.2 MPM93 (Liebe'93)

The Liebe'93 model (*Liebe et al.*, 1993) is an updated version of the MPM based on *Liebe* (1989). It has 44 oxygen and 34 water vapor absorption lines. For oxygen absorption a modified van Vleck-Weisskopf shape (Eq. 2.14) is used. At microwave frequencies, it uses different line widths $\Delta\nu$ and mixing parameters Y than the Liebe'87 model. $\Delta\nu$ and Y are taken from *Liebe et al.* (1992) and multiplied by 1.05 and 1.15, respectively. The exponent $x = 0.8$ in the temperature dependency of the line mixing coefficients Y is taken from *Rosenkranz* (1988). The dry air continuum absorption includes non-resonant contributions from oxygen and nitrogen. In contrast to the other

models used here, the water vapor continuum is described by a single pseudo-line at 1780 GHz, which is artificially added to the spectrum.

2.3.3 MPMf87/s93 (Rosenkranz'98)

For microwaves frequencies, the line absorption for oxygen used within the Rosenkranz'98 model (*Rosenkranz*, 1998, 1999) is identical to the Liebe'93 model. Note, that the line intensities $\mathcal{S}$ are defined in a different way and are provided in *Rosenkranz* (1993, pp. 80). In comparison with the Liebe'93 model, the only difference in oxygen line absorption is, that the unmodified line widths $\Delta\nu$ and mixing parameters Y from *Liebe et al.* (1992) are used. The line intensities $\mathcal{S}$ of water vapor lines are derived from the HITRAN database edition 1992 (*Rothman et al.*, 1992), and the implemented broadening coefficients are listed in *Rosenkranz* (1998). The water vapor continuum module is a composite of the self-broadening contribution from Liebe'93 and the foreign-broadening contribution from Liebe'87 (*Hewison et al.*, 2006). Like for oxygen a van Vleck-Weisskopf-shape function is used. However, for water vapor lines it is limited to a frequency range of $|\nu| < 750\,\mathrm{GHz}$.

2.3.4 MonoRTM

For this analysis, the most recent version MonoRTM v4.2 is used (*Clough et al.*, 2005). Frequencies ν, line widths $\Delta\nu$ and intensities $\mathcal{S}$ are taken from the HITRAN database edition 2004 (*Rothman et al.*, 2005). The MonoRTM uses the Humlicek-Voigt line shape (*Humlicek*, 1982). The line broadening and line mixing coefficients are taken from *Tretyakov et al.* (2005). The water vapor lines at 22 GHz and 183 GHz have been updated according to *Payne et al.* (2008). The included water vapor continuum is the $MT\_CKD\_2.4$ (*Mlawer et al.*, 1999).

2.3.5 AM

The AM model uses line frequencies ν, widths $\Delta\nu$, and intensities $\mathcal{S}$ from the HITRAN database edition 2008 (*Rothman et al.*, 2009). In contrast to the other models used here, the AM uses first (Y) and second-order line mixing coefficients (g and $\delta\nu$) from *Makarov et al.* (2011). Like for the MonoRTM, the broadening coefficients γ are from *Tretyakov et al.* (2005) and the water vapor continuum is the $MT\_CKD\_2.4$ (*Mlawer et al.*, 1999). The AM can be run with different line shapes (*Paine*, 2012, p. 36). Here, the default line shapes are used. For the coupled lines at 60 GHz, this is a modified Van Vleck-Weisskopf shape, which includes the line mixing coefficients Y, g, and $\delta\nu$ (*Makarov et al.*, 2011). Like in the Rosenkranz model, the same line shape with a cutoff frequency of 750 GHz is used for the water vapor absorption. This cutoff is compatible to the $MT\_CKD\_2.4$ continuum (*Paine*, 2012, p. 63) and leads to a pure Lorentz shape at high frequencies (*Paine*, 2012, p. 37).

3. Microwave Radiometry

Microwave radiometers (MWRs) are passive remote sensing instruments. They are commonly used to remotely sense atmospheric parameters. Passive remote sensing techniques take advantage of extinction features of the atmospheric constituents. Spectral measurements along absorption features can deliver profile information. A common application in the microwave region is the temperature profile retrieval from measurements along the oxygen absorption line at 60 GHz (*Westwater*, 1965). The profile retrieval is based on the fact that the emission observed at different frequencies originates from different heights, because the mixing ratio of oxygen is constant with height and and the opacity increases towards the center of the absorption complex. Also variable constituents like water vapor and liquid water can be observed by combining measurements at water vapor lines with measurements in atmospheric windows. The usage of microwave frequencies has the advantage, that the atmosphere is mostly transparent for these wavelengths, even in cloudy conditions. At high microwave frequencies in the atmospheric window, where scattering by ice particles becomes dominant, even snow can be observed by MWRs (*Noh et al.*, 2006, *Kneifel et al.*, 2010).

Although ground-based radiometers do not provide a wide spatial coverage, they have several advantages compared to space- and air-borne instruments, because they

- are less expensive in acquirement, operation, and maintenance,
- can provide long-term, high-resolution time series of atmospheric parameters, which are valuable for different purposes from process studies over data assimilation to climate monitoring,
- are not suffering from the background signal emitted by the Earth's surface emission like downward looking instruments, when observing the lower troposphere and in particular the planetary boundary layer,
- can serve as a testbed for radiometer components and space missions.

In this chapter, a general introduction of the MWR measurement principle is followed by a detailed view on the specific radiometer HATPRO-G2 used in this work.

3.1 Measurement Principle

The physical quantity that is measured by a radiometer is the spectral radiance I_ν of the volume V, which is observed by its antenna. Total power radiometers (cf. Sec. 3.2) are instruments that detect a signal that is a function of the received power P. P is received via a normalized antenna pattern $\mathcal{F}$ and within the spectral band width $\Delta\nu$ (Eq. 2.8):

$$P = \frac{1}{2} A \int_V I_\nu(\varphi,\theta)\, \mathcal{F}(\varphi,\theta)\, \Delta\nu)\, d\Omega \tag{3.1}$$

in W, where Ω is the solid angle and $\mathcal{F}$ weights the radiation that is received from directions defined by the angles φ and θ (cf. *Vohwinkel* (1988, pp. 13)). A is the effective antenna area (the factor 1/2 results from the fact that only one direction of polarization of the unpolarized atmospheric signal is detected).

When the observed volume can be assumed as a black body, the emitted radiation is given by the brightness $B_\nu(T)$ (Eq. 2.8). Equation 3.1 can be rewritten, when $B_\nu(T)$ is expressed as a series of expansion in terms of $h\,\nu/k\,T$:

$$B_\nu = \frac{2\nu^2}{c^2}\, k\, T \cdot \left[1 - \frac{h\,\nu}{k\,T} + \frac{1}{3}\cdot\left(\frac{h\,\nu}{k\,T}\right)^2 + ...\right]. \tag{3.2}$$

In case of $h\,\nu << k\,T$, the series can be truncated after the first term and B_ν simplifies to:

$$B_\nu^{RJ} = \frac{2\nu^2}{c^2}\, k\, T. \tag{3.3}$$

Equation 3.3 is the Rayleigh-Jeans approximation, which is widely used in microwave radiometry. It is used to define the Rayleigh-Jeans brightness temperature (cf. Sec. 3.1.1).

By far, most of the signal is received via a narrow antenna main lobe (ML). By defining an effective solid angle of the ML (*Vohwinkel*, 1988, p. 21)

$$\Omega_{ML} = \int_{ML} \mathcal{F}\, d\Omega, \tag{3.4}$$

Equation 3.5 becomes:

$$P = \frac{1}{2} A\, \Delta\nu \int_{ML} \mathcal{F}(\varphi,\theta)\, B_\nu^{RJ}\, d\Omega = \frac{1}{2} A\, \Delta\nu\, \Omega_{ML} \left(\frac{2kT}{\lambda^2}\right), \tag{3.5}$$

with $\Omega_{ML} = \lambda^2/A$ (*Janssen*, 1993, p. 18). For an ideal antenna without losses, this gives Nyquist's law (*Janssen*, 1993, p. 16):

$$P = \Delta\nu\, k\, T_A, \tag{3.6}$$

in W, with the antenna temperature

$$T_A = \frac{P}{k\,\Delta\nu}. \tag{3.7}$$

3.1.1 Brightness Temperature

Equation 3.3 is used to define the Rayleigh-Jeans brightness temperature T_b^{RJ} (*Janssen*, 1993, p. 6):

$$T_b^{RJ} = \frac{c^2}{2\,\nu^2\,k}\,I, \tag{3.8}$$

which is a convenient way of scaling the received radiation I_ν into the temperature domain. In case of a black body target, I_ν is given by B_ν. However, in microwave radiometry, this is not always a legitimate approximation as $h\,\nu$ can be in the order of $k\,T$ (cf. Sec. 3.3). For radiometer channels in an atmospheric window, for example at $\nu = 30\,\mathrm{GHz}$, with an assumed minimum brightness temperature of 10 K, $h\,\nu/k\,T$ is 0.14. Beyond the limits of the Rayleigh-Jeans approximation, T_b^{RJ} differs from the black body's physical temperature T by ΔT. In order to calculate ΔT the series expansion of B_ν (Eq. 3.2) is truncated after the third term:

$$\Delta T = T_b^{RJ} - T = -0.024 \cdot \nu + 0.000192 \cdot \frac{\nu^2}{T}, \tag{3.9}$$

where the temperature dependent second term in Equation 3.9 becomes negligible with increasing temperatures (Fig. 3.1). A detailed derivation of Equation 3.9 is given in Appendix A.

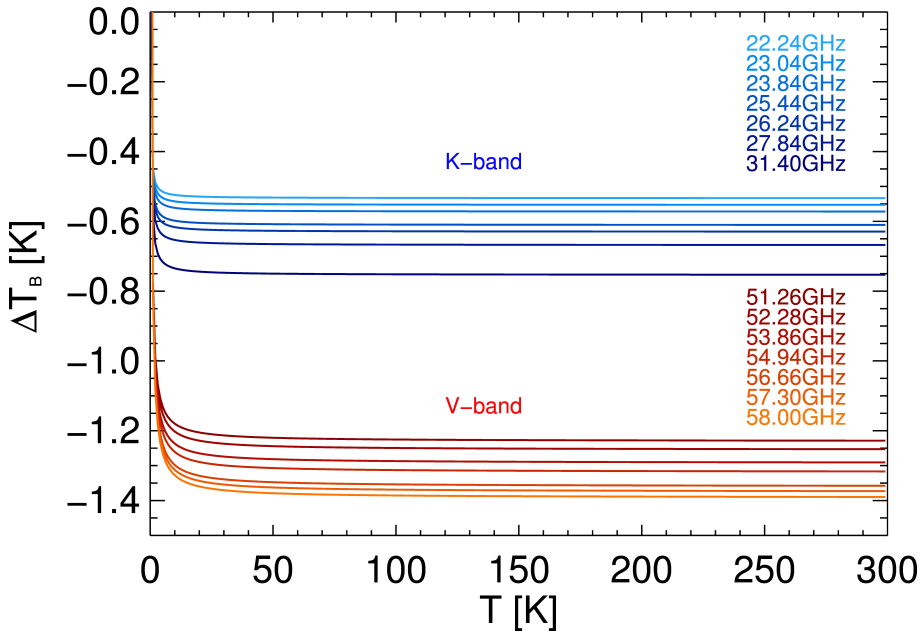

Figure 3.1: Brightness temperature correction: ΔT_b is the Rayleigh-Jeans brightness temperature T_b^{RJ} minus the physical temperature T for HATPRO-G2 channels.

A different definition of the brightness temperature is the Planck equivalent brightness temperature T_b, which is the inverse of the brightness B_ν (Eq. 2.8). The Planck equivalent T_b does not include the Rayleigh-Jeans approximation (Eq. 3.8). For a black body, T_b is equal to its physical temperature T. However, it can also be used to describe emission of non-black bodies like atmospheric gases (cf. Sec. 2.1). Then, the emitted intensity I_ν is equal to the spectral radiance B_ν of a black body with a physical temperature $T = T_b$.

3.1.2 Sensitivity

The total noise power P_{sys} of a radiometer channel includes contributions of the system noise power P_R and the antenna power P_A. Using Equation 3.3 gives:

$$T_{sys} = T_R + T_A. \tag{3.10}$$

The inherent noise temperature T_R describes noise that originates from resistor elements within the receiver. It is the sum of thermal noise (Nyquist noise) and electronic noise from active elements like diodes and transistors (e.g. shot noise or flicker noise) (cf. Sec. 3.1.3). T_R has to be quantified by calibration techniques (cf. Chap. 6) in order to measure an atmospheric signal T_A. The detection limit of measured brightness temperatures ΔT_b is determined by T_{sys}, the receiver's channel band width $\Delta\nu$, and the integration time t_{int}. $\Delta\nu$ is usually small compared to the received frequency

($\Delta\nu << \nu$), i.e. it can be assumed that white noise is received. This means that signal contributions T_A that are received within the channel band width $\Delta\nu$ and the integration time t_{int} are statistically independent: The corresponding voltages U_A can be described by a Gaussian probability function (cf. *Vohwinkel* (1988, p. 70)). This leads to an exponentially distributed output voltage U_{out} behind the detector (cf. Sec. 3.2), with a mean value and standard deviation of (cf. *Ulaby et al.* (1981, p. 363)):

$$\sigma(U_{det}) = \sqrt{\overline{U_{det}^2}}. \tag{3.11}$$

In order to cut off high frequency noise contributions, the final detector voltage U_{det} is obtained by averaging U_{out} over the integration time t_{int} and the band-pass filter frequency range $\Delta\nu$. Integration of the signal reduces the normalized standard deviation (*Ulaby et al.* (1981, p. 364), cf. Sec. 3.2):

$$\frac{\sigma_{det}}{U_{det}} = \frac{\sigma_{out}}{U_{out}} \cdot \frac{1}{\sqrt{\Delta\nu\, t_{int}}}. \tag{3.12}$$

Finally, using Equation 3.11 gives the radiometer sensitivity expressed in terms of the total noise temperature T_{sys}:

$$\Delta T_b = \frac{T_{sys}}{\sqrt{\Delta\nu\, t_{int}}}. \tag{3.13}$$

Equation 3.13 means, that the detection limit can be reduced by cooling, to reduce the instrumental noise T_R, and by averaging in time (t_{int}) and frequency ($\Delta\nu$). However, in reality, the detection limit is not constant in time. It is modulated by variations in the signal amplification. The amplification is described by the detector gain g (cf. Eq. 3.19). Relative gain variations $\Delta g/g$ are mainly due to small temperature changes within the receiver and affect the sensitivity by (*Vohwinkel* (1988), Fig. 3.2):

$$\Delta T_b = T_{sys} \cdot \sqrt{\frac{1}{\Delta\nu \cdot \tau} + \left(\frac{\Delta g}{g}\right)^2}. \tag{3.14}$$

The relative gain variations can be balanced by calibrating against a well known target (e.g. by hot load calibrations, cf. Chap. 3.3). However, variations on time scales below the calibration repetition rate can not be corrected. Alternatively, gain fluctuations can be compensated continuously, for example by Dicke-switching or balanced receivers (cf. *Vohwinkel* (1988, pp. 83) for details). For the radiometer HATPRO-G2, used in this work, $(\Delta g/g)^2$ are in the order of 10^{-4} (Tab. B.3).

3.1.3 Stability

A method to distinguish between different noise types is to calculate the Allan Standard Deviation (ASD) of a measurement time series (*Allan*, 1985). Furthermore,

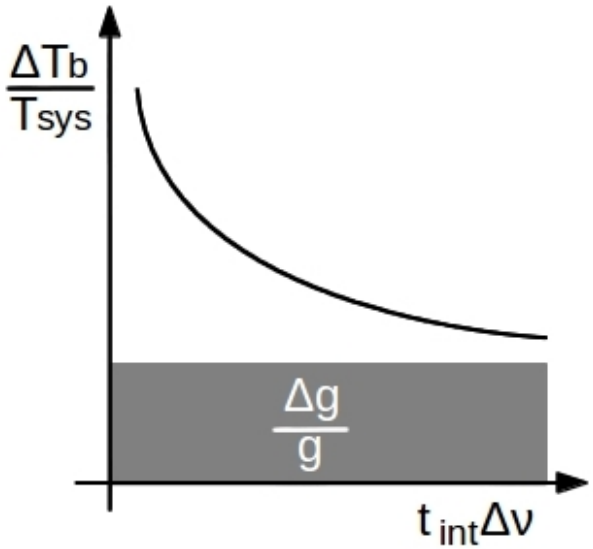

Figure 3.2: Illustration of the radiometer formula for the measurement sensitivity ΔT_b: At a given total noise T_{sys}, the measurement sensitivity can be improved by increasing the band width and/or the integration time. A limit is given by fluctuation of the receiver gain g.

the ASD allows to quantify the radiometric stability (*Land et al.*, 2007). In contrast to the common standard deviation, the ASD is based on differences between single measurements instead of deviation from a mean value (*Land et al.*, 2007).

Here, a five-hour observation of HATPRO-G2's internal ambient target outside the laboratory on August 15, 2011, is used to determine the ASD. Therefore, the data set is divided into N Δt wide bins (*Wiedner*, 2002):

$$\sigma_{ASD}(\Delta t) = \sqrt{\frac{1}{N-2}\sum_{j=1}^{N-1}\left(\overline{T_{sys}^{j-1}} - 2\,\overline{T_{sys}^{j+1}} + \overline{T_{sys}^{j}}\right)^2}, \tag{3.15}$$

where $\overline{T_{sys}}$ are bin averages of the total system noise T_{sys} for Δt, being a multiple of the observed integration time t_{int}. Limited by the length of the data set, Δt is varied between 1 s and about 1 h. When the ASD is plotted against the averaging time Δt in a log-log-diagram (Fig. 3.3), different noise types and drifts are characterized by different slopes (*Land et al.*, 2007, *Wiedner*, 2002). For short averaging times, the ASD decreases with a slope of about -0.5, which can be recognized as uncorrelated (white) frequency noise, which is thermal noise from radiometer parts (*Land et al.*, 2007, *Wiedner*, 2002). Within this domain, the noise contributions to measurements can be reduced by increasing the integration time (Eq. 3.13). For the given example, this domain extends to about 1 min for K-band and $4-5$ min for V-band channels (Fig. 3.3). The extended white noise domain in the V-band is explained by the fact, that these channels are stabilized by constant noise switching (cf. Sec. 4.3). For larger

Δt values the slope becomes zero. For K-band channels, there is a short transition with a slope of +0.5. These domains belongs to flicker noise and $1/f$-noise, respectively, which are induced by short-term fluctuations of temperature, pressure and the magnetic field within the instrument (*Wiedner*, 2002). Both noise types can be assumed as detector gain drifts (*Wiedner*, 2002), which can be compensated by hot load calibrations (cf. Sec. 3.3). The ASD results suggest a repetition rate of hot load calibrations of 1 min for HATPRO-G2.

For $\Delta t > 5$ min the slope approaches +1 (*Land et al.*, 2007). This drift is not due to the radiometer performance, but reflects the drift of the target temperature during the observation time. The observed T_b ranges within the 5 h were 1.5 K to 1.6 K for K-band and 2.3 K to 4.5 K for V-band channels. This drift can easily be corrected by subtracting the physical temperature of the target.

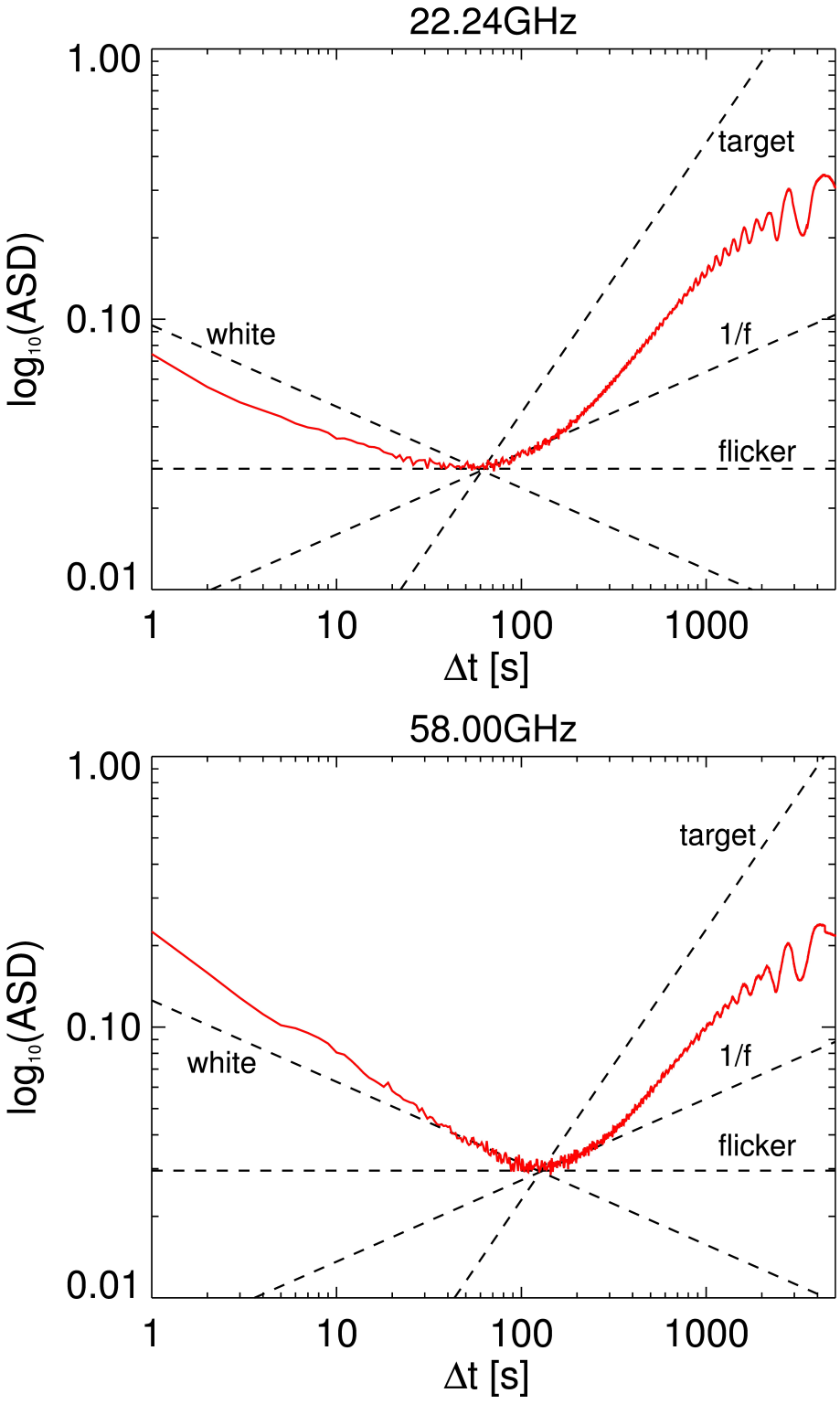

Figure 3.3: Allan Standard Deviation (ASD) of total noise power T_{sys} is calculated for different averaging times Δt. HATPRO-G2's internal ambient target is observed for several hours outside the laboratory on August 15, 2011, *red*: total noise power $T_{sys} = T_R + T_b$, *dashed lines*: slopes S that correspond to perfect white phase noise ($S = -0.5$), flicker noise ($S = 0.0$), $1/f$ (random walk frequency) noise ($S = +0.5$) and a drifting *target* ($S = +1.0$).

3.2 Total Power Receivers

Total power receivers provide a detector voltage U_{det} that is a function of the total noise power received within a frequency range $\Delta\nu$. Figure 3.4 shows a scheme of the receiver components.

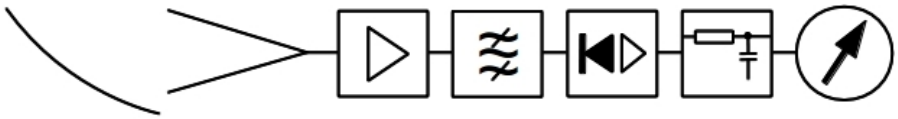

Figure 3.4: Schematic illustration of a total power radiometer: The receiving signal path from left to right: reflector; horn antenna; amplifier; band-pass filter; detector; integrator; output, after *Vohwinkel* (1988).

In MWRs, the reflector is typically realized by a parabolic mirror. The mirror collects radiation received within a limited beam-width, which can be described by the Half Power Beam Width (HPBW). The larger the reflector's diameter d, the narrower the beam. For parabolic reflectors, the HPBW decreases with increasing frequency ν:

$$HPBW \propto \frac{1}{d\,\nu}. \tag{3.16}$$

Alternatively, a focusing lens can be used. However, lenses can lead to additional reflection and losses.

The parabolic mirror focuses the radiation to a corrugated feedhorn antenna, which is commonly used with MWRs. Corrugated feedhorn antennas combine a broad band width, a large aperture, and single mode propagation (*Ulaby et al.*, 1981, pp. 165). Firstly, a broad band width is good for spectral measurements, because a single antenna can be used for several frequency channels. Secondly, a large reflector demands a large antenna aperture. Thirdly, higher order modes are suppressed, because horn antennas are characterized by a gradual transition between the free space and the adjacent wave guide structure (*Ulaby et al.*, 1981, pp. 165). Figure 3.5 shows a normalized two-dimensional projection of a typical antenna pattern. It is characterized by a central ML and several side lobes (SL). The relation between the ML and the first side lobe is given by the side lobe level (SLL). The beam is usually defined by the HPBW, which receives most of the incoming radiation.

From the antenna, the radiation is guided to the amplifier. Generally, the noise figure $F_n\,[dB]$ of the amplifier and the signal losses $L\,[dB]$ within the receiver chain, standardized by $T_0 = 290\,K$ (*Ulaby et al.*, 1981, p. 349), give the system noise temperature

$$T_R = (F_n - 1)\,T_0 + (L - 1)\,T_0, \tag{3.17}$$

where $T_0 = 290\,\mathrm{K}$. Nyquist's law (Eq. 3.6) says that the total received power P_A received from the atmosphere is in the order of $10^{-13}\,\mathrm{W}$ (*Vohwinkel*, 1988, p. 83). This means, high amplifications are needed to exceed typical detector limit being in the order of $1\,\mu\mathrm{W}$. Therefore, MWRs often use super-heterodyne receivers to down-convert the detected signal before amplification (cf. *Kraus* (1986, Sec. 7-0)). Though, advances in Monolithic Microwave Integrated Circuit (MMIC) technology made low noise amplifiers (LNAs) for frequencies up to 100 GHz available. These LNAs are characterized by F factors that are small enough to give a detection limit (Fig. 3.13) well below 1 K (cf. Sec. 4.3). This makes it possible to use direct signal detection for frequencies below 100 GHz. Neither local oscillators, nor mixers are needed.

The amplified signal enters the filter bank where radiometer channels are defined by band-pass filters. The band-pass filters convert the antenna voltage U_A to a Rayleigh distributed U_{in} that enters the square-law detector (*Ulaby et al.*, 1981, p. 363). The square-law detector rectifies U_{in} and gives output voltage U_{out} which is proportional to the received power ($U_{out} \sim U_{in}^2 \sim P_{sys}$) (*Ulaby et al.*, 1981, p. 363). U_{out} is exponentially distributed (*Ulaby et al.*, 1981, p. 363):

$$p(U_{out}) = \frac{1}{\overline{U_{out}}}\, e^{-U_{out}/\overline{U_{out}}}. \tag{3.18}$$

In order to cut off the high frequency noise contribution, the integrator provides the final detector voltage U_{det} by averaging U_{out} over the integration time t_{int} and the band-pass filter frequency range $\Delta\nu$. For a perfect square law detector, Nyquist's law (Eq. 3.6) gives a voltage U_{det}, which is proportional to the total system noise temperature T_{sys} (*Vohwinkel*, 1988, p. 72).

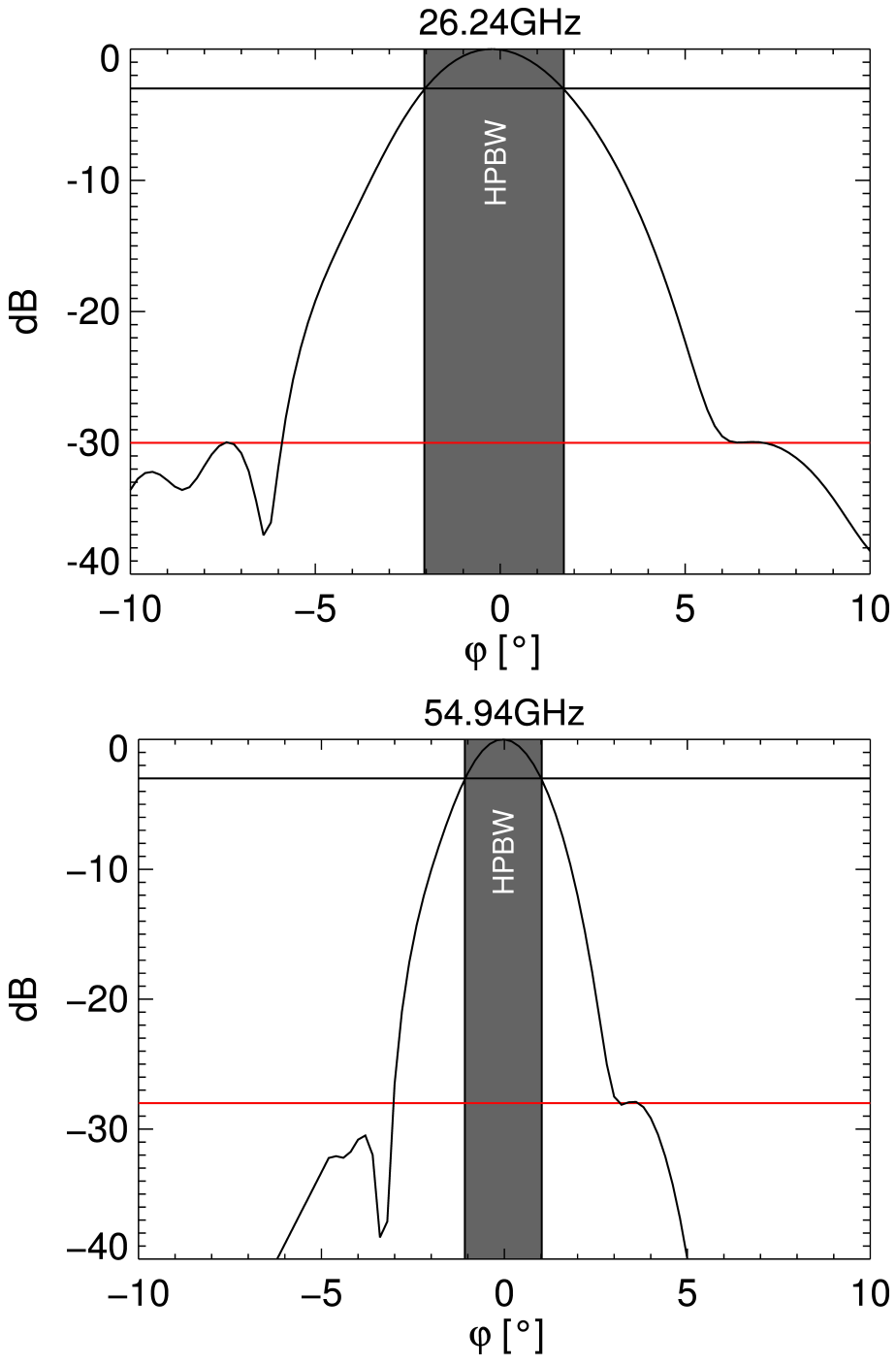

Figure 3.5: Horn antenna pattern simulated for the HATPRO-G2 (cf. Sec. 4.3) for two selected channels. Marked are the side lobe level (SLL, *red*) and the Half Power Beam Width (HPBW) (Tab. 4.2).

3.3 Calibration Techniques

The calibration of a radiometer is a critical point, because any inaccuracy will affect the quality of the physical products, which are retrieved from the measurements (*Liljegren*, 2002, *Löhnert and Maier*, 2012). A reliable calibration is therefore a precondition for the validation of radiative transfer models by MWR measurements (*Hewison et al.*, 2006).

Total power radiometers measure the electromagnetic power received within the channel band width (cf. Sec. 3.1). The signal is amplified and then transformed into a voltage by the detector. Calibrating a radiometer means to determine the relation between the detected voltage U_{det} and the received power - normally expressed as brightness temperature T_b. Measurements at reference targets are needed to derive a calibration characteristic ($T_b = f(U_{det})$) that can be applied to detected voltages. This relation can be expressed by a set of three calibration parameters:

$$U_{det} = g\, T_{sys}^{\alpha}, \tag{3.19}$$

with the detector gain $g\,[V/K]$, the total system noise temperature T_{sys} (Eq. 3.10) and the non-linearity parameter α (RPG-OS, 2011). The black body equivalent brightness temperature T_b is related to Planck's spectral radiance (Eq. 2.8).

Usually, there are different calibration procedures that are performed, when operating a radiometer. A procedure is called an absolute calibration, when all calibration parameters are derived. Typically, absolute calibrations are supplemented by more frequent calibrations, which update a subset of the calibration parameters. These are called relative calibrations. In the following, different calibration procedures are introduced.

3.3.1 Liquid Nitrogen Calibration

Ideally, a black body target at a physical temperature below the measured T_b should be used as a cold calibration point. In contrast to space-borne radiometers, which can directly use the cosmic background radiation of 2.736 K (*Noterdaeme et al.*, 2011), for ground-based radiometer cryogenically cooled targets are used. Under environmental pressure conditions, suitable cryogenics, like LN_2, are boiling. Assuming that the boiling point temperature is known, a target, homogeneously cooled by a cryogenic fluid, can be used as a cold reference. Theoretically, any cryogenic substance can be used. The main idea is that observed atmospheric T_b is within the targets' range. However, in atmospheric windows, measured T_b can be 10 K and even less. Therefore, the cold target should ideally have a temperature below 10 K. At standard pressure, Helium has a boiling point of 4.15 K (*Zhang et al.*, 2011) and would therefore be suitable to use. However, Helium is difficult to use, because it needs to be pressurized. In practice, LN_2 can be handled best and is therefore mostly used

with MWRs. However, its boiling point of 77.4 K at standard pressure (*Span et al.*, 2000) lies notably above the T_b range of low opacity radiometer channels. This has the disadvantage that uncertainties at the cold calibration increase towards lower T_b values (cf. Sec. 6.1.1).

2-Point Calibration

Besides the cold calibration point (T_C), a second target is needed to determine a relation between T_b and U_{det}. The second target provides the hot calibration point, which commonly is an internal black body target. The target should be at a homogeneous physical temperature T_H close to the maximum observed T_b values. Therefore, the target is actively heated or is at a temperature close to the ambient temperature. The corresponding calibration equations are:

$$Y = \left(\frac{U_H}{U_C}\right)^{\frac{1}{\alpha}}, \tag{3.20a}$$

$$T_R = \frac{T_H - Y \cdot T_C}{Y - 1}, \tag{3.20b}$$

$$g = \frac{U_H}{(T_R + T_H)}, \tag{3.20c}$$

where α describes the non-linearity of the receiver system. This is a reasonable approach, because in the relevant power regime the non-linearity is usually small, which means that α is close to 1. α cannot be determined from two calibration points. Consequently, if α is not provided independently (e.g. from a 4-point calibration, cf. Sec. 3.3.1), a linear relation between the U_{det} and T_b is assumed ($\alpha = 1$) (RPG-OS, 2011). Since the detector voltage of a total power receiver is directly related to the received power, Equations 3.20 are, strictly speaking, only valid within the limits of the Rayleigh-Jeans approximation (Eq. 3.3) and for α close to 1. As a consequence, the physical target temperatures T_C and T_H would need to be converted to Rayleigh-Jeans brightness temperatures using Equation 3.1, before they are inserted into the calibration Equations 3.20. However, even when using LN_2 as a cold reference, the second term in Equation 3.9 is below 0.1 K for frequencies up to about 150 GHz. This means, that in the analyzed frequency range, the difference between the Rayleigh-Jeans brightness temperature and the physical temperature is constant. Consequently, both target temperatures can directly be inserted into Equations 3.20. The resulting calibration parameters and measured T_b values are then Planck equivalent temperatures. Particularly, these assumptions are also valid for HATPRO-G2 ($\alpha \in [0.9, 1.0]$, $\nu \in [22\,\text{GHz}, 58\,\text{GHz}]$, cf. Sec. 6). Henceforth, calibration equations, apart from the tipping curve calibration, are expressed in terms of temperatures.

4-Point Calibration

A 4-point calibration procedure includes four calibration points (U_C, U_H, U_{CN}, U_{HN}, cf. Fig. 3.6). Measurements on the cold target (T_C) and the hot target (T_H) are repeated with additionally injected noise from an internal noise diode. Since the 4-point calibration has, compared to the 2-point calibration, two additional calibration points, two additional calibration parameters can be determined. This allows to determine the receiver non-linearity α and to calibrate an internal noise diode (T_N). The four calibration parameters, T_R, g, T_N, and α, are derived by solving the following system of equations:

$$U_C = g\,(T_R + T_C)^{\alpha}, \tag{3.21}$$
$$U_H = g\,(T_R + T_H)^{\alpha}, \tag{3.22}$$
$$U_{CN} = g\,(T_R + T_C + T_N)^{\alpha}, \tag{3.23}$$
$$U_{HN} = g\,(T_R + T_H + T_N)^{\alpha}, \tag{3.24}$$

where α is channel dependent (Fig. 3.6). The receiver non-linearity is assumed to be stable within a time period of several months (RPG-OS, 2011, p. 15). T_N can serve as a secondary calibration standard during operation (cf. Sec. 3.3.3).

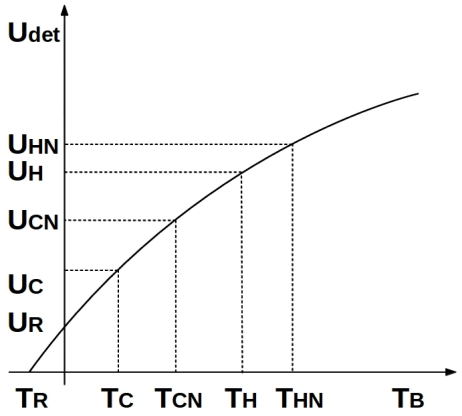

Figure 3.6: Schematic illustration of a 4-point calibration: The detector voltage U_{det} is measured at four calibration points: U_C, U_H, $U_{CN} = U_C + U_N$, and $U_{HN} = U_H + U_N$. T_R is the receiver noise temperature, U_N results from injected noise by the internal noise diode (T_N). The target temperatures T_C and T_H are known quantities. T_N and the non-linearity parameter α are determined by the calibration.

3.3.2 Tipping Curve Calibration

An alternative to the LN_2 calibration is the so-called tipping curve calibration, which can be used to calibrate low-opacity radiometer channels. The general idea is to replace the LN_2 target by the cold clear sky. *Han and Westwater* (2000) discuss this method in detail and specify an absolute calibration accuracy of better than 0.5 K for K-band channels.

In principle, the method uses opacity-air mass pairs from elevation scans (Fig. 3.7). At each elevation angle, the opacity τ (Eq. 2.19) is calculated by re-arranging Equation 2.24 (*Han and Westwater*, 2000):

$$\tau = ln\left(\frac{B(T_{mr}) - B(T_{back})}{B(T_{mr}) - B(T_b)}\right), \tag{3.25}$$

with the Planck spectral radiance B_ν from Equation 2.8 and the mean radiative temperature of the atmosphere (T_{mr}) as derived in Section 2.2. T_{mr} can be calculated independently from atmospheric profiles as a function of the frequency ν and the elevation angle φ (cf. Sec. 6.2).

The tipping curve calibration encompasses a large brightness temperature range, with cold sky temperatures on the one side and a comparatively warm T_{mr} on the other side. Furthermore, Equation 3.25 is highly non-linear. Therefore, it is necessary to perform the tipping curve calibration in the power domain ($B_\nu(T_b)$), because the Rayleigh-Jeans approximation T_b (Eq. 3.3) is not valid over the whole temperature range. The spectral radiances can be converted back to black body equivalent T_b by the inverse of Equation 2.8 afterwards.

In case of clear sky conditions and a homogeneously stratified and non-opaque atmosphere, the opacity scales linearly with the air mass for low optical depths along the slant path (Fig. 3.7). The slope of this linear relation is the zenith opacity τ^{zen}. Zenith T_b^{zen} and τ^{zen} are connected by

$$B_\nu(T_b^{zen}) = B_\nu(T_{back})\, e^{-\tau^{zen}} + B_\nu(T_{mr}^{zen}) \cdot (1 - e^{-\tau^{zen}}), \tag{3.26}$$

which provides an updated cold reference at zenith $B_\nu(T_b^{zen})$. In combination with a view on a hot target the cold reference can then be used within a 2-point calibration to derive the calibration parameters g and T_R (cf. Sec. 3.3.1). A problem arises, because $B_\nu(T_b)$ depends on the calibrated T_b itself. Therefore, the procedure is repeated iteratively and converges to optimal parameters g and T_R, assuming that α remains unchanged (Eq. 3.3.1). Initial T_b values in Equation 3.25 are set by using a prior calibration or an educated guess. For a perfect calibration, the final regression line would pass through the origin of the opacity-air mass diagram (Fig. 3.7). Quality thresholds, which guarantee the goodness of the fit, are used to filter out tipping curve calibrations under inhomogeneous conditions (cf. Sec. 6.2.5). However, even for

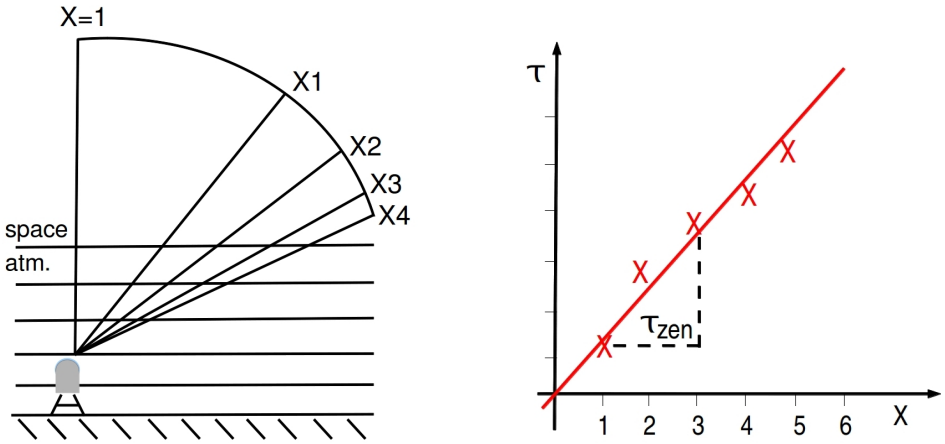

Figure 3.7: Tipping curve method: Under homogeneously stratified atmospheric conditions, the opacity τ scales with the air mass X along the slant path. A linear fit of τ/X-pairs(*red*) gives the zenith opacity τ_{zen} as the slope of the regression line (*red*).

calibrations that pass the thresholds, there is a residual impact on the calibration accuracy from atmospheric inhomogeneities within the scanned volume (cf. Sec. 6.2). This and other sources of uncertainty, like the pointing accuracy and the derivation of T_{mr}, are discussed in Section 6.2.

3.3.3 Noise Diode Calibration

The noise diode calibration is a relative calibration that can be used to derive a single calibration parameter, which can be the detector gain g or the receiver noise temperature T_R. T_N is set by an absolute calibration, for example by a LN_2 calibration. For burned-in noise diodes, T_N is stable enough to provide a secondary calibration standard for a several month period between two LN_2 calibrations (RPG-TM, 2011, RPG-IM, 2011, p. 13, 49). The detector gain g is stabilized by injecting noise periodically while the radiometer is pointing to the scene (T_{SC}). The injection period is well below the integration time. T_{SC} can be extracted from the total signal by using the fraction D of the detected signal with and without noise:

$$D = \left(\frac{U_N}{U}\right)^{\frac{1}{\alpha}} - 1, \tag{3.27a}$$

$$T_{SC} = \frac{T_N - D \cdot T_R}{D}. \tag{3.27b}$$

Knowing T_R from a previous hot load calibration (cf. Sec. 3.3.4) gives a corrected detector gain

$$g = \frac{U_{det}}{(T_R + T_{SC})^{\alpha}}. \tag{3.28}$$

If Gallium Arsenid (GaAs) technology is used for the MMICs, it is sufficient to perform a noise calibration with a much lower repetition rate, because the receiver is much more stable (RPG-TM, 2011, p. 13). In this case, the noise is injected while pointing to the ambient temperature target (T_H) and T_R is updated:

$$T_R = \frac{T_N - D \cdot T_H}{D}. \tag{3.29}$$

3.3.4 Hot Load Calibration

Similar to T_N, the temperature of a hot target T_H can also serve as a relative reference. T_H is known from an in-situ measurement. On the one hand, frequent hot load measurements can be used to correct for drifts of the detector gain g that occur on time scales above the repetition rate. On the other hand, if g is known from continuous noise switching, the receiver noise temperature T_R can be calculated:

$$g = \frac{U_{det}}{(T_R + T_H)^{\alpha}}, \tag{3.30}$$

$$T_R = \left(\frac{U_{det}}{g}\right)^{\frac{1}{\alpha}} - T_H. \tag{3.31}$$

4. Observations

The analyses of this work are mainly based on radiometer measurements from two different deployments. Between August and October 2009, the microwave radiometer HATPRO-G2 was part of the measurement campaign RHUBC-II, which was conducted at a extremely dry, high altitude site in the Atacama desert. After the campaign, HATPRO-G2 has been deployed at the JOYCE site, which offers typical mid-latitude, close to sea level conditions. HATPRO-G2 measurements of these two deployments span a wide range of atmospheric conditions. In the following, both deployments and the radiometer HATPRO-G2 are introduced in detail.

4.1 RHUBC-II

RHUBC-II is the second part of the Radiative Heating of Underexplored Bands Campaigns (RHUBC) conducted within the Atmospheric Radiation Measurement (ARM) program of the U.S. Department of Energy (DOE). Its primary focus was to characterize and improve the accuracy of gas absorption models using high spectral resolution radiance observations in spectral regions that are normally opaque at lower altitudes due to strong water vapor absorption and high air pressure (*Turner and Mlawer*, 2010). The measurement site was set up at 5320 m above mean sea level on the Cerro Toco, next to the Chajnantor Plateau (22.96°S, 67.77°W). The plateau is part of the Atacama Desert in Northern Chile, which is one of the driest regions on Earth. Here, the amount of Precipitable Water Vapor (PWV) ranges from 0.1 mm-5.0 mm (*Rutlland*, 1977).

RHUBC-II was conducted within the dry season between August and October 2009. The ARM program set up a Self-Kontained Instrument Platform (SKIP) providing infrastructure and power supply for a number of different instruments. Several radiometric instruments provide measurements almost across the entire infrared spectrum (*Turner et al.*, 2012). The microwave spectral range was covered by two MWRs: the G-Band Vapor Radiometer Profiler (GVRP), measuring around 183 GHz, and the HATPRO-G2. HATPRO-G2 (*Rose et al.*, 2005) took the data used in this work and is described in detail in Section 4.3. During RHUBC-II, HATPRO-G2 was operated in a continuous scanning mode. This observation strategy was chosen, because of two reasons: On the one hand, this allows to monitor the inhomogeneities of water vapor

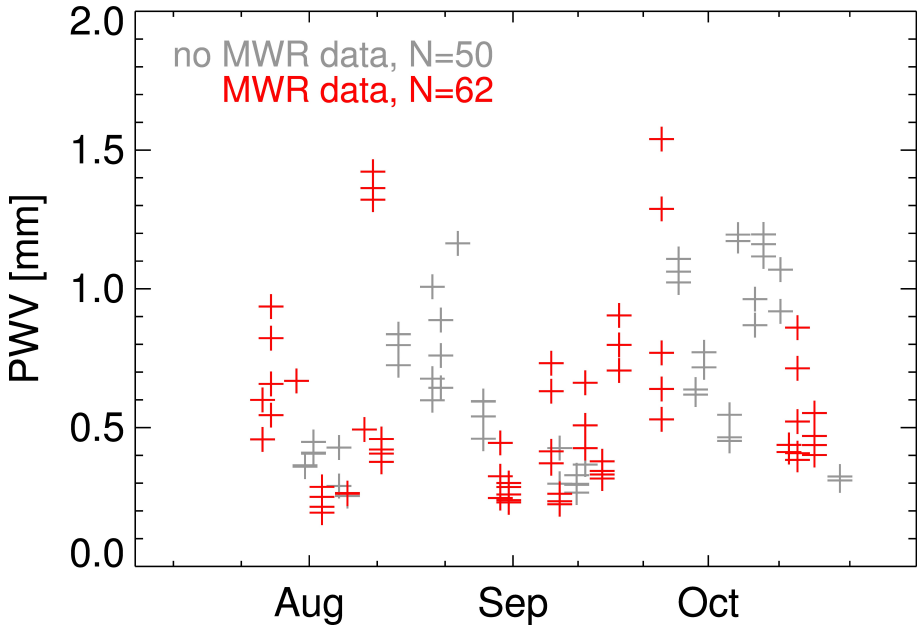

Figure 4.1: Times series of PWV for 112 RHUBC-II radiosondes, *red*: radiosondes launched under clear skies, with (*red*) and without (*gray*) coincident HATPRO-G2 measurements being available.

and temperature. On the other hand, this gives the opportunity to perform a large number of tipping curve calibrations, which helps to assess the uncertainty of the calibration method (cf. Sec. 6). HATPRO-G2 measured at symmetric elevation angles in a fixed azimuthal plane (250°/70°) at elevations 90°, 45°, 30°, 15°, 9.6°, and 4.8°. The complying air masses are 1.0, 1.4, 2.0, 3.9, 6.0, and 12.0. With an integration time of 1 s, each scan takes about 30 s. These scans are used to apply the tipping curve calibration to all K-band channels and two low-opacity V-band channels. The calibration procedures are explained in detail in Section 6.

Furthermore, 133 Vaisala RS92-K[1] radiosondes were launched and provide 112 quality controlled vertical profiles of pressure, temperature, and humidity under cloud-free conditions (cf. Sec. 7.1.1). ThePWV calculated from all radio soundings is below 1 mm for 97 of the 112 radiosondes (Fig. 4.1). (Fig. 4.2 gives an exemplary profiles for a typical dry RHUBC-II radio sounding with $PWV = 0.3$ mm). These are excellent conditions to evaluate absorption models at low pressure and under well defined dry conditions. The instrumentation was completed by an Automatic Weather Station (AWS), which recorded extraordinary constant surface conditions: a daily mean temperature of 266.3 ± 2.8 K, an air pressure of 532.2 ± 2.0 hPa, and a relative humidity of 23 ± 15 %.

[1]Vaisala RS92 datasheet, http://www.vaisala.com/Vaisala%20Documents/Brochures%20and%20Datasheets/RS92-D-Datasheet-B210763EN-B-LoRes.pdf

4.2 JOYCE

Since 2011 HATPRO-G2 measures operationally as part of the Jülich ObservatorY for Cloud Evolution (JOYCE), which was set up at the Juelich Research Center, Germany (FZJ) (92 m above mean sea level (MSL), $50° 54' 30.77'' N$, $6°24' 48.73'' E$). The data used for this work is taken from two experiments. One was conducted between November 10 to 17, 2011, the other one on May 23, 2012. During the first time period, repeated LN_2 calibrations were followed by the scan pattern that was also used during RHUBC-II. First of all, this allows to assess the repeatability of HATPRO-G2's LN_2 calibration – an aspect that could not be investigated from the single LN_2 calibration in the beginning of RHUBC-II. Secondly, the continuous scanning mode gives the opportunity to test the tipping curve procedure for two different atmospheric regimes: The low altitude results from Jülich ObservatorY for Cloud Evolution (JOYCE) are compared to the high altitude RHUBC-II results (cf. Sec. 6). In the second period, the impact of resonance effect on HATPRO-G2's LN_2 calibration (cf. Sec. 6.1.2) was assessed.

4.3 HATPRO-G2

The Humidity And Temperature PROfiler – Generation 2 (HATPRO-G2) is a total-power microwave radiometer (*Rose et al.*, 2005) (Fig. 4.3). The instrument specification, given in this section, are taken from RPG-TM, 2011. It uses direct detection and has 14 channels, which are located within the K- and V-band (Tab. 4.1). It was manufactured by Radiometer Physics GmbH (RPG) and is operated by the Institute for Geophysics and Meteorology of Cologne. In the K-band, atmospheric radiation is measured at seven channels along the slope of the water vapor absorption line at 22.235 GHz. Seven V-band channels measure along the lower frequency wing of the oxygen absorption complex centered around 60 GHz. The receivers of each frequency band are designed as filter-banks in order to acquire all frequency channels in parallel. All channels have been designed with characterized band-pass filters, allowing a clean frequency allocation of the signal. Furthermore, the filter shapes of HATPRO-G2's V-band channels have been measured with high spectral resolution. In this study, the exact shapes are used for measurement simulations (cf. Sec. 5.1). For all non-opaque channels the band-width is 230 MHz. At the more opaque channel frequencies the spectral gradient is low. Therefore, wider band-widths of 600 MHz, 1000 MHz, and 2000 MHz are used to provide a higher precision at equal integration times (*Crewell and Löhnert*, 2007). High resolution PWV and Liquid Water Path (LWP), and profiles of humidity and temperature are retrieved from T_b measurements.

Incoming radiation enters the corrugated feed horn antenna via a parabolic reflector (Fig. 4.4). The horn antennas' HPBWs are 3.3°-3.7° for the channels along the water vapor line and 2.5°-2.7° along the oxygen absorption complex. The HPBW is

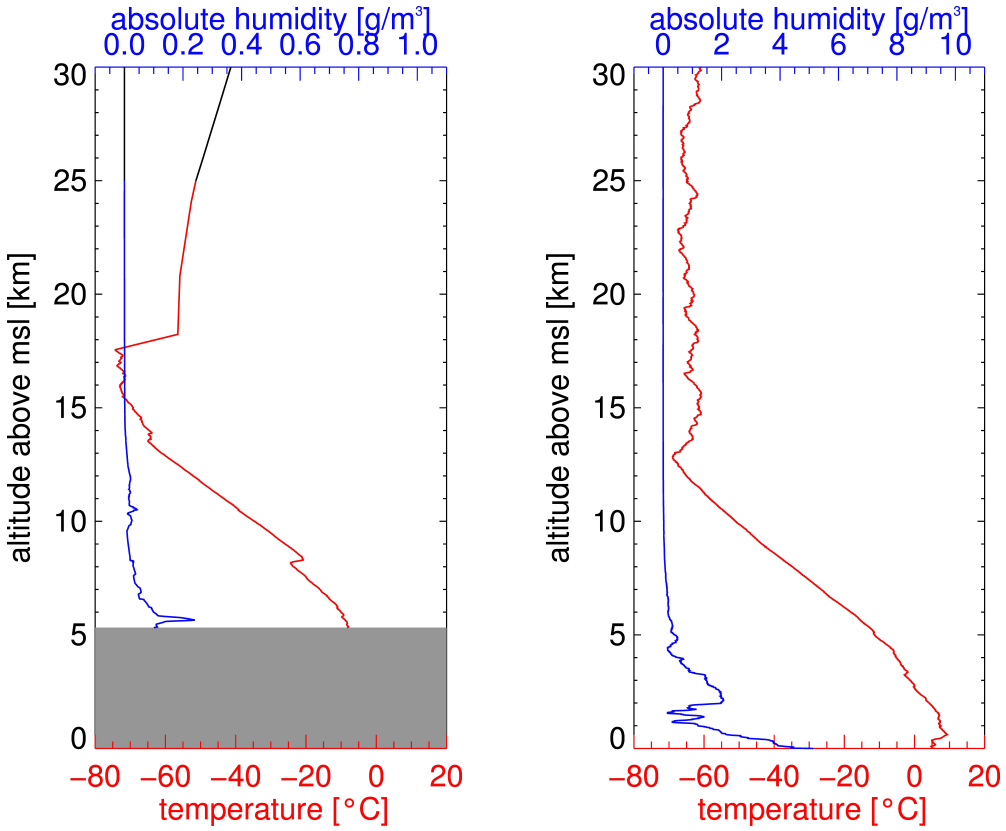

Figure 4.2: Radiosonde profiles for temperature (*red*), and humidity (*blue*). *Left*: a RHUBC-II sounding on September 13, 2009, launched at 5322 m, extended by climatological values for a subtropical climate with a dry stratosphere (*black*). *Right*: mid-latitude, close to sea level radio sounding of the German Weather Service (DWD) in Essen on November 16, 2011 at 12 UTC.

Figure 4.3: The Humidity And Temperature PROfiler – Generation 2 (HATPRO-G2) at the Juelich Research Center, Germany (FZJ).

not identical for all channels, but depends on the frequency (Eq. 3.16). The side lobe suppression is better than 30 dB (Tab. 4.2, Fig. 3.5). Model simulations reveal that 95% of the signal is received within two HPBWs. The incoming radiation power is equally distributed between the two receivers by wire grid beam splitter, which separates vertical and horizontal polarization components. A pin switch and a directional coupler allow to couple in artificial noise from an internal noise diode before the LNAs (Low Noise Amplifiers).

The LNAs (Fig. 4.5) have a gain of about 60 dB and a noise figure $F = 2.0$ dB. Combined with the total system losses of about $L = 2.0$ dB, T_R is below 400 K for the K-band and below 800 K for the V-band channels (RPG-OS, 2011). For an integration time of 1 s, the maximum detection limit ΔT_b is below 0.1 K, if the gain fluctuations are not considered (Eq. 3.13). HATPRO-G2 uses Gallium Arsenid (GaAs) Schottky diodes as detectors with a resolution of 1 mV/µW (RPG-TM, 2011, p.13). The signal is finally amplified and integrated by an operational amplifier (OP-Amp) and reaches the 16-bit Analog-to-Digital Converter (ADC). The whole receiver block is thermally stabilized within 0.03 K (RPG-OS, 2011, p.32).

Four different types of calibrations are implemented in HATPRO-G2's instrument software. At the beginning of every deployment period, the complete set of calibration parameters is determined by a LN_2 calibration. During operation the tipping curve calibration is used to update calibration parameters. Frequent noise diode and hot load calibrations guarantee the detector stability. Taking the RHUBC-II deployment as an example, Figures 4.6 and 4.7 illustrate a typical calibration schedule. Table 4.3 gives the in- and output variables of HATPRO-G2 calibrations during RHUBC-II.

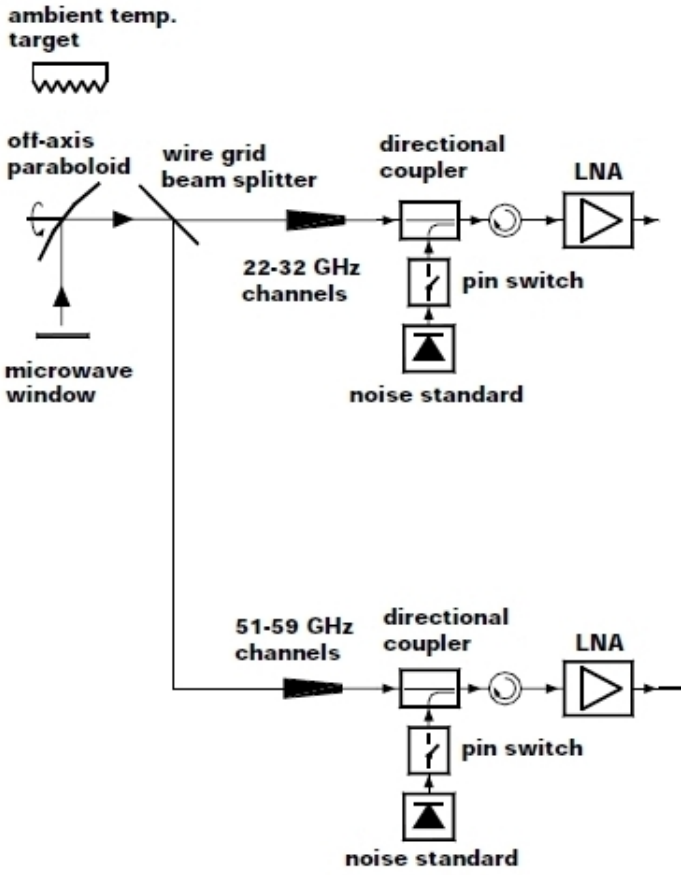

Figure 4.4: Sketch of HATPRO-G2 front-end, extracted from RPG-TM, 2011, p.5.

Unfortunately, only one LN_2 calibration was performed in the beginning of the deployment.

During the whole campaign, tipping curve calibrations were performed every 6 h (Tab. 4.3). T_N, T_R, and g are updated from every of the 97 successful tipping curves, while α is used from the LN_2 calibration. Noise diode calibrations were performed every 30 min. The noise diode temperature T_N from an LN_2 or a tipping curve calibration is used to update the receiver noise temperature T_R for K-band channels (Eq. 3.29). For HATPRO-G2's V-band channels, which need permanent noise switching (cf. Sec. 3.3), T_N is used to update the detector gain g continuously (Eq. 3.28). Additionally, hot load calibrations are performed every 5 min to correct for detector gain drifts within the K-band by updating g (Eq. 3.30). In the V-band, the hot load calibrations are used to update receiver noise temperature T_R (Eq. 3.30). In the following, the implementation of the different calibrations procedures (cf. Sec. 3.3) within HATPRO-G2's operation environment are discussed.

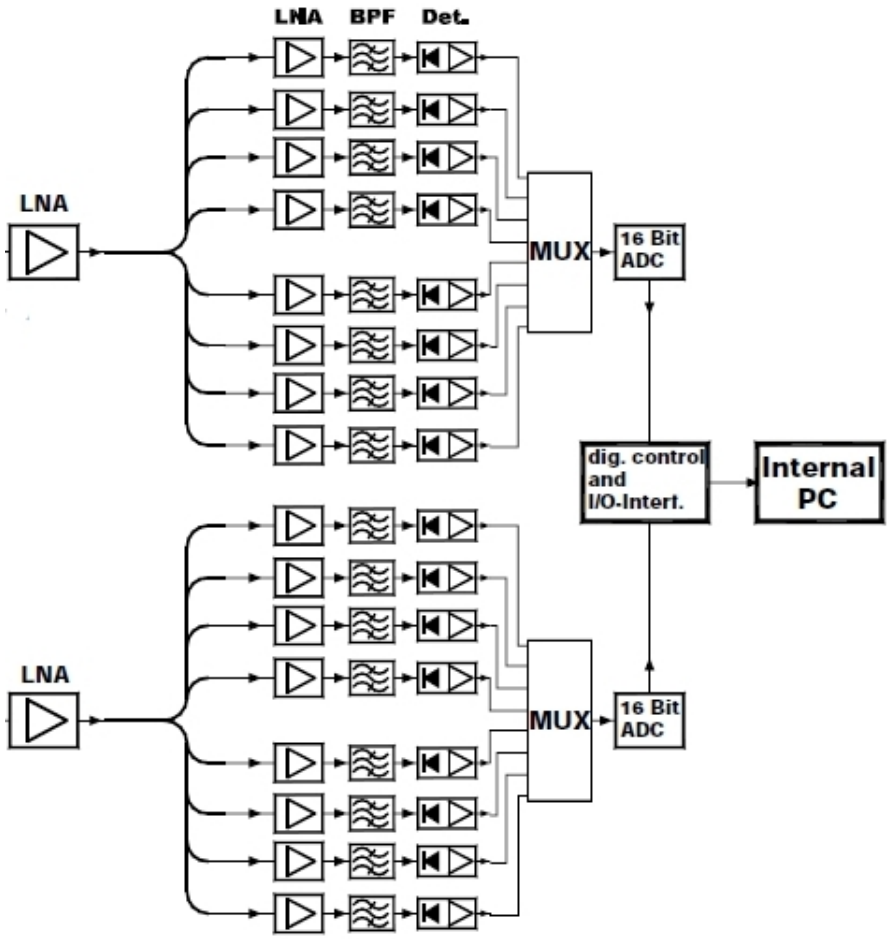

Figure 4.5: Sketch of HATPRO-G2 back-end, extracted from RPG-TM, 2011, p.5.

Liquid Nitrogen Calibration

HATPRO-G2 uses a 4-point calibration scheme (Eq. 3.19). An egg carton shaped microwave absorber, cooled by LN_2, and serves as a cold calibration target. The target is stored in a polystyrene basin, which is filled with about 25 L of LN_2, and mounted alongside the radiometer. It is observed from above, using a reflector tilted by 45° (RPG-IM, 2011, p.51) (Fig. 4.8).

The target's physical temperature is the actual boiling point of LN_2 (T_{LN2}), which is 77.36 hPa at standard pressure (*Span et al.*, 2000), and needs to be corrected for the deployment altitude (cf. Sec. 6.1.1). The hot load is a vented black body target at ambient temperature (T_H) inside the instrument. A temperature sensor located within the target measures T_H. A second sensor detects a mal-function of the used sensor when the deviation between both sensors is above 0.5 K. Typical integration times on the targets are 30 s at each calibration point. Thus, one LN_2 calibration takes about 2 min.

Table 4.1: HATPRO-G2 frequencies and band-pass filters.

$\nu\,[GHz]$	$\lambda\,[mm]$	$\Delta\nu\,[K]$
22.24	13.48	
23.04	13.01	
23.84	12.58	
25.44	11.78	230
26.24	11.43	
27.84	10.77	
31.40	9.55	
51.26	5.85	
52.28	5.73	230
53.86	5.57	
54.94	5.46	
56.66	5.29	600
57.30	5.23	1000
58.00	5.17	2000

Table 4.2: HATPRO-G2 antenna specifications: Half Power Beam Width (HPBW), side lobe level (SLL) and the antenna directivity D.

$Band$	$HPBW\,[^\circ]$	$SLL\,[dBc]$	$D\,[dB]$
K	3.3-3.7	< -30	33.2
V	2.2-2.5	< -50	38.9

Tipping Curve Calibration

As the HATPRO-G2 is designed for standard pressure conditions, tipping curve calibrations are not implemented for the oxygen channels. Close to sea level, these channels are too opaque to perform tipping curve calibrations. During RHUBC-II, the tipping curve calibration was routinely applied to the K-band channels channels every 6 h. The observed elevation scan angles, defined within the presetting, are 90.0°, 56.4°, 45.6°, 38.4°, 33.6°, and 30.0°. Scans were performed towards an azimuth angle of 70.0° N, with an integration time of 15 s at each of elevation. This rather long integration time is applied in order to reduce the impact of atmospheric noise. The scan is completed by a 15 s integration on the internal ambient target and repeated with additional noise injection. Altogether, this tipping curve procedure takes about 2 min. The opacity τ is calculated by Equation 3.25 with a first guess at zenith being $T_b^{zen} = 30\,\mathrm{K}$. Opacity-air mass pairs are linearly fitted to give the slope τ^{zen}, which is used to calculate a new T_b (Eq. 3.26). After 20 iterations, the quality of the fit is

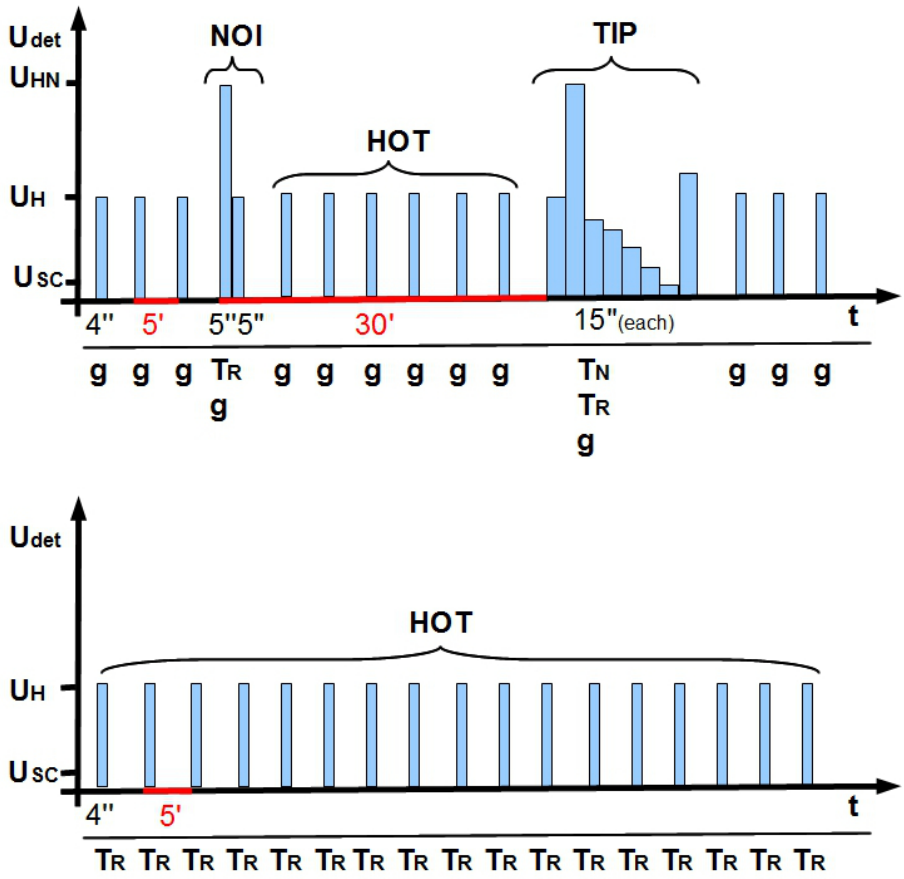

Figure 4.6: HATPRO-G2 calibration scheme during RHUBC-II. *Top*: operational scheme of the seven K-band channels (22.24 GHz – 31.40 GHz), hot load calibrations (HOT) every 5′ to correct drift of the detector gain g, noise diode calibrations (NOI) every 30′ to derive the receiver noise T_R, tipping curve calibrations (TIP) every 6 h to derive g, T_R, and the noise diode temperature T_N. *Bottom*: operational scheme for the V-band channels (51.26 GHz – 58.00 GHz), the detector gain g is adjusted by continuous noise switching between the scene (T_{SC}) and the noise diode (T_N), the receiver noise T_R is updated by hot load calibrations (HOT) every 5′.

tested by two criteria: for all channels the correlation between τ and air mass must be larger than 0.9995 and χ^2 must be $< 0.3 \cdot 10^6$ (cf. Sec. 6.2.5). If these tests are passed, zenith T_b is used as T_C in a 4-point calibration scheme with U_H, U^{zen}, U_{HN}, and U_N^{zen} from the elevation scan. Depending on the number of chosen elevation angles, the whole procedure takes a few minutes. It is assumed that T_b^{zen} does not vary within this time period.

Under the low pressure and low water vapor conditions found at RHUBC-II, the oxygen sensitive channels at 51.26 GHz and 52.28 GHz measure zenith brightness temperatures T_b^{zen} of below 40 K and 60 K, respectively. This offers the unique possibility to calibrate these channels by tipping curve calibrations. The results are used later

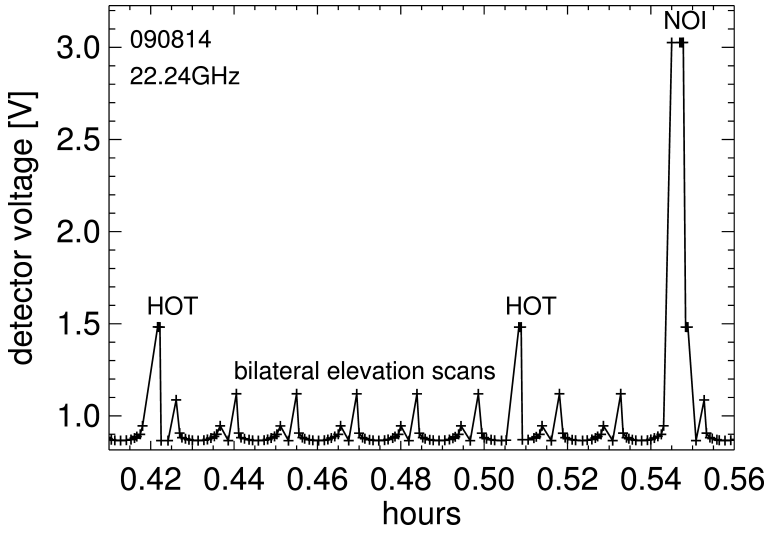

Figure 4.7: Exemplary 10-minute time series of detector voltages on August 14, 2009 for 22.24 GHz. HOT = hot load calibration, NOI = noise diode calibration (cf. Sec. 3.3 and Fig. 4.6).

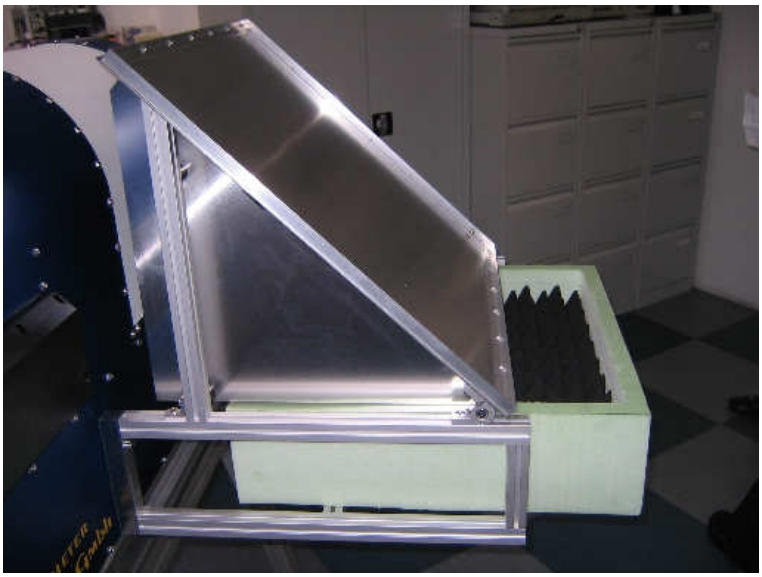

Figure 4.8: HATPRO-G2's LN_2 target, extracted from RPG-IM, 2011.

on for an independent evaluation of the LN_2 calibration (cf. Sec. 6.3). The original tipping curve procedure was extended in a way, that not only the K-band, but also the two V-band channels can be calibrated with tipping curves in post-processing. All tipping curve results originate from this extended procedure which uses the continuous elevation scans that were preformed during RHUBC-II. Only measurements at elevations 90.0°, 45.0°, 30.0°, and 19.8° are used. The corresponding relative air

mass values (Eq. 5.2) are 1.0, 1.4, 2.0, and 3.0. From each scan that passes the quality checks (cf. Sec. 6.2.5), zenith T_b is calculated from Equations 3.25 and 3.26. Another advantage of the extended procedure is that the quality thresholds can be varied and adapted to individual radiometer channels. In contrast to the manufacturer's calibration procedure, no additional noise is injected during scanning. This means, that zenith T_b can only be used in 2-point calibration scheme (cf. Sec. 3.3), where receiver noise temperature T_R and the detector gain g are determined.

Table 4.3: HATPRO-G2 calibration schedule during RHUBC-II: For both frequency bands, the calibration *type*, repetition *period* and *number* is given. The different calibration types are: liquid nitrogen ($LN2$), tipping curve (TIP), noise diode (NOI) and hot load calibrations (HOT), *pointing*: 90.0°=internal ambient target, 0.0°=LN_2 target, i= input parameter, o=output parameter.

K-band channels

type	$LN2$	TIP	NOI	HOT
period	-	6 h	30 min	5 min
number	1	97	4067	14503
pointing	−90°/0°	elev. scan	−90°	−90°
U_{det}	i	i	i	i
T_H	i	i	i	i
T_C	i	i	-	-
α	o	i	i	i
T_N	o	o	i	-
T_R	o	o	o	i
g	o	o	o	o

V-band channels

type	LN_2	TIP	NOI	HOT
period	-	6 h	cont.	5 min
number	1	-	-	14503
pointing	−90°/0°	-	scene	−90°
U_{det}	i	-	i	i
T_H	i	-	i	i
T_C	i	-	-	-
α	o	-	i	i
T_N	o	-	i	-
T_R	o	-	-	o
g	o	-	o	i

5. Measurement Simulation

In this work, HATPRO-G2 measurements are compared to T_b simulations (cf. Chap. 7). Therefore, a proper characterization of the measurements is essential for T_b simulations. There are three main aspects that have to be considered: the finite width of band-pass filters, the beam width of the antenna and the air mass along the slant signal path. The first aspect is important, when comparing T_b simulations with MWR measurements. The latter two aspects are also important for the tipping curve calibration, which needs beam-width corrected T_b observations at exact air mass values (cf. Sec. 3.3.2). The mentioned effects are analyzed for two different atmospheric regimes by using profiles from RHUBC-II radiosondes (5322 m above MSL) and from radiosondes launched by the German Weather Service (DWD) in Essen, Germany (150 m above MSL) as model input.

5.1 Band-Pass Filters

HATPRO-G2 is distinguished by sharp band-pass filters for each radiometer channels. Except for the opaque V-band channels, where the spectral absorption is nearly constant, the filter's Full Width Half Maximum (FWHM) is $\Delta\nu = 230$ MHz (Tab. 4.1). The nominal HATPRO-G2 channels are characterized by the mid-frequency, which is a weighted average over the band-pass filter. In case of symmetric filter functions and linear variations of absorption within the band-pass filters' frequency range, mid-frequencies sufficiently characterize the band-pass filters. However, a curved absorption spectrum within the band-pass filter's frequency range and asymmetric filter shapes can make a difference, when comparing measured and simulated T_b (cf. *Meunier et al.* (2013)).

In this case, T_b simulations should be convolved with the band-pass filter function before they are compared to T_b measurements. Two examples are given by the absorption spectra calculated for a RHUBC-II radiosonde profile on August 16, 2009 and for a sonde from Essen launched at 12 UTC on November 16, 2011 (Fig. 5.1). In the K-band, the spectra only reflect the higher water vapor content at low altitudes. The V-band spectra are more interesting: At sea level, single absorption lines strongly overlap due to pressure broadening and form a nearly smooth spectrum along the low-frequency wing of the absorption complex around 60 GHz. At the high altitude

of RHUBC-II, the single transition lines start to separate (cf. Sec. 2.1.1). It can be seen, that the curvature of the absorption spectrum increases within the band-pass' frequency range (Fig. 5.2). This leads to deviations from the linear relation between simulations at weighted mid-frequencies and simulations, which are convolved with the filter shape. In the following, this effect is investigated for HATPRO-G2 channels.

The exact filter shapes of the V-band channels have been measured at 2000 sample frequencies. For the non-opaque channels, this gives a spectral resolution of about 10 MHz. Two examples of the filter shapes are given in Figure 5.2. For the K-band channels, a Gaussian shaped filter function with $\Delta\nu = 230\,\mathrm{MHz}$ is assumed. T_b is simulated for n_{sam} sampling frequencies within the band width of each channel (T_b^{RTM}). T_b simulations are convolved with the normalized band-pass filter shape $\mathcal{B}$ ($\int \mathcal{B} = 1$) and then compared to simulations at mid-frequencies (T_b^{MID}):

$$\Delta T_b = \Big(\sum_{i=0}^{n_{sam}} T_b^{RTM}(\nu_i)\, \mathcal{B}(\nu_i) \Big) - T_b^{MID}. \tag{5.1}$$

The results are given in Figure 5.3. Obviously, the filter shape has significant impact on T_b in the V-band. The effect is strongest for channels with mid-frequencies at 53.86 GHz and 54.94 GHz. Around these frequencies, the gradient of the absorption spectrum is largest and considering the band-pass filter shape makes up to 1.2 K for RHUBC-II radio soundings. Furthermore, the band-pass effect agrees within 0.04 K for all radio soundings, which are used for the model to measurement comparison in Section 7.5. For the example close to sea level, the effect is smaller ($\leq 0.2\,\mathrm{K}$). In the K-band, the effect at zenith is negligible for both atmospheric conditions.

Since the results are very sensitive to the exact shape in the vicinity of the mid-frequencies, under-sampling of the filter shape may lead to significant errors. Therefore, the impact of a varied number of sample frequencies is investigated (Fig. 5.3). *Cimini et al.* (2009), who perform a model to measurements comparison in the Arctic, sample the MWRs' band-pass filters by 12 points with a 100 MHz resolution. Here it is found that for RHUBC-II at least 200 sampling frequencies are need to consider the band-pass effect sufficiently. For the low altitude radiosonde, even the full filter shape information of 2000 frequencies is needed. In this case, using 200 only frequencies instead of 2000, result in an discrepancy of almost 0.2 K at 53.86 GHz. Using only 100 frequencies, the discrepancy reaches even 0.7 K.

In case the filter shape is not known, it is a sensible approach to assume a simple filter shape. Therefore, results for a rectangular filter shape – where T_b simulations are equally weighted within the band width $\Delta\nu$ – are given for comparison (Fig. 5.3). Here, the rectangular filters are sampled with a resolution of 10 MHz. For HATPRO-G2's V-band channels the maximum difference to the exact solution (2000 sampling frequencies) is 0.4 K for RHUBC-II and 0.2 K for Essen. In any case, T_b simulations that assume rectangular filter shapes are preferable to mid-frequency results.

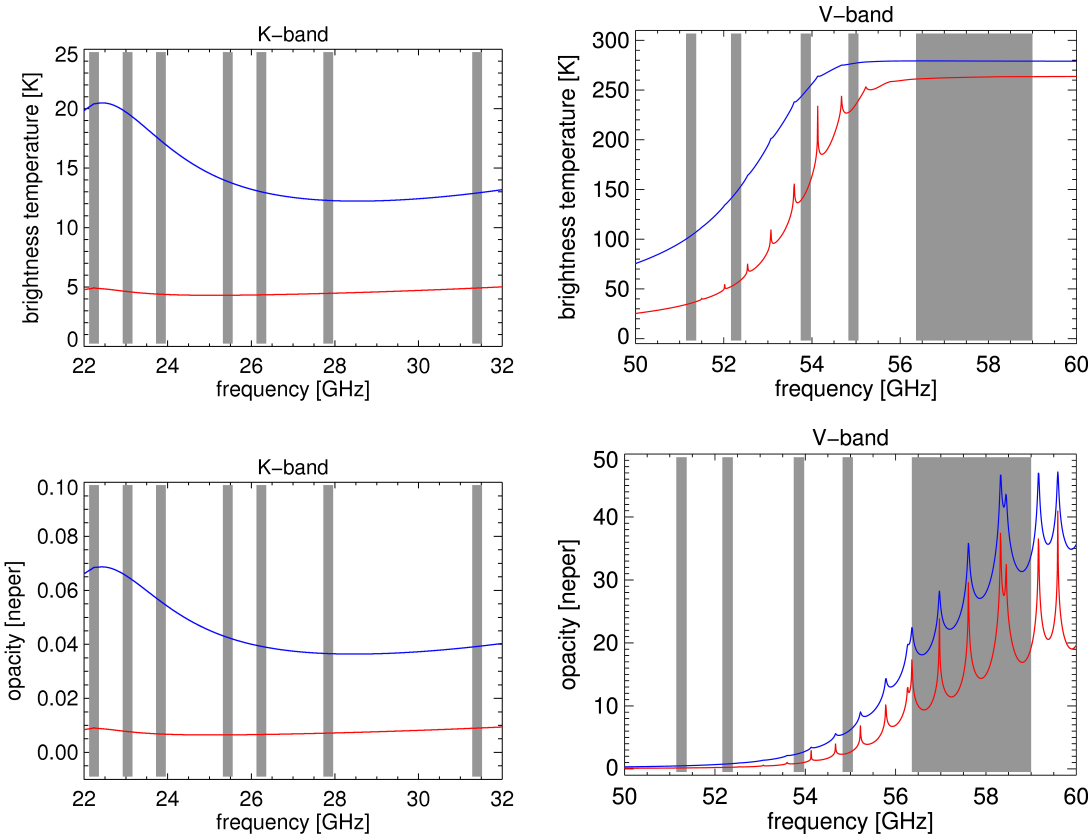

Figure 5.1: Highly spectrally resolved brightness temperatures (T_b, *top*) and opacities (τ, *bottom*). The spectra are based on radiative transfer calculations using the Rosenkranz'98 absorption model (*Rosenkranz*, 1998), for the spectral range covered by HATPRO-G2. Spectral features are the water vapor absorption line at 22.235 GHz (*left*) and the oxygen absorption complex around 60 GHz (*right*). At 530 hPa, pressure broadening is reduced and single transitions can be recognized in the low-frequency wing of the oxygen absorption complex. The upward looking spectrum is plotted for a very dry (PWV = 0.3 mm) RHUBC-II sounding from September 13, 2009 (*red*). For comparison, the spectrum is calculated for close to sea level conditions using a radio sounding from Essen taken on November 16, 2011, 12 UTC (PWV=7.5 mm, *blue*). HATPRO-G2 channels are illustrated by the half-power width of band-pass filters (*gray*). Note, that band-pass filters of the three most opaque channels overlap.

An alternative would be to assume Gaussian-shaped filters and weight the radiative transfer calculations accordingly (cf. Sec. 7.5).

Figure 5.4 shows the dependence on the elevation angle. Again, the V-band is primarily affected. Obviously, at both altitudes the band-pass effect is largest at zenith. With decreasing elevation angles, the channels start to saturate – beginning with the most opaque frequencies. At 10° and 53.86 GHz, the effect completely diminishes for RHUBC-II. Furthermore, the maximum has shifted to 52.28 GHz (≈ 0.3 K). Qualitatively, the same effect can be seen in the low altitude simulations. Apart from the 22.24 GHz channel, being closest to the absorption line, the effect is negligible in the K-band for both altitudes. At 22.24 GHz, T_b of RHUBC-II simulations decreases by 0.3 K, when going down to an elevation angle of 10°, while for Essen it is only 0.1 K. It can be summarized that the band-pass filter shapes mainly affect T_b simulations in the V-band and that the effect is largest for zenith pointing.

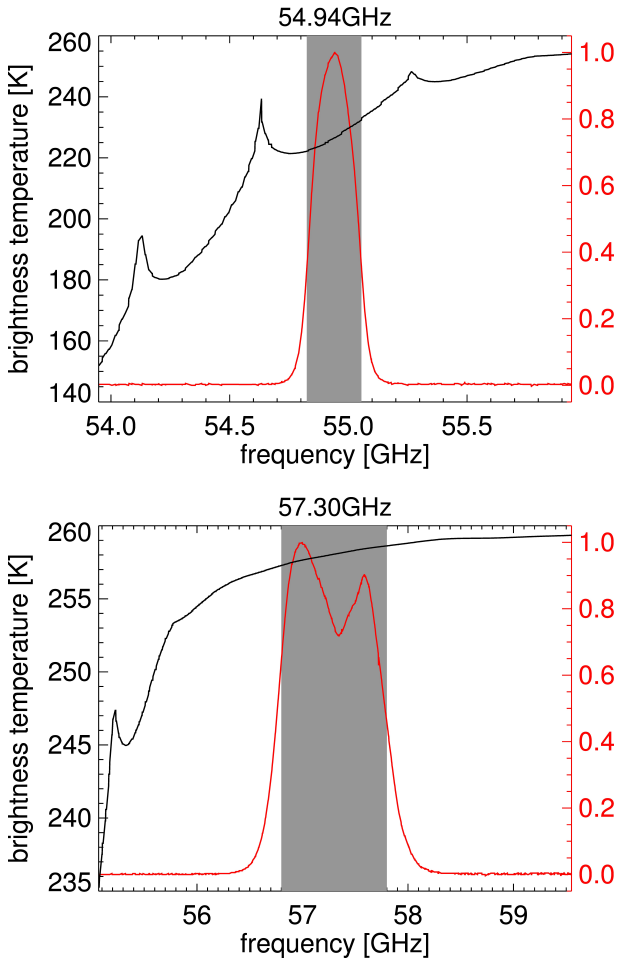

Figure 5.2: Band-pass filter shapes for selected V-band channels of HATPRO-G2. Plotted are the exact filters shapes (*red*), the nominal half-width (*gray shaded*), and the mean absorption spectra of the RHUBC-II radio soundings from August 16, 2009 (*black*).

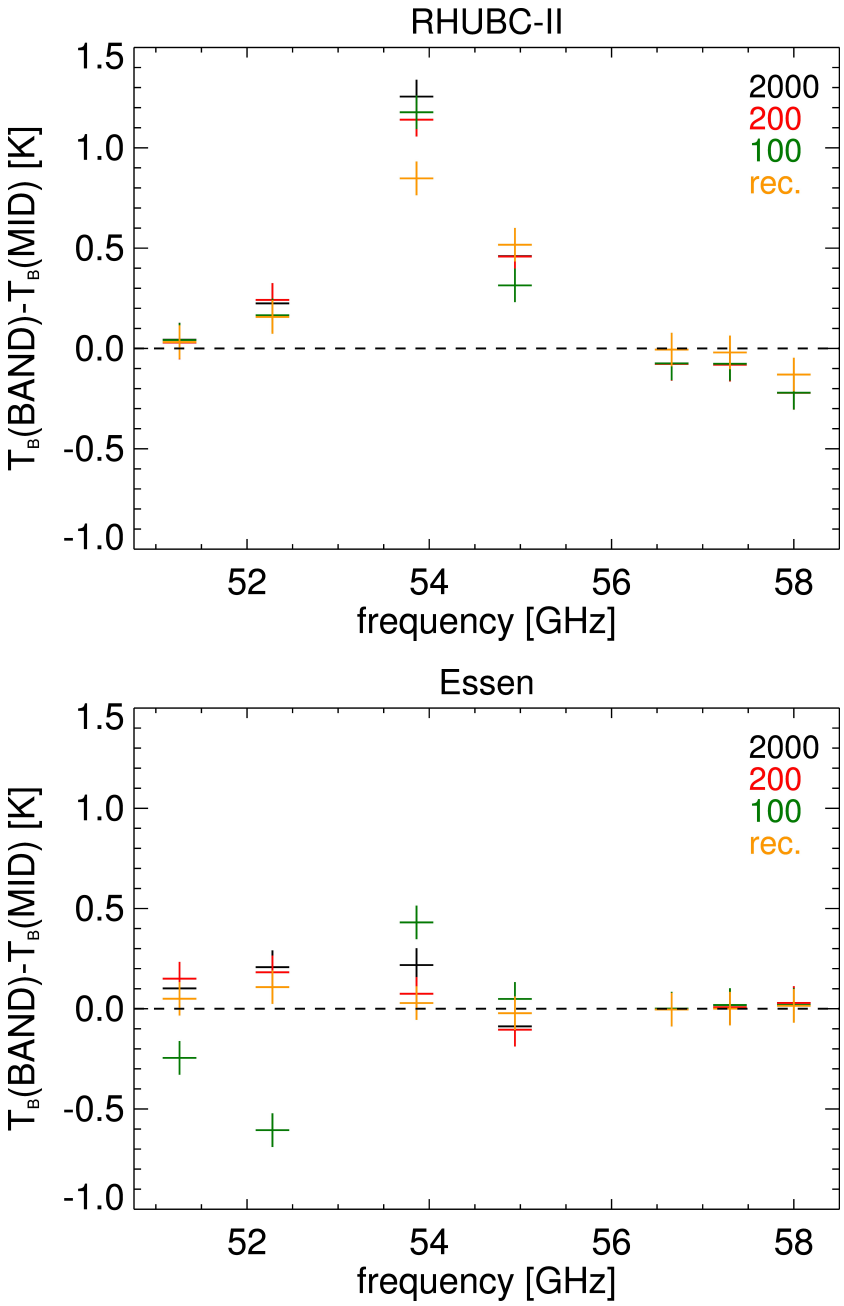

Figure 5.3: Band-pass effect in the V-band simulated for a high (*top*, RHUBC-II) and low altitude deployment (*bottom*, Essen) in dependence of the band-pass sampling. Plotted is the difference $\Delta T_b = T_b^{BAND} - T_b^{MID}$ (Eq. 5.1) from radiative transfer calculations using the Rosenkranz'98 model (*Rosenkranz*, 1998). T_b are simulated for four RHUBC-II soundings from August 16, 2009 and from three sondes launched in Essen on November 16, 2011, at 00 UTC, 12 UTC, and 24 UTC. Displayed are the numbers of frequencies that are used to characterize the filters. Additionally, results for a rectangular filter (*rec.*), sampled with 10 MHz, are given.

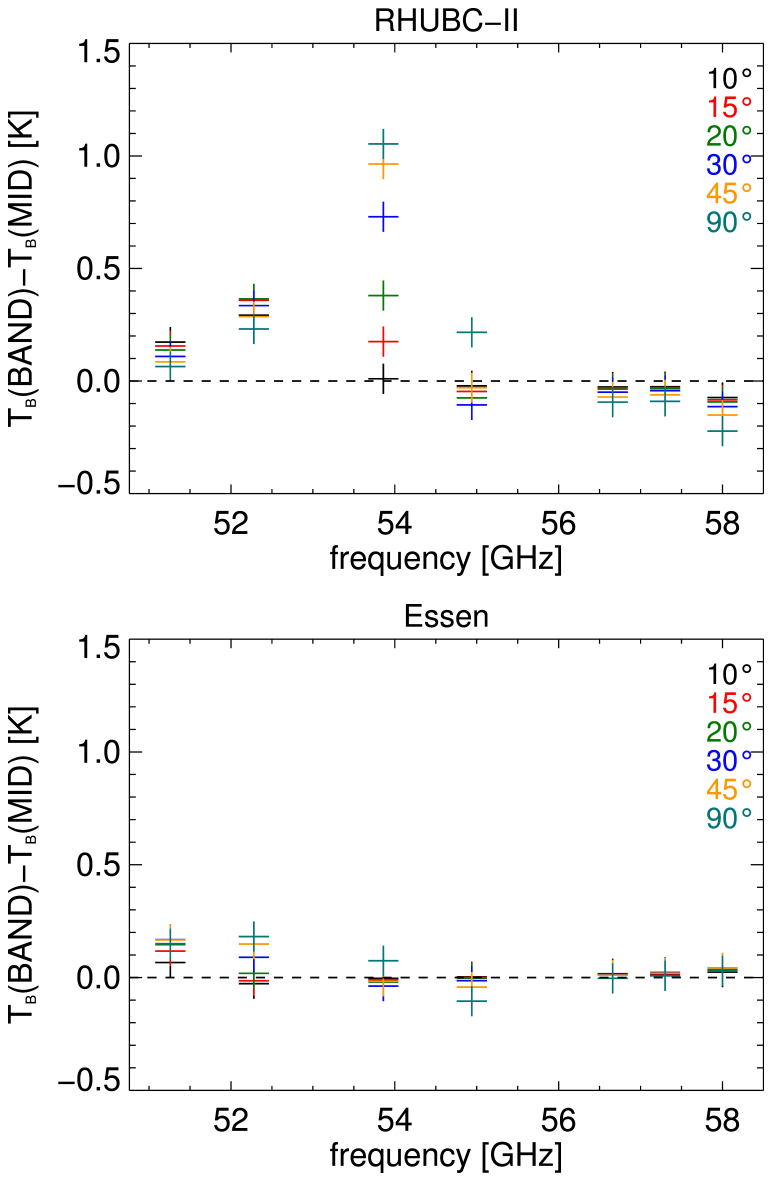

Figure 5.4: Band-pass effect in the V-band simulated for a high altitude (*top*, RHUBC-II) and low altitude deployment (*bottom*, Essen) in dependence of the elevation angle. Plotted is the mean difference $\Delta T_b = T_b^{BAND} - T_b^{MID}$ from radiative transfer calculations using the Rosenkranz'98 model (*Rosenkranz*, 1998). T_b are simulated for four RHUBC-II soundings from August 16, 2009 and three sondes launched in Essen on November 16, 2011, at 00 UTC, 12 UTC, and 24 UTC.

5.2 Air Mass

The relative air mass X is the opacity τ along its slant path through the atmosphere, normalized by its zenith value τ_{zen}. It is defined as:

$$X = \frac{\tau(\theta)}{\tau^{zen}}. \tag{5.2}$$

In case of an ideal plane-parallel, non-refracting atmosphere, the air mass depends only on the elevation angle θ. In this case, the relative air mass is

$$X_0 = \frac{1}{sin(\theta)}. \tag{5.3}$$

However, for real observations the relative air mass X differs from X_0, for off-zenith observations. On the one hand, the Earth's curvature reduces the air mass along the signal path. On the other hand, a height dependent refractive index increases the air mass, because refractive index gradient lead to atmospheric refraction. Both, the curvature and the refraction effect, increase when approaching the horizon. The curvature effect is usually predominant. Therefore, *Han and Westwater* (2000) suggest an air mass approximation for a non-refracting spherical atmosphere:

$$X^{Han} = X_0 - \frac{H}{R_e}(X_0^2 - 1), \tag{5.4}$$

with the Earth's radius R_e and the effective height:

$$H = \frac{1}{\tau^{zen}} \int \beta_a(z)\, z\, dz, \tag{5.5}$$

with the absorption coefficient β_a. H is the upper limit of height layers that effectively contribute to atmospheric absorption. It can be derived from radiative transfer calculations using radiosonde profiles (*Han and Westwater*, 2000). However, Equation 5.4 assumes that $z << R_e$, which includes that atmospheric absorption diminishes within the first kilometers. Even though this is a fairly good assumption as long as absorption decreases exponentially with height, it is not the exact solution. Additionally, Equation 5.4 does not consider atmospheric refraction.

Atmospheric refraction is considered by two approaches, which are introduced in the following. An approach, which is widely used in the weather radar community, is to parameterize refraction by a modified Earth's radius R_e. Usually, R_e is set to an effective radius of $(4/3)\, R_e$ (*Levis et al.*, 2010, p. 121). This model assumes small elevation angles and a linear variation of the refractive index with height. *Doviak and Zrnic* (1993, pp. 18) state that the effective radius model is sufficient for weather radar applications with heights smaller than 20 km and ranges up to 250 km. Additionally, the model cannot not be applied in case of strong atmospheric inversions. However, for the applications of this work, the path through the entire is needed, because

HATPRO-G2 channels are non-opaque, meaning that all height levels contribute to the received signal.

In this case, a ray-tracing method, which uses a realistic vertical profile of the refractive index $n'(s)$ (Eq. 2.2), is more appropriate. n' can be derived from atmospheric profiles. Refractive index gradients along the propagation path can be derived from Snellius' Law. For a spherically stratified atmosphere with l levels it is (*Levis et al.*, 2010, p. 121):

$$n'_0 \, r_0 \, sin(\theta_0) = n'_i \, r_i \, sin(\theta_i), \quad i = 0, 1, 2, ...l, \tag{5.6}$$

where the index 0 marks the surface value of the refractive index n' and the distance r to the Earth's center. θ_i is the exit zenith angle of level i. Together with the law of cosines, the signal path ds is determined for each height level l. Typically, n' decreases with height, i.e. the gradient of the refractive index is negative and $\theta_r > \theta_{r-1}$. Therefore, refraction usually extends the signal path through the atmosphere (cf. Sec. 5.2). One approach is to use a refractive index profile $n'(s)$ that is calculated by a radiative transfer model. Here, the Liebe'93 model (*Liebe et al.* (1993), cf. Sec. 2.3) is chosen for this purpose, because the complex refractive index n (Eq. 2.1) is directly calculated during the forward radiative transfer calculations. The real part n' includes of a non-dispersive part N_0 and a dispersive part N_{disp}:

$$(n' - 1) \times 10^6 = N_0 + N_{disp} \tag{5.7}$$

in $[ppm]$. Close to strong atmospheric absorption features, *Rüeger* (2002) recommends to consider N_{disp} as well. However, it is found that in HATPRO-G2's spectral range N_{disp} is negligible. Therefore, it is sufficient to use a bulk formulae like

$$n' = 1 + \left(c_1 \frac{p - e}{T} + c_2 \frac{e}{T} + c_3 \frac{e}{T^2} \right) \cdot 10^{-6}, \tag{5.8}$$

which allows to calculate n' at every profile level from the atmospheric temperature $T\,[K]$, the pressure $p\,[hPa]$, and the water vapor pressure $e\,[hPa]$. The coefficients c_1, c_2, and $c_3\,[K\,hPa^{-1}]$ are derived from climatological atmospheres. One of the most recent ones is given by *Rüeger* (2002) with $c_1 = 77.695\,\mathrm{K/hPa}$, $c_2 = 71.97\,\mathrm{K/hPa}$, and $c_3 = 3.75406\,\mathrm{K/hPa}$ for the "best available" $n'(s)$. Besides this set of coefficients, there are many others available and discussed in *Rüeger* (2002). Together with a radiosonde profile the path increments ds are used to calculate the opacity at each height level. Integration along the slant propagation path gives the total opacity $\tau(\theta)$. Finally, Equation 5.2 gives the relative air mass value X.

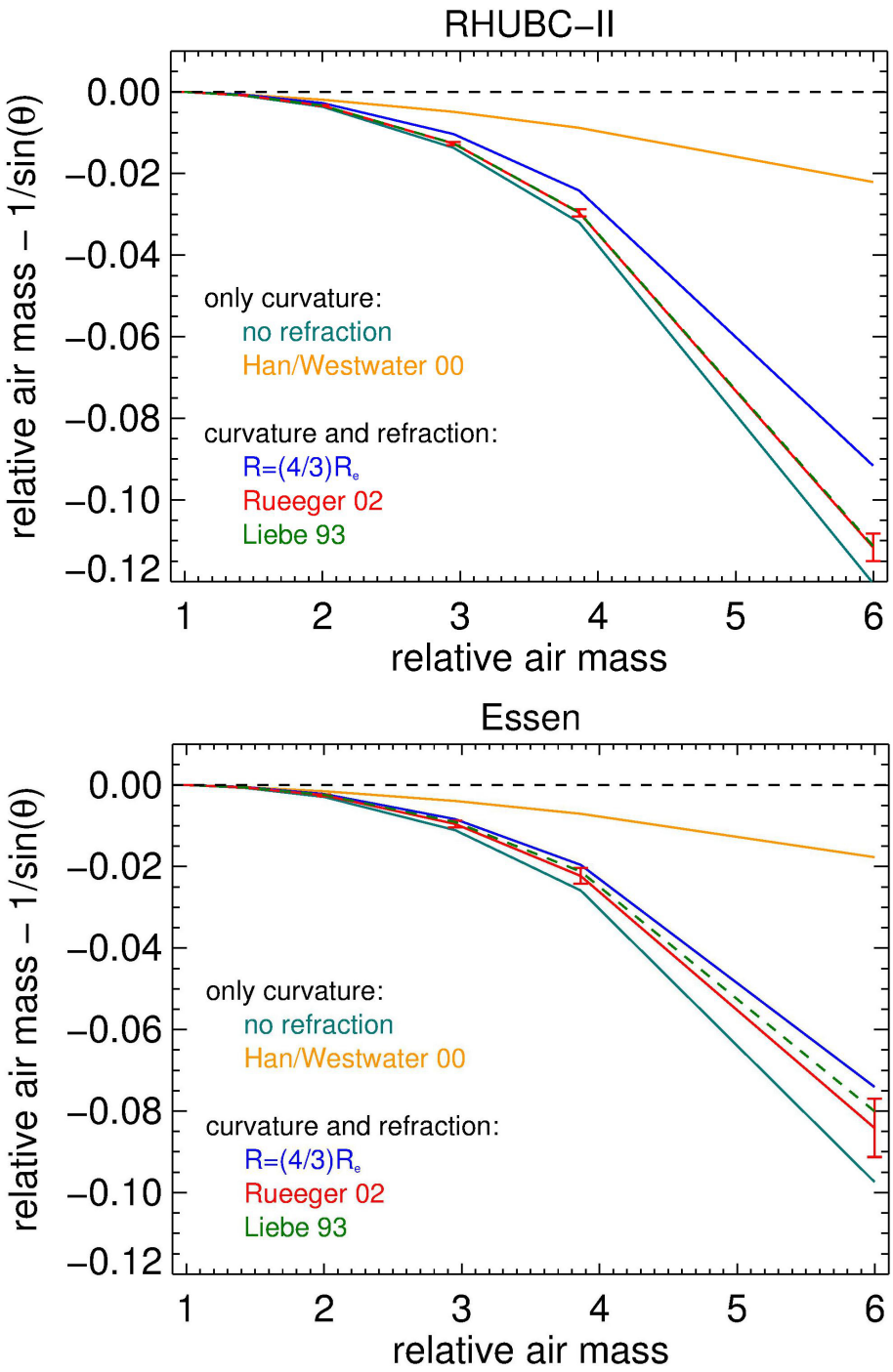

Figure 5.5: Relative air mass calculations shown as deviation from $X_0 = 1/sin(\theta)$ (plane-parallel, non-refracting) for different spherical approaches (cf. Sec. 5.2): no refraction (refractive index gradient is set to zero), (4/3) R_e (*Levis et al.*, 2010), Liebe 93 (*Liebe et al.*, 1993), Rueeger 02 (*Rüeger*, 2002), Han/Westwater 00 (*Han and Westwater*, 2000). *Top*: mean values of X derived from 112 RHUBC-II radio soundings (*error bars* give the standard deviation of the 112 soundings for Rueeger 02). *Bottom*: mean values of X derived from 60 radiosondes launched in Essen (*error bars* give the standard deviation of the 60 soundings for Rueeger 02).

The impact of different methods on calculated X and the corresponding T_b at different elevation angles is given for two different atmospheric regimes (Fig. 5.5 - 5.7). Refractive index profiles $n(s)$ and effective heights H are calculated from 112 RHUBC-II clear sky radio soundings and for one clear sky radiosonde launched in Essen at 00 UTC on November 16, 2011 – a day used for analyzing the tipping curve calibrations (cf. Chap. 6). Figure 5.5 compares relative air masses X in spherical atmospheres to the non-refracting plane-parallel case (X_0). The deviations are largest, when the ray-tracing method is applied to a non-refracting atmosphere. All other methods give larger air mass values. It can be seen, that the path prolongation due to refraction is relatively small for the realistic refractive index profiles according to *Rüeger* (2002) and from the Liebe'93 model. For the approaches , X differs from X_0 by more than 0.01 at three air masses. Figure 5.5 gives the mean results derived from 112 RHUBC-II sondes and for 60 sondes launched in Essen in November 16, 2011. At six air masses, the difference is ≈ -0.1 air masses, but only 10% of that value are due to refraction. For the sondes launched in Essen, the corresponding values are -0.01 at three air masses and ≈ -0.08 at six air masses, with almost 20% resulting from refraction.

In comparison, the $(4/3)\,R_e$ approach overestimates the relative air mass X. For RHUBC-II, the difference to the plane-parallel, non-refracting case is -0.09 at six air masses, refraction contributes about 30% to this value. For Essen, it is 0.09 – with 25% of this value caused by refraction. Although air mass calculations according to *Han and Westwater* (2000) do not consider refraction, the results are closest to X_0. At six air masses, the difference to X_0 is only 0.02 on average for RHUBC-II and 0.015 for Essen. The relative air masses X are considerably overestimated. At 150 m above MSL (Essen), air mass values are generally smaller. On the one hand, refraction is stronger, because the lower troposphere is included. On the other hand, even when refraction is not considered, relative air mass values from Equation 5.2 depend on the opacity $\tau(\theta)$. As the relation between the elevation angle θ and the $\tau(\theta)$ is not linear, air mass values decrease with increasing opacity. Compared to air masses derived for RHUBC-II, the refraction effect derived from Essen sondes is doubled, while the curvature effect is reduced by about 10%. This means, the deployment altitude has to be considered in the air mass calculations – a fact that is particularly important when no radiosonde profile is available. When using a standard profile instead, it has to be adapted to the deployment height.

In the following, it is discussed how T_b simulations are affected by the different air mass calculations. Figure 5.6 gives the T_b difference in dependence of the frequency ν at three air masses referred to the plane parallel case. T_b simulations are performed with the Rosenkranz'98 model for HATPRO-G2 frequencies. The first RHUBC-II sonde on August 16, 2009 and the 12 UTC Essen sonde on November 16, 2011 serve as input. The impact on T_b within the HATPRO-G2 range is highest for non-saturated V-band channels: For RHUBC-II sondes, it reaches 1.3 K at 52.28 GHz, for Essen it

is even almost 3.0 K.

The impact of refraction is given by the difference $\Delta T_b(\nu)$ between an approach that considers refraction (*Rüeger*, 2002) and the non-refracting case (Fig. 5.7). For RHUBC-II, $\Delta T_b(\nu)$ at three air masses is always below 0.1 K within HATPRO-G2's frequency range. Again, the effect is largest for the low-opacity V-band channels with $\Delta T_b(\nu) = 0.3$ K. For the Essen sonde, $\Delta T_b(\nu)$ exceeds 0.1 K in the V-band already at three air masses. Due to the much larger amounts of atmospheric water vapor at low altitudes, the maximum in the K-band is reached at very low elevation angles and close to the water vapor line. For six air masses, $\Delta T_b(\nu)$ is up to 0.6 K. This suggests that refraction needs to be considered, especially at lower altitude deployments with higher opacities.

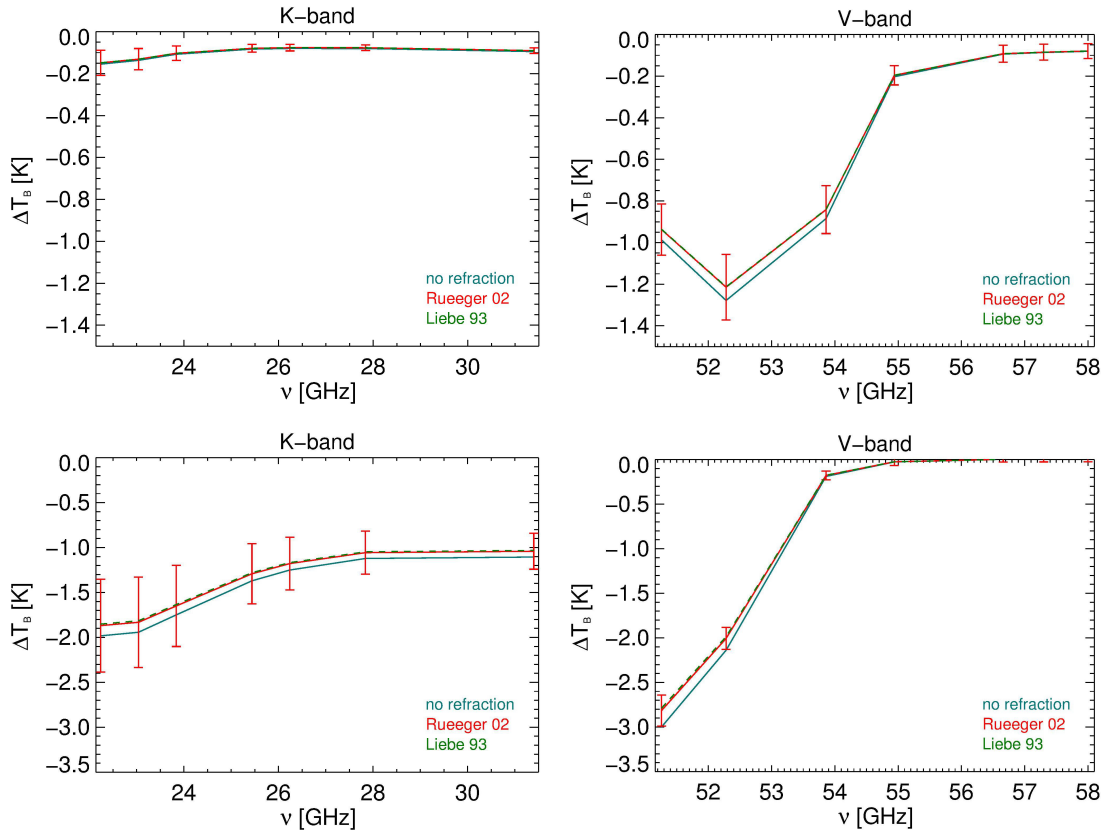

Figure 5.6: Impact of different air mass calculations on simulated T_b at three air masses for HATPRO-G2 channels. *Top*: simulations for 112 RHUBC-II radio soundings, *error bars*: standard deviation for Rueeger 02 (*Rüeger*, 2002). *Bottom*: simulations for 60 radiosondes launched in Essen during November 2011 . Mean $\Delta T_b = T_b(X) - T_b(X_0)$, $X_0(= 1/sin(\theta)) = 3$ (with the elevation angle θ), relative air mass X is calculated by different methods: no refraction (refractive index gradient is set to zero), Liebe 93 (*Liebe et al.*, 1993), and Rueeger 02 (*Rüeger*, 2002) (*error bars* give the standard deviation for 60 and 112 soundings, respectively).

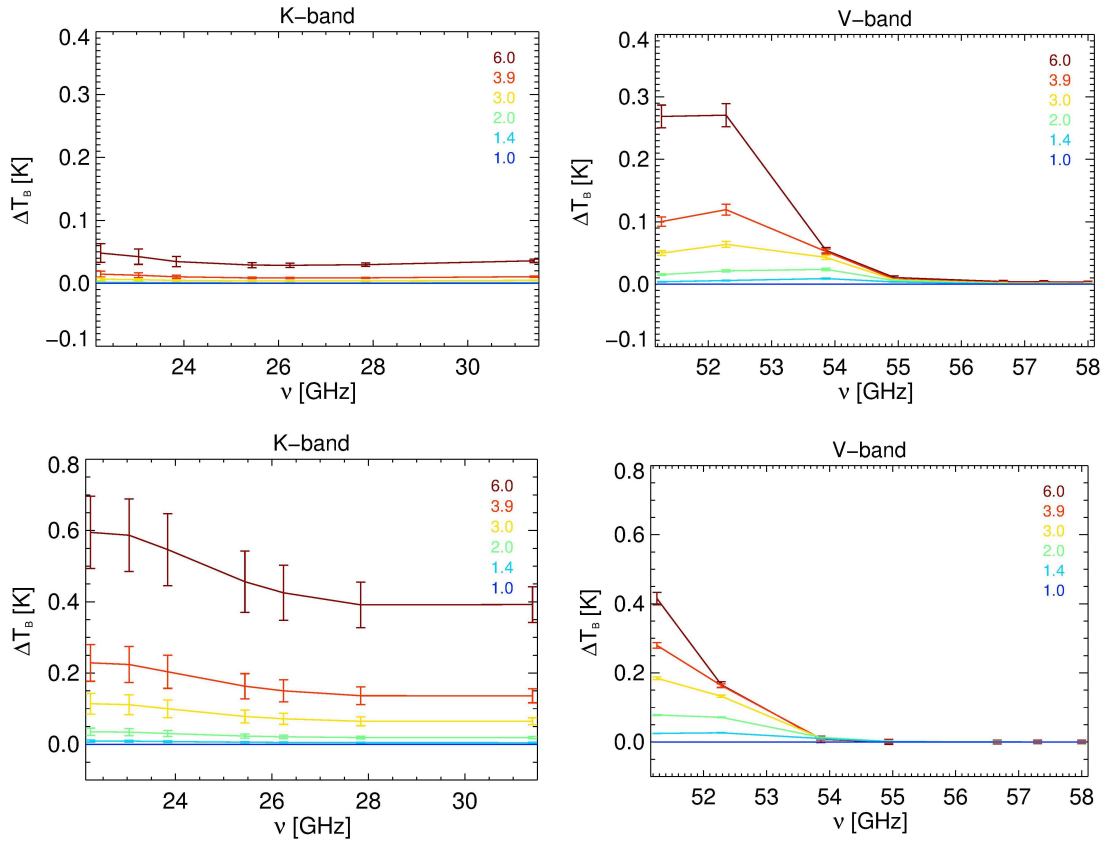

Figure 5.7: Impact of atmospheric refraction on simulated T_b at three air masses for HATPRO-G2 channels. *Top*: simulations for 112 RHUBC-II radio soundings. *Bottom* simulations for 60 DWD launched in Essen during November 2011. ΔT_b results from relative air mass calculation that neglect (zero line) and consider refraction (*Rüeger*, 2002). Atmospheric absorption is calculated by the Rosenkranz'98 model (*Rosenkranz*, 1998).

Additionally, the dispersive component N' of the refractive index (Eq. 5.7) is investigated by comparing T_b simulations that include N' from the Liebe'93 model with simulations using only non-dispersive refraction following *Rüeger* (2002). The effect is found to be negligible for air mass calculations. This means, although HATPRO-G2 measures along absorption lines, it is sufficient to use a ray-tracing method with a refractive index from a bulk formula like the one by *Rüeger* (2002). X values from ray-tracing in a spherical atmosphere and refraction parameterized after *Rüeger* (2002) are used to simulate T_b for the measurement to model comparison included in this work (cf. Sec. 7.5). Furthermore, corrections $\Delta X = X - X_0$ are used to correct the nominal air mass values X_0. In Section 6.2, the corrected opacity air mass-pairs are then used for the tipping curve calibrations.

5.3 Beam Width

Radiometer antennas do not receive their signal from a single direction, but over a broad region, which is defined by the antenna pattern (cf. *Han and Westwater* (2000)). The antenna pattern describes the anisotropy of the antenna gain (Fig. 3.5). Nevertheless, most of the signal is received via the antenna's main lobe whose size is characterized by the HPBW. However, even when assuming that contributions from outside the HPBW can be neglected, T_b simulations have to consider the beam width, because T_b does not scale linearly with the elevation angle φ_0 (cf. *Meunier et al.* (2013)). On the one hand, for low-opacity channels, the antenna will pick up more signal contributions from below the nominal elevation angle. Measured T_b will be higher compared to an idealized pencil beam. On the other hand, high-opacity channels, which start to saturate at low elevations, will give lower T_b measurements at elevation φ_0 than expected. This is illustrated in Figure 5.8: In case that the beam width is not considered ($T_b(\varphi_0)$), a positive curvature ($\partial^2 T_b/\partial\varphi^2) > 0$ (optically thin radiometer channels) results in an underestimation and ($\partial^2 T_b/\partial \varphi^2) < 0$ (e.g. optically thick HATPRO-G2 channels in the V-band) in an overestimation.

For T_b simulations, the beam width can be considered by including a one-dimensional antenna pattern $\mathcal{F}(\varphi)$ (cf. Sec.3.2). *Han and Westwater* (2000) use a theoretical approach to calculate a correction δT_b. Here, a numerical approach is taken to correct for HATPRO-G2's beam-width. HATPRO-G2's beam is modeled as a Gaussian-shaped lobe with an area of influence of two HPBWs being 7° for the K-band and 5° for the V-band channels (Tab. 4.2, cf. Sec. 4.3). It is resolved by equally distributed and weighted radiative transfer calculations around the nominal elevation angle with

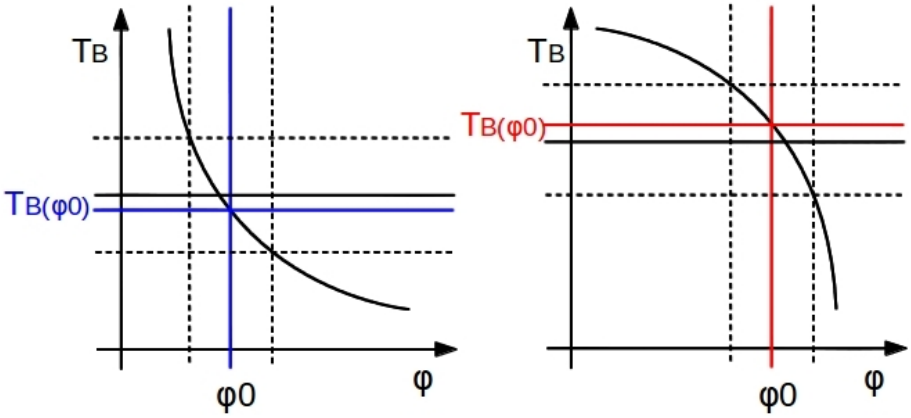

Figure 5.8: Schematic illustration of the beam width effect (cf. *Meunier et al.* (2013)). *Blue*: a positive curvature of $T_b(\varphi)$ ($(\partial^2 T_b/\partial\varphi^2) > 0$, i.e. optically thin) leads to an underestimation by the pencil-beam results ($T_b(\varphi_0) < T_b^{ANT}$). *Red*: a negative curvature of $T_b(\varphi)$ ($(\partial^2 T_b/\partial\varphi^2) < 0$, i.e. optically thick) leads to an overestimation by the pencil-beam results ($T_b(\varphi_0) > T_b^{ANT}$).

a resolution of 0.1° (air mass correction is included). In order to reproduce the measurements, T_b results are convolved with the antenna pattern:

$$T_b^{ANT}(\nu,\varphi) = \int_{-HPBW}^{+HPBW} T_b(\nu,\varphi)\,\mathcal{F}(\varphi)d\varphi. \tag{5.9}$$

The $T_b^{ANT}(\nu,\varphi)$ results for RHUBC-II and Essen radio soundings are given in Figure 5.9. For Essen, only the K-band channels show a positive curvature ($(\partial^2 T_b/\partial\varphi^2) > 0$). Under RHUBC-II conditions, the lowest opacity V-band channels at 51.26 GHz and 52.28 GHz have a positive curvature, too. Consequently, for these channels the beam width correction $\delta T = T_{ANT} - T_b(\varphi_0)$, plotted as a function of air mass $X(\varphi)$ in Figure 5.10, is also positive. Naturally, the beam width effect is zero at zenith and increases towards higher air mass values.

For the Essen profiles, δT_b is between 0.2 K and 0.5 K at three air masses. At six air masses, δT_b is already above 1.0 K in the K-band, while for RHUBC-II the correction is smaller than 0.6 K. This is due to the drier condition at high altitudes, which lead to lower opacities in the K-band. However, for RHUBC-II at 51.26 GHz and 52.28 GHz, δT_b is about 0.5 K at three air masses and 0.9 K and 1.7 K at six air masses, respectively. For both profiles, the saturated channels in the V-band are characterized by negative curvatures ($(\partial^2 T_b/\partial\varphi^2) < 0$, Fig. 5.9). Consequently, for these channels the beam width corrections are negative and reach $\delta T_b \approx -0.5$ K at six air masses.

The results indicate that a beam width correction is necessary, when simulating off-zenith measurements of MWRs, which usually have a beam width of several degree. In this work, $+\delta T_b$ is, on the one hand, used to correct T_b simulations that are compared to real measurements (cf. Sec. 7.5). On the other hand, δT_b is subtracted from the slant path measurements that are used for the tipping curve calibrations. Corrected T_b measurements then comply to the nominal air mass values $X_0(\varphi_0)$ (cf. Sec. 3.3.2).

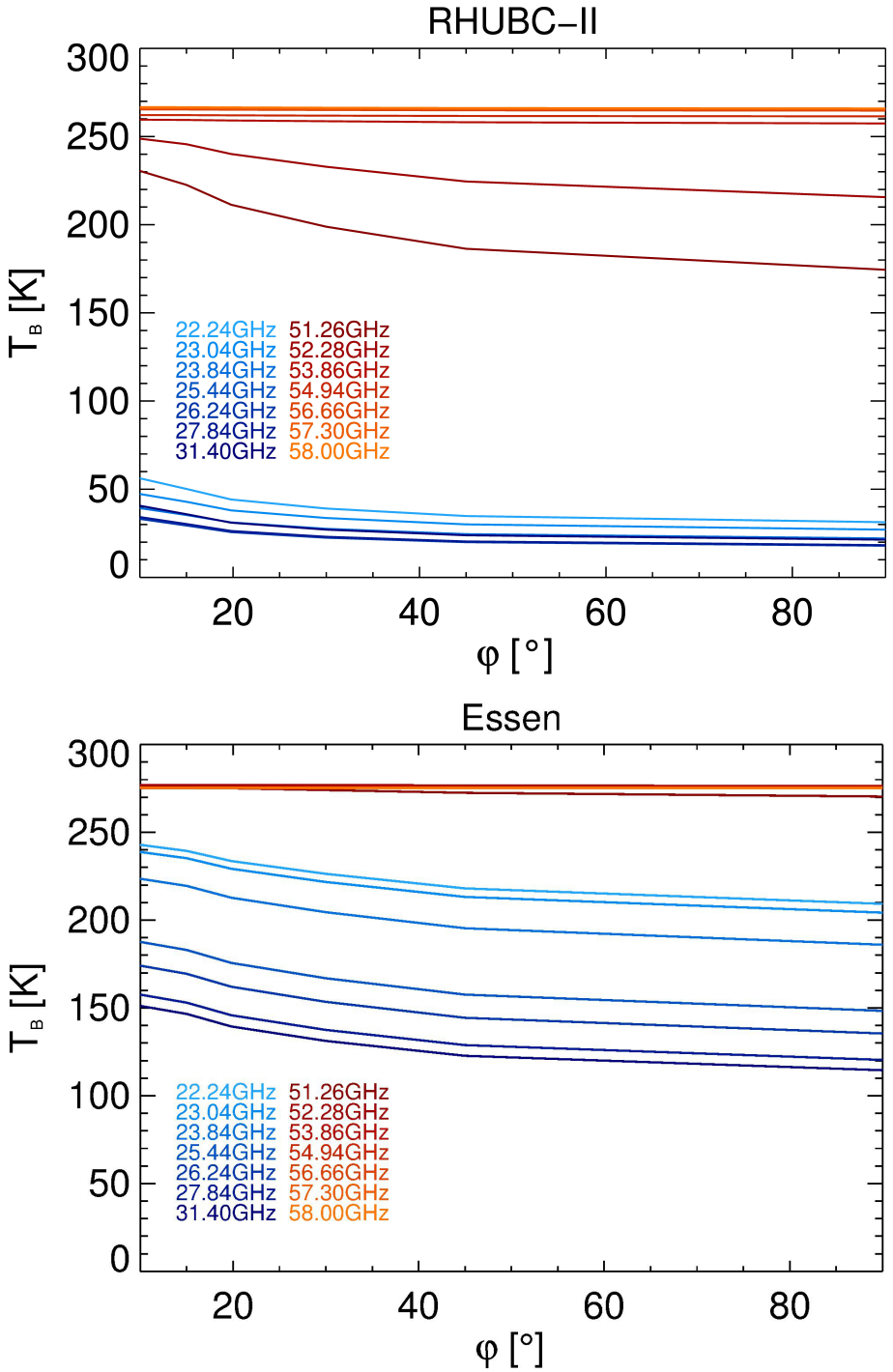

Figure 5.9: T_b simulations with the Rosenkranz'98 model (*Rosenkranz*, 1998) in dependence of the elevation angle φ for HATPRO-G2 channels. *Top*: mean results of four RHUBC-II radio soundings from August 16, 2009. *Bottom*: mean results of three radio soundings from Essen taken at $00\,UTC$, $12\,UTC$, and $24\,UTC$ on November 16, 2011.

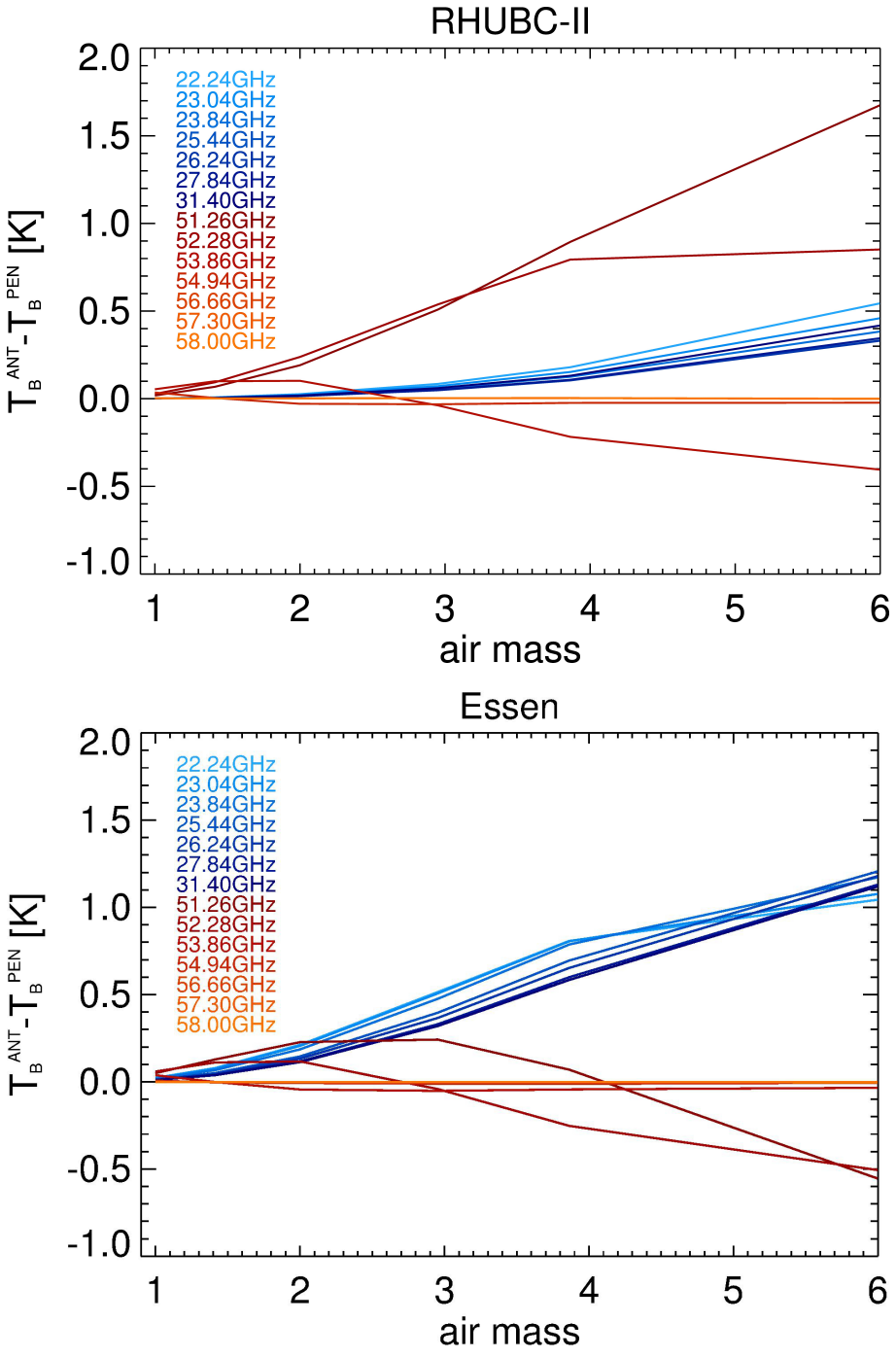

Figure 5.10: Beam width corrections of pencil beam results $\delta T_b = T_b^{ANT} - T_b^{PEN}$ for HATPRO-G2 channels. *Top*: mean results of four RHUBC-II radio soundings from August 16, 2009. *Bottom*: mean results of three radio soundings from Essen taken at $00\,UTC$, $12\,UTC$, and $24\,UTC$ on November 16, 2011.

6. Calibration Analysis

The Liquid Nitrogen (LN_2) and the tipping curve calibration, introduced in Section 3.3, are commonly used to calibrate ground-based microwave radiometers (MWRs). However, for radiometer channels along the oxygen absorption complex in the V-band, biases of 1 K-2 K are found when comparing T_b simulations with measurements based on a LN_2 calibration. *Hewison et al.* (2006) compare T_b simulations using different gas absorption models to MWR measurements. For K-band channels along the water vapor line at 22.235 GHz, they find that model results deviate by up to 1.4 K from the measurements. The maximum discrepancy for V-band channels along the low-frequency wing of the oxygen absorption complex at 60 GHz is 3.0 K. Even for the model which is closest to the measurements (*Rosenkranz*, 1998), the band average of absolute deviations is 0.3 K for the K-band and 1.1 K for the V-band. It is still not clear, whether the detected biases originate from uncertainties in the LN_2 calibration or from oxygen absorption models.

Obviously, there is a need to estimate the accuracy of calibration techniques by assessing their possible sources of uncertainty. *Hewison and Gaffard* (2003) assess measurement accuracies that result from each of the techniques for a passive microwave profiler with 12 K- and V-band frequencies. For the LN_2 calibration, they find calibration uncertainties of up to 1.6 K in the K-band and up to 0.8 K in the V-band. The assessed uncertainties of the applied tipping curve calibration are below 0.8 K.

In this work, the absolute accuracy of HATPRO-G2 measurements is assessed by propagating uncertainties of the calibration parameters through the LN_2 and the tipping curve calibration procedure. An analytical error propagation for the calibration parameters of the LN_2 calibration is given in Appendix C.

6.1 Liquid Nitrogen Calibration

For the LN_2 calibration, the contribution of each source of uncertainty is estimated by separately varying the individual input parameters for the detector voltages U_{det} (Eq. 3.19). For these simulations, the system of equations U_{det} (Eq. 3.3.1) is solved using Newton's method. The calibration parameters derived from these simulations can be compared to the ones of original calibration from August 11, 2009. The largest

part to the calibration uncertainty is induced by systematic effects at the reference targets. Here, two questions arise: What is the actual temperature of the target and how large is the reflective component that is added to the target's signal? However, there is also unsystematic calibration noise that affects the repeatability of a LN_2 calibration. In the following, the single effects are discussed one by one.

6.1.1 Boiling Point Correction for Liquid Nitrogen

When calibrating against a liquid nitrogen target, the LN_2 boiling point serves as reference. At standard pressure ($p_0 = 1013.25\,\mathrm{hPa}$), this is $T_0 = 77.36\,\mathrm{K}$. However, the boiling point depends on the atmospheric pressure p and has to be corrected accordingly. For HATPRO-G2, the corrected boiling point is calculated from surface pressure supplied by the internal sensor. At the RHUBC-II pressure level of 530 hPa, the correction is already about 5 K. Any inaccuracy in the applied correction impacts T_b – especially for scenes close to or below the cold calibration temperature. However, different instrument manufacturers use different formulae for the pressure dependent correction (Fig. 6.1):

$$T_{LN_2}^{RPG} = T_0 - 0.00825\,(1000.00 - p), \tag{6.1}$$

$$T_{LN_2}^{RAD} = 68.23 + 0.009037\,p, \tag{6.2}$$

with p in hPa. $T_{LN_2}^{RPG}$ and $T_{LN_2}^{RAD}$ refer to RPG-OS, 2011 and a operational manual by *Radiometrics*[1], respectively. The different formulations might be explained by the fact that the pressure dependency is often calculated for high technical pressures in the laboratory. At standard pressure, the discrepancy between these formulations is still mostly negligible. However, with decreasing pressure it increases and reaches 1.1 K at 530 hPa (Fig. 6.1). In Figure 6.1, the impact of the different boiling point corrections on the calibration is shown. The effect itself is not frequency dependent, but the impact on measured T_b increases with decreasing channel opacity. It can be seen, that moving away from the hot target increases the cold target's influence. Therefore, the window channel at 31.40 GHz is most affected ($> 1.5\,\mathrm{K}$). At the LN_2 boiling point, the discrepancy between the different corrections already exceeds 1 K (Fig. 6.1). The proper pressure-dependent correction for the LN_2 boiling point can be calculated from the Clausius-Clapeyron Equation for ideal gases:

$$\frac{1}{p}dp = \frac{\Delta H_{vap}}{RT^2}dT \Rightarrow ln\Big(\frac{p}{p_0}\Big) = \frac{\Delta H_{vap}}{R} \cdot \Big(\frac{1}{T_0} - \frac{1}{T}\Big), \tag{6.3}$$

with the boiling point temperature of LN_2 T and the ideal gas constant $R = 8.314\,\mathrm{J/mol\,K}$. Apart from the pressure, Equation 6.3 only depends on the heat of vaporization

[1] Profiler Operator's Manual for the MP-3000A, contact: Info@radiometrics.com

ΔH_{vap}, which is constant for an ideal gas. Based on Equation 6.3, a consistent formulation is now used within the HATPRO-G2 software:

$$T_{LN_2} = \frac{710.5241}{9.185 - ln\left(\frac{p}{1013.25}\right)}. \tag{6.4}$$

Using the atmospheric pressure during the LN_2 calibration at RHUBC-II of $p = 534.7\,\text{hPa}$, Equation 6.4 gives a boiling point of $T_{LN_2} = 72.2\,\text{K}$. For RHUBC-II measurements, this adapted boiling point decreases the calibrated T_b values by up to 1.4 K compared to the original LN_2 calibration (Eq. 6.1). Note, that the National Institute of Standards and Technology (NIST)[2] gives a boiling point of $T_{LN_2} = 72.3\,\text{K}$ at 534.7 hPa (*Span et al.*, 2000).

[2]http://webbook.nist.gov

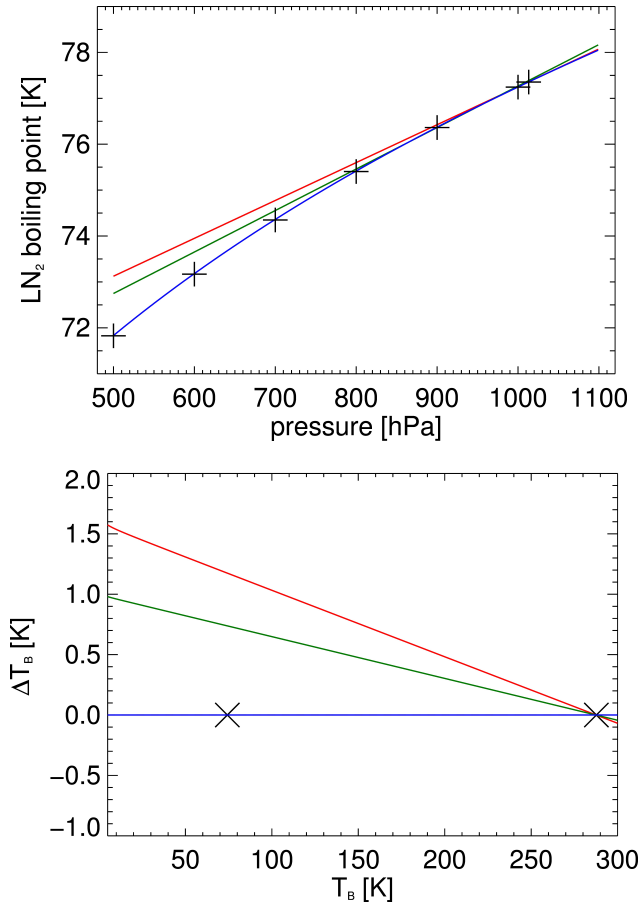

Figure 6.1: Pressure dependent boiling point correction for LN_2. Different radiometer manufacturers use different formulations. *Top*: Equation 6.1 (RPG-OS, 2011) (*red*), Equation 6.2[3] (*green*), new formulation (Eq. 6.4) (*blue*), and reference values from *Span et al.* (2000) (*crosses*). *Bottom*: impact on calibrated T_b for RHUBC-II pressure conditions from differences in the assumed temperature of the cold calibration target (T_{LN_2}), using the different corrections given above (*lines*). ×'s mark the cold and the hot calibration point.

6.1.2 Reflective Component at the Cold Load

When integrating on the cold load, a reflective component that is not emitted by the target itself contributes to the received signal. For HATPRO-G2, this contaminating radiation is assumed to be a single reflection of thermal radiation, emitted by the temperature stabilized receiver parts and reflected back from the LN_2 surface (Fig. 6.2). The temperature at the cold calibration point can be modelled as:

$$T_C = (1 - r_{LN_2})\, T_{LN_2} + r_{LN_2}\, T_{rec}, \tag{6.5}$$

where r_{LN_2} is the reflectivity of the LN_2 target and T_{rec} is the receiver temperature. This means, that the received radiation is composed of a direct contribution from the target (T_{LN_2}) and a reflective component:

$$T_{refl} = r_{LN_2} \cdot (T_{rec} - T_{LN_2}). \tag{6.6}$$

Theoretically, r_{LN_2} can be calculated from the refractive index gradient at the LN_2-air-interface. As the refractive index of air is approximately one, the gradient is equal to the refractive index of LN_2:

$$r_{LN_2} = \frac{(n_{LN_2} - 1)^2}{(n_{LN_2} + 1)^2}. \tag{6.7}$$

If the cold target was a perfect black body ($r_{LN_2} = 0$), the reflective component would be zero. The refractive index of LN_2 n_{LN_2} is derived from laboratory measurements. *Reesor et al.* (1975) measure at frequencies between 18 GHz and 26 GHz and determine $n_{LN_2} = 1.2$. *Benson et al.* (1983) give $n_{LN_2} = 1.20 \pm 0.03$ for a frequency range from 120 GHz to 300 GHz. *Vinogradov et al.* (1967) find $n_{LN_2} = 1.196 \pm 0.007$ at 130 GHz. Further results are $n_{LN_2} = 1.195$ (15.47 GHz) (*Smith et al.*, 1991) and $n_{LN_2} = 1.24 \pm 0.01$ (0.5 GHz-10.4 GHz) (*Hosking et al.*, 1993). Altogether, these experiments suggest to consider a constant refractive index of $n_{LN_2} = 1.2$ for all HATPRO-G2 channels, which cover frequencies between 22 GHz and 58 GHz. This gives a reflectivity of $r_{LN_2} = 0.0082$ (Eq. 6.7). For HATPRO-G2's receiver temperature $T_{rec} \approx 305$ K, this results in a reflective component of $T_{refl} = +1.9$ K at standard pressure (Eq. 6.6). T_{refl} is added to the boiling point temperature T_{LN_2} (cf. Sec. 6.1.1) during HATPRO-G2's LN_2 calibration procedure. However, n_{LN_2} is only known within an uncertainty range. The effect of this uncertainty on the calibration is discussed in the following section.

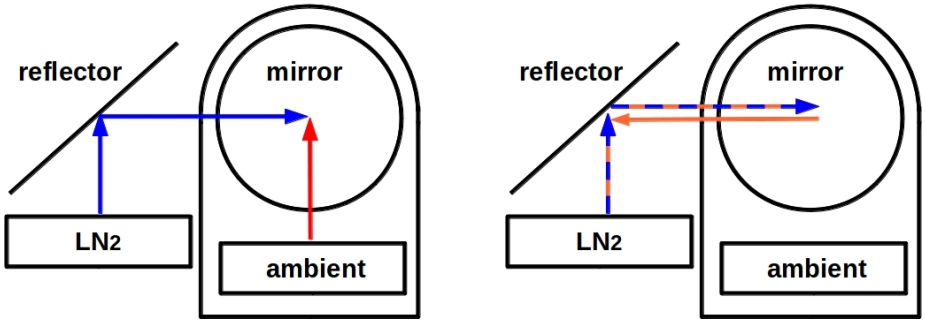

Figure 6.2: Illustration of HATPRO-G2's LN_2 calibration. *Left*: set up for the LN_2 calibration – a parabolic mirror points the receivers to the internal ambient temperature target (*red*) and the mounted LN_2 target (*blue*). *Right*: The signal measured at the cold calibration point, is composed of radiation from the thermally stabilized receiver parts (*orange*), which is partially reflected back from the LN_2 surface, and radiation emitted by the cold calibration target itself (*blue*).

Refractive Index of Liquid Nitrogen

The uncertainty range of the refractive index n_{LN_2} of LN_2 determined by *Benson et al.* (1983) is used to derive a minimum refractive index ($n_{LN_2}^{min} = 1.2 - 0.03 = 1.17$) and a maximum refractive index ($n_{LN_2}^{max} = 1.2 + 0.03 = 1.23$) (Tab. 6.1). The impact of the n_{LN_2} uncertainty is illustrated by Figure 6.3. The T_b difference from calibrations that use the two extreme refractive indices, increases with decreasing T_b. The maximum difference for RHUBC-II measurements ($T_b \approx 5\,\mathrm{K}$) is 1.4 K and decreases towards the hot calibration point, where it disappears. However, even for the most opaque V-band channels the impact is $0.1\,\mathrm{K} - 0.2\,\mathrm{K}$.

Under real measurement conditions outside the laboratory, the LN_2 surface is exposed to the environment. It may be perturbed by capillary waves and boiling bubbles, which might affect the reflectivity of the LN_2 target. In principle, satellite remote sensing takes advantage of this effect, when retrieving surface roughness (*Hollinger*, 1971). *Shitov et al.* (2011) state that the non-planar surface may lead to variations of the reflectivity r_{LN_2} caused by frequency dependent interferences. However, these variations are compensated during the calibration, because they are on time scales well below the target integration time.

Furthermore, a deformed surface could reflect external radiation into the receiver's main lobe. This radiation could originate from instrument parts at ambient temperature or even from the atmosphere with much lower temperatures. Nevertheless, there is no experimental evidence for the existence of such contributions for HATPRO-G2. The same is true for any side lobe contributions (cf. Sec. 5.3).

The boiling bubbles also reduce the density of the interacting LN_2 surface. This effect is not balanced within the target integration time. Even though, the effect on r_{LN_2} is hard to quantify, it can be assumed that the average number and size of

Table 6.1: Refractive indices, (n_{LN_2}) and reflectivities r_{LN_2} of the LN_2 surface and the resulting reflective components (T_{refl}) and noise diode temperatures T_N.

$\nu\,[GHz]$	n_{LN_2}	$r_{LN_2}\,[\%]$	$T_{refl}\,[K]$
original	1.20	0.82	1.9
min	1.17	0.61	1.4
max	1.23	1.06	2.3

the rising bubbles is constant. In order to demonstrate the sensitivity of r_{LN_2} on boiling bubbles, it is assumed, that on average 1% of the LN_2 surface consists of gas bubbles with a refractive index of 1. Then the refractive index $n_{LN_2} = 1.2$ is also reduced by 1%: $n_{bub} = 1.188$. The resulting reflectivity $r_{bub} = 0.0074$ (Eq. 6.7) reduces T_C by 0.2 K, when it is assumed that the contaminating signal originates from the receiver ($T_{rec} = 305\,\mathrm{K}$). This means, n_{LN_2} tends to be underestimated by laboratory measurements.

Apart from the uncertainties in n_{LN_2}, continuous observations of the LN_2 evaporating from the cold load, have revealed that the reflective component is not constant in time. It is modulated by a resonance effect, which is discussed in the following.

Resonance Effect

Observations have shown, that the reflective component at HATPRO-G2's cold calibration point (cf. Sec. 6.1.2) is modulated in time (*Pospichal et al.*, 2012). As the level of the LN_2 surface declines due to evaporation, the detector voltage shows a sinusoidal temporal evolution (Fig. 6.4). Because the isolator at the receiver entrance owns a non-zero reflectivity (*Forkman et al.*, 2003), the effect can be interpreted as an additional resonance affecting the signal that is received from the cold calibration target. The maximum amplitude of the standing wave occurs at resonant distances s between the LN_2 surface and the receiver entrance:

$$s = k \cdot \frac{\lambda}{2}, \quad k = 0, 1, 2, ..., \tag{6.8}$$

where s is a multiple of half the wavelength λ. The system between the two reflectors forms a weak resonator with a performance depending on s. While the level of the LN_2 declines, its distance to the receiver s increases and the resonance condition changes. The effect on T_C (Eq. 6.5) can be interpreted as a small perturbation $r_{res}(s)$ ($\overline{res(s(t))} = 0$). Via r_{res} these standing waves contribute to the reflective component and Equation 6.6 therefore has an additional component:

$$T_{refl} = (r_{LN_2} + r_{res}(s(t))) \cdot (T_{rec} - T_{LN_2}). \tag{6.9}$$

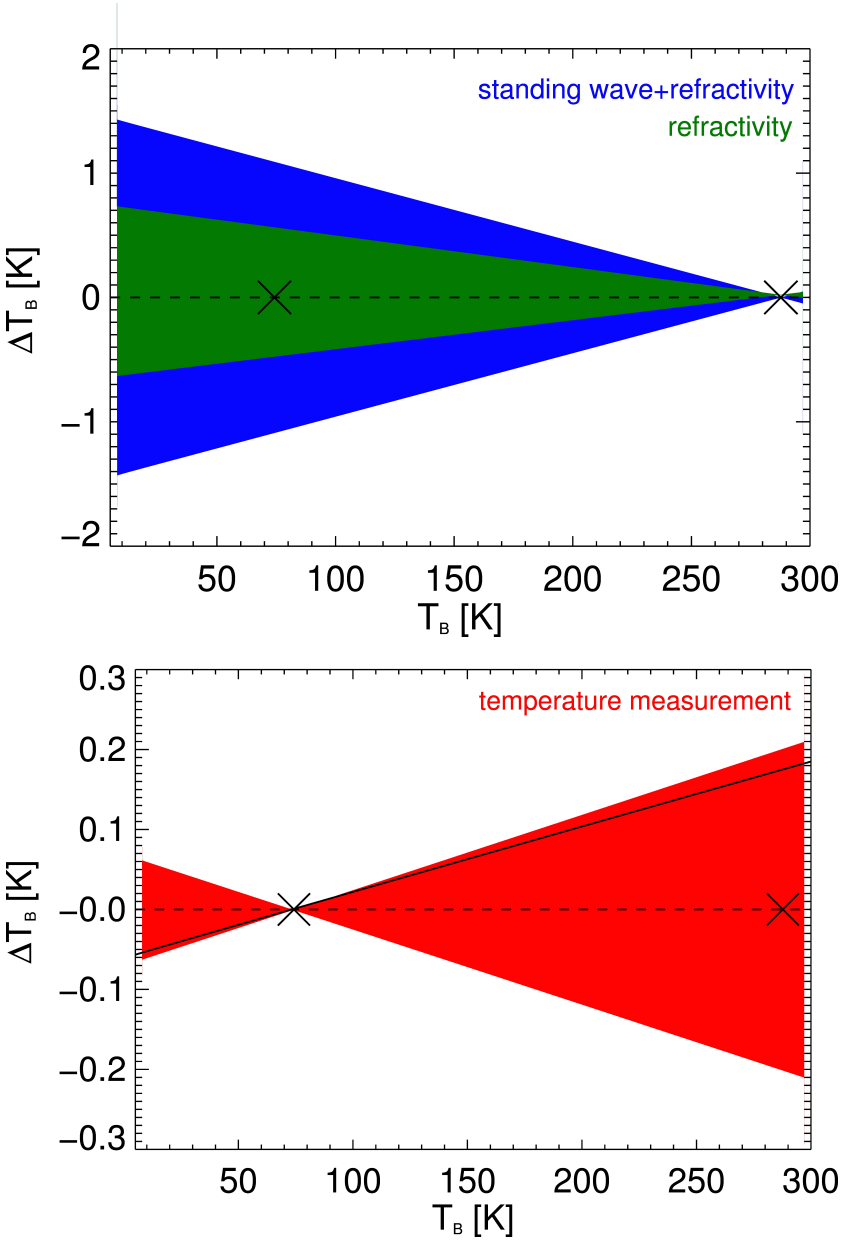

Figure 6.3: *Top*: impact of uncertainties in the reflectivity of the LN_2 target on the derived T_b. Plotted are uncertainty ranges resulting from the uncertainty for the refractive index of the LN_2 surface $n = 1.20 \pm 0.03$ (*Benson et al.*, 1983) (*green*) and due to resonances between the LN_2 surface and the receiver (cf. Sec. 6.1.2, *blue*). *Bottom*: impact of a non-zero reflectivity of the internal ambient target $r_H = 0.01$ and a reflective component from the receiver ($T_{rec} = 305\,\mathrm{K}$, *line*) on the derived T_b. The uncertainty range in derived T_b from errors in the in-situ temperature measurement of the internal ambient target $\Delta T_H = 0.2\,\mathrm{K}$ (*red*). ×'s mark the cold and the hot calibration point.

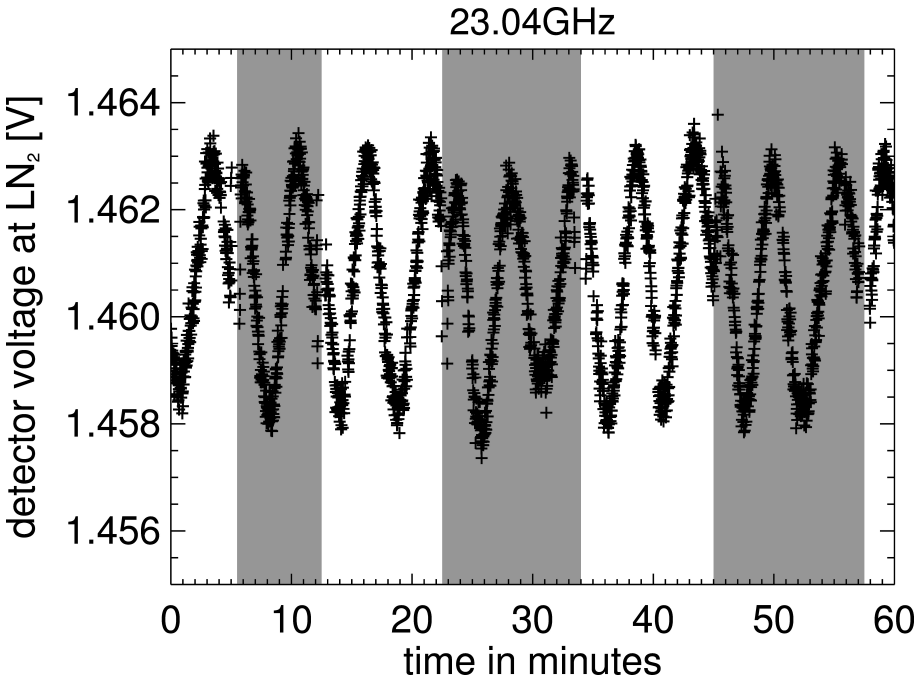

Figure 6.4: Time series of detector voltages measured on the LN_2 load on May 23, 2012 observed with HATPRO-G2 at JOYCE. The transitions between *white* and *gray* areas mark LN_2 refillings.

Note that r_{res} is unknown, because the reflectivity on the receiver end is not known. As r_{res} changes, the contributions of T_{LN_2} and T_{rec} to the total signal (T_C) are modulated in time (Fig. 6.5). On the one hand, in the resonant case, a maximum reflectivity r_{res} increases the contribution of the receiver. A calibration procedure that assumes $T_{refl} = 1.9\,\mathrm{K}$ leads to underestimated T_b measurements (Fig. 6.6). On the other hand, when r_{res} is at its minimum, the resonator transmittance is highest. In this case, more radiation from the target is received. When a LN_2 calibration is conducted at this point, the assumed reflective component is too large and calibrated T_b is overestimated.

Empirical evidence was collected at JOYCE during two intensive experimental days in May 2012, when the LN_2 target was continuously observed over several hours. LN_2 was refilled, when the absorber material began to appear at the surface of the evaporating LN_2. During one "evaporation cycle" between two refillings detected voltages show one to three full oscillations (Fig. 6.4). Besides the evaporation rate, the length of one evaporation cycle is determined by the volume of LN_2 above the absorber material of the cold target. The evaporation rate is driven by the environmental conditions, mainly by the wind. For HATPRO-G2 one cycle takes about 10 min when the calibration target is sheltered from the wind.

The experimental data have been analyzed for period, amplitude, and phase for all HATPRO-G2 channels. Statistical evidence for the standing wave is given by

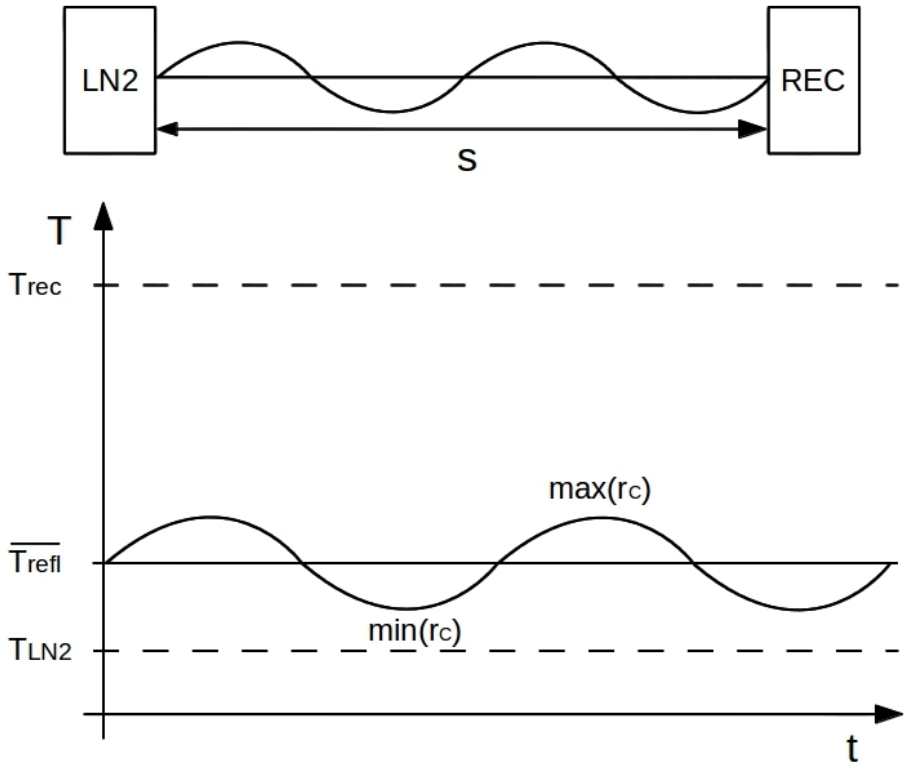

Figure 6.5: Illustration of resonances during cold load observations: Standing waves build up between the LN_2 surface and the receiver (REC), the distance s determines the contributions of the receiver and the LN_2 surface to the calibration signal.

the fact that the period of the temporal oscillation depends linearly on the channel frequency, when a constant evaporation rate is assumed. This means, the lower ν, the more frequent Equation 6.8 is fulfilled. Furthermore, differences in the relative phases between the oscillation of different channels have been detected. For example, when Equation 6.8 gives a maximum resonance for the HATPRO-G2 channel at 25.44GHz ($\lambda = 11.8\,\mathrm{mm}$), the channel 23.04GHz ($\lambda = 13.0\,\mathrm{mm}$) is always close to the resonance minimum.

Figure 6.4 shows a time series of the most affected channel at 23.04 GHz. For this channel, the mean peak-to-peak value of the oscillation from 24 refilling cycles is 1.1 K and the oscillation period is 279 s. Table 6.2 gives periods and amplitudes for all HATPRO-G2 channels. The period depends on the channel frequency and on the evaporation rate of LN_2. Due to the longer wavelengths λ, the periods are generally larger than for V-band channels. Also the oscillation amplitudes are generally larger for K-band channels. The smaller amplitudes for V-band channels can be explained by the fact that the oscillations are much harder to detect, because the noise level of these channels is about twice as high. However, within both bands, the amplitudes strongly depend on the channel frequency ν.

Since the observed oscillation amplitudes translate to an uncertainty of the cold

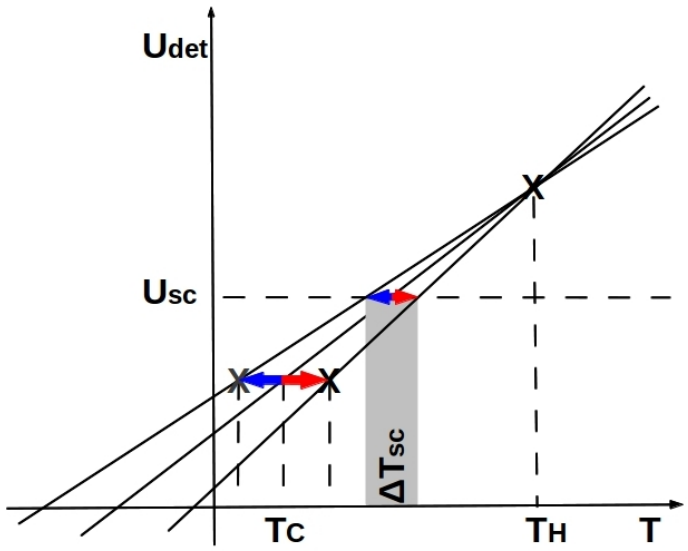

Figure 6.6: Illustration of the impact of the resonance effect on derived T_b during cold load observations: due to modulations of the reflective component T_{refl}, the target temperature $T_C = T_{LN_2} + T_{refl}$ may be underestimated (*blue arrow*) or overestimated (*red arrow*). As a consequence, uncorrected standing waves lead to an uncertainty ΔT_{SC}, when observing the scene.

calibration point, the standing wave phenomenon directly affects the absolute accuracy of the LN_2 calibration. Because the integration time within the LN_2 calibration is small compared to the oscillation periods, the maximum uncertainty is estimated to be the amplitude of the oscillation observed at each channel (Tab. 6.2). K-band channels show oscillation amplitudes of 0.1 K to 0.6 K. In the V-band, the noise level is generally higher, making it more difficult to detect oscillations. This might have led to a reduction of amplitudes in the V-band, which are only 0.1 K-0.3 K. For both receiver bands, amplitudes in the band's center show higher amplitude, because the horn antennas and amplifiers are optimized to the central frequency. Figure 6.3 shows the impact of the resonances on calibrated T_b for 23.04 GHz. This channel has the largest uncertainty. At the boiling point of LN_2 the uncertainty equals the amplitude of the oscillation, which is 0.57 K (Fig. 6.4). For RHUBC-II measurements, with T_b below 10 K, the maximum uncertainty reaches 0.7 K.

The standing wave's impact on the LN_2 calibration can be reduced by increasing the integration time on the LN_2 target. The impact could be eliminated completely by integrating exactly over one oscillation period. However, the oscillation periods are channel dependent (1 min − 7 min). Therefore, a more practical solution is to determine average calibration parameters from repeated calibrations, while the LN_2 evaporates. This approach has recently been implemented in HATPRO-G2's LN_2 calibration procedure. Still, there remains an uncertainty, because with an integration time of 30 s a 4-point calibration takes about 2 min. Consequently, only five cali-

Table 6.2: Results for periods and amplitudes of signal oscillations while observing HATPRO-G2's LN_2 target from experiments conducted at JOYCE on May 23, 2012.

$\nu\,[GHz]$	Period $[s]$	Amplitude $[K]$
22.24	287 ± 5	0.27 ± 0.01
23.04	279 ± 2	0.57 ± 0.02
23.84	303 ± 7	0.17 ± 0.01
25.44	397 ± 16	0.11 ± 0.01
26.24	250 ± 5	0.19 ± 0.01
27.84	277 ± 9	0.18 ± 0.02
31.40	202 ± 4	0.15 ± 0.01
51.26	139 ± 5	0.23 ± 0.05
52.28	118 ± 7	0.11 ± 0.04
53.86	168 ± 15	0.06 ± 0.03
54.94	146 ± 9	0.08 ± 0.03
56.66	88 ± 7	0.04 ± 0.03
57.30	181 ± 13	0.06 ± 0.02
58.00	82 ± 4	0.06 ± 0.03

brations can be performed within one evaporation cycle. This leads to errors when averaging the calibration parameters calibration, especially for the channels with long oscillation periods. The number of calibrations during one cycle can be enhanced by reducing the integration time, as long as the corresponding measurement accuracy is still acceptable (Eq. 3.13). In any case, a strong ventilation of the target should be prevented, because this increases the evaporation rate significantly. Consequently, the oscillation period decreases and with it the number of possible calibrations during one cycle. Furthermore, strong ventilation increases the roughness of the LN_2 surface. This effect results in a further reduction of the calibration uncertainty. The surface roughness can influence the target's reflectivity r_C.

6.1.3 Reflective Component at the Hot Load

In contrast to the cold calibration point, HATPRO-G2's standard calibration procedure assumes the internal ambient temperature target to be a perfect black-body ($r_H = 0$). Consequently, there is no reflective component at the hot calibration point. It can be argued that in reality, this is not the case. Figure 6.3 illustrates the sensitivity of the calibrated T_b on the hot load reflectivity r_H. When assuming that 1% of the radiation originates from the receiver ($T_{rec} = 305\,\mathrm{K}$) and not from the target itself, T_b values close to the hot calibration point are affected by up to 0.4 K. This means the opaque channels in the V-band are most affected. The impact decreases towards the cold calibration point T_C. Below T_C the effect is of opposite sign and reaches almost 0.2 K at very low measured T_b values.

6.1.4 Hot Load Temperature Measurement

As mentioned in Section 4.3, there are two sensors inside the ambient target, that measure the in-situ temperature. The mean bias between the two temperatures, which was encountered during RHUBC-II is less than 0.05 K. This means that notably residual temperature gradients inside the vented target can be excluded. The largest temperature difference between the two sensors, that occurred during RHUBC-II, was 0.2 K. This value is used to assess the uncertainty of the in-situ temperature measurements. Calibrated T_b of the saturated V-band channels are affected by 0.2 K (Fig. 6.3). Towards the cold calibration point, the impact of the temperature measurement of T_H drops linearly. All other channels are affected by less or equal 0.1 K.

The internal ambient target is used as hot calibration point (T_H) for all HATPRO-G2 calibration types (Tab. 4.3). Therefore, all types are influenced by the uncertainties of the target's black body properties and the in-situ measurement of the target temperature.

6.1.5 Detector Non-Linearity

The receiver non-linearity α is determined by HATPRO-G2's 4-point calibration scheme (cf. Sec. 3.3.1). In order to assess the benefit of considering the non-linearity, calibration results are compared to results from a classical 2-point calibration scheme, which assumes a linear relation between U_{det} and measured T_b ($\alpha = 1$). Figure 6.7 gives the effect of α in dependence of the measured T_b. Naturally, the effect of non-linearity is close to zero at the two calibration points. For all channels, the maximum of 0.3 K is reached towards very low T_b values. The effect is slightly larger in the V-band, because α is smaller, which means that the receiver non-linearity is stronger (Tab. 6.3). The reason is that a different technology is used for the receiver integrated circuits. In contrast to the K-band channels, where GaAs technology is used, the V-band receiver uses integrated circuits made from Indium Phosphide (InP). InP

MMICs have a much lower 1 dB compression point, which is a measure for the linear range of detector response. Nevertheless, the effect depends on T_b: The maximum difference is reached at the lower end of the measured T_b range. Measurements below 10 K are underestimated by up to 0.2 K, when using a 2-point calibration scheme. Therefore, K-band channels, which measure at lower opacities, are most affected. In any case, considering the detector non-linearity noticeably improves the calibration.

In the next step the uncertainty of α is assessed. α cannot be determined independently, because it characterizes the non-linearity of the whole radiometer system. Furthermore, it also depends on the other calibration parameters being the receiver noise temperature T_R, the noise diode temperature T_N, and the detector gain g, because it is determined within a 4-point calibration scheme (cf. Sec. 3.3.1). This leads to a variability of α over subsequent calibrations. The variability in α is investigated by 28 LN_2 calibrations that were performed with HATPRO-G2 at JOYCE between July 2010 and May 2012 (for details on the calibration parameters cf. Tab. B.2, App. B). Within the considered time period, drifts of α are generally small found (Tab. B.1, App. B). Therefore, the standard deviation of α over all 28 calibrations reflects the random uncertainty of the α determination. The relative uncertainty is below 0.2% for all HATPRO-G2 channels (Tab. 6.3). It can be concluded that α is solely a frequency dependent instrument property. For the K-band channels, the variability is largest at 22.24 GHz and tends to decrease with frequency. Figure 6.7 shows the impact on calibrated T_b, when the original α is varied within the range of its uncertainty. Again, the effect is largest for small measured T_b. Combined with the higher variability of α, K-band channels are most affected. Here, the effect ranges between ± 0.02 K and ± 0.04 K. In the V-band, the effect is below ± 0.02 K and is therefore negligible. The effect is even further reduced, when an α that is averaged over several LN_2 calibrations is used.

Table 6.3: Mean and standard deviation of the non-linearity parameter α for HATPRO-G2 channels with mid-frequencies ν. Derived from 28 LN_2 calibrations performed with HATPRO-G2 at Jülich ObservatorY for Cloud Evolution (JOYCE) (92 m above MSL) between July 2010 and May 2012.

$\nu\,[GHz]$	$\overline{\alpha}$	$\Delta\alpha/\alpha\,[\%]$	$\nu\,[GHz]$	$\overline{\alpha}$	$\Delta\alpha/\alpha\,[\%]$
22.24	0.9891	0.19	51.26	0.9646	0.07
23.04	0.9950	0.18	52.28	0.9734	0.15
23.84	0.9920	0.11	53.86	0.9715	0.07
25.44	0.9887	0.11	54.94	0.9699	0.08
26.24	0.9906	0.11	56.66	0.9691	0.08
27.84	0.9918	0.11	57.30	0.9619	0.11
31.40	0.9950	0.12	58.00	0.9574	0.07

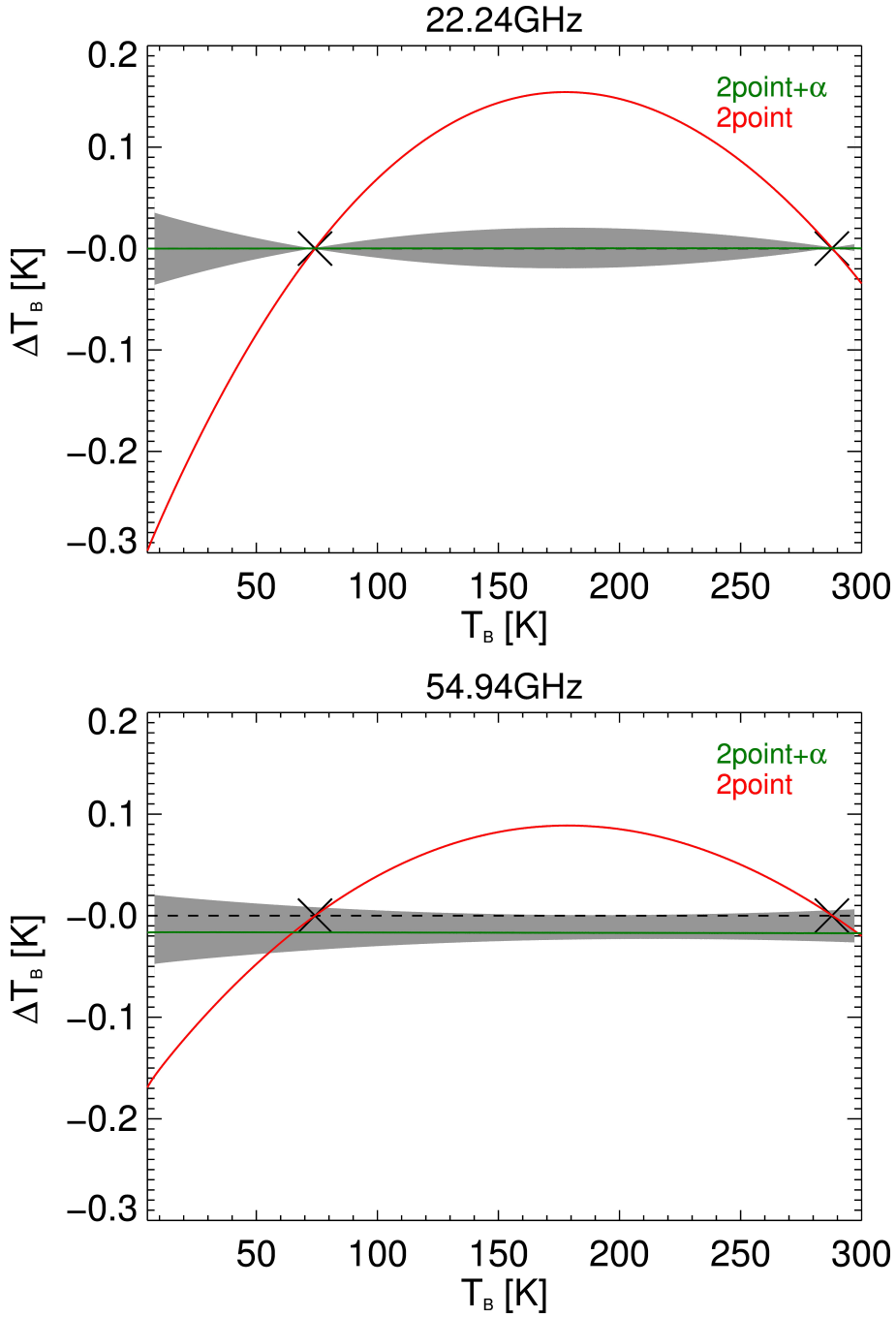

Figure 6.7: The effect of the non-linearity parameter α of the radiometer system on calibrated T_b for selected HATPRO-G2 channels. The solution of the 4-point calibration serves as reference. Plotted are the results for the 2-point calibration scheme with $\alpha = 1$ and no noise injection (*red*), the results for a 2-point calibration using α from the original 4-point calibration performed at the beginning of RHUBC-II (*green*), and the uncertainty range resulting from the random uncertainty of α (Tab. 6.3, *gray*).

6.2 Tipping Curve Calibration

As an alternative to the LN_2 calibration, the cold calibration point T_C may also be provided by a tipping curve calibration. T_C can then be used within a 2-point or 4-point calibration scheme to derive the calibration parameters. The procedure that is applied to HATPRO-G2 measurements is described in Section 4.3. However, at this point the accuracy of tipping curve calibrations is assessed by analyzing different sources of uncertainty that affect the derivation of T_C. The tipping curve result for T_C is a zenith brightness temperature T_b^{TIP}. In this work, T_b^{TIP} values are derived in post-processing from the original T_b measurements, which are based on an LN_2 calibration ($T_b^{LN_2}$). This allows a direct comparison of both calibration techniques (cf. Sec. 6.3). Before the comparison, different aspects have to be taken into account. The first is the realistic simulation of the radiometer beam considering the pointing, the air mass, and the beam width. The second is the impact of external parameters like the mean radiative temperature (T_{mr}). Finally, efficient thresholds within the calibration procedure that guarantee the quality of the results have to be set. All aspects affect the total uncertainty associated with a tipping curve calibration. This uncertainty is assessed in the following.

The tipping curve procedure is evaluated for two different atmospheric regimes: on the one hand, for an extremely dry atmosphere observed from high altitudes (RHUBC-II) and, on the other hand, for a mid-latitude atmosphere observed from close to sea level (JOYCE) (cf. Chap. 4). At both deployment sites, the same radiometer (HATPRO-G2) performed the same continuous elevation scan pattern in the $70.0°N/\ 250.0°N$ azimuthal plain. Each scan can be used for a tipping curve calibration of the low-opacity radiometer channels. At JOYCE, these are the seven K-band channel. RHUBC-II condition allow to calibrate two low-opacity V-band channels as well. For the analysis, one clear sky day is selected from each deployment: August 16, 2009, for RHUBC-II ($PWV < 1\,\mathrm{mm}$) and November 16, 2011, for JOYCE ($PWV = 7.5\mathrm{mm}$).

6.2.1 Pointing Error

An accurate pointing of the radiometer beam is essential for the tipping curve calibration, because it is based on measurements, which are very sensitive to the actually observed air mass. *Han and Westwater* (2000) state, that a pointing error of 1° may lead to a calibration error of several Kelvin. Most affected are radiometer channels that observe large T_b differences under changing elevation angles (Fig. 5.8). Whenever pointing inaccuracies are systematic, they can be corrected. A systematic mis-pointing could result from a mis-aligned reflection mirror or, most commonly, due to a tilted instrument. As *Han and Westwater* (2000) point out, this tilt can be balanced by performing elevation scans towards opposite directions and averaging

measurements of symmetric elevation angles prior to the tipping curve procedure. In case no obstacles inhibit bilateral scanning, this is the preferred way for deployment sites with similar atmospheric conditions towards both scanning directions. This approach is chosen for the tipping calibration using JOYCE measurements.

In contrast to JOYCE, the RHUBC-II site is characterized by inhomogeneous surroundings leading to drier air masses over the hillside of Cerro Toco ($70.0°N$) compared to the open plateau ($250.0°N$). This is also reflected in the T_b measurements collected by HATPRO-G2: At four air masses, T_b measurements in the K-band are lower by up to 2 K towards the hill side, which corresponds to lower PWV values. At first sight, this difference can be balanced following *Han and Westwater* (2000). However, a distinct diurnal cycle of the T_b difference between to the two scanning directions with an amplitude of 1.4 K at 22.24 GHz can be identified. These changes cannot result from a systematic pointing error, but are due to the inhomogeneous atmospheric conditions. Under such conditions, it is found that the number of successful calibrations in the K-band is reduced significantly, when using bilateral scans (cf. Sec. 6.2.5). For the three channels closest to the water vapor absorption line, the total number of successful tipping curves is reduced from 164 to only 43. This can be explained by the fact that the scanning directions are not only characterized by different mean PWV values, but also by different water vapor variabilities. Therefore, the approach for RHUBC-II is to use single-sided elevation scans.

When using single-sided elevation scans, it is important to quantify the pointing error. In contrast to the K-band, at 51.26 GHz and 52.28 GHz, there is no diurnal cycle as they are hardly influenced by atmospheric water: The T_b differences between the two scanning directions reach $2\,\mathrm{K} - 3\,\mathrm{K}$ at four air masses. A comparison with radiative transfer simulations reveal that large parts of these differences are systematic and can be explained by an instrument tilt of $\approx 0.2°$ (Fig. 6.8). This does only hold, if it is assumed that within 0.2° the relation between T_b and air mass can be approximated as linear. Still, an unsystematic contribution resulting from possible inaccuracies of the pointing and atmospheric inhomogeneities can not be balanced. Nevertheless, it is concluded that the corrected pointing is accurate within 0.05° (Fig. 6.8). The impact of this residual uncertainty on the tipping curve calibration is determined by varying the correction within the uncertainty range. While there is no impact on K-band channels, the V-band channels at 51.26 GHz and 52.28 GHz are affected by 0.1 K.

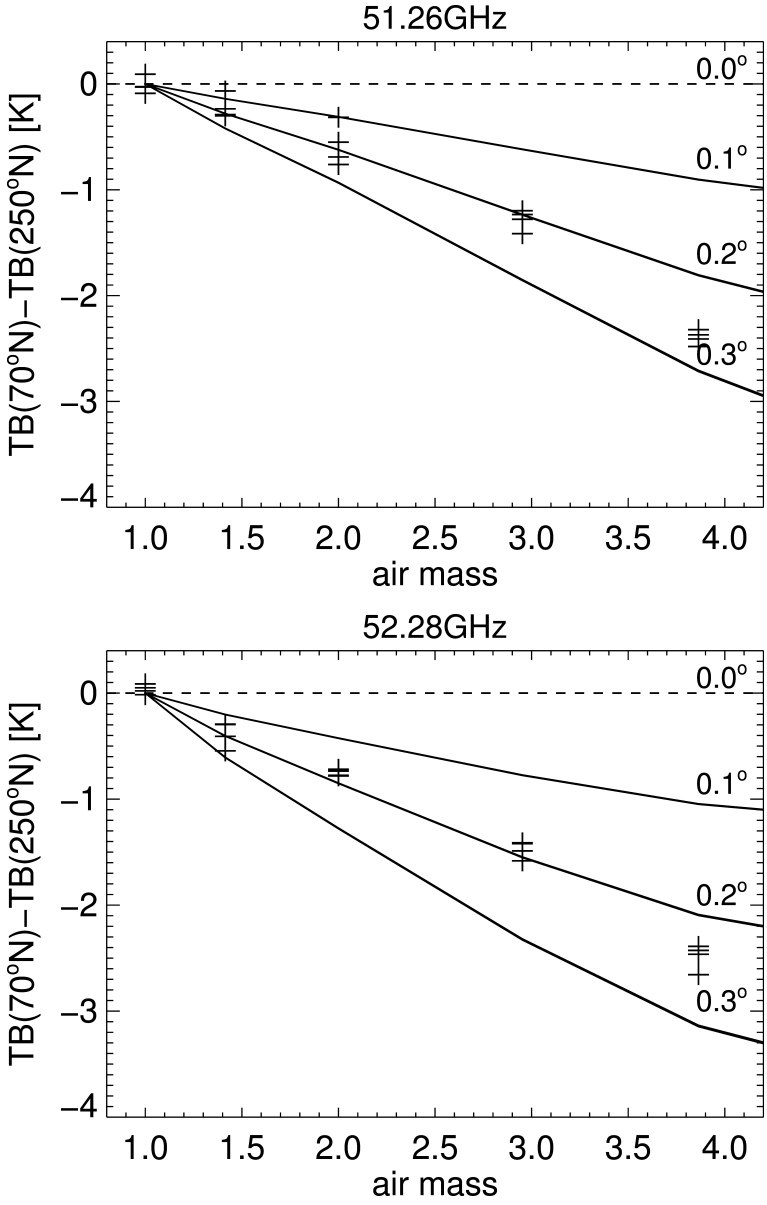

Figure 6.8: Determination of systematic pointing errors. Plotted are the T_b difference of HATPRO-G2 measurements towards the azimuth directions $70.0°N$ and $250.0°N$ as a function of air mass (*crosses*). HATPRO-G2 measurements are averaged during radiosonde ascents (5 min before until 1 h after each launch). Additionally, radiative transfer calculations provide almost equal results for the four clear sky radio sondes launched at $09.27LT$, $10.39LT$, $12.03LT$, $13.44LT$ on August 16, 2009 (*lines*). Air masses are modified to simulate a tilt t of the radiometer of 0.1°, 0.2°, and 0.3°, simulated T_b differences are $\Delta T_b = T_b(elevation + t) - T_b(elevation - t)$. For the simulations the Rosenkranz'98 model (*Rosenkranz*, 1998) is used, the air mass is corrected according to *Rüeger* (2002), the antenna beam width and exact band-pass filters are considered.

6.2.2 Air Mass Correction

The tipping curve procedure exploits a linear relation between opacities and the corresponding air mass values. While the opacities are derived from radiometer measurements, the air mass values can only be approximated from the nominal elevation angles $\varphi_0 = 90° - \theta_0$ (Eq. 5.3). However, the calibration results are sensitive to the assumed air mass values. Therefore, it is important to simulate accurate air mass values.

Following the results of Section 5.2, a ray-tracing method is used to calculate the relative air mass X. X includes the effect of Earth's curvature and atmospheric refraction. As frequency dependent contributions to atmospheric refraction are negligible, it is sufficient to determine the refractive index profile after *Rüeger* (2002). The air masses are calculated by using the spatially and temporally closest available radiosonde profile. For RHUBC-II, this is one of the four soundings launched directly at the deployment site on August 16, 2009. At JOYCE, no operational radio soundings are available. Therefore, one of the three operational DWD soundings from Essen on November 16, 2011, ($00\,UTC$, $12\,UTC$, and $24\,UTC$) is used. The launch point is only about 70 km away from the JOYCE site and about 60 m higher.

Even when the uncertainty of X is assumed to be the standard deviation of all 112 RHUBC-II (Fig. 5.6), it has a negligible effect on the tipping curve results, if only scans down to three air masses are used (cf. Sec. 6.2.5). When the uncertainty X for JOYCE is estimated by the standard deviation of 60 radiosondes launched in Essen during November 2011 (Fig 5.6), measured T_b based on tipping curve results would be affected by less than 0.1 K. This impact is negligible, when assuming that the uncertainty is better characterized by the variation between radio soundings on the analyzed day.

Han and Westwater (2000) derive a theoretical T_b correction from a Gaussian shaped antenna pattern and an effective scale height. When X is not derived numerically from the ray-tracing, but using this approach (Eq. 5.4), T_b results for RHUBC-II are underestimated by 0.1 K at 51.26 GHz and 52.28 GHz. The K-band is not affected. In contrast, when the correction suggested by *Han and Westwater* (2000) is applied to calibrations at JOYCE, the K-band channels results deviate from the ray-tracing result between -0.2 K and $+0.3$ K.

6.2.3 Beam Width Correction

As shown in Section 5.3, it is important to consider the antenna beam width, when measuring off-zenith. Therefore, it is important to correct the T_b measurements that are used to derive opacity-air mass pairs. In contrast to the air mass correction, where the air mass is modified to fit the T_b measurement, T_b measurements are corrected for the beam width to fit the calculated air masses. The T_b corrections (ΔT_b) for each

channel are derived from radiative transfer simulations across HATPRO-G2's beam widths for each nominal elevation scan angle φ_0. In case of RHUBC-II, the nominal elevation angles φ_0 are additionally corrected by 0.2° to balance the instrument's tilt (cf. Sec. 6.2.1). The simulations consider the exact relative air mass values X. ΔT_b is calculated for the four RHUBC-II soundings on August 16, 2009, and three Essen soundings on November 16, 2011. While for low-opacity channels ΔT_b is > 0, it becomes negative, when radiometer channels start to saturate with increasing air mass (cf. Sec. 5.3). The corrections are given in Table 6.4. Tipping curve results from calibrations that include the beam width exceed results from calibrations without the correction by up to 0.5 K for RHUBC-II in the V-band. While for RHUBC-II the effect on the K-band is negligible, the correction for JOYCE in the K-band is −0.2 K.

Table 6.4: T_b corrections (ΔT_b) from radiative transfer simulations using four clear sky RHUBC-II radio soundings from August 16, 2009, (*top*) and three clear sky radiosondes launched on November 16, 2011, in Essen at the operational radiosonde station of the German Weather Service (DWD), which is closest closest to JOYCE (*bottom*).

RHUBC-II

	nominal elevation angle φ_0				
$\nu\,[GHz]$	45.0	30.0	19.8	15.0	9.6
22.24	+0.0	+0.0	+0.1	+0.2	+0.5
23.04	+0.0	+0.0	+0.1	+0.2	+0.5
23.84	+0.0	+0.0	+0.1	+0.1	+0.4
25.44	+0.0	+0.0	+0.0	+0.1	+0.3
26.24	+0.0	+0.0	+0.0	+0.1	+0.3
27.84	+0.0	+0.0	+0.1	+0.1	+0.3
31.40	+0.0	+0.0	+0.1	+0.1	+0.4
51.26	+0.1	+0.1	+0.5	+0.9	+1.7
52.28	+0.1	+0.2	−0.5	−0.8	+0.9

JOYCE

	nominal elevation angle φ_0				
$\nu\,[GHz]$	45.0	30.0	19.8	15.0	9.6
22.24	+0.1	+0.2	+0.5	+0.8	+1.0
23.04	+0.1	+0.2	+0.5	+0.8	+1.1
23.84	+0.1	+0.2	+0.5	+0.8	+1.2
25.44	+0.1	+0.1	+0.4	+0.7	+1.2
26.24	+0.0	+0.1	+0.4	+0.7	+1.2
27.84	+0.0	+0.1	+0.3	+0.6	+1.1
31.40	+0.0	+0.1	+0.3	+0.6	+1.1

6.2.4 Mean Radiative Temperature

The tipping curve procedure uses two external parameters, which are not derived from radiometer measurements: the background radiation T_{back} and the mean radiative temperature T_{mr} of the atmosphere (Eq. 2.26). The first is assumed to be exact (*Noterdaeme et al.*, 2011), the latter is discussed here.

Within the tipping curve procedure the mean radiative temperature T_{mr} is needed to calculate zenith T_b from the opacity τ (Eq. 2.26). A first approach is to derive T_{mr} from climatological atmospheric profiles (*Han and Westwater*, 2000). The second approach is to use the ambient surface temperature T_{surf} as a predictor for T_{mr} in a linear regression scheme (*Han and Westwater*, 2000). In contrast to radiosonde profiles, for most deployments surface temperature measurements are continuously available. Furthermore, *Han and Westwater* (2000) find that the contribution of T_{mr} to the total calibration error is reduced by about a factor three, when this approach is used instead of a climatological profile. They derive linear regression coefficients for T_{mr} and T_{surf} for a large set of radiosonde profiles. This approach is also used in this work. For RHUBC-II, τ is calculated using the 112 available radiosonde profiles as input for the Rosenkranz'98 absorption model (*Rosenkranz*, 1998). Then, the predictand T_{mr} is calculated for the nine non-opaque HATPRO-G2 channels from $22.24 - 52.28\,\mathrm{GHz}$ and different elevation angles from Equation 2.26. The surface temperature, taken from the campaign's AWS, is averaged over a time period of 5 min before and 1 h after launch of each sonde in order to improve the comparability with the radiosonde measurements. Finally, linear regression coefficients are calculated from the obtained T_{mr}-T_{surf}-pairs.

For 22.24 GHz, the Root Mean Square Error (RMSE) is 3.2 K at three air masses. The RMSE decreases towards higher frequencies. At three air masses, it is 1.1 K and 1.2 K at 51.26 GHz and 52.28 GHz, respectively. The regression allows to estimate T_{mr} from the continuous ambient surface temperature measurements throughout the campaign. Figure 6.9 shows the sensitivity of calibrated zenith T_b to uncertainties in T_{mr}. Assuming an uncertainty of only T_{mr} of one RMSE, affects T_b in the V-band by $\approx 0.1\,\mathrm{K}$. In the K-band, the effect has virtually no impact. Therefore, it is concluded that for the studied cases, T_{mr} can be derived from surface temperatures with sufficient accuracy for the tipping curve calibration.

In order to exclude the effect of biases within the radiative transfer calculations, these are compared to results from the Liebe'93 and the Liebe'87 model. At three air masses, the different models result in a T_{mr} that agrees within 0.1 K. T_b results are not affected by such small differences.

For routine operation, for example at JOYCE, there are usually no radio soundings available. However, HATPRO-G2 possesses an internal procedure to determine T_{mr} (RPG-OS, 2011). The procedure uses regression coefficients that have been determined from a set of mid-latitude, low altitude radiosonde profiles. The atmospheric

conditions included in the regression are similar to the ones found at JOYCE. Therefore, it is assumed that the internal procedure can be used. In this case, T_{mr} is a function of surface temperature, pressure, and relative humidity. Surface values are measured by the built-in environmental sensors (RPG-OS, 2011). It can be assumed, that K-band calibrations at sea level are also not affected by the uncertainty within T_{mr}, because the impact of T_{mr} on T_b results is mainly determined by the channel opacity. K-band measurements at JOYCE do not exceed 22 K for the analyzed day. This value is far below the typical temperatures measured at 51.26 GHz and 52.28 GHz during RHUBC-II.

6.2.5 Atmospheric Inhomogeneities

Tipping curve calibrations assume a horizontally stratified atmosphere. Whenever atmospheric conditions deviate from this assumption, T_b results are affected. Here, the impact of atmospheric inhomogeneities on the calibration uncertainty is quantified for both deployments. Furthermore, two approaches that reduce the impact of inhomogeneities are discussed: the quality control for a single elevation scan and averaging the results of several calibrations.

Quality Control

In order to reduce the impact of atmospheric inhomogeneities, quality criteria are applied to opacity-air mass-pairs of each tipping curve elevation scan. A series of several subsequent calibrations, like it is used here, helps to adjust the criteria sufficiently. The applied criteria limit the deviation from the linearity between relative air mass X and the opacity τ and should guarantee the goodness of the fit. Namely, these are the linear correlation coefficient

$$corr(\tau, X) = \frac{\sum_{i=0}^{n} (\tau_i^{calc} - \overline{\tau^{calc}}) \cdot (X_i^{calc} - \overline{X^{calc}})}{\sqrt{\sum_{i=0}^{n} (\tau_i^{calc} - \overline{\tau^{calc}})^2 \cdot \sum_{i=0}^{n} (X_i^{calc} - \overline{X^{calc}})^2}} > corr_{min}, \tag{6.10}$$

with the total number of opacity-air mass-pairs n, and $\chi^2(\tau, X)$, which measures the absolute difference between calculated opacities (τ_i^{calc}, Eq. 3.25) and linearly fitted values (τ_i^{fit}):

$$\chi^2_{abs} = \sum_{i=0}^{n} (\tau_i^{calc} - \tau_i^{fit})^2 < \chi^2_{max}. \tag{6.11}$$

Although both values are not statistically robust for the number of considered opacity-air mass-pairs, it has been shown that they help to assess the quality of an elevation

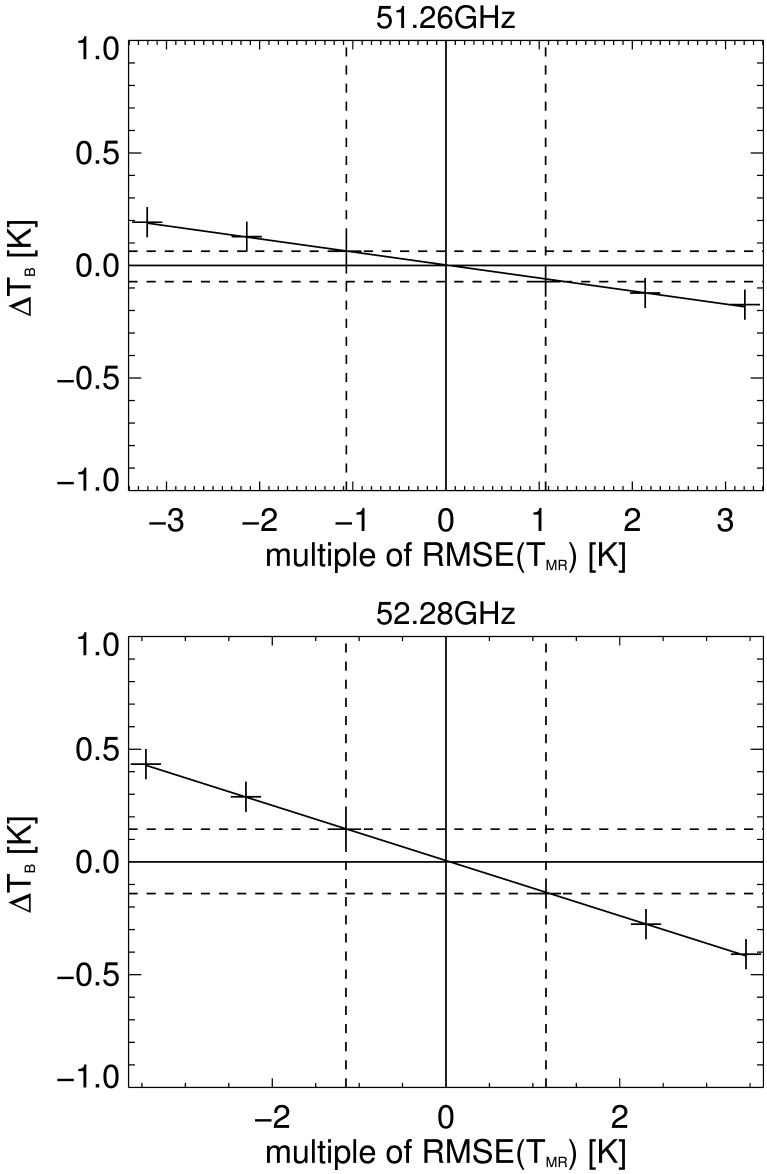

Figure 6.9: T_{mr} sensitivity of the tipping curve calibration at 51.26 GHz and 52.28 GHz. Plotted is the impact ΔT_b from uncertainties in the derivation of the mean radiative temperature T_{mr} on tipping curve results (*crosses*). T_{mr} is varied by $\pm 3 \cdot \mathrm{RMSE}(T_{mr})$ (Root Mean Square Error), *solid* lines give a linear regression between ΔT_b and T_{mr}. The *dashed* lines give the uncertainty area of 1 RMSE(T_{mr}) and the resulting uncertainty of T_b. The previously derived $RMSE(T_{mr})$ is 1.3 K (51.26 GHz) and 1.4 K (52.28 GHz).

scan. Within HATPRO-G2's internal calibration procedure, the thresholds are set to $corr_{min} = 0.9995$ and $\chi^2_{max,abs} = 3 \times 10^{-7}$ for all channels. For JOYCE, these default thresholds are sufficient, because they were defined for mid-latitude, close to sea level conditions. However, for RHUBC-II, also V-band channels are calibrated. Consequently, the calibration procedure has to cover a large range of opacities. On

the one hand, there are extremely low opacities in the K-band, on the other hand, V-band channels are characterized by relatively high opacities. When the absolute χ^2 criterion (Eq. 6.11) is used, the V-band channels are hardly able to meet it. For this work, the χ^2 criterion is therefore given by a relative formulation:

$$\chi^2 = \sum_{i=0}^{n} \frac{(\tau_i^{calc} - \tau_i^{fit})^2}{\tau_i^{calc}}. \tag{6.12}$$

The question is, how should the two thresholds be set to detect poor tipping curve conditions. Figures 6.10 and 6.11 show, how the number of successful tipping curves is affected by varying thresholds. Naturally, when the correlation threshold is raised, the number of successful tipping curves decreases. From Figure 6.11 it can be seen, that the χ^2 criterion is complementary, because even scans with very high correlations may fail. Therefore, $corr_{min}$ and χ^2_{max} should be adapted to the given deployment conditions. On the one hand, the criteria can be tightened as long as they can still be met by some tipping curve scans. On the other hand, tightening the criteria becomes non-beneficial, when the tipping curve results are not affected any more. The impact of different thresholds is also shown in Tables 6.5 to 6.8.

With values larger than 0.9999, correlations are by far highest for the V-band channel calibrations for RHUBC-II (Fig. 6.10). Moreover, for V-band channels, scans towards the open plane (250°N) show higher correlations than towards the hill slope (70°N). This orographic dependence is an argument against the use of bilateral tipping curves and makes the tilt compensation necessary (cf. Sec. 6.2.1). Although, the χ^2_{max} is defined relative to τ (Eq. 6.12), χ^2 values are higher than in the K-band. In return, K-band channels show smaller correlations, because of the higher water vapor variability. On average, the correlation coefficients in the K-band are higher and the χ^2 values are lower for JOYCE than for RHUBC-II. Obviously, the water vapor variability of the studied low altitude case is smaller than for the low water vapor RHUBC-II conditions. This shows, that the horizontal water vapor variability is not completely determined by the PWV. As a compromise between a sufficiently large number of successful calibrations and a good fit quality, it is concluded that $corr_{min} = 0.9995$ and a relative threshold of $\chi^2_{max} = 1 \times 10^{-5}$ is most appropriate for both deployment sites.

Table 6.5: Tipping curve results for RHUBC-II - A: mean T_b differences at zenith $\Delta T_b = T_b^{TIP} - T_b^{LN_2}$ and standard deviation (in parentheses) in Kelvin from n successful single-sided tipping curve calibrations at RHUBC-II on August 16, 2009. T_b^{LN2} values are based on the LN_2 calibration on August 11, 2009, improved by the modified boiling point correction (Eq. 6.4). Results from calibrations including a beam-width correction and an exact air mass calculation are given in column *corr*, the uncorrected results are given in column *uncorr*.

RHUBC-II	$corr_{\min} = 0.9995$ / $\chi^2_{\max} = 1 \times 10^{-5}$			
$\nu\,[GHz]$	*corr.*	n	*uncorr.*	n
22.24	−1.3(0.2)	49	−1.2(0.2)	39
23.04	−0.7(0.2)	50	−0.7(0.2)	49
23.84	−0.5(0.2)	69	−0.5(0.2)	68
25.44	−0.5(0.2)	125	−0.4(0.2)	133
26.24	+1.0(0.2)	85	+1.0(0.2)	95
27.84	−1.3(0.1)	67	−1.3(0.1)	71
31.40	−0.5(0.2)	101	−0.5(0.2)	101
51.26	−0.4(0.4)	120	−0.2(0.5)	130
52.28	−0.7(0.3)	216	−0.4(0.3)	223

For RHUBC-II, 245 tipping curve scans were performed on August 16, 2009. The number of successful tipping curves depends on the channel frequency. While it is small for the three K-band channels next to line center ($47 - 68$), there are 115 and 212 successful tipping curves for the V-band channels at 51.26 GHz and 52.28 GHz, respectively (Tab. 6.5, 6.6).

In agreement with Section 6.2.1, this indicates the high inhomogeneity of atmospheric water vapor, which is most pronounced close to the line center at 22.235 GHz. For JOYCE, 248 elevation scans were performed on November 16, 2011, (Tab. 6.7, 6.8). Similar to RHUBC-II, the number of successful K-band calibrations tends to be smaller towards the line center. For all channels the number ranges between 93 and 103 ($corr_{min} = 0.9995$, $\chi^2_{max} = 1 \times 10^{-5}$).

So far, each channel has been investigated separately. The quality criteria can be tightened by requesting that all calibrated channels have to meet the thresholds. However, it turns out that this criterion is too hard, as it is not met by any tipping curve scan of the two deployments.

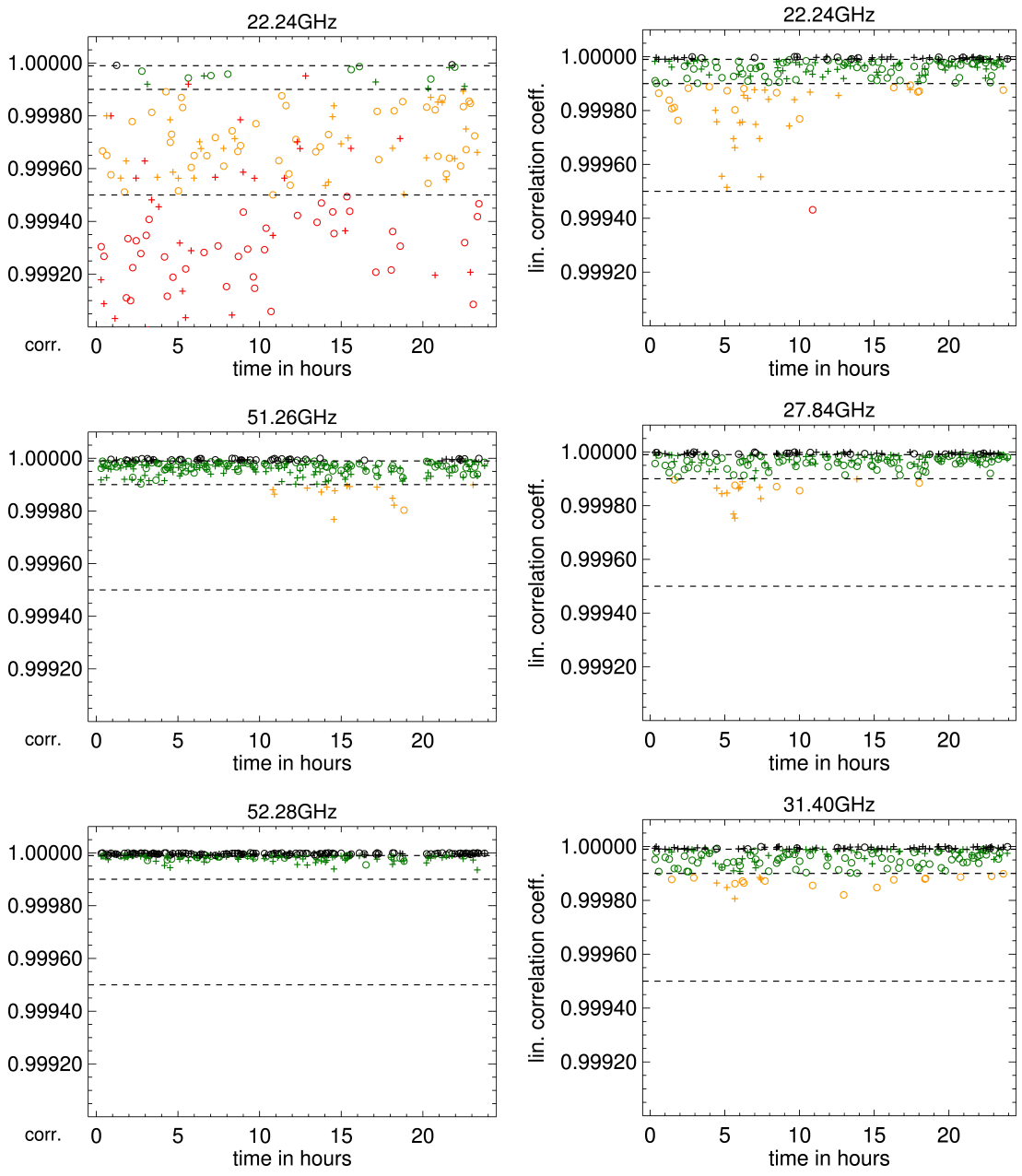

Figure 6.10: Linear opacity-air mass correlations for selected HATPRO-G2 channels. Plotted are the results of repeated tipping curve calibrations on August 16, 2009, during RHUBC-II (*left*) and on November 16, 2011, at JOYCE (*right*). *Crosses*: scans towards 70°N, *circles*: scans towards 250°N, *dashed lines*: different hypothetical quality thresholds $corr_{min}$. Failed tipping curves with $corr < corr_{min} = 0.9995$ and/or $\chi^2 > \chi_{max} = 1 \times 10^{-5}$ are marked in *red*. The other colors mark successful tipping curve calibrations, when only the correlation threshold is applied: $corr_{min} = 0.9995$ (*orange*), $corr_{min} = 0.9999$ (*green*), $corr_{min} = 0.99999$ (*black*).

Table 6.6: Tipping curve results for RHUBC-II - B: T_b^{TIP} is calculated for different quality control thresholds within the tipping curve calibration (cf. Sec. 6.2.5): *thresh.*1: $corr_{min} = 0.9995, \chi_{max} = 3^{\star} \times 10^{-7}$, *thresh.*2: $corr_{min} = 0.9999, \chi_{max} = 1 \times 10^{-5}$. $\star$: $\chi^2_{max} = \chi^2_{abs,max}$ is formulated as an absolute threshold (Eq. 6.11), in any other case it is a relative threshold (Eq. 6.12).

RHUBC-II	beam width + air mass corr. incl.			
$\nu\,[GHz]$	*thresh.*1	n	*thresh.*2	n
22.24	−1.3(0.2)	74	−1.3(0.2)	16
23.04	−0.7(0.2)	64	−0.7(0.2)	21
23.84	−0.5(0.2)	96	−0.5(0.2)	23
25.44	−0.5(0.2)	143	−0.4(0.2)	32
26.24	+0.9(0.2)	97	+0.9(0.2)	21
27.84	−1.3(0.1)	84	−1.3(0.1)	13
31.40	−0.5(0.2)	133	−0.5(0.2)	31
51.26	−0.4(0.5)	13	−0.4(0.4)	120
52.28	−0.8(0.3)	27	−0.7(0.3)	216

Table 6.7: Tipping curve results for JOYCE - A : mean T_b differences at zenith $\Delta T_b = T_b^{TIP} - T_b^{LN2}$ and standard deviation (in parentheses) in Kelvin from n successful single-sided tipping curve calibrations at JOYCE on November 16, 2011. T_b^{LN2} values are based on the LN_2 calibration on November 10, 2011. Results from calibrations including a beam width correction and an exact air mass calculation are given in column *corr.*, the uncorrected results are given in column *uncorr.*

JOYCE	$corr_{\min} = 0.9995\,/\,\chi^2_{\max} = 1 \times 10^{-5}$			
$\nu\,[GHz]$	*corr.*	n	*uncorr.*	n
22.24	+1.6(0.3)	93	+1.8(0.3)	83
23.04	+0.8(0.3)	84	+1.0(0.3)	78
23.84	+1.2(0.3)	96	+1.4(0.3)	86
25.44	+1.2(0.2)	103	+1.3(0.2)	103
26.24	+1.3(0.2)	101	+1.5(0.2)	96
27.84	+0.8(0.2)	103	+0.9(0.2)	101
31.40	+2.4(0.6)	103	+2.5(0.6)	102

Table 6.8: Tipping curve results for JOYCE - B: T_b^{TIP} is calculated for different quality control thresholds within the tipping curve calibration (cf. Sec. 6.2.5): $thresh.1$: $corr_{min} = 0.9995, \chi_{max} = 3^{\star} \times 10^{-7}$, $thresh.2$: $corr_{min} = 0.99999, \chi_{max} = 1 \times 10^{-5}$. $\star$: $\chi^2_{max} = \chi^2_{abs,max}$ is formulated as an absolute threshold (Eq. 6.11), in any other case it is a relative threshold (Eq. 6.12).

JOYCE	beam width + air mass corr. incl.			
$\nu\,[GHz]$	$thresh.1$	n	$thresh.2$	n
22.24	+1.5(0.2)	42	+1.6(0.2)	18
23.04	+0.9(0.1)	46	+0.7(0.4)	9
23.84	+1.1(0.2)	55	+1.1(0.3)	20
25.44	+1.2(0.2)	91	+1.1(0.3)	52
26.24	+1.3(0.2)	89	+1.5(0.2)	27
27.84	+0.8(0.2)	101	+0.7(0.2)	35
31.40	+2.4(0.6)	97	+2.7(0.2)	32

6.2.6 Calibration Results

In order to give a first overview of the tipping curve results for the two analyzed days, the opacity τ is calculated for each nominal elevation angle φ_0 during the tipping curve procedure are mapped to zenith by

$$\tau^{MAP} = \frac{\tau}{sin(\varphi_0)}. \tag{6.13}$$

Time series of τ^{MAP} give an impression of the residual atmospheric inhomogeneities for the two deployment sites during the analyzed days (Fig. 6.12 and 6.13). For the V-band channels, calibrated during RHUBC-II on August 16, 2009, the positive effect of the tilt correction is clearly evident (Fig. 6.12). When τ^{MAP} is averaged for each of the azimuth directions, the daily mean difference between both directions reduces by a factor six at 51.26 GHz and a factor three at 52.28 GHz. The calibration results for two K-band channels plotted for the JOYCE deployment (Fig. 6.13), which is located in a more homogeneous environment, nicely show the evolution of water vapor under mostly clear skies during November 16, 2011. For JOYCE, the τ results from single-sided elevation scans agree towards both scanning directions. Therefore, it can be assumed that HATPRO-G2 is not tilted, while operating at JOYCE (Fig. 6.13).

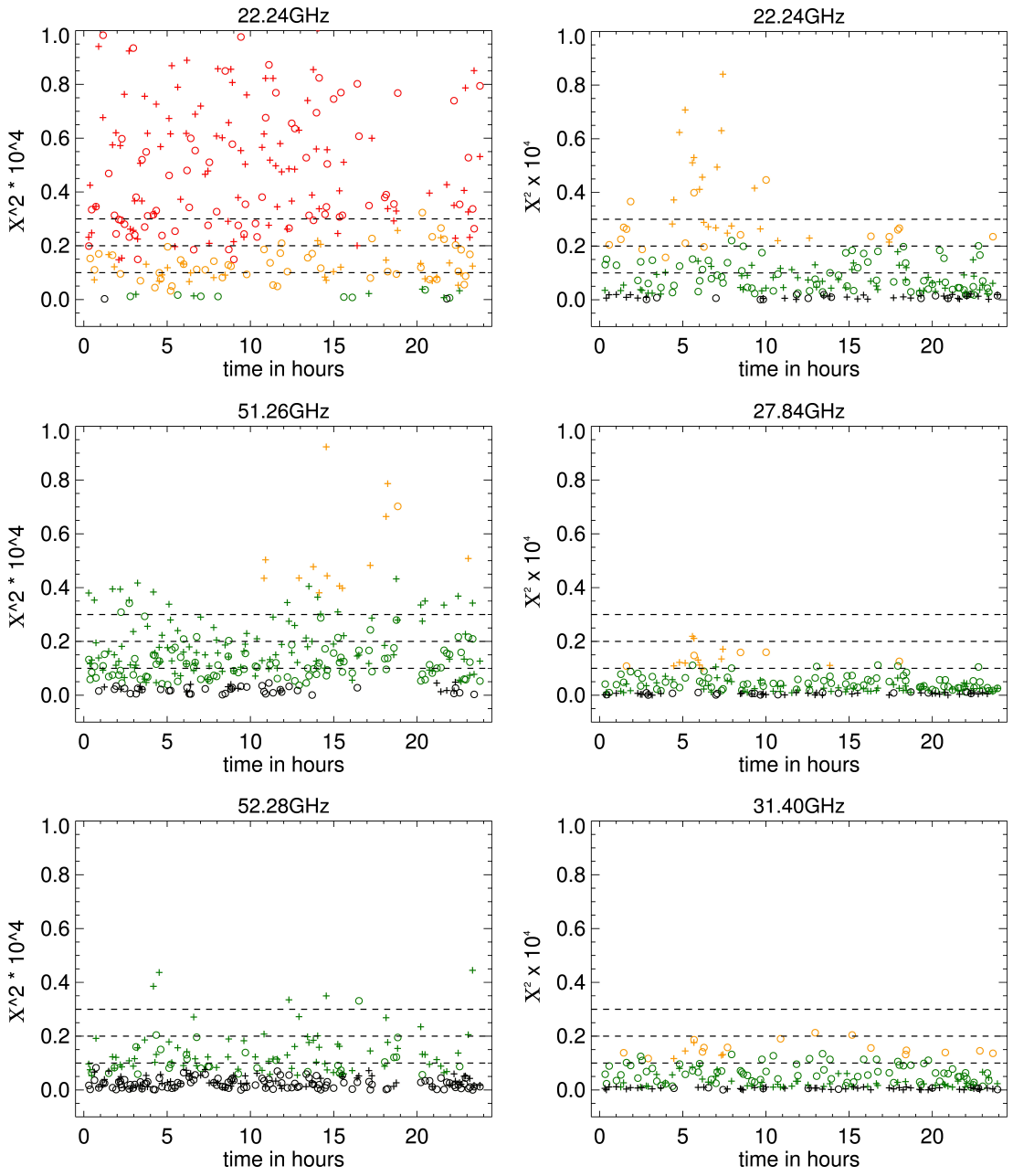

Figure 6.11: χ^2 values of tipping curve scans for selected HATPRO-G2 channels. Plotted are the results of repeated tipping curve calibrations on August 16, 2009, during RHUBC-II (*left*) and on November 16, 2011, at JOYCE (*right*). *Crosses*: scans towards 70°N, *circles*: scans towards 250°N, *dashed lines*: different hypothetical quality thresholds χ_{max}. Failed tipping curves with $corr < corr_{min} = 0.9995$ and/or $\chi^2 > \chi_{max} = 1 \times 10^{-5}$ are marked in *red*. The other colors mark successful tipping curve calibrations, when only the correlation threshold is applied: $corr_{min} = 0.9995$ (*orange*), $corr_{min} = 0.9999$ (*green*), $corr_{min} = 0.99999$ (*black*).

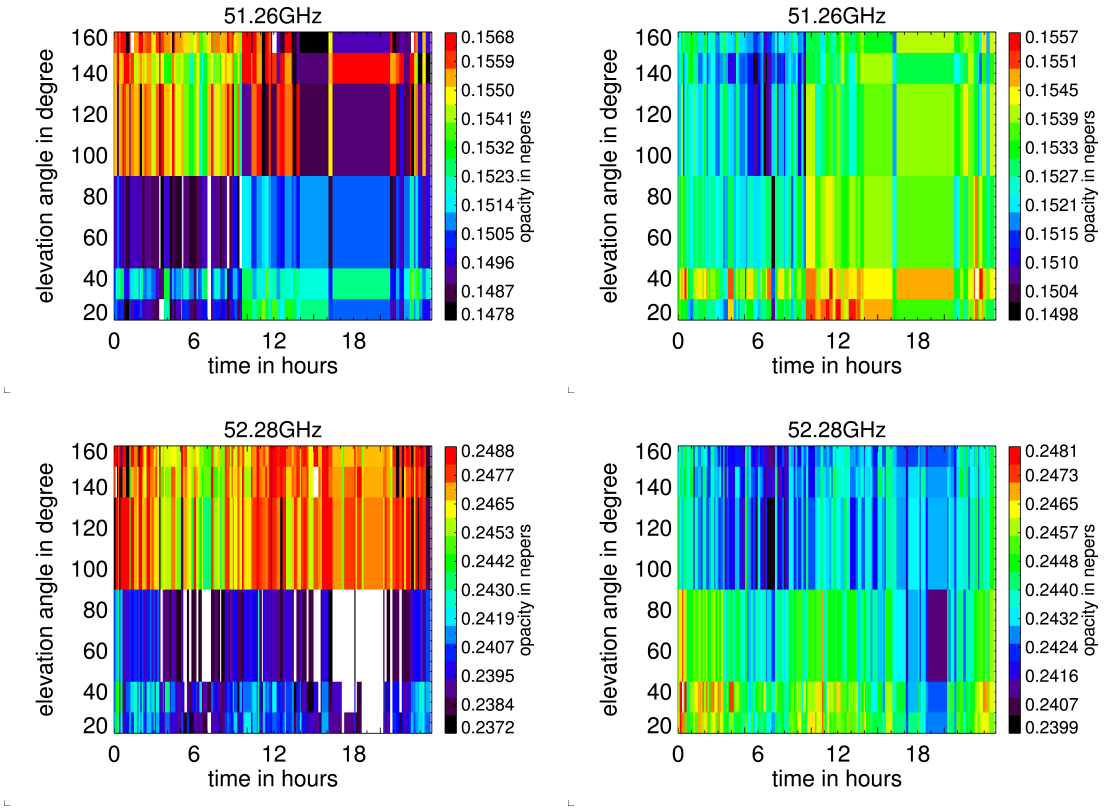

Figure 6.12: Opacity map from tipping curve calibrations during RHUBC-II: Time series of opacity τ^{MAP} (Eq. 6.13) calculated from tipping curve calibrations on August 16, 2009, and mapped to zenith for 51.26 GHz and 52.28 GHz. τ^{MAP} is updated with every successful elevation scan and is calculated for original elevation angles (*left*) and elevation angles, which are corrected to compensate a radiometer tilt of 0.2° (cf. Sec. 6.2.1, *right*). The quality control thresholds are $corr_{min} = 0.9995$ and $\chi^2_{max} = 1 \times 10^{-5}$ for all channels.

Zenith T_b^{TIP}, that result from the calculated opacities, are directly compared to corresponding zenith measurements that are based on a LN_2 calibration (T_b^{LN2}). A time series of

$$\Delta T_b = T_b^{TIP} - T_b^{LN2} \tag{6.14}$$

for all successful tipping curve calibrations during August 16, 2009, (RHUBC-II) and November 16, 2011, (JOYCE) is given in Figures 6.14 and 6.15. "Successful" means that an elevation scan meets both quality criteria with the thresholds $corr_{min} = 0.9995$ and $\chi^2_{max} = 1 \times 10^{-5}$ (cf. Sec. 6.2.5). The scanned air masses are: 1.0, 1.4, 2.0, and 3.0. As mentioned in Section 6.2.1, bilateral scans are used for JOYCE. In this case, subsequent scans towards both azimuth directions have to meet the quality thresholds.

For RHUBC-II, ΔT_b refers to the LN_2 calibration performed on August 11, 2009,

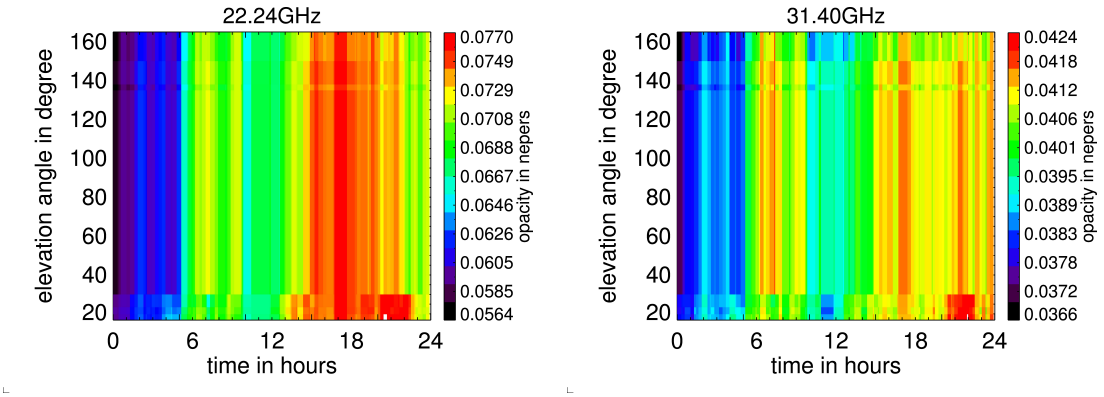

Figure 6.13: Opacity map from tipping curve calibrations at JOYCE: Time series of opacity τ^{MAP}, calculated from successful single-sided tipping curve calibrations on November 16, 2011, and mapped to zenith for selected HATPRO-G2 channels. τ^{MAP} is updated with every successful elevation scan. The quality control thresholds are $corr_{min} = 0.9995$ and $\chi^2_{max} = 0.1 \times 10^{-4}$ for all channels.

which is improved by the modified boiling point correction (Eq. 6.4). The differences show a rather large offset between the two calibration techniques. The daily mean difference $\overline{\Delta T_b}$ is channel dependent. For K-band channels, it ranges between -1.3 K (22.24 GHz) and $+1.0$ K (26.24 GHz). In the V-band, $\overline{\Delta T_b}$ is -0.4 K and -0.7 K at 51.26 GHz and 52.28 GHz, respectively. In contrast, the standard deviation $\sigma(\Delta T_b)$ from all scans of the day is rather small. It is 0.1 K-0.2 K for the K-band channels and 0.4 K and 0.3 K at 51.26 GHz and 52.28 GHz, respectively. For JOYCE, ΔT_b refers on the last LN_2 calibration performed on November 10, 2011. Here, $\overline{\Delta T_b}$ of K-band channels ranges between $+1.6$ K and $+2.4$ K. Although the time series in Figure 6.15 show larger variations throughout the day due to water vapor variability than for RHUBC-II, $\sigma(\Delta T_b)$ does not exceed 0.6 K. Nevertheless, at 31.40 GHz the tipping curve results show a distinct diurnal cycle with more than 2 K between minimum and maximum.

The standard deviation $\sigma(\Delta T_b)$ is induced by random processes like atmospheric turbulence. Therefore, $\sigma(\Delta T_b)$ gives the unsystematic uncertainty of a single tipping curve calibration. It is assumed to be mainly caused by atmospheric inhomogeneities and cannot completely be removed by the quality thresholds (cf. Sec. 6.2.5). One possibility to eliminate the random variability is to take the daily mean average of the tipping curve results $\overline{T_b^{TIP}}$. A similar approach is taken by *Liljegren* (1999) who introduces a rolling dataset of calibration parameters to the calibration procedure of ARM radiometers. *Schneebeli and Mätzler* (2009) choose a different approach and successfully reduce the "calibration noise" of a microwave radiometer using a Kalman filtering scheme. Regardless of which approach is chosen to eliminate the calibration noise, the questions is, how frequent tipping curve calibrations should be performed

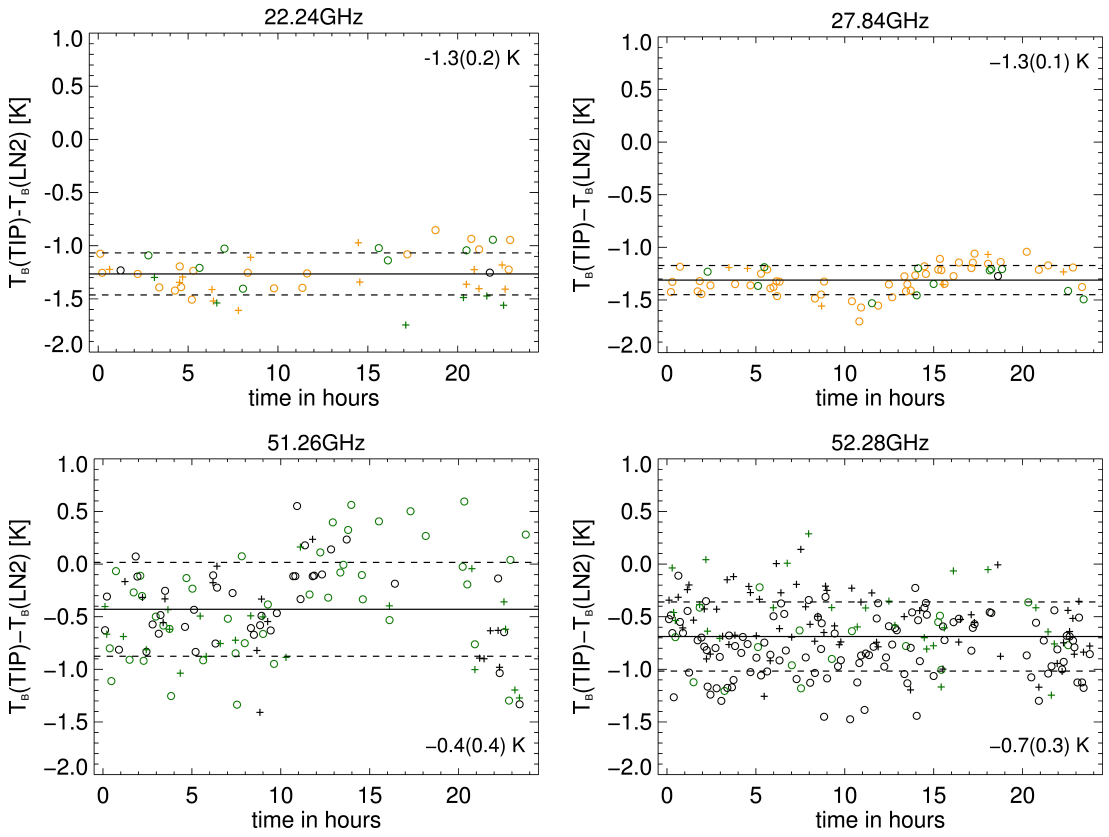

Figure 6.14: Time series of RHUBC-II tipping curve results: Plotted are the differences between T_b^{TIP} (August 16, 2009) and $T_b^{LN_2}$ from the original LN_2 calibration (August 11, 2009), improved by the modified boiling point correction (Eq. 6.4), for selected HATPRO-G2 channels. Results are given for single-sided elevation scans towards $70.0°N$ (*crosses*) and towards $250.0°N$ (*circles*). The daily mean value (*solid*) and the standard deviation (*dashed*) for scans towards both directions are given in numbers within each subfigure. The quality control thresholds are set to $corr_{min} = 0.9995$, $\chi^2_{max} = 1 \times 10^{-4}$. The color coding is according to Figure 6.10: $corr_{min} > 0.9995$ (*orange*), $corr_{min} > 0.9999$ (*green*), and $corr_{min} > 0.99999$ (*black*).

and how many calibrations should be averaged for the optimal result. This leads over to the investigation of the repeatability of the two analyzed calibration techniques (cf. Sec. 6.3.1).

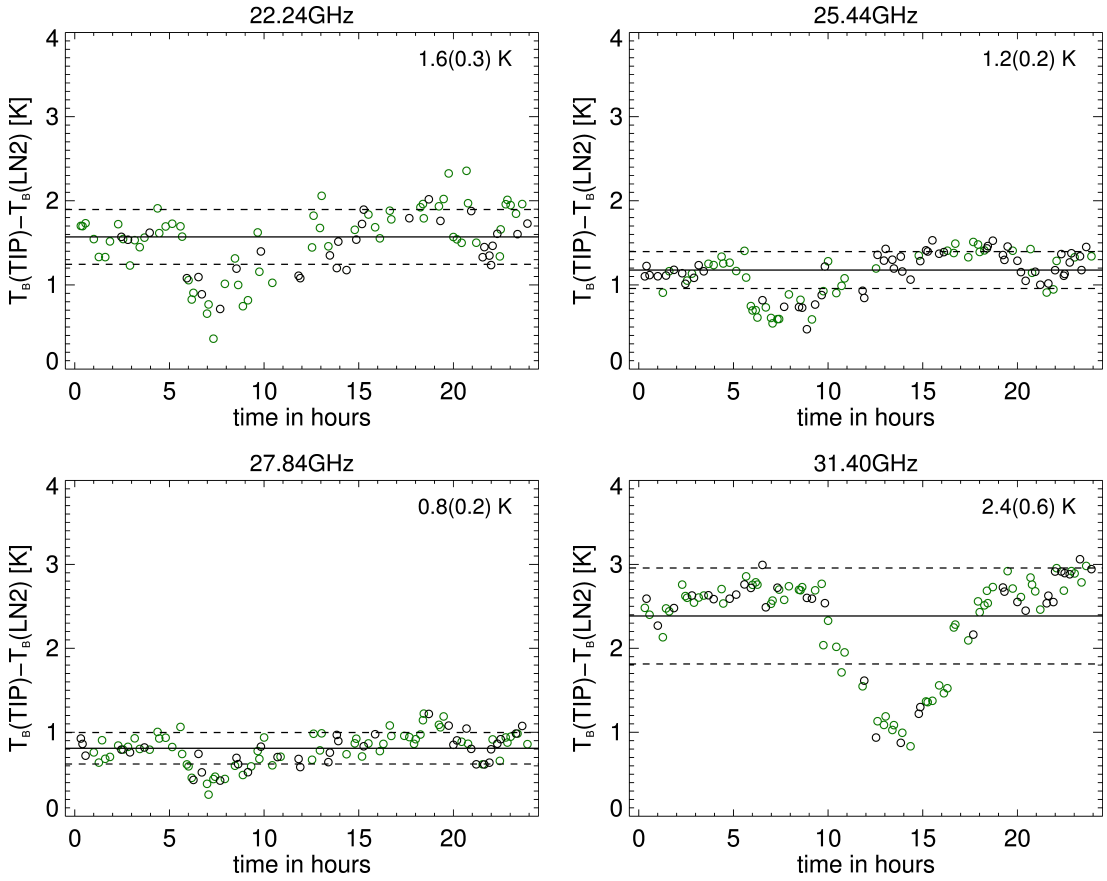

Figure 6.15: Time series of JOYCE tipping curve results: Plotted are the differences between T_b^{TIP} (November 16, 2011) and $T_b^{LN_2}$ from the prior LN_2 calibration (November 10, 2011) for selected HATPRO-G2 channels. Results are given for bilateral elevation scans in the $70.0°N/250.0°N$ azimuth plane (*crosses*). The daily mean value (*solid*) and the standard deviation (*dashed*) are given in numbers within each subfigure. The quality control thresholds are set to $corr_{min} = 0.9995$, $\chi^2_{max} = 1 \times 10^{-4}$. The color coding is according to Figure 6.10: $corr_{min} > 0.9995$ (*orange*), $corr_{min} > 0.9999$ (*green*), and $corr_{min} > 0.99999$ (*black*).

6.3 Comparative Assessment of Calibration Techniques

In order to assess the absolute accuracy of the LN_2 and the tipping curve calibration, possible sources of uncertainty for a single calibration of HATPRO-G2 have been discussed in the previous sections. The discussed uncertainties include systematic and unsystematic effects, because both affect the uncertainty T_b measurements. At this point, both techniques are investigated concerning their repeatability. Afterwards, zenith T_b results from both calibration techniques are compared to each other with respect to their total uncertainty (cf. Sec. 6.3.2).

6.3.1 Repeatability

In this section, the unsystematic uncertainty of calibration results is investigated in order to determine the repeatability of HATPRO-G2's absolute calibration procedures. Since in practice, single calibrations are often used to provide calibration parameters for measurement periods, which extend over several months, a good repeatability is of great importance. Unfortunately, for RHUBC-II, only one LN_2 calibration was performed in the beginning of the deployment. Therefore, the repeatability of the LN_2 calibration has to be assessed by repeated HATPRO-G2 calibrations at JOYCE. On this account, the variability of the calibration parameters from eleven subsequent LN_2 calibrations is analyzed. The eleven calibrations were preformed within about 2 h on November 10, 2011, using the same HATPRO-G2 radiometer that was also deployed at RHUBC-II. The mean calibration parameters determined by the different LN_2 calibrations and their standard deviations are listed in Table B.3 (App. B). The LN_2 calibrations are compared to subsequent 43 successful standard bilateral tipping curve calibrations of K-band channels that were performed between November 10 and November 17, 2011 (Fig. 6.16).

It can be assumed that the receiver non-linearity parameter and the signal from the noise diode are constant over the whole analyzed period of one week. Therefore, any change of determined α and T_N within this time period reflects their random uncertainty, which can be expressed by the standard deviation. However, the receiver noise temperature and the detector gain vary on time scales of seconds to minutes (Fig. 6.17). Consequently, the standard deviation of g and T_R over subsequent absolute calibrations do not reflect the random variability and cannot be used to quantify the calibration repeatability (Tab. B.3, App. B). The changes within g and T_R could be excluded by determining the repeatability only from the variability of T_N. However, the four calibration parameters are the solution of a single system of equations (Eq. 3.19), meaning the parameters are not independent from each other. An increase of one parameter, compared to a previous calibration, could be balanced by a decrease of another. Thus, the chosen approach to estimate the calibration repeatability is to use T_b, which combines all four parameters:

$$T_b = \left(\frac{U}{g}\right)^{\alpha} - T_N - T_R. \tag{6.15}$$

In order to consider changes in g and T_R, T_b is calculated from observations just before each calibration by Equation 6.15 (T_b^{BEFORE}). For the K-band channels, hot load calibrations are performed every 5 min (Fig. 6.17). It is assumed, that the detector gain is not significantly changing between two hot load calibrations. Therefore, this method is not applicable to the V-band channels, where the gain is continuously adjusted by noise switching (Fig. 6.17).

In the K-band, the last observation T_b^{BEFORE} after a hot load calibration and before a LN_2 calibration, is based on a recently updated detector gain g. For eight of the eleven calibrations in the K-band, T_b measurements and detected voltages are available within this time window. The used T_R has been determined by the prior LN_2 calibration. As the time between two LN_2 calibrations ranges only between 5 min and 10 min, the receiver noise can be assumed as constant for K-band channels (Fig. 6.17). For both calibration types, T_b^{BEFORE} is calculated from zenith observations. The detector voltages corresponding to T_b^{BEFORE} are then used with the calibration parameters from the following calibration (T_b^{CAL}). Finally, pairs of T_b values are gained for each of the calibrations. The difference between them is:

$$\Delta T_b = T_b^{CAL} - T_b^{BEFORE}. \tag{6.16}$$

Although only based on a limited number of calibrations, the Root Mean Square Deviation (RMSD) of ΔT_b:

$$RMSD = \sqrt{\overline{(\Delta T_b)^2}} \tag{6.17}$$

is a fairly good measure of the mean variation between two consecutive calibrations – under the condition that systematic biases can be excluded. The $RMSD(\Delta T_b)$ is defined as repeatability of a single calibration, while systematic biases are included in the mean difference $\overline{\Delta T_b}$. Apart from 23.04 GHz, with $RMSD = 0.8$ K, the repeatability $RMSD(\Delta T_b)$, derived from the eleven LN_2 calibrations, is better than 0.5 K for K-band channels (Tab. 6.9). Systematic biases can be excluded, because $|\overline{\Delta T_b}|$ is ≤ 0.1 K (Tab. 6.9). The repeatabilities derived for LN_2 calibrations agree well with the uncertainty range that has been assessed for the resonance effect (cf. Sec. 6.1.2). The standing wave that builds up between the receiver an the LN_2 surface erratically affects the repeatability, because the level of LN_2 slightly deviates from calibration to calibration (cf. Sec. 6.1.2). For example, the RMSD is largest at 23.04 GHz, the channel which is most affected by the standing wave. The assumption is supported by the linear correlation coefficient of 0.88 between the oscillation amplitudes (Tab. 6.2) and the RMSD for HATPRO-G2's K-band channels. This shows, how sensitive the calibration is on the LN_2 filling level of the cold calibration load and how important it is

to minimize the resonance effect by averaging over several calibrations (cf. Sec. 6.3.2).

The repeatability $RMSD(\Delta T_b)$, derived for 43 tipping curve calibrations in the K-band, ranges between 0.2 K and 0.6 K (Tab. 6.9). $|\overline{\Delta Tb}|$ is well below 0.1 K for all channels and can therefore be neglected. Additionally, for each channel the RMSD is comparable with the standard deviation $\sigma(\Delta T_b^{TIP})$, which reflects the impact of atmospheric inhomogeneities on calibrated T_b (Tab. 6.7, 6.8). In case of the 43 analyzed calibrations, channels that are less affected by atmospheric inhomogeneities (small σ) are characterized by a better repeatability. However, when the calibration are repeated on shorter time scales, this is not necessarily the case. As an example, the RMSD of tipping curve calibrations can also directly be derived from $\Delta T_b = T_b^{TIP} - T_b^{LN2}$ of many calibrations performed on a single day (November 16, 2011, cf. Sec. 6.2.6). At this day, several successful tipping curve calibration are available within every hour. In this case, the RMSD and $\sigma(\Delta T_b^{TIP})$ are in the same range, but the channel dependencies are completely uncorrelated. For example at 22.24 GHz, the RMSD is negligibly small, while $\sigma(\Delta T_b^{TIP})$ is 0.3 K. At this channel, the derived repeatability is good, because the atmospheric inhomogeneity changes on time scales larger than the repetition rate of tipping curve calibrations (Fig. 6.15). For RHUBC-II on August 16, 2009, the $RMSD$ results for K-band channels are comparable to JOYCE (< 0.3 K). At 51.26 GHz and 52.28 GHz, the repeatability is only slightly higher, with 0.7 K and 0.5 K for 51.26 GHz and 52.28 GHz, respectively. For these channels, the RMSD is larger than $\sigma(\Delta T_b)$.

The previous section has led to the question, how many tipping curve calibrations should be used to optimally reduce the noise that is included in a single calibration. Averaging over several calibrations is beneficial, because there is a residual calibration noise, which is not removed by the quality thresholds (cf. Sec. 6.2.5). The larger the number of calibrations used, the better the noise reduction. However, it is also important that the used calibrations cover the whole range of variations caused by the residual calibration noise. In this case, for the repeatability $RMSD(\Delta T_b)$ is in the same order as $\sigma(\Delta T_b)$ for all calibrated channels. This means, an extended period of successful tipping curve calibrations is preferable to very frequently repeated calibrations within a small time period. Note, that the maximum averaging period is limited by the long-term stability of the radiometer. For HATPRO-G2, this is the recommended interval of for LN_2 calibrations, which is $5-6$ months (RPG-OS, 2011, p.15). For longer periods, significant drifts of HATPRO-G2 calibration parameters are detected. The drifts, observed over a period of 22 months (Tab. B.1, App. B), occur mainly in the noise diode temperature of T_N and reach up to 1.5 K in the V-band.

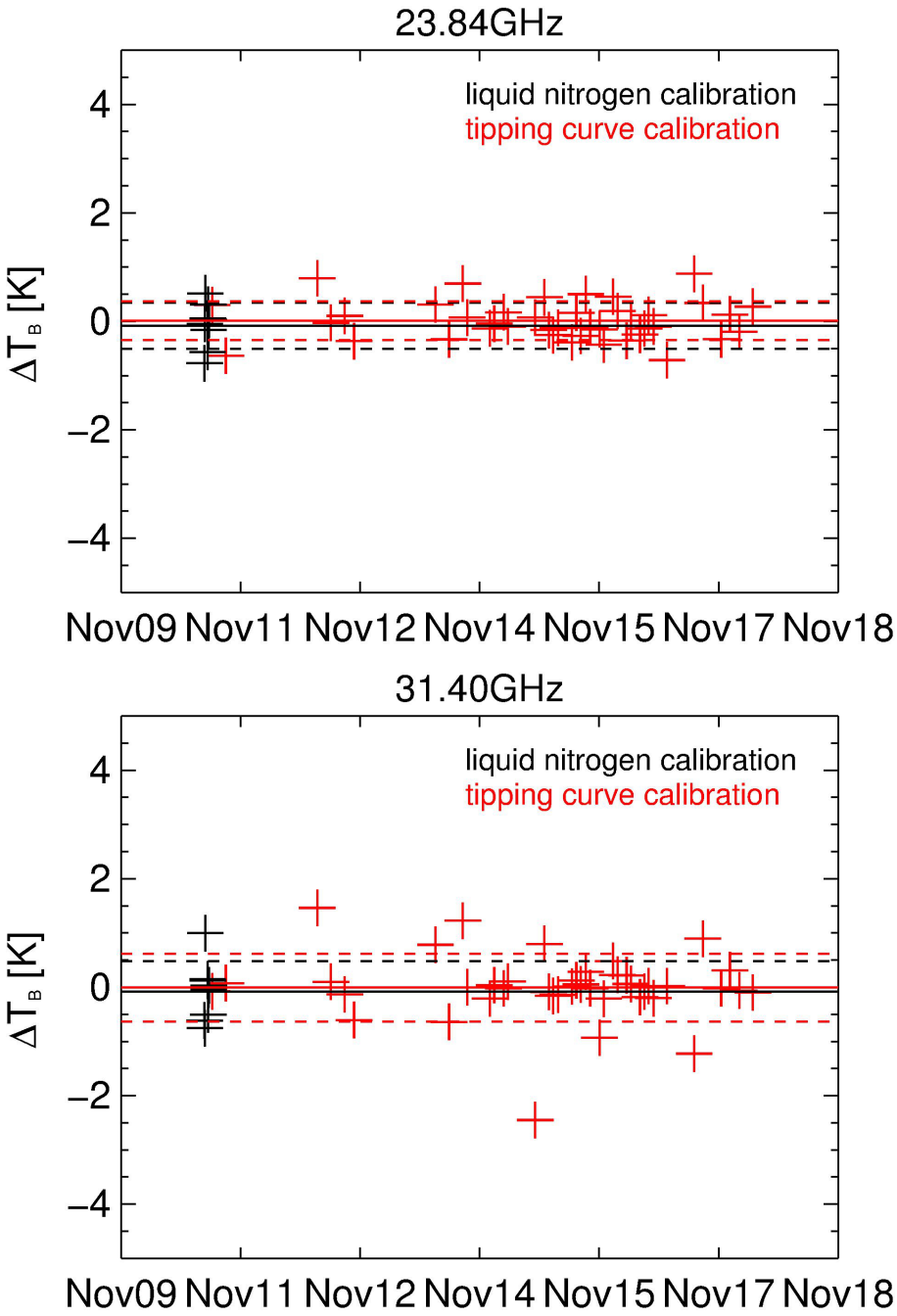

Figure 6.16: T_b difference between subsequent HATPRO-G2 calibrations for two selected HATPRO-G2 channels. ΔT_b values are derived from LN_2 calibrations and tipping curve calibrations performed at JOYCE between November 10 and 17, 2011. ΔT_b considers changes of detector gain g and receiver noise temperature T_R between two calibrations (Fig. 6.17). The *solid* (*dashed*) horizontal lines give the mean (standard deviation) for each calibration technique.

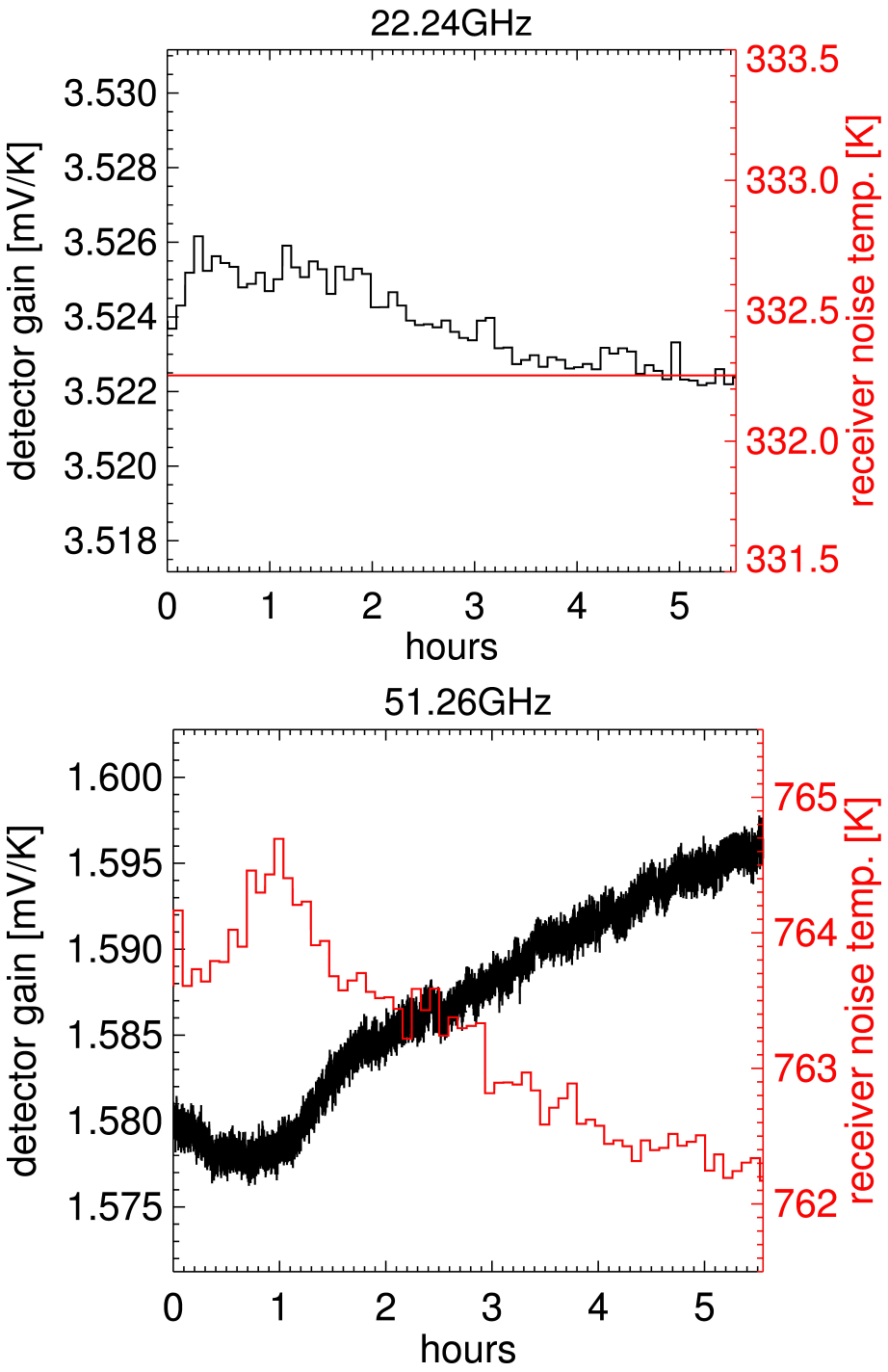

Figure 6.17: Time series of calibration parameters measured on the hot load for selected HATPRO-G2 channels. The measurements are taken at JOYCE on August 15, 2011. For K-band channels (*top*), the detector gain g (*black*) is adjusted by hot load calibrations repeated every 5 min (no noise diode calibration is performed). For V-band channels (*bottom*), g (*black*) is adjusted by continuous noise switching, the receiver noise temperature (T_R, *black*) is updated by hot load calibrations repeated every 5 min (cf. Sec. 4.3).

Table 6.9: Results from repeated LN_2 and tipping curve calibrations, performed with HATPRO-G2 at JOYCE, for eleven LN_2 calibrations on November 10, 2011, and 43 successful tipping curve calibrations between November 10 and November 17, 2011.

11 LN_2 calibrations				43 tipping curve calibrations			
$\nu\,[GHz]$	$RMSD$	$\overline{\Delta T_b}$	$\sigma(\Delta T_b)$	$\nu\,[GHz]$	$RMSD$	$\overline{\Delta T_b}$	$\sigma(\Delta T_b)$
22.24	0.4	+0.1	0.4	22.24	0.2	0.0	0.5
23.04	0.8	+0.1	0.9	23.04	0.4	0.0	0.4
23.84	0.4	+0.1	0.4	23.84	0.5	0.0	0.4
25.44	0.4	+0.1	0.4	25.44	0.4	0.0	0.3
26.24	0.4	+0.0	0.4	26.24	0.4	0.0	0.3
27.84	0.5	+0.1	0.5	27.84	0.3	0.0	0.3
31.40	0.5	+0.1	0.6	31.40	0.3	0.0	0.6

6.3.2 Total Calibration Uncertainties

The individual uncertainties for a single calibration, which have been assessed for the two calibration techniques, are summed up in Tables 6.10, 6.11). The calibration results of both techniques, are compared on the basis of the assessed total uncertainties of calibrated HATPRO-G2 measurements (Fig. 6.18, 6.19). The comparison is based on the daily mean difference $\overline{\Delta T_b} = T_b^{TIP} - T_b^{LN2}$ of zenith measurements from each of the two deployments. $\overline{T_b^{TIP}}$ is the average result from numerous calibrations performed on August 16, 2009, (RHUBC-II) and on November 16, 2011 (JOYCE). In contrast to RHUBC-II, where only a single LN_2 calibration is available (August 11, 2009), $\overline{T_b^{LN_2}}$ is based on the mean results of eleven LN_2 calibrations performed on November 10, 2011 (cf. Sec. 6.3.1). The impact of total uncertainties on T_b measurements depends on the channel frequency and T_b itself. Therefore, total uncertainties of a single calibration are determined for each HATPRO-G2 channel and the daily mean values $\overline{T_b^{TIP}}$ and $\overline{T_b^{LN2}}$. The mean T_b values of each channel are considered to be typical for each of the two sites under clear sky conditions. However, one has to keep in mind that the uncertainties vary with changing atmospheric conditions. For both deployments, the two calibration techniques are compared to T_b simulations based on the best knowledge of the atmospheric profiles for HATPRO-G2 channels (Fig. 6.18, 6.19). The spread of T_b results from five different gas absorption models (cf. Sec. 2.3) gives an impression of the uncertainty that is associated with T_b simulations.

At RHUBC-II, the low pressure conditions allow to calibrate the K-band and also the two V-band channels at 51.26 GHz and 52.28 GHz. Zenith T_b from tipping curves are generally smaller than T_b derived from the original LN_2 calibration (August 11,

2009). Daily mean tipping curve calibration results for the chosen quality thresholds ($corr_{min} = 0.9995$, $\chi_{max} = 1 \times 10^{-5}$), ΔT_b deviate by up to $-2.8\,\mathrm{K}$ (22.24 GHz) from the original LN_2 calibration results. The minimum is $-0.6\,\mathrm{K}$ at 26.24 GHz. For the two V-band channels, the difference is $-1.8\,\mathrm{K}$ at 51.26 GHz and $-2.0\,\mathrm{K}$ at 52.28 GHz. However, the discrepancy between the two calibration techniques is reduced significantly, when the boiling point correction, improved for low pressure conditions, is used (Eq. 6.4). Corrected ΔT_b ranges between $-1.3\,\mathrm{K}$ (22.24 GHz and 27.84 GHz) and $+1.0\,\mathrm{K}$ (26.24 GHz) in the K-band (Tab. 6.5). At 51.26 GHz and 52.28 GHz, the biases are reduced to $-0.4\,\mathrm{K}$ and $-0.7\,\mathrm{K}$, respectively. Nevertheless, apart from the K-band channel at 27.84 GHz, the tipping curve calibration provides always smaller T_b results. When the new boiling point correction is included, the total uncertainty ranges of both calibration techniques overlap for the two V-band channels and for most K-band channels (Fig. 6.18). Only for the channels at 22.24 GHz and 27.84 GHz are slightly outside the overlap range ($-0.2\,\mathrm{K}$ and $-0.4\,\mathrm{K}$, respectively). Despite that, the three lowest K-band channels show a bias, which systematically increases towards the line center. This rises the question, whether an atmospheric signal has contaminated the LN_2 calibration via a reflective component (cf. Sec. 6.1.2). Such an external signal could reduce the reflective component and therefore calibrated T_b. Since antenna beam width increases with decreasing frequency, this effect may additionally depend on the channel frequency.

Finally, the question, which technique gives results that are closer to the truth, cannot be answered. Nevertheless, radiative transfer calculations for the K-band channels and the tipping curve calibration results agree very well. Zenith T_b measurements, calibrated by the tipping curve calibration, only deviate by less than 1 K from simulated T_b values using RHUBC-II radiosonde profiles of the analyzed day (cf. Sec. 7.5). In contrast, the LN_2 calibration suffers from large uncertainties at the cold calibration point: The influence of standing waves can be reduced by averaging calibration results, but the T_b uncertainty resulting from an uncertain refractive index of LN_2 remains. For the two V-band channels the uncertainty of the tipping curve is much larger than in the K-band, because most effects that impact the uncertainties grow with channel opacity. In the V-band, both calibration techniques are in good agreement, when the LN_2 calibration uses the improved boiling point correction (cf. Sec. 6.1.1). Like in the K-band, the LN_2 calibration, suffers from resonances and an uncertain refractive index of LN_2. Therefore, the T_b uncertainties for non-opaque channels are still smaller for the tipping curve calibration.

Of course, the LN_2 calibration results can be tuned to the tipping curve results by adapting n_{LN_2}. However, when doing this, each channel provides a significantly different n_{LN_2} value. Furthermore, this excludes an independent comparison of both calibration techniques. As mentioned in Section 6.2.6, the impact of atmospheric inhomogeneities can be minimized by averaging over several calibrations. For August 16, the total calibration uncertainty can be reduced by the standard deviation $\sigma(\Delta T_b)$

of all successful tipping curve results of the day (Fig. 6.5). As a result, the assessed calibration uncertainty would disappear in the K-band and reduces from ±0.6 K to ±0.2 K at 51.26 GHz and from ±0.7 K to ±0.4 K at 52.28 GHz (Tab. 6.5).

In contrast to RHUBC-II, the tipping curve results at JOYCE are larger by 0.8 K to 2.4 K (Fig. 6.7). Furthermore, the uncertainty ranges of the two calibration techniques only overlap at 23.04 GHz and 27.84 GHz. The largest deviation between the two techniques occurs at 31.40 GHz (2.4 K). Most probable, it is caused by the comparably weak performance of the tipping curve calibration (cf. Sec. 6.2.6). In the V-band, no tipping curve calibrations can be applied. Note, that the boiling point correction has no influence at close to standard pressure conditions at JOYCE. Like for RHUBC-II, averaging the daily tipping curve results for the K-band from November 16, eliminates the assessed total uncertainty (Tab. 6.11). In contrast to RHUBC-II, the results can not be compared to radiative transfer calculations, because no coincident radiosonde profiles are available for JOYCE.

It is concluded, that a single LN_2 calibration can not be used for the validation gas absorption models at non-opaque radiometer channels. On the one hand, because the total uncertainty range for these channels is in the order of 1 K, and therefore too large (Tab. 6.10, 6.11). The reason is that a single calibration is affected by the standing wave effect, which is up to ±0.7 K. On the other hand, the LN_2 calibration results for K-band channels do neither sufficiently agree with the tipping curve results nor with radiative transfer calculations. Therefore, the tipping curve calibration is the preferred choice for the measurement to model comparison at RHUBC-II (cf. Sec. 7.5), where only a single LN_2 calibration is available. Generally, it is suggested to use the tipping curve calibration whenever possible. This is especially true for low opacity conditions, where the uncertainty of tipping curve results are small (Fig. 6.14). Furthermore, the tipping curve results at 51.26 GHz and 52.28 GHz for RHUBC-II might give the opportunity to further improve the LN_2 calibration throughout the band. In the V-band, an improved LN_2 calibration is valuable for further validation of absorption models. The tipping curve calibration is also the preferred choice for the measurement to model comparison at RHUBC-II in Section 7.5, where the daily mean $\overline{\Delta T_b^{TIP}}$ provides an offset that is used to correct T_b measurements at 51.26 GHz and 52.28 GHz, originally based on the LN_2 calibration. The corrected T_b values are then compared to radiative transfer simulations.

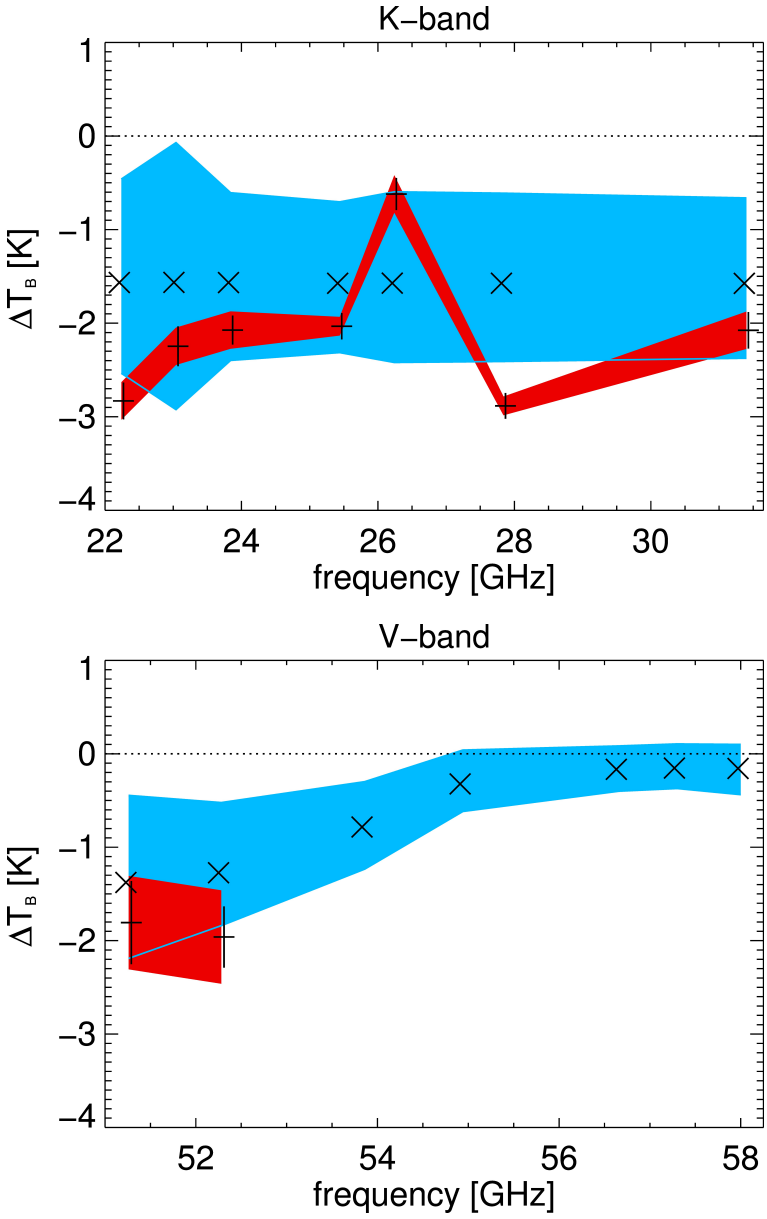

Figure 6.18: Calibration comparison for HATPRO-G2 channels at RHUBC-II. $\Delta T_b = T_b^{CORR} - T_b^{ORIG}$ is the difference of daily mean brightness temperatures measured on August 16, 2009, resulting from two different calibrations. Both, T_b^{CORR} and T_b^{ORIG}, are based on the LN_2 calibration on August 11, 2009. However, T_b^{CORR} includes the boiling point correction for the cold calibration target (Eq. 6.1). Plotted are LN_2 calibration results (X), using the improved boiling point correction (Eq. 6.4), and the estimated uncertainty range of a single LN_2 calibration (Tab. 6.10). Furthermore, tipping curve results from successful tipping calibrations on August 16, 2009 (+) and their standard deviations (*error bars*) are given. The used quality thresholds are $corr_{min} = 0.9995$, $\chi^2_{max} = 1 \times 10^5$. The estimated uncertainty range, associated with a single tipping curve calibration (Tab. 6.10), is marked in *red*.

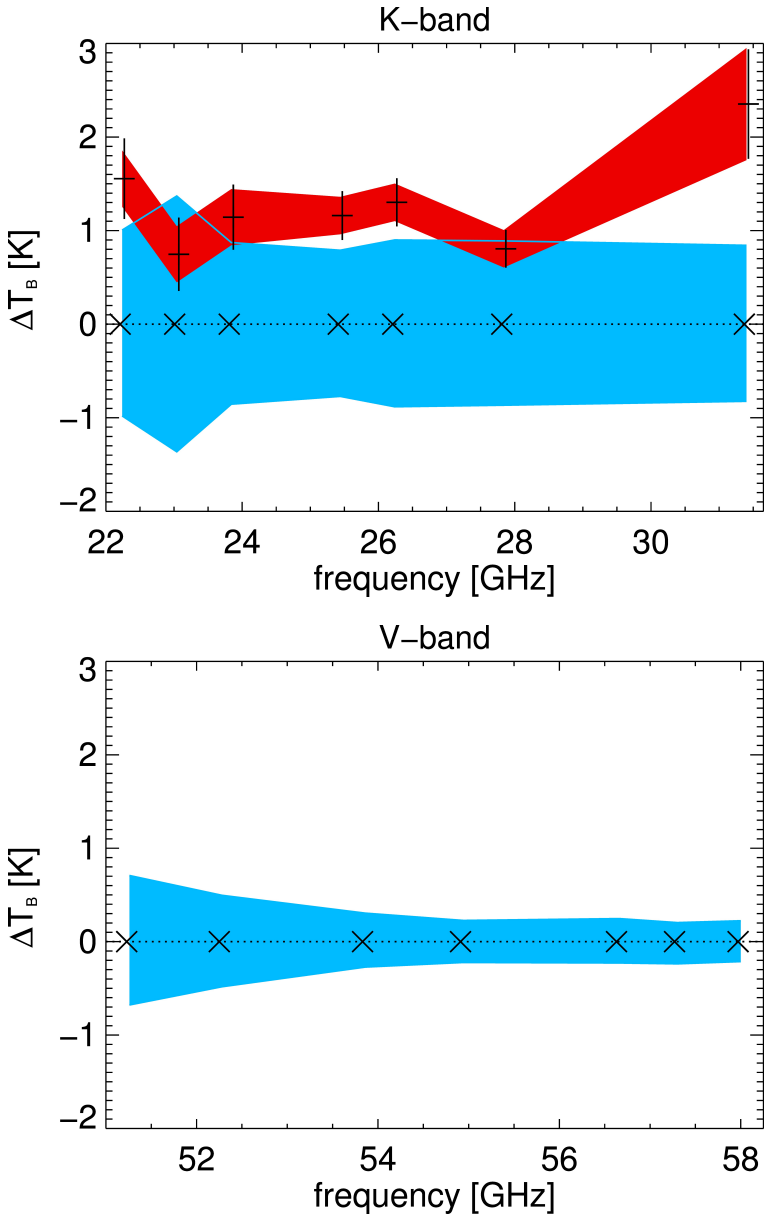

Figure 6.19: Calibration comparison for HATPRO-G2 at JOYCE. ΔT_b refer on the mean zenith T_b that are based on averaged calibrations parameters from eleven LN_2 calibration on November 10, 2011. Plotted are LN_2 calibration results (X) and the estimated uncertainty range of a single LN_2 calibration (Tab. 6.11). Furthermore, tipping curve results from successful tipping calibrations on November 16, 2011 (+) and their standard deviations (*error bars*) are given. The used quality thresholds are $corr_{min} = 0.9995$, $\chi^2_{max} = 1 \times 10^5$. The estimated uncertainty range, associated with a single tipping curve calibration (Tab. 6.11), is marked in *red*.

Table 6.10: Assessed total calibration uncertainties for RHUBC-II in Kelvin. For the LN_2 calibration, the total uncertainty results from uncertainties of the refractive index of the LN_2 surface (n_{LN_2}), from resonances between the receiver and the LN_2 target (res), from uncertainties in the in-situ hot load measurement (hot), and from the detector non-linearity (α). The uncertainties are assessed for the mean T_b values measured at each channel on August 16, 2009. For the tipping curve calibration, the total uncertainty results from the derivation of the mean radiative temperature (T_{mr}), from the beam pointing (poi), and from atmospheric inhomogeneities (atm).

RHUBC-II Liquid Nitrogen Calibration

$\nu\,[GHz]$	n_{LN_2}	res	hot	α	total
22.24	±0.7	±0.4	±0.1	±0.04	±1.2
23.04	±0.7	±0.8	±0.1	±0.04	±1.6
23.84	±0.7	±0.2	±0.1	±0.03	±1.0
25.44	±0.7	±0.1	±0.1	±0.03	±0.9
26.24	±0.7	±0.3	±0.1	±0.03	±1.1
27.84	±0.7	±0.2	±0.1	±0.03	±1.0
31.40	±0.7	±0.2	±0.1	±0.02	±1.0
51.26	±0.6	±0.3	±0.1	±0.03	±1.0
52.28	±0.6	±0.1	±0.0	±0.00	±0.7
53.86	±0.4	±0.1	±0.0	±0.00	±0.5
54.94	±0.1	±0.0	±0.1	±0.00	±0.2
56.66	±0.1	±0.0	±0.2	±0.00	±0.3
57.30	±0.1	±0.0	±0.2	±0.01	±0.3
58.00	±0.1	±0.0	±0.1	±0.01	±0.2

RHUBC-II Tipping Curve Calibration

$\nu\,[GHz]$	mean radiative temperature (T_{mr})	poi	atm	total
22.24	±0.0	±0.0	±0.2	±0.2
23.04	±0.0	±0.0	±0.2	±0.2
23.84	±0.0	±0.0	±0.2	±0.2
25.44	±0.0	±0.0	±0.1	±0.1
26.24	±0.0	±0.0	±0.2	±0.2
27.84	±0.0	±0.0	±0.1	±0.1
31.40	±0.0	±0.0	±0.2	±0.2
51.26	±0.1	±0.1	±0.4	±0.6
52.28	±0.3	±0.1	±0.3	±0.7

Table 6.11: Assessed total calibration uncertainties for JOYCE in Kelvin. For the LN_2 calibration, the total uncertainty results from uncertainties of the refractive index of the LN_2 surface (n_{LN_2}), from resonances between the receiver and the LN_2 target (*res*), from uncertainties in the in-situ hot load measurement (*hot*), and from the detector non-linearity (α). The uncertainties are assessed for the mean T_b values measured at each channel on November 16, 2011. For the tipping curve calibration, the total uncertainty results from the derivation of the mean radiative temperature (T_{mr}), from the beam pointing (*poi*), and from atmospheric inhomogeneities (*atm*).

JOYCE	Liquid Nitrogen Calibration				
$\nu\,[GHz]$	n_{LN_2}	res	hot	α	total
22.24	±0.7	±0.4	±0.1	±0.03	±1.2
23.04	±0.7	±0.7	±0.1	±0.03	±1.5
23.84	±0.7	±0.2	±0.1	±0.03	±1.0
25.44	±0.7	±0.1	±0.1	±0.03	±0.9
26.24	±0.7	±0.3	±0.1	±0.03	±1.0
27.84	±0.7	±0.2	±0.1	±0.03	±1.0
31.40	±0.7	±0.2	±0.1	±0.03	±1.0
51.26	±0.4	±0.2	±0.0	±0.01	±0.6
52.28	±0.3	±0.1	±0.1	±0.00	±0.5
53.86	±0.1	±0.0	±0.1	±0.01	±0.2
54.94	±0.0	±0.0	±0.2	±0.01	±0.2
56.66	±0.0	±0.0	±0.2	±0.01	±0.2
57.30	±0.0	±0.0	±0.2	±0.00	±0.2
58.00	±0.0	±0.0	±0.2	±0.01	±0.2

JOYCE	Tipping Curve Calibration			
$\nu\,[GHz]$	T_{mr}	poi	atm	total
22.24	±0.0	±0.0	±0.3	±0.3
23.04	±0.0	±0.0	±0.3	±0.3
23.84	±0.0	±0.0	±0.3	±0.3
25.44	±0.0	±0.0	±0.2	±0.2
26.24	±0.0	±0.0	±0.2	±0.2
27.84	±0.0	±0.0	±0.2	±0.2
31.40	±0.0	±0.0	±0.6	±0.6

7. Investigation of Gas Absorption Models

Radiative transfer calculations, which use different existing gas absorption models, lead to deviating results. The differences are largest in the V-band, where absorption lines strongly overlap and absorption is difficult to simulate (cf. Sec. 2.1). In this frequency range, T_b simulations may deviate by several Kelvin and accurate measurements are needed for validation (cf. Sec. 7.4). In this respect, MWR measurements and radiative transfer calculations have been compared within several previous studies (*Cimini et al.*, 2004, *Mattioli et al.*, 2005, *Liljegren et al.*, 2005, *Hewison et al.*, 2006). However, these comparisons are based on measurements taken at mid-latitude, close to sea level deployments. *Cimini et al.* (2009) have extended the analysis to Arctic conditions for PWV values between 0.9 mm and 3.6 mm and find inconsistencies between MWR measurements and radiative transfer calculations.

Within this work, the first comparable analysis for a dry high altitude site with PWV values ranging between 0.2 mm and 1.5 mm is presented. The advantage of a high altitude comparison is, that it gives insight in the absorption processes in the middle-to-upper troposphere. RHUBC-II observations at 5322 m provide HATPRO-G2 measurements with coincident radio soundings, which can be used as input for radiative transfer models. This setup is well-suited for investigating different existing gas absorption models (cf. Sec. 2.3) without any disturbing influence of liquid water, which cannot be derived by auxiliary measurements. Furthermore, RHUBC-II conditions allow to calibrate HATPRO-G2's K-band channels and also two V-band channels by tipping curves (cf Sec. 6.2). For these channels, the tipping curve calibration provides a second reference in addition to the LN_2 calibration.

Chapter 5 provides the framework for appropriate radiative transfer simulations of HATPRO-G2 measurements from radio soundings. Furthermore, the uncertainty assessments of Chapter 6 help to quantify the confidence level of radiometer measurements. The resulting T_b simulations consider the exact air mass along the slant observation path, the antenna beam width, and the shape of band-pass filters.

7.1 Radiosonde Profiles

For RHUBC-II, 112 quality controlled profiles from Vaisala RS92-K[1] radiosondes with a high vertical resolution are available. The profiles are used to simulate T_b's, which are compared to HATPRO-G2 measurements. HATPRO-G2 measurements are sensitive to atmospheric liquid water. Since it is not possibly to retrieve profiles of Liquid Water Content (LWC) from MWR measurements (*Crewell et al.*, 2009), the contribution of liquid water cannot be sufficiently included within radiative transfer calculations. Therefore, it is important to exclude radio soundings with water clouds occurring during the ascent. In this work, clear sky conditions are defined by the absence of water clouds, because HATPRO-G2 measurements are insensitive to ice clouds (*Löhnert and Maier*, 2012).

7.1.1 Clear Sky Detection

On the basis of visual inspection, there were no nearby water clouds reported during any of the 112 radiosonde ascents. The objective identification of clear skies is complemented by an approach to detect clear sky conditions via the Liquid Water Path (LWP) retrieved from HATPRO-G2 measurements (*Löhnert and Maier*, 2012). For RHUBC-II, the LWP is calculated by a statistical retrieval algorithm, based on the procedure suggested by *Löhnert and Crewell* (2003). For all 63 radiosondes with coincident HATPRO-G2 measurements, the retrieved LWP is very close to zero (Fig. 7.1). More important for the clear sky detection than the absolute LWP values is, that clouds are characterized by a high LWP variability. Therefore, the temporal variability of LWP during each radiosonde ascent is assessed as well (*Löhnert and Maier*, 2012). As zenith observations at RHUBC-II are only available about every 30 s, the standard deviation of LWP is calculated for 20 min intervals. However, atmospheric liquid water varies on much shorter time scales. This variability is smeared over the averaging interval, because it is undersampled, making it more difficult to define a clear sky threshold for the standard deviation $\sigma(LWP)$. Here, $\sigma = 0.004\,\mathrm{g/m^2}$ is found to be a reasonable clear sky threshold (Fig. 7.1). Higher values give evidence for the presence of liquid water clouds. Only if $\sigma(LWP)$ of all 20 min intervals during an ascent (5 min before and 1 h after launch) is under this threshold, the sonde is assumed to be a clear sky radiosonde. Finally, 62 of the 63 radio soundings with coincident HATPRO-G2 measurements are assumed to represent clear sky conditions and are used for the following T_b simulations (Fig. 7.1).

[1]Vaisala RS92 datasheet, http://www.vaisala.com/Vaisala%20Documents/Brochures%20and%20Datasheets/RS92-D-Datasheet-B210763EN-B-LoRes.pdf

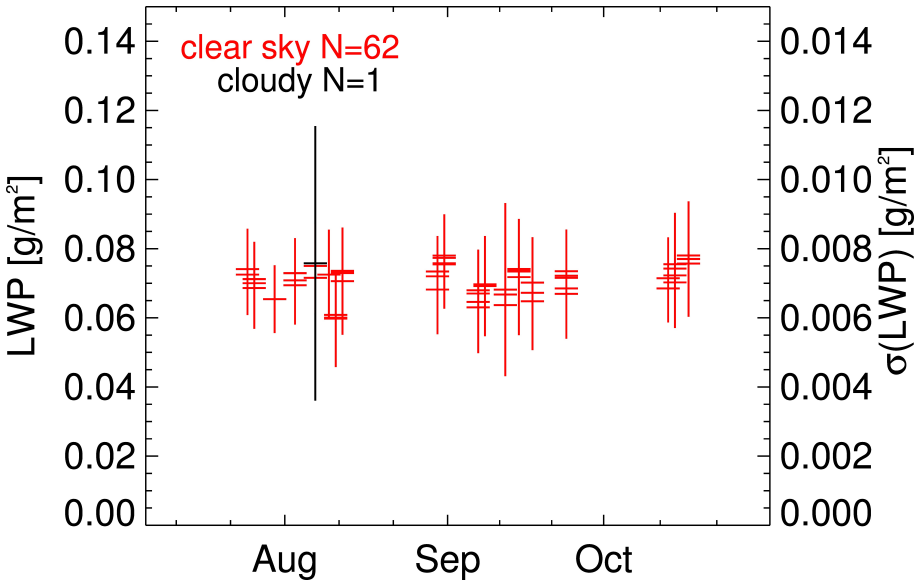

Figure 7.1: LWP from HATPRO-G2 measurements during the time of RHUBC-II radiosonde ascents. The center of the crosses give the mean LWP values (*left* axis), the vertical extend of the crosses give the standard deviations (*right* axis). 62 are launched under clear sky conditions (*red*), for a single one water clouds are detected (*black*).

7.1.2 Profile Extension

RHUBC-II sondes have usually been terminated about 18 km above MSL. Since also height levels above the recorded profiles affect T_b at ground, radiosonde profiles for temperature, pressure, and humidity are extended beyond the tropopause. This is especially important under the low opacity RHUBC-II conditions. It is assumed that the temporal variability of the stratosphere is small enough to use climatological profiles. This approach has also been used in other studies. For example, *Hewison et al.* (2006) extend radiosonde profiles taken in Payerne, Switzerland with a mid-latitude winter profile. Here, a subtropical standard atmosphere with a dry stratosphere is used to extend all RHUBC-II profiles from the highest observed level to 70 km above MSL. Comparative radiative transfer calculations show that for RHUBC-II conditions, K-band channels are almost not affected by the extension. Only for the lowest frequency channel at 22.24 GHz, T_b increases by 0.07 K, when extending the profile. This means, in the K-band, the impact of stratospheric water from heights above 18 km is negligible. However, in the V-band, a notable contribution due to the stratospheric temperature inversion can be recognized with a T_b increase of $0.1\,\mathrm{K} - 0.5\,\mathrm{K}$ for the low opacity channels below 56 GHz. Apart from the MonoRTM, which is insensitive to the used extension, all models show the same T_b effect due to the profile extension.

7.1.3 Uncertainties of Humidity and Temperature Profiles

The quality of the input profiles is an important component of the uncertainty that is associated with T_b simulations. Thus, the uncertainties of the atmospheric profiles have to be assessed. The manufacturer gives a total uncertainty of 5% for the relative humidity profile[2] . However, *Miloshevich et al.* (2009) detect significant mean biases of the humidity profile to other measurements and provide an empirical bias correction. They give a relative accuracy for corrected relative humidity of ±4.5%. For RHUBC-II, the radiosonde humidity profiles have been corrected after *Miloshevich et al.* (2009). The uncertainty is further reduced by adapting the humidity profile to agree with RHUBC-II observations of the 183 GHz microwave radiometer GVRP. ARM scientists use GVRP observations to retrieve a relative humidity offset and a scale factor profile for seven atmospheric height ranges.

However, even the corrected radiosonde profiles of temperature and humidity might still be biased and affect calculated T_b. Besides the given uncertainty of the temperature profile $(\pm 0.5\,\mathrm{K})^2$, a maximum residual uncertainty of 20 % for PWV is assumed. Taking these uncertainty ranges and scaling the original profiles helps to estimate the sensitivity of calculated T_b errors in radiosonde measurements. Figure 7.2 gives the result for the four extreme cases, i.e profiles with PWV being 80% and 120% of the original value, respectively, and a "warm"/"cold" ($T = T \pm 0.5\,\mathrm{K}$) temperature profile. For K-band channels, the impact of a biased humidity increases towards the absorption line. For the V-band channels, T_b changes due to a humidity bias causes changes below 0.1 K. Naturally, the influence of the radiosonde temperature equals the added bias for opaque channels. The influence drops to zero with decreasing channel frequency, but still cannot be neglected for the 53.86 GHz and 54.94 GHz channels, where it is ±0.2 K and ±0.4 K, respectively. For the lowest two V-band channels, the effect is inverted due to water vapor continuum absorption and reaches 0.1 K at 51.26 GHz.

7.2 Radiative Transfer Calculations

Radiative transfer calculations are performed for the five different gas absorption models, introduced in Section 2.3:

- Liebe'87
- Liebe'93
- Rosenkranz'98
- MonoRTM v4.2
- AM v7.2.

[2]Vaisala RS92 datasheet, http://www.vaisala.com/Vaisala%20Documents/Brochures%20and%20Datasheets/RS92-D-Datasheet-B210763EN-B-LoRes.pdf

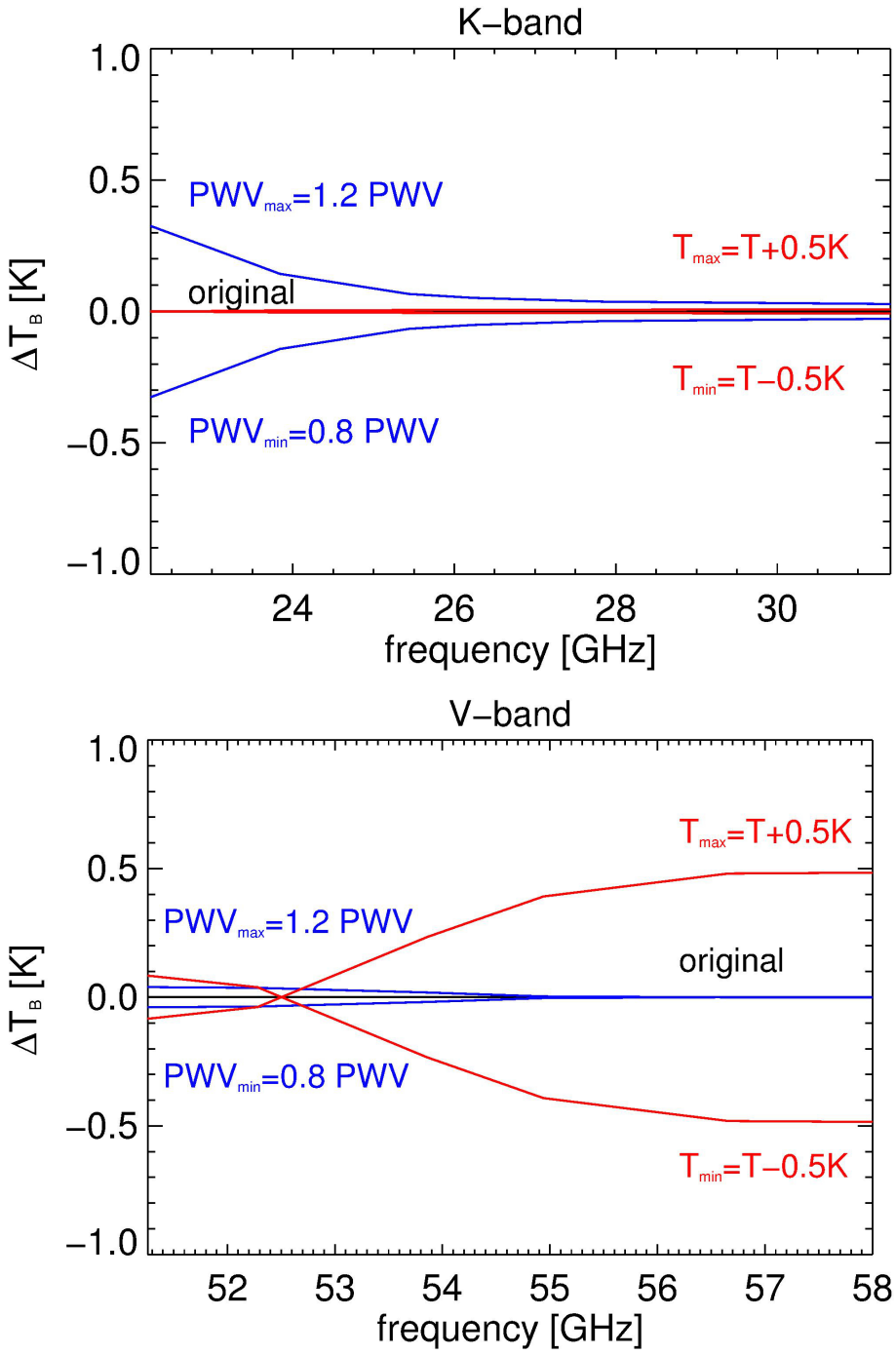

Figure 7.2: Sensitivity of T_b simulations using the Rosenkranz'98 model (*Rosenkranz*, 1998) for HATPRO-G2's K-band (*top*) and V-band (*bottom*) channels to biased radiosonde profiles: T_b differences $\Delta T_b = T_b^{MODIFIED} - T_b^{ORIGINAL}$ are given for four modified profiles: $PWV_{min} = 0.8\,PWV$ and $PWV_{max} = 1.2\,PWV$ (*blue*), $T_{max} = T + 0.5\,\mathrm{K}$ and $T_{min} = T - 0.5\,\mathrm{K}$ (*red*). Plotted are the mean results for 62 clear sky RHUBC-II radio soundings with coincident HATPRO-G2 data being available.

High-resolution profiles of pressure, temperature, and humidity profiles from 62 RHUBC-II clear sky radio soundings are used as input. The calculations only include absorption due to water vapor, oxygen, and nitrogen. The models Liebe'87, Liebe'93, Rosenkranz'98 and MonoRTM are also capable of simulating liquid water absorption, which can be strong in the observed frequency range. In order to allow both, an intercomparison of all models and a comparison HATPRO-G2 clear sky measurements, the liquid water concentration is always set to zero. The AM model is able to simulate absorption by trace gases like ozone or carbon dioxide. Even though the impact on the observed frequency is negligible, trace gas concentration is formally set to zero. Furthermore, the models have different approaches to treat the propagation of radiation through the atmosphere. The MPM-based models Liebe'87, Liebe'93, and Rosenkranz'98 consider the effect of Earth's curvature and atmospheric refraction by using the exact relative air mass as input. The MonoRTM calculates the curvature effect and atmospheric refraction on the basis of a parameterization of *Gallery et al.* (1983). In contrast, the AM includes atmospheric refraction, but has no explicit air mass correction. It assumes a plane parallel atmosphere (*Paine*, 2012). Therefore, the T_b comparison is only performed at zenith, where possible impacts of these effects diminish.

7.3 HATPRO-G2 Measurements

Throughout the campaign, the compared HATPRO-G2 measurements are based on the best available calibration at each channel. In the V-band, HATPRO-G2 measurements are originally based on the LN_2 calibration that was performed in the beginning of the campaign. The high-opacity V-band channels rely on this LN_2 calibration, which has been improved by the adapted boiling point correction for LN_2 (cf. Sec. 6.1.1). For the two low opacity V-band channels at 51.26 GHz and 52.28 GHz, the total uncertainty of the tipping curve calibration is much smaller than for the LN_2 calibration and is therefore used instead. The best available calibration is an average of several tipping curve calibrations. Throughout the campaign, measurements at 51.26 GHz and 52.28 GHz are adapted to the tipping curve calibration by applying the daily mean offset $\overline{T_b^{TIP} - T_b^{MWR}}$ between the two calibration techniques that was detected on August 16, 2009 (cf. Sec. 6.2.6).

Unfortunately, HATPRO-G2 operations have been interrupted repeatedly during the campaign. These interruptions were mostly caused by power outages and lasted from several hours to several days. HATPRO-G2 measurements reveal that some K-band channels are significantly affected by these interruptions. Therefore, K-band observations can neither be compared on the basis of the LN_2 calibration, nor can they be corrected by the same constant offset $\overline{T_b^{TIP} - T_b^{MWR}}$, which is applied to the V-band channels. As an alternative, the tipping curve calibrations, which were

operationally repeated every 6 h, are used (Tab. 4.3). Throughout the campaign, 97 successful calibrations met the quality thresholds given in Table 6.6.

7.4 Inter-Model Comparison

The absorption parameters used by the different models are derived from different data sets. Therefore, the introduced absorption models are compared to each other for two different atmospheric regimes. Two high-resolution clear sky radiosonde profiles serve as model input: a dry RHUBC-II sounding ($p_{surf} = 534$ hPa, $PWV = 0.3$ mm) and a typical mid-latitude, close to sea level sounding from Essen, Germany (1004 hPa, $PWV = 7.5$ mm). The five introduced absorption models are used to simulate zenith T_b for both profiles, with a frequency resolution of 10 MHz. Figure 7.3 shows that for the RHUBC-II sonde, T_b values in the K-band are within 0.2 K for all models except the MonoRTM, which deviates by up 0.7 K close to the line center. For the Essen sounding, apart from the Liebe'87 model, T_b values in the K-band agree within 0.5 K (Fig. 7.4). T_b values from the Liebe'87 model show a constant negative bias relative to the Liebe'93 model of about 0.6 K throughout the band. In the V-band, deviations are larger. At RHUBC-II, the differences between the models are, not surprisingly, largest at the sharp peaks of separated oxygen absorption lines, with a maximum of 34 K at 54.13 GHz. However, also between the peaks, where HATPRO-G2 channels situated (cf. Sec. 4.3), there are also notable differences of more than 2 K. For the Essen sondes the differences in the V-band between the Liebe'93 and the AM even reach values of more than 4 K close to 50 GHz. This indicates the need of validating the different models with HATPRO-G2 measurements.

7.5 Measurement to Model Comparison

HATPRO-G2 T_b measurements at RHUBC-II in the K-band and V-band are compared to T_b simulations at zenith, using the five gas absorption models mentioned above. 62 clear sky radio soundings provide the atmospheric profiles (cf. Sec. 7.1.1), which serve as input for the introduced different gas absorption models (cf. Sec. 7.2). For the comparison, HATPRO-G2 measurements are simulated on the basis of the results of Chapter 5. In the first place, this means that T_b simulations are not just calculations at the nominal channel mid-frequencies, but consider the shape of HATPRO-G2's band-pass filters. In the K-band, band-passes are assumed to be Gaussian shaped with a half-width of 230 MHz (Tab. 4.1). For V-band channels, the exact filter shapes, derived from laboratory measurements, are used (Fig. 5.1). While the band pass effect on T_b is largest at zenith (cf. Sec. 5.1), corrections for the antenna beam width and exact air mass calculations almost vanish at zenith.

In order to compare T_b simulations with the MWR observations, measured T_b is av-

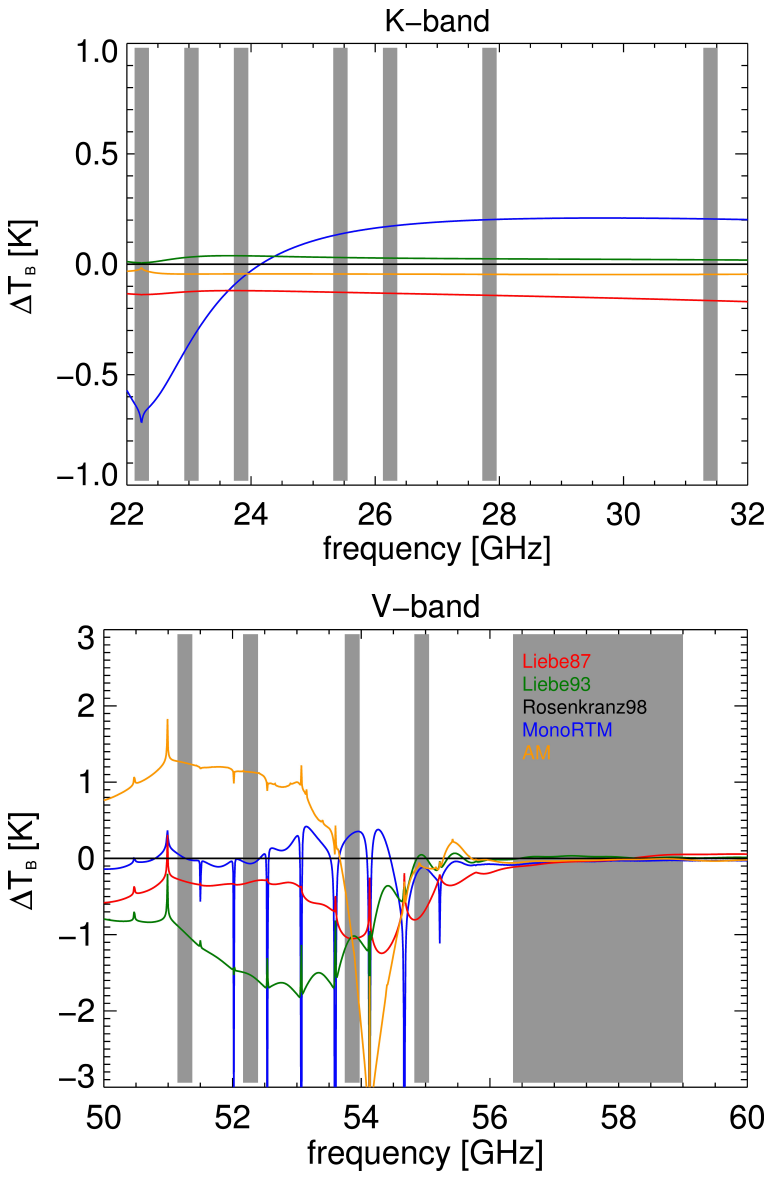

Figure 7.3: Inter-model comparison in the K- and V-band for RHUBC-II: ΔT_b is the difference of zenith T_b simulated by the models Liebe'87 (*Liebe and Layton*, 1987), Liebe'93 (*Liebe et al.*, 1993), MonoRTM (*Clough et al.*, 2005), and AM (*Paine*, 2012) to T_b results of the Rosenkranz'98 model (*Rosenkranz*, 1998). Radiative transfer calculations are performed with a frequency resolution of 10 MHz. The input profile is provided by a very dry RHUBC-II radiosonde, launched on September 13, 2009 ($p_{surf} = 534$ hPa, $PWV = 0.3$ mm).

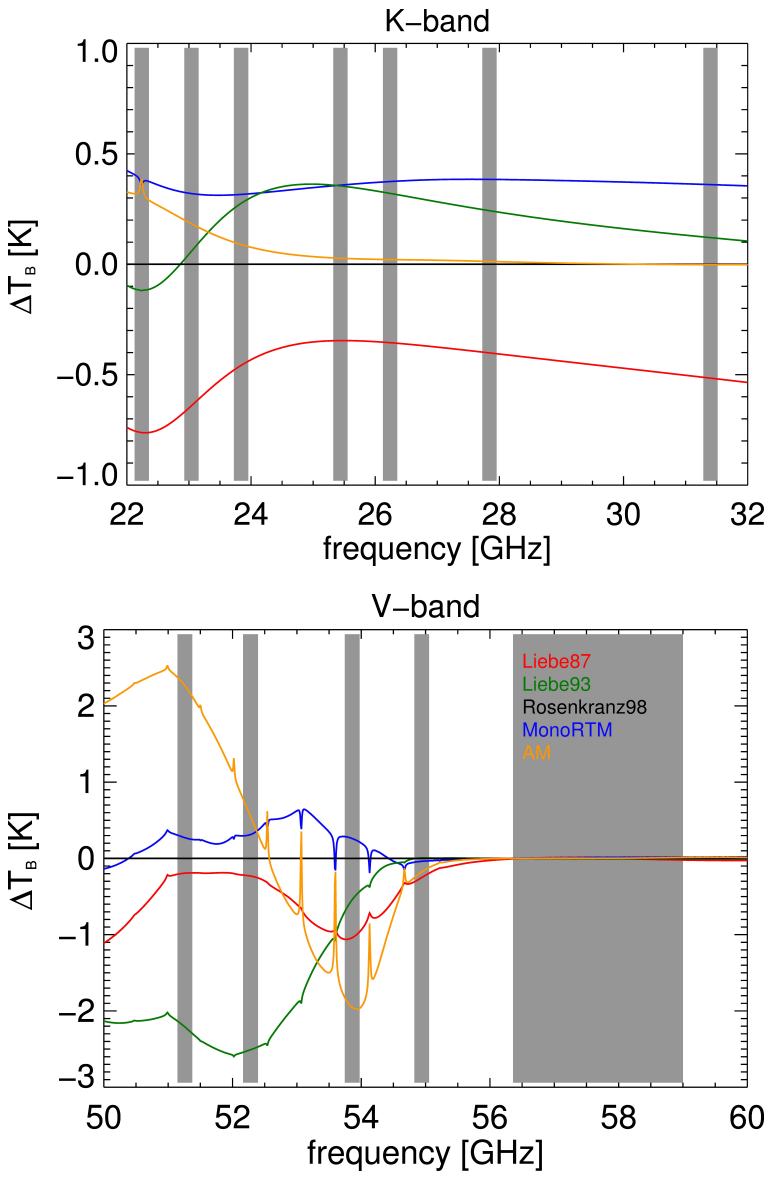

Figure 7.4: Inter-model comparison in the K- and V-band for Essen: ΔT_b is the difference of zenith T_b simulated by the models Liebe'87 (*Liebe and Layton*, 1987), Liebe'93 (*Liebe et al.*, 1993), MonoRTM (*Clough et al.*, 2005), and AM (*Paine*, 2012) to T_b results of the Rosenkranz'98 model (*Rosenkranz*, 1998). Radiative transfer calculations are performed with a frequency resolution of 10 MHz. The input profile is provided by a sonde launched by the German Weather Service (DWD) in Essen on November, 16, 2011 ($p_{surf} = 1004$ hPa, $PWV = 7.5$ mm).

eraged over the radiosonde flight time. The averaging time range extends from 5 min before to 1 h after each radiosonde launch. The standard deviation of HATPRO-G2 measurements within this time window is below 0.2 K in the K-band and 0.4 K in the V-band.

A first overview on the comparison's results is given in Figures 7.5 and 7.6, where the measurements T_b^{MWR} are directly opposed to the simulations T_b^{RTM} of all five models. Additionally, the results for all channels are summarized in Tables 7.1 and 7.2. The standard deviation $\sigma(T_b^{RTM} - T_b^{MWR})$ is not larger than 0.5 K for all channels. The common ground of all models is that σ agrees within 0.1 K, which implies that all models respond similarly to atmospheric variations captured by the observations. Under RHUBC-II conditions, the K-band channels are almost transparent. Nevertheless, for measured T_b values of below 6 K, corresponding to a small signal-to-noise-ratio, it is remarkable that the channel at 22.24 GHz shows a very high linear correlation (> 0.95), between measurements and simulations (Fig. 7.5).

Furthermore, measurements at 22.24 K agree with all models within 0.3 K. Only the MonoRTM gives a positive bias $\Delta = T_b^{RTM} - T_b^{MWR}$ of +0.3 K. Apart from this, the biases in the K-band are always negative. Its absolute values are always smaller than 1.0 K. While the Liebe'93 and the Rosenkranz'98 models give a zero bias close to the absorption line center, the bias for the other K-band channels is smallest for the MonoRTM being less or equal 0.5 K.

The slope that is obtained from a linear regression for T_b^{MWR} and T_b^{RTM} is close to 1 at 22.24 GHz and steadily decreases with channel frequency for all models. The same behavior is observed for the linear correlation $corr(T_b^{RTM}, T_b^{MWR})$ and can be explained by the fact that the dynamic T_b range decreases with channel opacity and is below 1 K for the window channels. Such small variations are in the order of the measurement accuracy and therefore, no assessment of the absorption models can be made. Finally, the impact of different parameterizations of the water vapor continuum (*Turner et al.*, 2009) is found to be negligible, because the absolute humidity during RHUBC-II is too small. Since the maximum deviation between the model results and the bias Δ are below 1 K, it is concluded that, at this stage, it is not possible to validate the absorption models in the K-band.

In the V-band, T_b differences between the models and between measurements and simulations are larger than in the K-band. Δ is largest at 54.94 GHz, where it ranges between −1.8 K (AM) and −2.8 K (Liebe'93). The largest differences between the models is found for the lowest opacity V-band channels at 51.26 GHz and 52.28 GHz. Here, the AM model is closest to the measurement (+0.1 K, +0.5 K). Despite the large biases for non-saturated V-band channels, the slope is close to one for most of the models, because the dynamic T_b range is much larger than in the K-band. For the three opaque V-band channels above 56 GHz, the measurement-to-model difference Δ ranges between −0.3 K and −0.6 K . The models agree within 0.1 K for these channels. Similar to the K-band channels, Δ is almost always negative. In contrast

to the K-band channels, it is concluded that the large biases of the non-opaque V-band channels allow to address the validity the models for these channels.

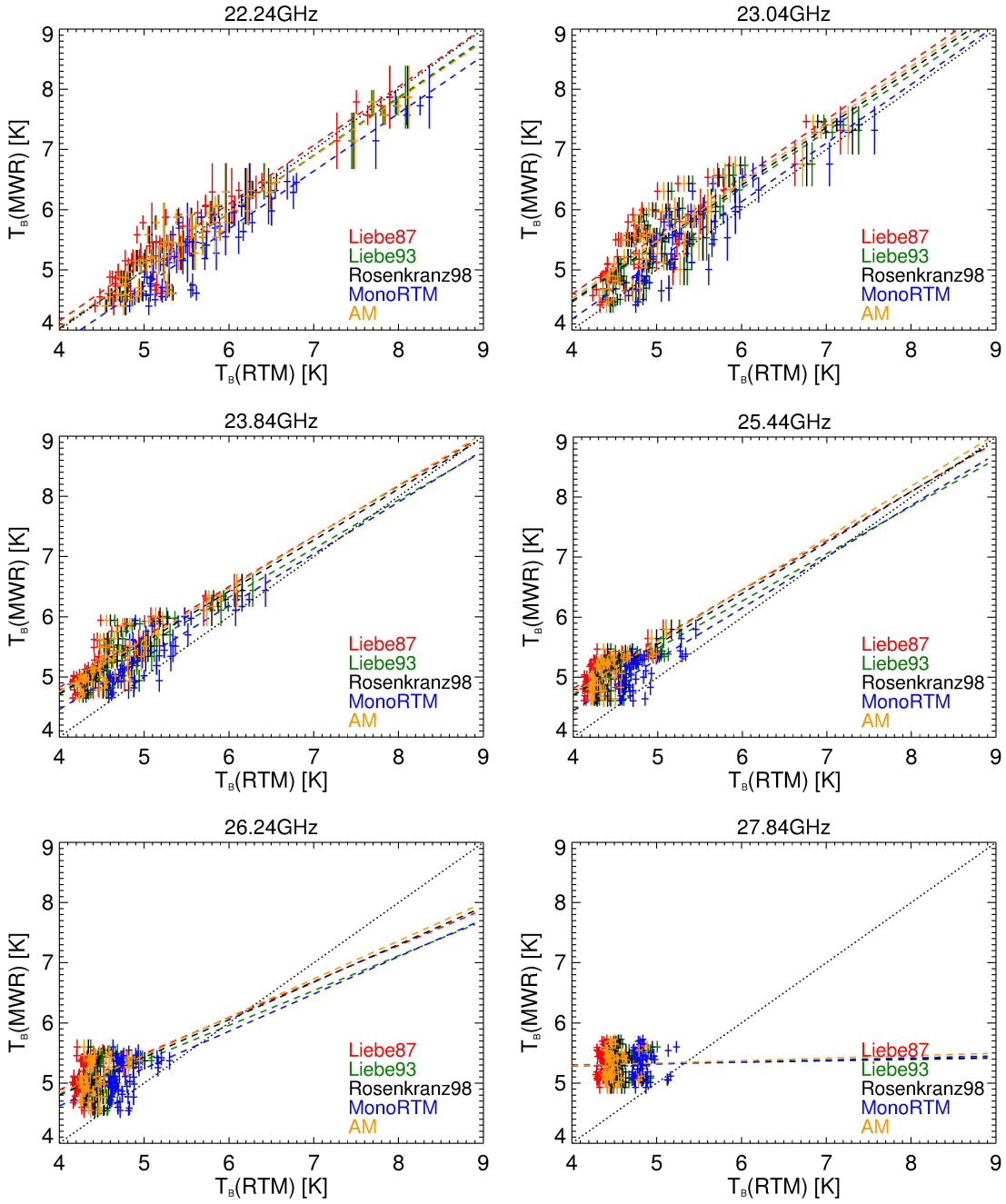

Figure 7.5: Measurements to model comparison in the K-band – scatter plots: zenith T_b simulations for selected HATPRO-G2 in the K-band for 62 clear sky RHUBC-II radio soundings using five different gas absorption models: Liebe'87 (*Liebe and Layton*, 1987), Liebe'93 (*Liebe et al.*, 1993), Rosenkranz'98 (*Rosenkranz*, 1998), MonoRTM (*Clough et al.*, 2005) and AM (*Paine*, 2012). T_b measurements are based on tipping curve calibrations. The vertical extension of the crosses gives the standard deviation of HATPRO-G2 measurements during radiosonde ascents.

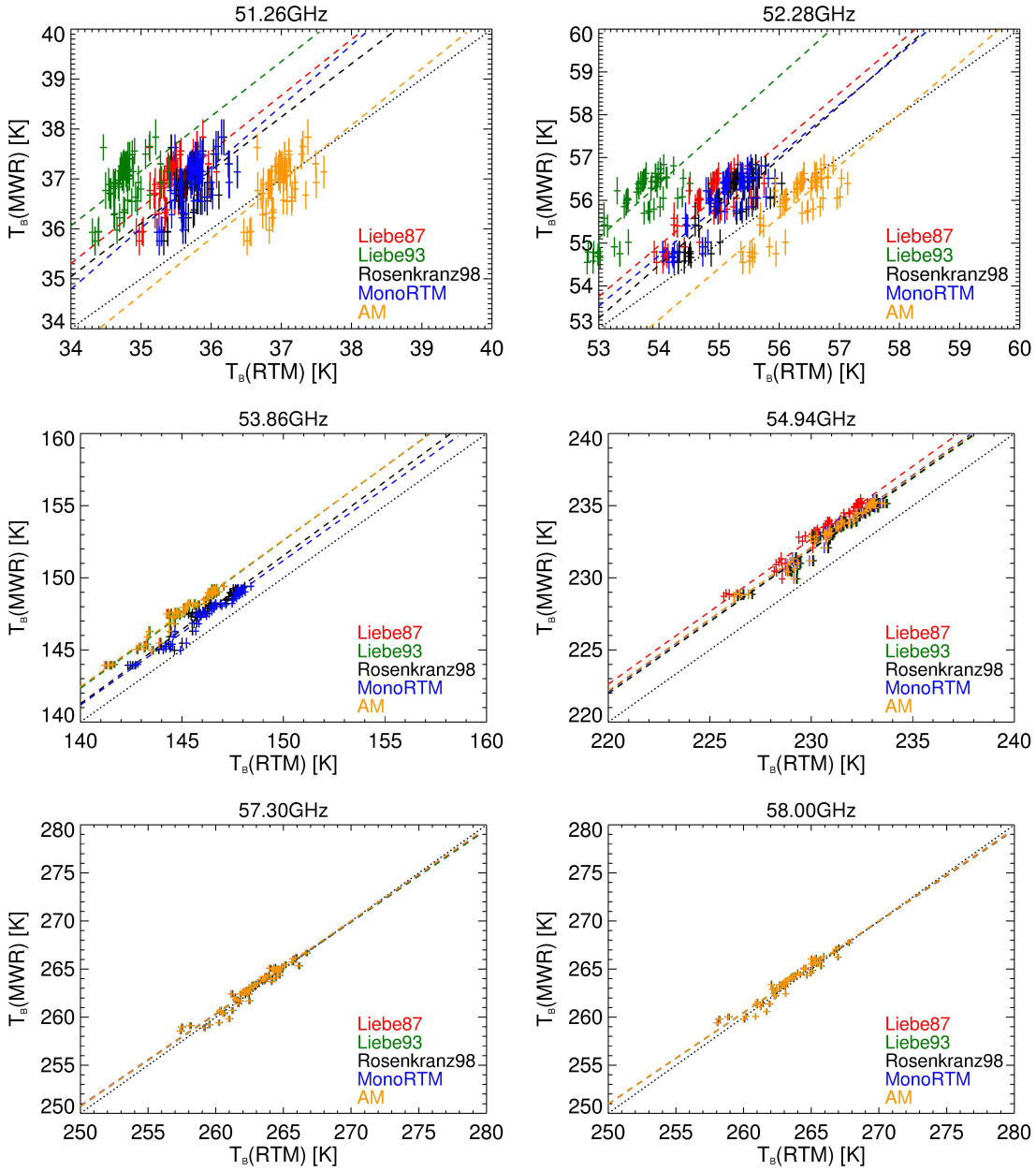

Figure 7.6: Measurements to model comparison in the V-band – scatter plots: zenith T_b simulations for selected HATPRO-G2 in the V-band for 62 clear sky RHUBC-II radio soundings using five different gas absorption models: Liebe'87 (*Liebe and Layton*, 1987), Liebe'93 (*Liebe et al.*, 1993), Rosenkranz'98 (*Rosenkranz*, 1998), MonoRTM (*Clough et al.*, 2005), AM (*Paine*, 2012), T_b measurements at 51.26 GHz and 52.28 GHz are based on tipping curve calibrations, T_b measurements above 53 GHz are based on the LN_2 calibration performed on August 11, 2009. The vertical extension of the crosses gives the standard deviation of HATPRO-G2 measurements during radiosonde ascents.

Validation of the models is only possible, when the measurement accuracy is included. Therefore, the spectral characteristic of the mean biases $\overline{\Delta}$ over all 62 clear sky radiosondes and the total uncertainty of radiometer calibration are given in Figure 7.7. Close to the water vapor line in the K-band, models and measurements deviate by less than 1 K. The best available T_b measurements are based on tipping curve calibrations. For RHUBC-II the estimated uncertainty range of this method is only ± 0.1 K to ± 0.2 K. The consequence is, that T_b simulation lie mostly are outside the measurement limits. The maximum deviation is 0.5 K. Only close to the line center, some models agree with the measurements: At 22.24 K all models except the MonoRTM and at 23.04 GHz the AM and the Liebe'87 give results within the measurement accuracy.

As expected, the differences in V-band are much larger. Mostly, T_b measurements are higher than simulations. When evaluating the model performance, the situation at 51.26 GHz and 52.28 GHz is clear: The AM, with biases of +0.1 K and +0.5 K, respectively, is closest to the measurements. At 51.26 GHz and 52.28 GHz, the AM is the only model that gives results within the uncertainty range of the applied tipping curve calibration. It is followed by the Rosenkranz'98 (-1.1 K, -0.5 K), and the MonoRTM (-1.1 K, -0.7 K). Finally, the Liebe'87 model gives -1.4 K and -0.9 K and the Liebe'93 model -2.1 K for both channels. Furthermore, at 52.28 GHz only T_b simulations by the AM and the Rosenkranz'98 are within the uncertainty limits of the measurements (± 0.5 K). This indicates issues with the assumed half-width of the water vapor line and the simulation of continuum absorption.

As mentioned above, measurements of the other channels are based on the LN_2 calibration. For the channel at 53.86 GHz, only the MonoRTM, with a bias of -0.2 K, and the Rosenkranz'98, with a bias of -0.4 K, lie within the uncertainty range of the measurements. At 54.94 GHz, the absolute bias for all models is larger than 1.5 K, which is about 1 K outside the uncertainty range of the measurements. Finally, the bias does not exceed 0.6 K for the three saturated channels above 56 GHz, but is still outside the radiometer's measurement uncertainty. The mean offset found for the saturated channels might be explained by a systematic displacement of the radiosonde profiles in the first several hundred meters above the site level, because the sondes were mostly launched under strong westerly winds. Within this height range the surrounding orography could lead to systematic deviations between the temperature measured by the sonde and the temperature directly above the site, which is observed by the saturated radiometer channels.

At this point, it has to be mentioned again that the tipping curve calibration gives smaller deviations between the measurements and radiative transfer calulations than the LN_2 calibration – even when the LN_2 calibration is improved by the modified boiling point correction (Eq. 6.4, cf. Sec. 6.3). It can be concluded that in the K-band, all simulated T_bs agree within 0.5 K. Apart from the channels very close to the line center, simulation are too cold by several tenth of a Kelvin. The biases seem to

small for general validation of the used absorption coefficients. With respect to the V-band channels, this work supports the study of *Cadeddu et al.* (2007) who state, that the accuracy of simulated T_b is most sensitive to the line mixing coefficients. For example, 51.26 GHz and 52.28 GHz the MonoRTM and the AM deviate from each other by more than 1 K. Both models, use the same broadening coefficients for the line widths, but different line mixing coefficients (*Tretyakov et al.*, 2005). In this respect, HATPRO-G2 measurements support the use of line mixing coefficients suggested by *Makarov et al.* (2011), which are only used within the AM model. For the same channels, the modification of the line widths and mixing parameters within the Liebe'93 model results in the largest deviation from the measurements (cf. Sec. 2.3.2). While at 53.86 GHz the MonoRTM and Rosenkranz'98 lie within the measurements' uncertainty limits, all models fail the observations at 54.94 GHz. At 54.94 GHz, even the AM, which is closest to the observations, lies outside the measurement uncertainty limits by more than 1 K. This strongly suggests that further research on oxygen spectroscopy is needed within this frequency range.

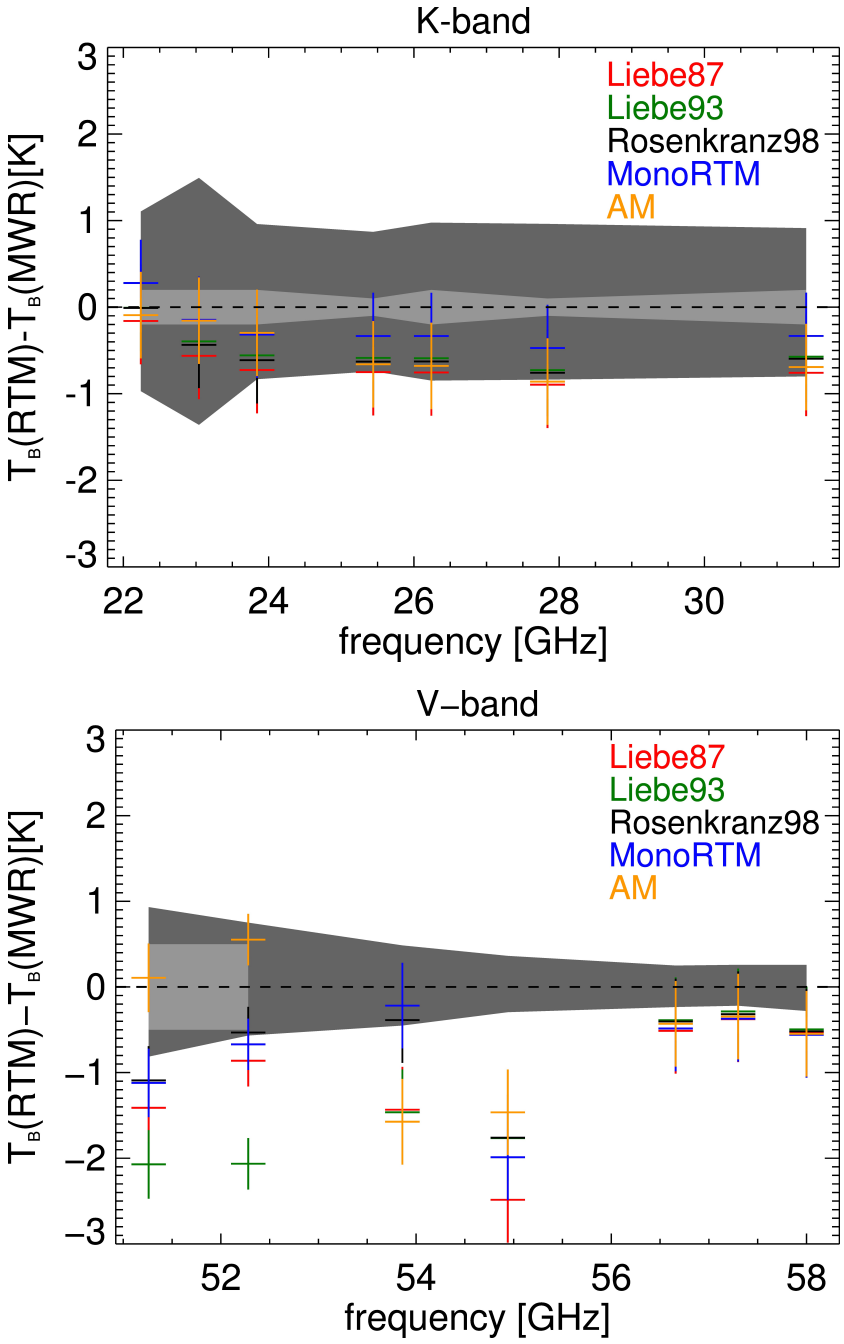

Figure 7.7: Measurement to model comparison – T_b differences: zenith T_b simulations for all HATPRO-G2 in the K-band (*top*) and V-band (*bottom*) for 62 clear sky RHUBC-II radiosondes using five different gas absorption models: Liebe'87 (*Liebe and Layton*, 1987), Liebe'93 (*Liebe et al.*, 1993), Rosenkranz'98 (*Rosenkranz*, 1998), MonoRTM (*Clough et al.*, 2005), AM (*Paine*, 2012), T_b measurements in the K-band and V-band channels at 51.26 GHz and 52.28 GHz are based on tipping curve calibrations, T_b measurements in V-band above 53 GHz are based on the LN_2 performed on August 11, 2009. The vertical extension of the crosses gives the standard deviation of T_b simulations over all 62 radiosondes, *shaded*: assessed total uncertainty ranges (cf. Sec. 6.3.2) of the LN_2 calibration (*dark gray*) and the tipping curve calibration (*light gray*).

Table 7.1: Measurement to model comparison at HATPRO-G2's K-band channels: results from the scatter plots in Figure 7.5 for all five absorption models, the bias $\Delta = (T_b^{RTM} - T_b^{MWR})$, the standard deviation of $\sigma(\Delta)$, the linear correlation coefficient $corr(T_b^{MWR}, T_b^{RTM})$ and the fitted offset and slope(T_b^{MWR}, T_b^{RTM}).

model	$\nu\,[GHz]$	$\Delta\,[K]$	$\sigma\,[K]$	*corr*	$offset$	*slope*
Liebe'87	22.24	−0.2	0.3	0.951	+0.3	0.975
Liebe'93		−0.0	0.3	0.951	+0.2	0.963
Rosenkranz'98		−0.0	0.3	0.951	+0.3	0.953
MonoRTM		+0.3	0.3	0.951	−0.0	0.960
AM		−0.1	0.3	0.951	+0.3	0.964
Liebe'87	23.04	−0.6	0.3	0.890	+0.7	0.967
Liebe'93		−0.4	0.3	0.890	+0.6	0.946
Rosenkranz'98		−0.4	0.3	0.890	+0.6	0.962
MonoRTM		−0.1	0.3	0.890	+0.3	0.976
AM		−0.2	0.4	0.892	+1.2	0.802
Liebe'87	23.84	−0.7	0.3	0.846	+1.5	0.836
Liebe'93		−0.6	0.3	0.847	+1.5	0.808
Rosenkranz'98		−0.6	0.2	0.847	+1.3	0.850
MonoRTM		−0.3	0.3	0.846	+1.0	0.861
AM		−0.3	0.4	0.846	−2.5	0.563
Liebe'87	25.44	−0.8	0.2	0.660	+1.5	0.820
Liebe'93		−0.6	0.2	0.661	+1.5	0.787
Rosenkranz'98		−0.6	0.2	0.661	+1.3	0.847
MonoRTM		−0.3	0.2	0.660	+1.0	0.855
AM		−0.7	0.2	0.662	+1.7	0.759
Liebe'87	26.24	−0.8	0.3	0.352	+2.5	0.599
Liebe'93		−0.6	0.3	0.354	+2.5	0.578
Rosenkranz'98		−0.6	0.3	0.355	+2.3	0.625
MonoRTM		−0.3	0.3	0.350	+0.4	0.620
AM		−0.7	0.3	0.353	+0.4	0.610
Liebe'87	27.84	−0.9	0.2	0.012	+5.2	0.022
Liebe'93		−0.7	0.3	0.014	+5.2	0.024
Rosenkranz'98		−0.8	0.2	0.014	+5.2	0.025
MonoRTM		−0.5	0.2	0.018	+5.1	0.034
AM		−0.7	0.3	0.022	+5.2	0.036
Liebe'87	31.40	−0.8	0.3	0.121	+3.8	0.366
Liebe'93		−0.6	0.3	0.125	+3.7	0.367
Rosenkranz'98		−0.6	0.3	0.127	+3.6	0.391
MonoRTM		−0.3	0.3	0.125	+3.5	0.390
AM		−0.7	0.3	0.133	+3.5	0.426

Table 7.2: Measurement to model comparison at HATPRO-G2's V-band channels: results from the scatter plots in Figure 7.6 for all five absorption models, with the bias $\Delta = (T_b^{RTM} - T_b^{MWR})$, the standard deviation of $\sigma(\Delta)$, the linear correlation coefficient $corr(T_b^{MWR}, T_b^{RTM})$ and the fitted offset and slope(T_b^{MWR}, T_b^{RTM}). Most remarkable results are given in red numbers.

model	$\nu\,[GHz]$	$\Delta\,[K]$	$\sigma\,[K]$	*corr*	*offset*	*slope*
Liebe'87	51.26	−1.4	0.4	0.558	−3.2	1.129
Liebe'93		−2.1	0.4	0.515	−1.7	1.107
Rosenkranz'98		−1.1	0.4	0.497	−1.3	1.066
MonoRTM		−1.1	0.4	0.611	−6.9	1.225
AM		+0.1	0.4	0.565	−5.2	1.139
Liebe'87	52.28	−0.9	0.4	0.826	−9.7	1.192
Liebe'93		−2.1	0.4	0.815	−11.9	1.107
Rosenkranz'98		−0.5	0.4	0.814	−12.6	1.259
MonoRTM		−0.7	0.4	0.838	−9.1	1.177
AM		+0.5	0.4	0.827	−11.9	1.201
Liebe'87	53.86	−1.4	0.3	0.976	−2.0	1.029
Liebe'93		−1.4	0.3	0.976	−2.1	1.030
Rosenkranz'98		−0.4	0.3	0.976	−3.6	1.032
MonoRTM		−0.2	0.3	0.977	−0.2	1.008
AM		−1.6	0.3	0.977	−0.7	1.021
Liebe'87	54.94	−2.5	0.4	0.981	−0.3	1.014
Liebe'93		−1.8	0.4	0.981	+2.3	0.999
Rosenkranz'98		−1.8	0.4	0.981	+1.2	1.004
MonoRTM		−2.0	0.4	0.981	+1.6	1.003
AM		−1.5	0.4	0.981	+2.5	0.997
Liebe'87	56.66	−0.5	0.5	0.969	+6.3	0.978
Liebe'93		−0.4	0.5	0.969	+8.0	0.972
Rosenkranz'98		−0.4	0.5	0.969	+6.9	0.976
MonoRTM		−0.5	0.5	0.969	+6.2	0.979
AM		−0.4	0.5	0.969	+6.5	0.977
Liebe'87	57.30	−0.4	0.5	0.969	+9.3	0.966
Liebe'93		−0.4	0.5	0.970	+10.4	0.962
Rosenkranz'98		−0.3	0.5	0.969	+10.2	0.963
MonoRTM		−0.4	0.5	0.969	+10.7	0.961
AM		−0.3	0.5	0.969	+10.4	0.962
Liebe'87	58.00	−0.5	0.5	0.968	+11.9	0.958
Liebe'93		−0.5	0.5	0.969	+11.9	0.957
Rosenkranz'98		−0.5	0.5	0.968	+12.6	0.955
MonoRTM		−0.6	0.5	0.968	+11.6	0.960
AM		−0.5	0.5	0.968	+11.3	0.977

8. Summary

The main motivation of this work is the observed systematic differences between temperature profiles from radiosondes and those derived from microwave radiometer (MWR) measurements. It is still unclear, to which extent these biases are caused by uncertainties in the oxygen absorption models or by uncertainties in the radiometer calibration (cf. Chap. 1). Therefore, radiative transfer calculations, using different existing absorption models, have been compared to MWR measurements within several studies (*Cimini et al.*, 2004, *Mattioli et al.*, 2005, *Liljegren et al.*, 2005, *Hewison et al.*, 2006, *Cimini et al.*, 2009). For radiometer V-band channels around 60 GHz, biases between the simulations and measurements at zenith direction of more than 2 K are found. Furthermore, the deviations between the different gas absorption models are of the same order. However, absorption model validation and improvement are only possible on the basis of accurate MWR measurements, which are better than 1 K. At this stage, a detailed analysis of the measurement uncertainties is needed. The absolute accuracy of MWR measurements is determined by the radiometer's calibration. Therefore, in this work, two important calibration techniques used with ground-based MWRs, have been analyzed with respect to the total uncertainty they induce to brightness temperature T_b measurements. The total uncertainties, which are inherent in the LN_2 calibration and the tipping curve calibration – both used with the microwave radiometer HATPRO-G2 (cf. Sec. 4.3) – are assessed by investigating possible sources of uncertainty (cf. Chap. 6).

Liquid Nitrogen Calibration

It is found that the uncertainty of T_b measurements is mainly caused by the uncertainty of the cold LN_2 target temperature (cf. Sec. 6.1). For HATPRO-G2 the uncertainty is induced by thermal radiation of the temperature stabilized receiver parts, which is partially reflected back from the LN_2 surface. This has to be considered, when observing the LN_2 target. First of all, the reflectivity of the LN_2 surface is not exactly known. The resulting uncertainty of the assumed temperature for the cold target is about 1 K. Secondly, standing waves, which build up between the LN_2 surface and the receiver, lead to additional differences of up to approximately 1 K, when observing the cold target. However, it is important to mention, that the impact

of standing waves can sufficiently be reduced by averaging the parameters of several LN_2 calibrations.

The impact of total uncertainty within a single LN_2 calibration has been assessed for typical T_b values observed during the dry conditions of RHUBC-II, 5322 m above MSL, and at the mid-latitude JOYCE site, 92 m above MSL (cf. Chap. 4). For RHUBC-II, the T_b uncertainties have been determined to be 0.9 K-1.6 K in the K-band and to be 0.2 K-1.0 K in the V-band. For JOYCE, the total uncertainty is 0.9 K−1.5 K in the K-band and 0.2 K-0.6 K in the V-band. The T_b uncertainties for JOYCE tend to be smaller, because typical T_b values are closer to the LN_2 target in the K-band, and closer to the ambient temperature target in the V-band. Furthermore, the pressure dependent boiling point correction for LN_2, which was used by HATPRO-G2, is only exact for standard pressure conditions. Therefore, the boiling point correction of LN_2 has been modified and is now valid for all altitudes. At 530 hPa, the improved boiling point correction shifts the cold target temperature, compared to the previously used formulation, by more than 1 K (cf. Sec. 6.1.1). Finally, it is found that the T_b accuracy benefits from considering the receiver non-linearity, which is determined within a 4-point calibration scheme. The effect of the non-linearity is up to 0.3 K, when measuring T_b below 10 K, typical for K-band observations during RHUBC-II.

Tipping Curve Calibration

In comparison to the LN_2 calibration, the tipping curve calibration does not depend on a fixed cold target (*Han and Westwater*, 2000). It uses elevation scans to determine a cold calibration point and is based on the assumption of a horizontally homogeneous atmosphere. As T_b measurements from different elevation angles are used, most accurate results are gained by considering the finite antenna beamwidth and by calculating the exact air mass values along the slant observation path (cf. Chap. 5). Both effects increase with channel opacity and reduce the measured T_b of low-opacity channels. In this work, measurements between one and three air masses are used for the tipping curve calibrations. The derived exact air masses consider the Earth's curvature and atmospheric refraction. When these effects are considered, the K-band tipping curve results for JOYCE are affected by 0.1 K-0.2 K compared to a plane parallel, non-refracting atmosphere and a perfect pencil beam. At RHUBC-II, only the two V-band channels show a notable effect. Zenith T_b derived from tipping calibrations is reduced by 0.3 K for both channels. Even though quality thresholds are set to guarantee horizontal homogeneity (cf. Sec. 6.2.5), there is a residual impact of inhomogeneities, which contributes to the total calibration uncertainty. The residual impact on a single tipping curve calibration are different for the two deployments. For K-band channels, it is 0.1 K-0.2 K at RHUBC-II and 0.2 K-0.6 K at JOYCE. Fortunately, for RHUBC-II conditions the two V-band channels at 51.26 GHz and 52.28 GHz are transparent enough to be calibrated by tipping

curves. For these two channels, atmospheric inhomogeneities lead to an uncertainty range of 0.4 K and 0.3 K, respectively. Furthermore, the V-band channels are also effected by small contributions caused by uncertainties in the beam pointing and the derivation of the mean radiative temperature T_{mr}, which is used within the calibration procedure (cf. Sec. 3.3.2). In total, this gives an T_b uncertainty of 0.6 K and 0.7 K at 51.26 GHz and 52.28 GHz, respectively.

The variation between subsequent tipping curve calibrations, i.e. the repeatability, can be up to 0.5 K (cf. Sec. 6.3.1). Therefore, several tipping curve calibrations should be averaged as suggested by *Liljegren* (1999). As a consequence, the atmospheric noise is reduced and with it the total measurement accuracy (*Liljegren*, 1999). In this respect, it is concluded, that the averaged calibrations should, on the one hand, cover a time period, which is large enough to include atmospheric variations. On the other hand, the time period should not be too large, because of long-term drifts or even abrupt changes of the receiver response (cf. Sec. 6.3.1). Nevertheless, one good tipping curve calibration is better than many calibrations of different quality. Furthermore, even a single successful tipping curve leads to more accurate measurement than the LN_2 calibration – even when the impact of standing waves is eliminated. Therefore, it is concluded that the tipping curve calibration is the preferable technique and should be used whenever the atmospheric conditions allow. Still, it seems beneficial to perform both calibration techniques simultaneously in order to detect possible calibration problems.

It can be summarized, that the assessed uncertainty ranges of the two calibration techniques mostly overlap for RHUBC-II (cf. Sec. 6.3.2). At JOYCE, the uncertainty ranges overlap only for two of the seven K-band channels. This means that there are further calibration uncertainties, which are not included in the accuracy assessment. With one exception, these uncertainties are below 0.5 K. Only for the 31.40 GHz channel calibrated at JOYCE, the unexplained uncertainty is larger than 1 K. Most probably, this points to non-identified issues within the tipping curve calibration procedure close to sea level.

Measurement to Model Comparison

On the basis of the error assessment of HATPRO-G2 measurements, RHUBC-II observations offer the unique opportunity to validate gas absorption models in a very dry middle-to-upper troposphere. Thus, the work is completed by a comparison of MWR measurements, based on the best available calibration, to T_b simulations for 62 clear sky radiosondes that were launched during the campaign (cf. Chap. 7). The radiative transfer calculations use five commonly used gas absorption models: the Liebe'87 (*Liebe and Layton*, 1987), Liebe'93 (*Liebe and Layton*, 1987), Rosenkranz'98 (*Rosenkranz*, 1998) models, based on the MPM (*Liebe*, 1985), the MonoRTM (*Clough et al.*, 2005), used by ARM, and the AM (*Paine*, 2012), developed in the astronomer's

community (cf. Sec. 2.3). However, in agreement with previous studies (*Cimini et al.*, 2004, *Mattioli et al.*, 2005, *Liljegren et al.*, 2005, *Hewison et al.*, 2006), T_b simulations in the V-band from different absorption models deviate by up to 2 K. T_b simulations outside the assessed uncertainty range of HATPRO-G2 measurements can be ascribed to the model, i.e. the used absorption parameters. In contrast to the K-band, where different absorption models deviate by less than 1 K, measurements in V-band are higher by more than 2 K in the maximum. Particularly, at 54.94 GHz, radiative transfer calculations lie outside the uncertainty limits of HATPRO-G2 observations by at least 1 K. However, the results for non-opaque V-band channels strongly depend on the used absorption model (cf. Sec. 7.5). For these frequencies, the AM model performs best. At 51.26 GHz and 52.28 GHz the bias is only 0.1 K and 0.5 K, respectively, for measurements based on tipping curve calibrations. With this respect, the results of this analysis support the use of line mixing coefficients suggested by *Makarov et al.* (2011), which are only used within the AM model.

9. Outlook

The uncertainty assessment performed in this work gives insight into the calibration performance of a ground-based MWR during a dry high altitude deployment (RHUBC-II) and a mid-latitude, close to sea level deployment (JOYCE). More studies are needed to explain the differences between the LN_2 calibration and the tipping curve calibration method. Therefore, upcoming measurement deployments should be accompanied by an accuracy analysis of both calibration methods. Particularly, it would be valuable to repeat the sensitivity study for radiometer measurements under different atmospheric conditions.

An important aspect concerning the LN_2 calibration is to guarantee its reproducibility for repeated calibrations. The elimination of perturbing standing waves has already been included in HATPRO-G2's operating software. However, there are further aspects that have to be investigated in the future. Recent experiments provide evidence that in case the LN_2 target is ventilated by air, the boiling point of the calibration target steadily increases within several minutes. The most probable explanation is that oxygen condensates into the LN_2 as long as the boiling point of the target is below the boiling point of liquid air. Nevertheless, the main problem of HATPRO-G2's LN_2 calibration is, that the actual target temperature is not exactly known, because of reflections at the LN_2-air interface. At this point, it is worth to rethink the calibration setup in a way that reflections are eliminated.

Concerning the accuracy of tipping curve calibrations, there are two main aspects that limit the accuracy of MWR measurements. First of all, the calibration results are very sensitive to the beam pointing. HATPRO-G2 has an elevation stepper with a resolution of 0.6°. However, the accuracy and the resolution of the stepper motor is not important, as long as the exact observation angle is measured and stored. In this regard, the manufacturer has improved the elevation control of HATPRO-G2 during the course of this work. Secondly, there is the impact and the treatment of atmospheric inhomogeneities. Averaging of tipping curve calibration is a good possibility to reduce calibration noise due to atmospheric inhomogeneities. Nevertheless, there still is some potential to reduce the variation range of subsequent calibrations. The main goal is to identify horizontally homogeneous conditions. In this work, the linear correlation coefficient and χ^2 of opacity-air mass pairs are used to assess homogeneity. However, it was found that the residual impact on successful tipping curve calibra-

tions, can only be reduced up to a certain level. Beyond this level, stricter thresholds only reduce the number of successful calibrations, but not their variability. Therefore, it may be necessary to think of other strategies that guarantee atmospheric homogeneity. This could be, for example, hemispheric scans, which assess the atmospheric variability of a larger spatial domain, or by adding additional thresholds, for example the variability of the retrieved liquid water path. The latter aspect is interesting with regard to the HATPRO-G2 window channel at 31.40 GHz, where tipping results show variations of up to 4 K within several hours. In this respect, any impact of the receiver performance should be excluded in the future by a sophisticated monitoring of the instrument's stability.

The results of this work may help to improve the LN_2 and the tipping curve calibration, which is essential for the establishment of a ground-based radiometer network. Such a network is needed for temperature and humidity profiling, which is essential for weather forecasting applications. However, it can only provide quality controlled data on an operational basis, if the accuracy of brightness temperatures is sufficient and the calibration uncertainties are well documented. Furthermore, in combination with ongoing studies in atmospheric spectroscopy, improved MWR measurements will be useful in the future to further investigate gas absorption. Finally, an improved gas absorption will raise the accuracy of temperature and humidity profiles that are retrieved from MWR measurements.

LIST OF FIGURES

LIST OF TABLES

LIST OF ABBREVIATIONS

ACRF . . . . . ARM Climate Research Facility

AERI . . . . . Atmospheric Emitted Radiance Interferometer

ADC . . . . . Analog-to-Digital Converter

AM . . . . . Atmospheric Model

AMSU . . . . . Advanced Microwave Sounding Unit

ASD . . . . . Allan Standard Deviation

ARM . . . . . Atmospheric Radiation Measurement

AWS . . . . . Automatic Weather Station

DWD . . . . . German Weather Service

DOE . . . . . U.S. Department of Energy

FWHM . . . . . Full Width Half Maximum

FZJ . . . . . Juelich Research Center, Germany

GaAs . . . . . Gallium Arsenid

GVRP . . . . . G-Band Vapor Radiometer Profiler

HATPRO-G2 . . . . . Humidity And Temperature PROfiler – Generation 2

HITRAN . . . . . HIgh-resolution TRANsmission

HPBW . . . . . Half Power Beam Width

IR . . . . . Infrared

InP . . . . . Indium Phosphide

JOYCE . . . . . Jülich ObservatorY for Cloud Evolution

LN_2 . . . . . Liquid Nitrogen

LTE . . . . . local thermal equilibrium

LNA . . . . . low noise amplifier

LWC . . . . . Liquid Water Content

LWP . . . . . Liquid Water Path

MWR . . . . . microwave radiometer

ML . . . . . main lobe

MSL . . . . . mean sea level

MMIC . . . . . Monolithic Microwave Integrated Circuit

MonoRTM . . . . . Monochromatic Radiative Transfer Model

MPM . . . . . Millimeter-wave Propagation Model

MT_CKD . . . . . Mlawer-Tobin/Clough-Kneizys-Davies water vapor continuum

NIST . . . . . National Institute of Standards and Technology

NWP . . . . . Numerical Weather Prediction

OP-Amp . . . . . operational amplifier

PWV . . . . . Precipitable Water Vapor

RHUBC . . . . . Radiative Heating of Underexplored Bands Campaign

RHUBC-II . . . . Radiative Heating of Underexplored Bands Campaign – Part II

RH . . . . . relative humidity

RMSD . . . . . Root Mean Square Deviation

RMSE . . . . . Root Mean Square Error

RPG . . . . . Radiometer Physics GmbH

RTM . . . . . radiative transfer model

SKIP . . . . . Self-Kontained Instrument Platform

SLL . . . . . side lobe level

SSM/I . . . . . Special Sensor Microwave Imager

LIST OF SYMBOLS

α		non-linearity parameter
γ	MHz/hPa	broadening coefficient
$\mathcal{F}$		antenna pattern
β_a	$Np\,m^{-1}$	linear absorption coefficient
κ_ν	$Np\,m^2\,kg^{-1}$	mass absorption coefficient
j_ν	$W\,sr^{-1}\,Hz^{-1}\,kg{-}1$	emission coefficient
β_e	$Np\,m^{-1}$	extinction coefficient
B_ν	$W\,m^{-2}\,sr^{-1}\,Hz^{-1}$	Planck spectral radiance
$\Delta\nu$	GHz	line width
$\mathbf{D}$		antenna directivity
φ	$^\circ$	elevation angle
R_e	m	Earth's radius
F_n	dB	noise figure
g	$V\,K^{-1}$	detector gain
ϵ		complex dielectric constant
F	GHz^{-1}	absorption line shape
$\mathbf{H}$	m	effective height
I_ν	$W\,m^{-2}\,sr^{-1}\,Hz^{-1}$	spectral radiance
L	Np	attenuation
ν_0	GHz	center frequency

n		complex refractive index
n'		refractive index
R_e	m	Earth's radius
$\mathcal{S}$	$cm^2\,Hz$	absorption line intensity
T_b	K	brightness temperature
T_{back}	K	cosmic background temperature
θ	$^\circ$	zenith angle
T_{mr}	K	mean radiative temperature
T_N	K	noise diode temperature
T_R	K	receiver noise temperature
τ	Np	opacity
x		size parameter
X		relative air mass
Y		line mixing parameter

APPENDICES

APPENDIX A

Radiative Transfer

Brightness Temperature Correction

The Planck spectral radiance

$$B_\nu = \frac{2h\nu^3}{c^2} \cdot \frac{1}{exp\left(\frac{h\nu}{kT}\right) - 1} \tag{A.1}$$

can be expanded in terms of $h\nu/kT$:

$$B_\nu = \frac{2h\nu^3}{c^2} \cdot \frac{1}{\left(1 + \frac{h\nu}{kT} + ...\right) - 1} \tag{A.2a}$$

$$= \frac{2\nu^2}{c^2} \cdot k \cdot T \cdot \frac{\frac{h\nu}{kT}}{\left(1 + \frac{h\nu}{k_T} + ...\right) - 1} \tag{A.2b}$$

$$= \frac{2\nu^2}{c^2} \cdot k \cdot T \cdot \left[1 - \frac{h\nu}{kT} + \frac{1}{3} \cdot \left(\frac{h\nu}{kT}\right)^2 + ...\right]. \tag{A.2c}$$

For $h\nu << kT$, the series expansion can be truncated after the first term. This is the Rayleigh-Jeans-Approximation is widely used in microwave radiometry:

$$B_\nu^{RJ} = \frac{2\nu^2}{c^2}\, k\, T_b^{RJ}. \tag{A.3}$$

The difference between the physical temperature T and the Rayleigh-Jeans brightness temperature T_b^{RJ} can be approximated by truncating Equation A.2c after the third term and setting

$$B_\nu^{RJ} = B_\nu \tag{A.4a}$$

$$\Leftrightarrow T_b^{RJ} = T \cdot \left[1 - \frac{h\nu}{kT} + \frac{1}{3} \cdot \left(\frac{h\nu}{kT}\right)^2\right] \tag{A.4b}$$

$$\Leftrightarrow T_b^{RJ} - T = -\frac{h\nu}{kT} + \frac{1}{3} \cdot \left(\frac{h\nu}{kT}\right)^2 \equiv \Delta T_b \tag{A.4c}$$

$$\Leftrightarrow \Delta T_b = -0.024 \cdot \nu + 0.000192 \cdot \frac{v^2}{T}. \tag{A.4d}$$

Radiative Transfer Equation

Changes of the spectral radiance $I_\nu(0)$ due to emission/absorption along its propagation path $\mathcal{P} = \int_0^{s_0} ds$ are given by

$$\frac{dI_\nu}{ds} = -I_\nu(0)\,\beta_a(s) + \rho\, j_\nu, \tag{A.5}$$

with the absorption coefficient β_a, the emission coefficient j_ν, and the mass density ρ. For local thermal equilibrium (LTE) conditions Kirchhoff's law (Eq. 2.9) gives

$$\frac{dI_\nu}{ds} = \beta_a(s)\,(-I_\nu(0) + B_\nu(T)). \tag{A.6}$$

Using $d\tau = \beta_a\, ds$ (Eq. 2.19), this differential equation is solved as follows:

$$\Rightarrow \frac{dI_\nu}{d\tau_\nu} = -I_\nu + B_\nu(T) \tag{A.7a}$$

$$\Leftrightarrow \frac{dI_\nu}{d\tau_\nu}\, e^{-\tau_\nu} + I_\nu\, e^{-\tau_\nu} = B_\nu(T)\, e^{-\tau_\nu} \tag{A.7b}$$

$$\Leftrightarrow \frac{d}{d\tau_\nu}(I_\nu\, e^{-\tau_\nu}) = B_\nu(T)\, e^{-\tau_\nu} \tag{A.7c}$$

$$\Rightarrow \int_0^{\tau_\nu(0)} \frac{d}{d\tau_\nu}(I_\nu\, e^{-\tau_\nu})\, d\tau_\nu = \int_0^{\tau_\nu(0)} B_\nu(T)\, e^{-\tau_\nu}\, d\tau_\nu \tag{A.7d}$$

$$\Leftrightarrow I_\nu(\tau_\nu(0))\, e^{-\tau_\nu(0)} - I_\nu(0) \;= \int_0^{\tau_\nu(0)} B_\nu(T)\, e^{-\tau_\nu(s)}\, d\tau_\nu \tag{A.7e}$$

$$\Leftrightarrow I_\nu(0) = I_\nu(s(0)) \;+ \int_0^{s(0)} B_\nu(T)\, e^{-\tau_\nu(s)}\, \beta_a ds. \tag{A.7f}$$

APPENDIX B

Experimental Data

Table B.1: Drifts liquid nitrogen calibration parameters within 22 months : derived from 28 HATPRO-G2 LN_2 calibrations performed at the Juelich Research Center, Germany ($FZJ, 92\,\mathrm{m}$ above MSL) between July 2010 and May 2012. Significant drifts are colored *red* (significance level 0.05).

$\nu\,[GHz]$	$drift(\alpha)\,10^5$	$drift(T_N)\,[K]$	$drift(T_R)\,[K]$	$drift(g)\,[\mu V/K]$
22.24	−7.6	+0.2	−0.0	+6.6
23.04	−1.6	+0.1	−0.0	+1.1
23.84	−3.0	+0.1	−0.0	+0.9
25.44	−3.0	+0.1	−0.0	−1.9
26.24	−0.1	+0.1	−0.0	+6.3
27.84	−0.1	+0.1	−0.0	+4.3
31.40	+0.9	0.1	−0.0	+3.2
51.26	+2.4	+1.0	+0.6	−5.5
52.28	+8.3	+1.3	+0.7	−4.2
53.86	+3.4	+1.4	+0.1	−6.1
54.94	+2.5	+1.2	−0.0	−6.5
56.66	+3.7	+1.3	+0.1	−11.5
57.30	+7.9	+1.3	+0.0	−15.3
58.00	+0.1	+1.5	−0.0	+5.2

Table B.2: Liquid nitrogen calibration parameters I: Mean and standard deviation (σ) of the non-linearity parameter α for HATPRO-G2 channels with mid-frequencies ν. Values derived from 11 LN_2 calibrations performed with HATPRO-G2 at the Juelich Research Center, Germany (FZJ, 92 m above MSL) on November 10, 2011.

$\nu\,[GHz]$	$\overline{\alpha}$	$\Delta\alpha$	$\overline{T_N}\,[K]$	$\Delta T_N\,[K]$	$\overline{T_R}\,[K]$	$\Delta T_R\,[K]$	$\Delta g/\overline{g}\cdot 100\%$
22.24	0.9893	0.0019	401.7	0.7	332.4	1.5	1.4
23.04	0.9952	0.0020	399.5	0.6	313.6	1.9	1.5
23.84	0.9930	0.0011	353.9	0.4	248.5	1.0	0.8
25.44	0.9891	0.0011	342.9	0.4	232.5	1.1	0.9
26.24	0.9910	0.0011	370.8	0.5	237.9	1.1	1.0
27.84	0.9923	0.0008	363.7	0.4	248.6	0.9	0.6
31.40	0.9960	0.0009	338.1	0.5	293.8	1.2	0.7
51.26	0.9645	0.0006	1501.3	2.1	760.1	1.5	0.5
52.28	0.9730	0.0010	1345.1	2.5	602.3	1.0	0.7
53.86	0.9715	0.0007	1230.3	1.8	572.3	1.1	0.5
54.94	0.9698	0.0007	1183.9	1.7	600.6	1.1	0.6
56.66	0.9688	0.0006	1082.0	1.5	524.7	1.0	0.4
57.30	0.9617	0.0006	1068.1	1.3	536.7	1.1	0.5
58.00	0.9572	0.0005	1137.0	1.5	588.7	1.1	0.4

Table B.3: Liquid nitrogen calibration parameters II: Mean and standard deviation (σ) of the non-linearity parameter α for HATPRO-G2 channels with mid-frequencies ν. Derived from 28 LN_2 calibrations performed with HATPRO-G2 at the Juelich Research Center, Germany (FZJ) (92 m above MSL), between July 2010 and May 2012.

$\nu\,[GHz]$	$\overline{\alpha}$	$\sigma(\alpha)$	$\overline{T_N}\,[K]$	$\sigma(T_N)\,[K]$	$\overline{T_R}\,[K]$	$\sigma(T_R)\,[K]$	$\sigma(g)/\overline{g}\cdot 100\%$
22.24	0.9891	0.0019	401.064	2.0	332.9	2.3	2.4
23.04	0.9950	0.0018	399.011	1.7	314.0	2.7	1.4
23.84	0.9920	0.0011	353.403	1.5	248.8	1.9	0.8
25.44	0.9887	0.0011	342.523	1.5	232.9	1.9	1.3
26.24	0.9906	0.0011	370.471	1.6	238.3	2.2	1.9
27.84	0.9918	0.0011	363.253	1.5	248.8	1.9	1.3
31.40	0.9950	0.0012	340.124	3.9	293.9	2.1	1.2
51.26	0.9646	0.0007	1500.14	10.8	762.3	7.4	3.5
52.28	0.9734	0.0015	1341.81	12.6	607.0	9.9	39.8
53.86	0.9715	0.0007	1227.28	12.8	573.2	4.3	3.2
54.94	0.9699	0.0008	1181.34	11.6	601.7	4.3	3.2
56.66	0.9691	0.0008	1079.61	11.8	526.8	4.4	6.3
57.30	0.9619	0.0011	1083.83	11.9	538.8	4.3	7.7
58.00	0.9574	0.0007	1134.77	13.8	590.8	5.1	2.1

APPENDIX C

Error Analysis

2-point Calibration Calibration Scheme

The absolute errors of calibration parameters, used within HATPRO-G2's LN_2 calibration, are assessed.

Cold Load Temperature

Assuming that standing waves between the LN_2 surface and the receiver can be eliminated (cf. Sec. 6.1.2), the error of the cold load temperature T_C is detemined by the reflectivity of the LN_2 target

$$r_{LN_2} = \frac{(n_{LN_2} - 1)^2}{(n_{LN_2} + 1)^2} \tag{C.1}$$

$$\Delta r_{LN_2} = \frac{\partial r_{LN_2}}{\partial n_{LN_2}} \cdot \Delta n_{LN_2} = \frac{4(n_{LN_2} - 1)}{(n_{LN_2} + 1)^3}, \tag{C.2}$$

where $n_{LN_2} = 1.2 \pm 0.03$ (*Benson et al.*, 1983) is the refractive index of LN_2. For $r_{LN_2} \neq 0$ a contaminating signal from the receiver (T_{rec}) leads to a reflective component

$$T_{refl} = r_{LN_2} \cdot (T_{rec} - T_C), \tag{C.3}$$

$$\Delta T_{refl} = \sqrt{((T_{rec} - T_C) \cdot \Delta r_{LN_2})^2 + (r_{LN_2} \cdot \Delta T_{rec})^2}, \tag{C.4}$$

which finally affect the temperature at the cold calibration point $T_C \pm \Delta T_C$. If the physical temperature of the LN_2 target is exactly known ($\Delta T_{LN2} = 0$), a receiver temperature of $T_{rec} \pm \Delta T_{rec} = 305 \pm 0.03\,\mathrm{K}$ (RPG-TM, 2011, p.17) and standard pressure ($T_{LN_2} = 77.36\,\mathrm{K}$) affect the absolute error of T_C by:

$$r_{LN_2} = \frac{(n_{LN_2}-1)^2}{(n_{LN_2}+1)^2} = 0.00826447, \tag{C.5}$$

$$T_C = r_{LN_2} \cdot T_{LN_2} + (1 - r_{LN_2}) \cdot T_{rec}, \tag{C.6}$$

$$\Delta r_{LN_2} = \frac{\partial r_{LN_2}}{\partial n} \cdot \Delta n_{LN_2} = \frac{4(n-1)}{(n+1)^3} = 0.00225394, \tag{C.7}$$

$$\Delta T_C = \sqrt{((T_{rec} - T_{LN_2}) \cdot \Delta r_{LN_2})^2 + ((1 - r_{LN_2}) \cdot \Delta T_{LN_2})^2 + (r_{LN_2} \cdot \Delta T_{rec})^2} = 0.5\,\mathrm{K}. \tag{C.8}$$

Hot Load Temperature

An absolute error of the ambient target temperature measurement of $\Delta T_{amb} = 0.2\,\mathrm{K}$ (cf. Sec. 6.1.4) and a detector stability of $\Delta T_{rec} = 0.03$ (RPG-TM, 2011, p.17) is assumed. With a hypothetical reflectivity of the internal ambient target of $r_{amb} = 0.01 \pm 0.005$, a receiver temperature of 305 K and a target temperature $T_{amb} = 273\,\mathrm{K}$, the error propagates as follows:

$$T_H = r_{amb} \cdot T_{amb} + (1 - r_{amb}) \cdot T_{rec}, \tag{C.9a}$$

$$\Delta T_H = \sqrt{((T_{rec} - T_{amb}) \cdot \Delta r_{amb})^2 + ((1 - r_{amb}) \cdot \Delta T_{amb})^2 + (r_{amb} \cdot \Delta T_{rec})^2} = 0.5\,\mathrm{K}. \tag{C.9b}$$

Error Propagation of the Calibration Parameters

When the analytically assessed errors for T_C and T_H (Eq. C.8) are doubled, they give the uncertainty ranges as they are derived in Section 6.1. The cold and hot load temperatures affect the calibration parameters g (detector gain) and T_R (receiver noise), which are determined by a 2-point calibration scheme. It has been found, that results of the error analysis of the 2-point calibration scheme are also valid for the 4-point calibration scheme. Therefore, the parameters from a 2-point calibration can also be used to determine the error of additionally injected noise T_N. Note, that the absolute calibration error, determined by the analytical error propagation, cannot directly be transfered to total T_b uncertainties, when observing the scene.

$$Y = \left(\frac{U_H}{U_C}\right)^{\frac{1}{\alpha}}, \quad T_R = \frac{T_H - Y \cdot T_C}{Y - 1}, \quad g = \frac{U_H}{(T_R + T_H)}, \quad T_N = \left(\frac{U_{HN}}{g}\right)^{\frac{1}{\alpha}} - T_R - T_H, \tag{C.10a}$$

$$\Delta Y = \sqrt{\left(\frac{U_H^{\frac{1}{\alpha}-1}}{\alpha U_C^{\frac{1}{\alpha}}} \cdot \Delta U_D\right)^2 + \left(\frac{U_H^{\frac{1}{\alpha}}}{\alpha U_C^{\frac{1}{\alpha}+1}} \cdot \Delta U_D\right)^2 + \left(\frac{1}{\alpha^2} ln\Big(\frac{U_H}{U_C}\Big)\Big(\frac{U_H}{U_C}\Big)^{\frac{1}{\alpha}} \cdot \Delta\alpha\right)^2}, \tag{C.10b}$$

$$\tag{C.10c}$$

$$\Delta T_R = \sqrt{\left(\frac{\partial T_R}{\partial T_H} \cdot \Delta T_H\right)^2 + \left(\frac{\partial T_R}{\partial T_C} \cdot \Delta T_C\right)^2 + \left(\frac{\partial T_R}{\partial Y} \cdot \Delta Y\right)^2}, \tag{C.10d}$$

$$= \sqrt{\left(\frac{1}{Y-1} \cdot \Delta T_H\right)^2 + \left(\frac{Y}{Y-1} \cdot \Delta T_C\right)^2 + \left(\frac{T_C(1-2Y) + T_H}{(Y-1)^2} \cdot \Delta Y\right)^2}, \tag{C.10e}$$

$$\tag{C.10f}$$

$$\Delta g = \sqrt{\left(\frac{\partial g}{\partial U_H} \cdot \Delta U_D\right)^2 + \left(\frac{\partial g}{\partial T_H} \cdot \Delta T_H\right)^2 + \left(\frac{\partial g}{\partial T_R} \cdot \Delta T_R\right)^2}, \tag{C.10g}$$

$$= \sqrt{\left(\frac{1}{(T_R + T_H)} \cdot \Delta U_D\right)^2 + \left(\frac{\alpha \cdot U_H}{(T_R + T_H)^{(\alpha+1)}} \cdot \Delta T_H\right)^2 + \left(\frac{\alpha \cdot U_H}{(T_R + T_H)^{(\alpha+1)}} \cdot \Delta T_R\right)^2}, \tag{C.10h}$$

$$\tag{C.10i}$$

$$\Delta T_N = \sqrt{\left(\frac{\partial T_N}{\partial U_{HN}} \cdot \Delta U_D\right)^2 + \left(\frac{\partial T_N}{\partial g} \cdot \Delta g\right)^2 + \left(\frac{\partial T_N}{\partial T_R} \cdot \Delta T_R\right)^2 + \left(\frac{\partial T_N}{\partial T_H} \cdot \Delta T_H\right)^2}, \tag{C.10j}$$

$$\tag{C.10k}$$

$$= \sqrt{\left(\frac{U_{HN}^{\frac{1}{\alpha}-1}}{\alpha g^{\frac{1}{\alpha}}} \cdot \Delta U_D\right)^2 + \left(\frac{U_{HN}^{\frac{1}{\alpha}}}{\alpha g^{(\frac{1}{\alpha}+1)}} \cdot \Delta g\right)^2 + \left(\frac{1}{\alpha^2} ln\Big(\frac{U_{HN}}{g}\Big)\Big(\frac{U_{HN}}{g}\Big)^{\frac{1}{\alpha}} \cdot \Delta\alpha\right)^2 + \Delta T_R^2 + \Delta T_H^2}. \tag{C.10l}$$

Table C.1: Error propagation for HATPRO-G2's LN_2 calibration parameters, based on eleven calibrations performed at JOYCE on November 10, 2011. Assumed errors are the refractive index of the LN_2 surface $\Delta n_{LN_2} = 0.03$ (*Benson et al.*, 1983), $\Delta T_H = 0.3\,\mathrm{K}$ of the ambient target in-situ measurement, and the random noise of detector voltages $\Delta U_{det} = 0.02\,\mathrm{V}$, which has been determined from a multi-hour time series on the ambient target.

$\nu\,[GHz]$	ΔY	$\Delta T_R\,[K]$	$\Delta g\,[\mu V/K]$	$\Delta T_N\,[K]$
22.24	0.00258	0.9	6.9	2.0
23.04	0.00255	0.9	7.6	1.9
23.84	0.00348	1.0	9.4	2.1
25.44	0.00302	0.9	12.3	1.9
26.24	0.00336	0.9	11.7	2.0
27.84	0.00308	0.9	12.6	1.9
31.40	0.00292	0.8	12.5	1.7
51.26	0.00313	0.8	8.2	2.5
52.28	0.00628	0.9	8.1	3.5
53.86	0.00344	0.8	12.1	2.4
54.94	0.00306	0.7	12.7	2.2
56.66	0.00328	0.7	15.6	2.2
57.30	0.00313	0.7	16.4	2.1
58.00	0.00251	0.7	17.6	2.0

Bibliography

Allan, D. W. *Characterization, Optimal Estimation, and Time Prediction of Precision Clocks*. Tech. Rep., National Bureau of Standards, Boulder, CO, 80303, 1985. URL `http://www.dtic.mil/cgi-bin/GetTRDoc?AD\=ADA497937`, latest download on Nov. 30, 2012.

Bauer, P., Geer, A. J., Lopez, P., and Salmond, D. *Direct 4D-Var assimilation of all-sky radiances. Part I: Implementation*. Q. J. Roy. Meteor. Soc., 2010. 136(652): pp. 1868–1885.

Benson, J., Fischer, J., and Boyd, D. A. *Submillimeter and Millimeter Optical Constants of Liquid Nitrogen*. Int. J. Infrared Milli., 1983. 4(1): pp. 145–152.

Boukabara, S. A., Clough, S. A., Moncet, J. M., Krupnov, A. F., Tretyakov, M. Y., and Parshin, V. V. *Uncertainties in the Temperature Dependence of the Line-coupling Parameters of the Microwave Oxygen Band: Impact Study*. IEEE Trans. Geosci. Remote Sens., 2005. 43(5): pp. 1109–1114.

Cadeddu, M. P., Payne, V. H., Clough, S. A., Cady-Pereira, K., and Liljegren, J. C. *Effect of the Oxygen Line-parameters Modeling on Temperature and Humidity Retrievals From Ground-based Microwave Radiometers*. IEEE Trans. Geosci. Remote Sens., 2007. 45(7): pp. 2216–2223.

Chandrasekhar, S. *Radiative Transfer*. New York: Dover Publications, 1960.

Cimini, C., Marzano, F. S., Ciotti, P., Han, Y., Cimini, D., Keihm, S. J., and Westwater, E. R. *Atmospheric Microwave Radiative Models Study Based on Ground-Based Multichannel Radiometer Observations in the 20-60 GHz Band*. Fourteenth ARM Science Team Meeting, 2004. URL `http://www.radiometrics.com/cimini-04.pdf`, latest download on Nov. 30, 2012.

Cimini, D., Caumont, O., Löhnert, U., Alados-Arboledas, L., Bleisch, R., Fernández-Gálvez, J., Huet, T., Ferrario, M. E., Madonna, F., Maier, O., Nasir, F., Pace, G., and Posada, R. *An International Network of Ground-based Microwave Radiometers for the Assimilation of Temperature and Humidity Profiles into NWP models*. Ninth International Symposium on Tropospheric Profiling, L'Aquila, Italy, 3-7 September,

2012. URL http://cetemps.aquila.infn.it/istp/proceedings/Session%20P%20-%20Posters/P45_Cimini.pdf, latest download on Nov. 30, 2012.

Cimini, D., Nasir, F., Westwater, E. R., Payne, V. H., Turner, D. D., Mlawer, E. J., Exner, M. L., and Cadeddu, M. P. *Comparison of Ground-based Millimeter-Wave Observations and Simulations in the Arctic Winter*. IEEE Trans. Geosci. Remote Sens., 2009. 47(9): pp. 3098–3106.

Clough, S. A., Shephard, M. W., Mlawer, E. J., Delamere, J. S., Iacono, M. J., Cady-Pereira, K., Boukabara, S. A., and Brown, P. D. *Atmospheric Radiative Transfer Modeling: A Summary of the AER Codes*. J. Quant. Spectrosc. Radiat. Transfer, 2005. 91(2): pp. 233–244.

Crewell, S., Ebell, K., Löhnert, U., and Turner, D. D. *Can liquid water profiles be retrieved from passive microwave zenith observations?* Geophys. Res. Lett., 2009. 36(6).

Crewell, S. and Löhnert, U. *Accuracy of Boundary Layer Temperature Profiles Retrieved With Multifrequency Multiangle Microwave Radiometry*. IEEE Trans. Geosci. Remote Sens., 2007. 45: pp. 2195–2201.

Doviak, R. J. and Zrnic, D. S. *Doppler Radar an Weather Observations*. New York: Dover Publications, 1993.

Forkman, F., Eriksson, P., and Winnberg, A. *The 22 GHz Radio-aeronomy Receiver at Onsala Space Observatory*. J. Quant. Spectrosc. Radiat. Transfer, 2003. 77(1): pp. 23–42.

Gaffard, C. and Hewison, T. J. *Radiometrics MP3000 Microwave Radiometer Trial Report*. 2003. URL http://tim.hewison.org/TR26.pdf, latest download on Nov. 30, 2012.

Gallery, W. O., Kneizys, F. X., and Clough, S. A. *Air Mass Computer Program for Atmosperic-Transmittance/Radiance Calculation: FSCATM*. 1983. 828(AFGL-TR-83-0065): pp. 23–42.

Geer, A. and Bauer, P. *All-sky Assimilation of Radiances from Microwave Sounders at ECMW*. 542. EUMETSAT Conference, Oslo, Norway, 5-9 September, 2011. URL http://www.eumetsat.int/Home/Main/AboutEUMETSAT/Publications/ConferenceandWorkshopProceedings/2011/SP_2011114105950658, latest download on Nov 30, 2012.

Grody, N. C. *Remote Sensing of the Atmosphere from Satellites using Microwave Radiometry*. M. A. Janssen (Editor), *Atmospheric Remote Sensing by Microwave Radiometry*, Chap. 6, pp. 259–333. New York: Wiley-Interscience, 1993.

Güldner, J. and Spänkuch, D. *Remote Sensing of the Thermodynamic State of the Atmospheric Boundary Layer by Ground-based Microwave Radiometry*. J. Atmos. Ocean. Tech., 2000. 18: pp. 925–933.

Han, Y. and Westwater, E. R. *Analysis and Improvement of Tipping Calibration for Ground-based Microwave Radiometers*. IEEE Trans. Geosci. Remote Sens., 2000. 38(3): pp. 1260–1276.

Hewison, T. J. *1D-VAR Retrieval of Temperature and Humidity Profiles from a Ground-Based Microwave Radiometer*. IEEE Trans. Geosci. Remote Sens., 2007. 45(7): pp. 2163–2168.

Hewison, T. J., Cimini, D., Martin, L., Gaffard, C., and Nash, J. *Validating Clear Air Absorption Models using Ground-based Microwave Radiometers and Vice-versa*. Meteorol. Z., 2006. 15(1): pp. 27–36.

Hewison, T. J. and Gaffard, C. *Radiometrics MP3000 Microwave Radiometer Performance Assessment*. 2003. URL `http://tim.hewison.org/TR29.pdf`, latest download on Nov. 30, 2012.

Hollinger, J. P. *Passive Microwave Measurements of Sea Surface Roughness*. IEEE Trans. Geosci. Remote Sens., 1971. 9(3): pp. 165–169.

Hollinger, J. P., Pierce, J.-L., and Poe, G. A. *SSM/I Instrument Evaluation*. IEEE Trans. Geosci. Remote Sens., 1990. 28(5): pp. 781–790.

Hosking, M. W., Tonkin, B. A., Proykova, Y. G., Hewitt, A., Alford, N. M., and Button, T. W. *The Dielectric Constant of Liquid Nitrogen over the Frequency Range 0.5 to 10.4 GHz*. Supercond. Sci. Technol., 1993. 6: pp. 549–552.

Humlicek, J. *Optimized Computation of the Voigt and Complex Probability Functions*. J. Quant. Spectrosc. Radiat. Transfer, 1982. 27(4).

Janssen, M. A. *An Introduction to the Passive Microwave Remote Sensing of Atmospheres*. M. A. Janssen (Editor), *Atmospheric Remote Sensing by Microwave Radiometry*, Chap. 1, pp. 1–36. New York: Wiley-Interscience, 1993.

Kidder, S. Q., Jones, A. S., Purdom, J. S. W., and Greenwald, T. J. *First local area products from the NOAA-15 Advanced Microwave Sounding Unit (AMSU). Battlespace Atmospheric and Cloud Impacts on Military Operations Conference*. Air Force Research Laboratory, Hanscom Air Force Base, MA, 1998. pp. 447–451.

Kneifel, S., Löhnert, U., Battaglia, A., Crewell, S., and Siebler, D. *Snow scattering signals in ground-based passive microwave radiometer measurements*. J. Geophys. Res., 2010. 115(D16).

Kraus, J. D. *Radio Astronomy – 2nd Edition*. Powell, Ohio: Cygnus-Quasar Books, 1986.

Land, D. V., Levick, A. P., and Hand, J. W. *The Use of the Allan Deviation for the Measurement of the Noise and Drift Performance of Microwave Radiometers*. Meas. Sci. Technol., 2007. 18: pp. 1917–1928.

Levis, C. A., Johnson, J. T., and Teixeira, F. L. *Radiowave Propagation*. New Jersey: Wiley, 2010.

Liebe, H. J. *An updated Model for Millimeter Wave Propagation in Moist Air*. Radio Sci., 1985. 20(5): pp. 1069–1089.

Liebe, H. J. *A Contribution to Modeling Atmospheric MM-wave Properties*. Frequenz (J. Telecom.), 1987. 41(1/2): pp. 31–36.

Liebe, H. J. *MPM – an Atmospheric Millimeter-Wave Propagation Model*. 1989. 10(6): pp. 631–650.

Liebe, H. J., Hufford, G. A., and Cotton, M. G. *Propagation Modelling of Moist Air and Suspended Water/Ice Particles at Frequencies below 1000 GHz. Atmospheric Propagation Effects though Natural and Man-Made Obscurants for Visible to MM-Wave Radiation*, 542. AGARD Conference, Palma de Mallorca, Spain, 1993.

Liebe, H. J. and Layton, D. H. *Millimeter-wave Properties of the Atmosphere: Laboratory Studies and Propagation Modeling*. Tech. Rep., Boulder, Colorado, 1987.

Liebe, H. J., Rosenkranz, P. W., and Hufford, G. A. *Atmosperic 60-GHz Oxygen Spectrum: New Laboratory Measurements and Line Parameters*. J. Quant. Spectrosc. Radiat. Transfer, 1992. 48(5/6): pp. 629–643.

Liljegren, J. C. *Automatic Self-Calibration of ARM Microwave Radiometers*. Ninth ARM Science Team Meeting, 1999. URL `http://www.arm.gov/publications/proceedings/conf09/extended_abs/liljegren1_jc.pdf`, latest download on Nov. 30, 2012.

Liljegren, J. C. *Microwave Radiometer Profiler Handbook*. 2002. URL `http://www.wmo.int/pages/prog/gcos/documents/gruanmanuals/Z_instruments/mwrp_handbook.pdf`, latest download on Nov. 30, 2012.

Liljegren, J. C., Boukabara, S. A., Cady-Pereira, K., and Clough, S. A. *The Effect of the Half-Width of the 22-GHz Water Vapor Line on Retrievals of Temperature and Water Vapor Profiles with a Twelve-Channel Microwave Radiometer*. IEEE Trans. Geosci. Remote Sens., 2005. 43(5).

Löhnert, U. and Crewell, S. *Accuracy of cloud liquid water path from ground-based microwave radiometry 1. Dependency on cloud model statistics.* Radio Sci., 2003. 38(3).

Löhnert, U. and Maier, O. *Assessing the Potential of Passive Microwave Radiometers for Continuous Temperature Profile Retrieval using a three Year Data Set from Payerne.* Atm. Meas. Tech., 2012. 5. Doi:10.5194/amt-5-1121-2012, 2012.

Makarov, D. S., Tretyakov, M. Y., and Rosenkranz, P. W. *60-GHz Oxygen Band: Precise Experimental Profiles and Extended Absorption Modeling in a Wide Temperature Range.* J. Quant. Spectrosc. Radiat. Transfer, 2011. 112.

Mattioli, V., Westwater, E. R., Gutman, S. I., and Morris, V. R. *Forward Model Studies of Water Vapor using Scanning Microwave Radiometers, Global Positioning System, and Radiosondes during the Cloudiness Inter-Comparison Experiment.* IEEE Trans. Geosci. Remote Sens., 2005. 43(5): pp. 1012–1021.

Meunier, V., Löhnert, U., Kollias, P., and Crewell, S. *Biases Caused by the Instrument Bandwidth and Beam Width on Simulated Brightness Temperature Measurements from Scanning Microwave Radiometers.* Atm. Meas. Tech., 2013. 6(5).

Miloshevich, L. M., Vömel, H., Whiteman, D. N., and Leblanc, T. *Accuracy Assessment and Correction of Vaisala RS92 Radiosonde Water Vapor Measurements.* J. Geophys. Res., 2009. 114(D11).

Mlawer, E. J., Tobin, D. C., Clough, S. A., and Brown, P. D. *Recent Developments in the Water Vapor Continuum.* Ninth ARM Science Team Meeting Proceedings, San Antonio, Texas, 1999.

Nash, J., Oakley, T., Vömel, H., and Wei, L. *Instruments and Observing Methods, Report No. 107, WMO Intercomparison of High Quality Radiosonde Systems.* Tech. Rep., World Meteorological Oraganization, 2010. URL `http://www.wmo.int/pages/prog/www/IMOP/publications/IOM-107_Yangjiang.pdf`, latest download on Nov. 28, 2012.

Noh, Y. J., Liu, G., Seo, E.-K., Wang, J. R., and K. Aonashi, K. *Development of a Snowfall Retrieval Algorithm at High Microwave Frequencies.* J. Geophys. Res., 2006. 111.

Noterdaeme, P., Petitjean, P., Srianand, R., Ledoux, C., and López, S. *The Evolution of the Cosmic Microwave Background Temperature.* Astronomy and Astrophysics, 2011. 526: p. L7.

Paine, S. *The am atmospheric model.* 2012. URL `https://www.cfa.harvard.edu/~spaine/am/`, SMA technical memo #152, version 7.2.

Payne, V. H., Delamere, J. S., Cady-Pereira, K. E., Mlawer, E. J., Moncet, J.-L., Gamache, R. R., and Clough, S. A. *Air-broadened Half-Widths of the 22 GHz and 183 GHz Water Vapor Line*. IEEE Trans. Geosci. Remote Sens., 2008. 46(11): pp. 3601–3617.

Petty, G. W. *A first Course in Atmospheric Radiation – 2nd Edition*. Madison, Wisconsin: Sundog Publishing, 2006.

Pospichal, B., Maschwitz, G., Küchler, N., and Thomas Rose, T. *Standing Wave Patterns at Liquid Nitrogen Calibration of Microwave Radiometers*. Ninth International Symposium on Troposheric Profiling, L'Aquila, Italy, 3-7 September, 2012.

Reesor, G. E., Dagg, I. R., and Mohabi, S. *The Complex Dielectric Constant of Liquid Nitrogen in the Region 18 to 26 GHz*. Can. J. Phys., 1975. 53(23).

Rose, T., Crewell, S., Löhnert, U., and Simmer, C. *A Network Suitable Microwave Radiometer for Operational Monitoring of the Cloudy Atmosphere*. Atmos. Res., 2005. 75: pp. 183–200.

Rosenkranz, P. W. *Shape of the 5 mm Oxygen Band in the Atmosphere*. IEEE Trans. Antennas Propag., 1975. 23(4): pp. 498–506.

Rosenkranz, P. W. *Interference Coefficients for Overlapping Oxygen Lines in Air*. J. Quant. Spectrosc. Radiat. Transfer, 1988. 39: pp. 287–297.

Rosenkranz, P. W. *Absorption of Microwaves by Atmospheric Gases*. M. A. Janssen (Editor), *Atmospheric Remote Sensing by Microwave Radiometry*, Chap. 2, pp. 37–75. New York: Wiley-Interscience, 1993.

Rosenkranz, P. W. *Water Vapor Microwave Continuum Absorption: A Comparison of Measurements and Models*. Radio Sci., 1998. 33(4): pp. 919–928.

Rosenkranz, P. W. *Correction to: "Water Vapor Microwave Continuum Absorption: A Comparison of Measurements and Models"*. Radio Sci., 1999. 34(4): p. 1025.

Rothman, L. S., D. Jacquemart, A., A. Barbe, Benner, D. C., Birk, M., Brown, L. R., Carleer, M. R., Chakerian Jr., C., Chance, K., Coudert, L. H., Dana, V., Devi, V. M., Flaud, J.-M., Gamache, R. R., Goldman, A., Hartmann, J.-M., Jucks, K. W., Maki, A. G., Mandin, J.-Y., and Massie, S. T. *The HITRAN 2004 Molecular Spectroscopic Database*. J. Quant. Spectrosc. Radiat. Transfer, 2005. 96: pp. 139–204.

Rothman, L. S., Gamache, R. R., Tipping, R. H., Rinsland, C. P., Smith, M. A. H., Benner, D. C., Devi, V. M., Flaud, J.-M., Camy-Peyret, C., Perrin, A., Goldman, A., Massie, S. T., Brown, L. R., and Toth, R. A. *The HITRAN Molecular Database:*

Editions 1991 and 1992. J. Quant. Spectrosc. Radiat. Transfer, 1992. 48(5/6): pp. 469–507.

Rothman, L. S., Gamache, R. R., Tipping, R. H., Rinsland, C. P., Smith, M. A. H., Benner, D. C., Devi, V. M., Flaud, J.-M., Camy-Peyret, C., Perrin, A., Goldman, A., Massie, S. T., Brown, L. R., and Toth, R. A. *The HITRAN 2008 molecular spectroscopic database*. J. Quant. Spectrosc. Radiat. Transfer, 2009. 110: pp. 533–572.

RPG-IM, Radiometer Physics GmbH. *Installation and Maintenance Guide*. 2011. URL `http://www.radiometer-physics.de/rpg/html/Download.html`, latest download on Nov. 28, 2012.

RPG-OS, Radiometer Physics GmbH. *Instrument, Operation and Software Guide*. 2011. URL `http://www.radiometer-physics.de/rpg/html/Download.html`, latest download on Nov. 28, 2012.

RPG-TM, Radiometer Physics GmbH. *Technical Instrument Manual*. 2011. URL `http://www.radiometer-physics.de/rpg/html/Download.html`, latest download on Nov. 28, 2012.

Rüeger, J. M. *Refractive Index Formulae for Radio Waves. JS83 Integration of Techniques and Corrections to Achieve Accurate Engineering*. FIG XXII International Congress, Washington, 2002.

Rutlland, J. *On the Extreme Aridity of Coastal and Atacama Deserts in Chile*. Ph.D. thesis, University of Wisconsin - Madison, 1977.

Schneebeli, M. and Mätzler, C. *A Calibration Scheme for Microwave Radiometers using Tipping Curves and Kalman Filtering*. IEEE Trans. Geosci. Remote Sens., 2009. 47(12).

Shitov, S. V., Uvarov, A. V., Ermakov, A. B., and Vystavkin, A. N. *Measurement of the Reflector Antenna Absorption at Terahertz Frequencies by the Method of a Balanced Radiometer*. Tech. Phys., 2011. 56(11).

Smith, P. A., Davis, L. E., Button, T. W., and Alford, N. M. *The Dielectric Loss Tangent of Liquid Nitrogen*. Supercond. Sci. Technol., 1991. 4: pp. 128–129.

Span, R., Lemmon, E. W., Jacobsen, R. T., Wagner, W., and Yokozeki, A. *A Reference Equation of the State for the Thermodynamic Properties of Nitrogen for Temperatures from 63.151 to 1000 K and Pressures to 2200 MPa*. J. Phys. Chem. Ref. Data, 2000. 29: pp. 1361–1433.

Townes, C. H. and Schawlow, A. L. *Microwave Spectroscopy*. New York: McGraw-Hill, 1955.

Tretyakov, M., Koshelev, M. A., Dorovskikh, V. V., Makarov, D., and Rosenkranz, P. W. *60-GHz Oxygen Band Precise Broadening and Central Frequencies of Fine-Structure Lines, Absolute Absorption Profile at Atmospheric Pressure, and Revision of Mixing Coefficients*. J. Mol. Spectrosc., 2005. 231: pp. 1–14.

Turner, D. D., Cadeddu, M. P., Löhnert, U., Crewell, S., and Vogelmann, A. M. *Modification to the Water Vapor Continuum in the Microwave Suggested by Ground-Based 150-GHz Observations*. IEEE Trans. Geosci. Remote Sens., 2009.

Turner, D. D. and Mlawer, E. J. *The Radiative Heating in Underexplored Bands Campaigns*. B. Am. Meteorol. Soc., 2010. pp. 911–923.

Turner, D. D., Mlawer, E. J., Bianchini, G., Cadeddu, M. P., Crewell, S., Delamere, J. S., Knuteson, R., Maschwitz, G., Mlynzcak, M., Paine, S., Palchetti, L., and Tobin, D. *Ground-based High Spectral Resolution Observations of the Terrestrial Thermal Spectrum Under Extremely Dry Conditions*. Geophys. Res. Lett., 2012. 39.

Ulaby, F. T., Moore, R. K., and Fung, A. K. *Microwave Remote Sensing – Active and Passive – Volume 1*. Artech House, 1981.

Vinogradov, E. A., Dianov, E. M., and Irisova, N. A. *Dielectric Characteristics of Liquid Nitrogen at lambda = 2.3 mm*. Sov. Phys. Tech. Phys., 1967. 11: p. 983.

van Vleck, J. H. and Weisskopf, V. F. *On the Shape of Collision-Broadened Lines*. Rev. Mod. Phys., 1945. 17: pp. 227–236.

Vohwinkel, B. *Passive Mikrowellenradiometrie*. Vieweg, 1988.

Westwater, E. R. *Ground-based Passive Probing using the Microwave Spectrum of Oxygen*. Journal of Research, Section D-Radio Science, 1965. 69D(1): pp. 1201–1211.

Wiedner, M. C. *Noise Characterization and Allan Variances of Water Vapor Monitors*. SMA report 148, 2002. URL `http://www.cfa.harvard.edu/sma/memos/148.pdf`, latest download on Nov. 30, 2012.

Zhang, Y., G, E. J. R., and Yang, S. *Corrected Values for Boiling Points and Enthalpies of Vaporization of Elements in Handbooks*. J. Chem. Eng. Data, 2011. 56: pp. 328–337.

Danksagung

The data used in this paper were collected as part of the ARM Program sponsored by the U.S. DOE, Office of Science, Office of Biological and Environmental Research, Climate and Environmental Sciences Division. The microwave radiometer HATPRO-G2 was funded by the German Science Foundation (DFG, INST 216/519-1FU66). The intensive experiments on HATPRO-G2's LN_2 conducted at the JOYCE site were part of Nils Küchler's bachelor thesis. Parts of his analysis of the standing wave phenomena are also included in this work. Thank you, Nils. I enjoyed working with you.
An dieser Stelle möchte ich allen danken, die mich in den letzten Jahren unterstützt haben und zum Gelingen der Arbeit beigetragen haben.

Danke, Susanne, für die Deinen vollen Einsatz bei der Betreuung meiner Arbeit.
Danke, Uli für die vielen guten Gespräche und das Sich-Hineindenken.
Danke, Mario für das tapfere Korrekturlesen, und natürlich für all die Systemarbeit, die ich in letzter Zeit sehr vernachlässigt habe.
Danke, Rainer für Deine tatkräftige Unterstützung beim Experimentieren.
Thank you, Dave for all your good ideas.
Danke, Sonja, denn es ist gut, wenn man nicht alleine schreibt ... und dann auch noch mit Süssigkeiten versorgt wird.
Danke, Thomas, Danke, Harry, für Eure fachliche Unterstützung
Danke, Kerstin, weil es immer gut ist, eine Kerstin in der Nähe zu haben.
Danke,Birger, für Deine Gastfreundschaft am Forschungszentrum.
Thank you Emiliano for taking care of me during our "Italienreise".
And finally, many Thanks to the whole working group. I really enjoyed the recent years with all of you.

Ein Dank auch an meine Eltern, ohne die ich diese Zeilen jetzt nicht schreiben würde.
Danke, hermano, für Dein Vertrauen in mich.
Danke, Malte, Danke, Jan für die mutmachenden Gespräche von Doktorand zu Doktorand.

Danke Ela, Danke Frida, Danke Hanne für alles und, dass es Euch gibt.
Ich freue mich darauf, Euch mal wieder öfter zu sehen.

Erklärung

Ich versichere, dass ich die von mir vorgelegte Dissertation selbständig angefertigt, die benutzten Quellen und Hilfsmittel vollständig angegeben und die Stellen der Arbeit - einschließlich Tabellen, Karten und Abbildungen -, die anderen Werken im Wortlaut oder dem Sinn nach entnommen sind, in jedem Einzelfall als Entlehnung kenntlich gemacht habe; dass diese Dissertation noch keiner anderen Fakultät oder Universität zur Prüfung vorgelegen hat; dass sie - abgesehen von unten angegebenen Teilpublikationen - noch nicht veröffentlicht worden ist sowie, dass ich eine solche Veröffentlichung vor Abschluss des Promotionsverfahrens nicht vornehmen werde. Die Bestimmungen dieser Promotionsordnung sind mir bekannt. Die von mir vorgelegte Dissertation ist von Prof. Dr. S. Crewell betreut worden.

Köln, den 29. 11. 2013

Gerrit Maschwitz